國 立 交 通 大 學

光電工程研究所

博士論文

長波長與短波長面射型雷射製程之研究

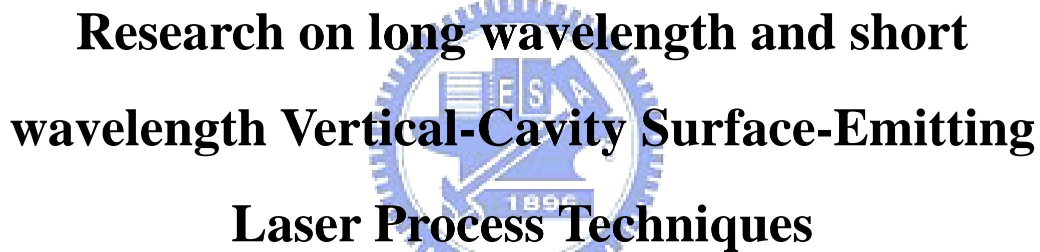

Research on long wavelength and short wavelength Vertical-Cavity Surface-Emitting Laser Process Techniques

研究生: 蔡睿彥 Student: Jui-Yen Tsai

指導教授: 王興宗 Advisor: Shing-chung Wang

中華民國九十四年七月

長波長與短波長面射型雷射製程之研究

Research on long wavelength and short wavelength Vertical-Cavity Surface-Emitting Laser Process Techniques

研究生: 蔡睿彥　　　　**Student: Jui-Yen Tsai**

指導教授: 王興宗　　　　**Advisor: Shing-chung Wang**

國立交通大學
光電工程研究所
博士論文

A dissertation
Submitted to Institute of Electro-Optical Engineering
College of Electrical Engineering and Computer Science
National Chiao Tung University
In Partial Fulfillment of the Requirements
For the Degree of
Doctor of Philosophy
In Electro-Optical Engineering
July 2005
Hsin-chu, Taiwan, Repubic of China

中華民國九十四年七月

長波長與短波長面射型雷射製程技術之研究

研究生：蔡睿彥　　　　　　　　　　　指導教授：王興宗 教授

國立交通大學光電工程研究所

摘要

本論文研究與製作以金屬有機氣相化學沉積法 (Metalorganic chemical vapor deposition, MOCVD)成長之長波長與短波長面射型雷射。面射型雷射其具有圓形光束輸出、低製作成本、單一縱模操作、以及整合二維陣列的潛在特性，因此在長波長範圍之光纖通信、短距數據通信與短波長範圍之高密度光學資訊儲存、高速掃瞄輸出、商業化光源及顯示應用上，成為極具潛力的發光源。本論文針對此二主要課題進行研究：研究及製作 0.45 μm 短波長氮化鎵系列之面射型雷射與 1.3-1.5 μm 長波長磷化銦系列的面射型雷射。

對於氮化鎵系列之面射型雷射，我們研究了氮化銦鎵/氮化鎵主動層材料之最佳條件。這些最佳條件包含量子井的數目、厚度及矽摻雜於位障層，皆會影響主動層之發光效率，這些優化之參數已由發光二極體 (LED) 證實。低銦含量(<20 %)量子井之LED，在 20 毫安培之最大光輸出其最佳量子井數目為 6 個週期、量子井厚度為 3.2 nm。矽摻雜於位障層可明顯提升發光效率，矽摻雜流量=0.19 sccm於位障層之LED在 20 毫安培之最大光輸出比矽摻雜流量=0.12 sccm於位障層之LED高了約 20 %。我們也製作了使用一維光子晶體反射鏡得到高取出效率之藍光LED。此一維光子晶體反射鏡包含了 14 週期堆疊之TiO_2/SiO_2介電材料，在大角度範圍比傳統布拉格反射鏡 (DBR)具有較高反射率。在相同波長比傳統LED之輸出功率有 80 %的提升。我們也已經實現了光激發之氮化鎵面射型雷射，其結構包含了由MOCVD成長之 25 對AlN/GaN 布拉格反射鏡 (DBR)、3λ長共振腔以及 8 對Ta_2O_5/SiO_2介電材料。已成功光激發的氮化鎵面射型雷射，其雷射波長為 448 nm，線寬只有 0.25 nm。

在傳統製作長波長面射型雷射的材料中，缺乏折射率差異大的材料組合以製作高反射率的布拉格反射鏡，加上傳統長波長雷射的主動層材料，其高溫特性不佳，也缺乏可氧化之電流侷限材料，使得不易製作長波長面射型雷射。因此，在長波長面射型雷射研究中，我們優化長波長雷射主動層的各種參數，我們發現量子井中的應力參數、多量子井的應力補償、以及摻雜條件的多寡皆會影響雷射特性，我們優化各項參數，得到最好的臨界電流密度為 1.4 kA/cm^2。另一方面，我們使用MOCVD成長磷化銦系列的布拉格反射鏡，成功製作出高反射率的布拉格反射鏡，並研究其光學及電氣特性。同時，我們也嘗試製作以磷化銦搭配空氣，在只有三對組合下成功得到 99 %高反射率的布拉格反射鏡。我們已成功的製作出以光激發操作的磷化銦系列的布拉格反射鏡，加上週期性增益之共振腔，再加上以介電材料製成的布拉格反射鏡組合而成的長波長面射型雷射，以連續光激發的方式操作，其等效的臨界電流密度為 2 kA/cm^2，雷射波長為 1562 nm。

我們也製作了電激發式的長波長面射型雷射，發展了選擇性蝕刻、Si 離子蝕刻、磊晶再成長之埋藏式穿透接面技術，但是仍然有許多電流侷限、散熱問題需要進一步解決，在本研究中尚未達到電激發式操作，但這些研究經驗對未來製作出電激發式的長波長面射型雷射提供了良好的基礎。

Research on long wavelength and short wavelength Vertical-Cavity Surface-Emitting Laser Process Techniques

Student: Jui-Yen Tsai Advisor: Dr. Shing-Chung Wang

Institute of Electro-Optical Engineering
National Chiao Tung University

Abstract

In this study, we have developed the fabrication of long wavelength and short wavelength vertical cavity surface emitting lasers (VCSELs) by metal organic chemical vapor deposition (MOCVD). The vertical cavity surface-emitting laser (VCSEL) featuring circular-beam output, low production-cost, single longitudinal-mode operation, and possible integration of two-dimensional array are potentially suitable for fiber communication systems and short distance data transmission systems in long wavelength range, and for high-density optical data storage (for example: CDs and DVDs) and high-scan-speed laser printing, commercial lighting source and display applications in short wavelength range. In this thesis, we concentrate on these two topics. To investigate and develop the 1.3-1.5 μm InP-based VCSELs and ~0.45 μm GaN-based VCSELs.

For InGaN/GaN-based VCSELs, we investigated the optimized conditions of the InGaN/GaN active layers. The overall optimization of these factors consists of quantum well number, thickness and Si-doped barrier. The optimization of InGaN/GaN MQW is established by light-emitting diodes. It is shown clearly that the EL output power at 20 mA of low In-content (< 20 %) LED sample with six-wells

and 3.2 nm-thick thickness is highest. We have studied the effect of Si doping on the GaN barriers. As increasing Si doping in the barriers, the PL shows an increase of emission intensity and a blueshift of peak energy. With the same MQW emission peak at about 460 nm and driving current of 20 mA, it is found that the light output power of the LED with Si flow rate of 0.19 sccm is 20 % of magnitude higher than that of LED with Si flow rate of ~ 0.12 sccm. This result shows that PL intensity and LED output power of the MQW samples with Si-doped barrier layers are dramatically increased.

Additionally, we also fabrication high extraction efficiency of InGaN LEDs with an omnidirectional One-dimensional Photonic Crystals (1D PC) incorporated into the bottom of InGaN blue LED chips. The designed omnidirectional 1D PC composed of two different transparent optical materials TiO_2 and SiO_2 layers stacked alternately. It is shown that the omnidirectional 1D PC has a higher reflectance and a wider reflection angle than a conventional distributed Bragg reflector (DBR). With the same MQW emission peak at about 450 nm and at 20 mA, it is found that the light output powers of the LED with 1D PC is about 11.7 mW and an up to 80 % enhancement in the extracted light intensity is demonstrated.

We have demonstrated the optically pumped GaN-based VCSELs structure grown by MOCVD. The 25 pair AlN/GaN DBR structure and 3λ cavity layer were consisted in this VCSEL structure. The AlN/GaN mirror with 25 pairs of DBR can achieve the high reflectivity of 94 % and the wide FWHM of reflectance spectrum about 33nm. The Ta_2O_5/SiO_2 mirror with 8 pairs of DBR can achieve the high reflectivity of 97.5 % and the wide FWHM of reflectance spectrum about 115nm. The PL emission of and the FWHM of emission spectrum of overall VCSEL structure were 448 nm and 1.4 nm, respectively. The narrow FWHM of 1.4 nm is attributed to the Febry-Perot cavity effect. The stimulated emission of fabricated GaN-based

VCSEL was achieved and observed by using the optical pumping system. The GaN VCSEL emits 448nm blue wavelength with a linewidth of 0.25 nm. It evidently expresses the behavior from spontaneous emission to stimulated emission.

For InP-based VCSELs, the absence of high refractive index contrast in InP-lattice-matched materials impeded the development of 1.3-1.5 μm VCSELs. In addition, active layers with insufficient gain at elevated temperature, absence of natural oxidized current aperture and poor heat conductance in material systems for long wavelength range are problems in making LW-VCSELs. We have determined InGaAlAs as the gain material and applied it into the conventional edge emitting lasers to find out the optimized conditions of the active layers. The amount of compressively strain in quantum wells, the net amount of strain in multiple quantum wells (MQWs) with more pairs, and the impurity concentration strongly influenced the performance of edge emitting lasers. The overall optimization of these factors makes us obtaining low threshold current density of 1.4 kA/cm^2. On the other hand, we have fabricated InP/InGaAlAs-based DBR with excellent electrical and optical properties using MOCVD and the growth interruption technique. Meanwhile, we have successfully fabricated, and demonstrated a rigid InP/airgap structure with high reflectivity at 1.54 μm using InGaAs as the sacrificial layer. The 3-pair InP/airgap DBR structure has a peak reflectivity at 1.54 μm with a stop-band width of about 200 nm.

We also successfully have demonstrated the optically pumped InP-based VCSELs with the 35 pairs InP/InGaAlAs DBRs and 10 pairs SiO_2/TiO_2 top dielectric mirrors and a 2λ thick cavity composed of periodic strain compensated MQWs to fully utilize the gain in every quantum well. The optically pumped VCSELs operated at room temperature with equivalent threshold current density calculated to be 2 kA/cm^2. The wavelength of the output beam is 1562 nm. We fabricated electrically

driven continuous wave LW-VCSELs by using selectively etched undercut apertures technique, Si-implant technique, regrowth technique. Electrically driven continuous wave operation has not yet to be achieved. Many issues in making electrically driven LW-VCSELs still need to be resolved in the future.

誌 謝

這四年的博士班生涯，心中由衷的感謝指導老師王興宗教授與郭浩中教授細心指導與教誨，讓我學習到認真作研究的態度、實驗的技巧以及規劃整體實驗的能力。在產學合作及待人處世方面，兩位指導老師的風範更讓我受益良多。

這些年來，特別感謝實驗室余長治、朱振甫、盧廷昌學長在各方面的幫助與指導，同梯的亞衒、芳儀、道鴻、忻宏在實驗上的幫忙及學習過程相互的勉勵。感謝林佳鋒、李兆逵、賴利宏學長在求學過程的指導與鼓勵，及博士班學弟志強、榮堂、泓文、誼安在實驗上的協助。感謝各屆學弟妹哲偉、聖彬、峻偉、文君、妙佳、偉倫、俊毅、永龍、威佑、文燈、裕鈞、傳煜、永昌、瑞溢、國峰、敏瑛、薏婷在實驗上的幫忙以及為實驗室的付出。感謝口試委員彭隆瀚老師、李三良老師、李柏璁老師對我論文的指導與建議。感謝所有幫助過我的老師與朋友們!

最後特別感謝我親愛的家人及女友，在我心情低落時，對我的包容與支持。讓我能無後顧之憂的順利完成學業。

謝謝大家！！

睿彥　于94年7月4日

交通大學光電工程所

Content

Abstract (in Chinese)……………………………………………………………………...i

Abstract (in English)……………………………………………………………………..iii

Acknowledgements…………..…………………………………………………………....vii

Contents……………………………………………………………………….….viii

Table Captions…………………………………………………………………….….xii

Figure Captions…………………………………………………………….....……xiii

Chapter 1 Introduction

1.1 The Background and History of Semiconductor lasers………………… …..1

Semiconductor laser……………………………………………………………1

Optical communication…………………………………………….……..…2

1.2 Vertical Cavity Surface Emitting Lasers…………………………………..…3

Structure………………………………………….…...……………….……3

Advantages and drawbacks………………………………………………….……4

VCSEL applications…………………………………….……………………..…7

1.3 Overview of this Thesis……………………………………………………..…12

Reference………………………………………………………….………..…..15

Chapter 2 Fundamental pricipal of Vertical Cavity Surface Emitting Lasers

2.1 General Characteristics in Semiconductor Lasers……….....……….20

Semiconductor Laser Oscillation Conditions………………..…………..…20

General Characteristics of VCSELs……………………….……………….24

Transverse Modes in VCSELs……………………………………….....…26

2.2 Modeling the Gain Mediums……………………………………..….….28

Optical Gain in Semiconductors……………………………..…………28

Optical Gain in Quantum Well Structures………………………………31

Nonradiative Transitions…………………………………………..…33

Optical Gain in Strained Quantum Wells……………………………..……34

2.3 Characteristics of Distributed Bragg Reflectors………..………36

Transfer Matrix Method…………………………………..……..……36

Reflection Delay and Penetration Depth of DBRs……….……………..…39

2.4 Analysis of the Heat Flow……………………………….……...41

Reference…………………………………………………………..43

Chapter 3 Principal Issues in Design of Vertical Cavity Surface Emitting Lasers for short to long wavelength

3.1 Development of long wavelength VCSEL ……………………...…..71

3.2 Development of short wavelength VCSELs…………………...…76

Reference…………………………………………………………..78

Chapter 4 Fabrication of short Wavelength Vertical Cavity Surface Emitting Lasers

4.1 Optimization of the InGaN/GaN Active Layers……………….....83

The Effect of thickness and number on InGaN quantum well…………..…83

The Effect of Si-doped barrier……….……………………………..…88

4.2 Enhancement of Light Output in InGaN-based Light-Emitting Diodes with Omnidirectional One-dimensional Photonic Crystals……………………………………………….………..92

4.3 Optically Pumped short-wavelength VCSELs………………..……97

Fabrication of GaN-based VCSEL………………………………………98

Reflectance Spectrum and Photoluminescence……………….…………………98
The Characteristics of Optically Pumped GaN-based VCSEL…………...99
Reference……………………………………………………………101

Chapter 5 Fabrication of Long Wavelength Vertical Cavity Surface Emitting Lasers

5.1 Characterization and Optimization of the Active Layers…...…....124
InP-Based Gain Materials…………………………………………………124
Fabrication of Long Wavelength FP EELs……………………………..…126
The Effect of Strain……………………………………………………..…128
The Effect of QW number…………………………………………………129
5.2 Fabrication of the Distributed Bragg Reflectors… ……………….130
5.2.1 Comparisons between Gain Materials in Long Wavelength Range
Reflectors………………………………………………………………130
Introduction………………………………………………………….…130
Experimental Procedure……………………………………………..…132
Results and Discussion…………………………………………...…133
5.2.2 Distributed Bragg Reflectors for Long Wavelength VCSELs using
InP/Air-gap ……………………………………………………….………137
Design and Fabrication…………………………………..….……138
Optical Characterization………………………………………….…140
5.3 Optically Pumped LW-VCSELs ……………….……………….……140
The Structure of LW-VCSEL……………………………………….…...141
The Results of Optical Pumping………………..……………………..…142
5.4 Electrically Pumped LW-VCSELs ……………………………..…143
5.4.1 Selectively etched undercut apertures in InP-based LW-VCSELs…...143

5.4.2 Fabrication of LW-VCSELs by Ion-implantations…………………144

5.5.3 Long Wavelength Light Emitting Diodes with Buried Tunnel Junctions……………………………………………………………...146

Reference ……………………………………………………………….……149

Chapter 6 Conclusions

6.1 Summary of short wavelength VCSELs……………………….…..182

6.2 Summary of long wavelength VCSELs……………………………183

Publication List

Table captions

Table 2-1 Comparison of threshold conditions for EEL vs VCSEL.

Table 2-2 Magnitude of $|M|^2$ for various material systems.

Table 2-3 Magnitude of $|M_T|^2/|M|^2$ for different transitions and polarizations.

Table 2-4 Various material combinations for making high reflectivity DBRs

Figure captions

Chapter 1

Figure 1-1 Schematic illustration of edge-emitting lasers and VCSELs.

Figure 1-2 The absorption spectrum of plastic optical fiber (POF).

Chapter 2

Figure 1-1 Schematic illustration of edge-emitting lasers and VCSELs.

Figure 2-1 Schematics of edge emitting lasers.

(a) The typical EELs with DH structures. The electrodes outside the P and N cladding layers provide the electrical current. The laser output goes out from both cleaved facets.

(b) The 2-D cross-section of EELs. The refractive index profile shown on the left side have a high index value for the active region, which serves a natural optical waveguide for the laser mode. The conduction and valence band diagram for the EELs shown on the right side explains carrier confinement in DH structures.

(c) Schematics of laser operation conditions with optical gain, γ, internal loss, α_i, cavity length, L, and mirror reflectivity, R.

Figure 2-2 Typical semiconductor laser output power vs. injection current relation (L-I curve).

Figure 2-3 The gain, optical mode and power spectrum for a Fabry-Perot laser.

Figure 2-4 Operation of a Fabry-Perot laser.

Figure 2-5 (a) General VCSEL schematic indicating coordinate system. (b) Cross-sectional schematic indicating active layer thickness, L_a, cladding layer thickness, L_p, and VCSEL effective cavity length, L.

Figure 2-6 The gain and optical mode spectrum for a VCSEL. Since the effective cavity length of VCSEL is on the order of half wavelength, the longitudinal mode

spacing is larger than linewidth for typical semiconductor gain medium. The property of short cavity makes VCSEL a single longitudinal device.

Figure 2-7 Schematics of alignment between gain and cavity mode peak at different temperature. Temperature increases as sequence as (a), (b) and (c). The gain peak red-shifts faster than the cavity mode as the temperature increases.

Figure 2-8 Schematics of optical waveguide for oxide VCSEL. Due to the complex 3-D structure for oxide VCSEL, the analysis of transverse mode can be assumed an optical waveguide using effective index model. The effective refractive index of core region can be calculated as n_1, while that of outer region is n_2.

Figure 2-9 (a) The spectrum of the oxide-confined VCSEL with a 6x6 μm square aperture operated at 0.9 I_{th} (~1 mA).

(b) The upper-left image is the top view of the VCSEL and the dash line indicates the scanning area. Below the top view of the VCSEL is the total spontaneous emission image observed directly from the microscope.

(c) On the other side is the spectrally resolved near field images corresponding to the emission peaks (a) to (k) labeled in the spectrum.

Figure 2-10 The relationship between energy and k-space and illustration of k-selected transition in parabolic shape band structure.

Figure 2-11 Illustration of an incident light gaining its power after passing through a portion of gain medium

Figure 2-12 Allowed and forbidden transitions in a quantum well.

Figure 2-13 Valence band structures of unstrained bulk semiconductor such as GaAs

Figure 2-14 Three major types of nonradiative recombination paths

Figure 2-15 Illustration of thin epilayer of lattice constant a_c grown under biaxial (a) compression and (b) tension on substrate with lattice constant a_s.

Figure 2-16 Qualitative band energy shift of the conduction band and three valence bands for

biaxial compressive and tensile strain.

Figure 2-17 Band-edge profiles in real space along the growth (z) direction and the quantized subband dispersions in k space along the k_x direction (perpendicular to the growth direction) for a quantum well with (a) a compressive strain, (b) no strain, and (c) a tensile strain.

Figure 2-18 (a) Plane wave incident on a thin film, (b) Notation for two films on a substrate.

Figure 2-19 The simulated results for a stack of InGaAlAs/InAlAs DBRs with 10, 20, 30, and 40 pairs. (a) The reflectance, (b) The phase upon the reflection, (c) The delay time.

Figure 2-20 The illustration of the penetration depth concept. A linear phase mirror is replaced by a fixed phase mirror displaced by length L_{DBR}, into the mirror. The linear term in the phase characteristic is absorbed by the distance L_{DBR}, whereas the θ_o term assures that the phase of the equivalent and the original mirror match at the center frequency.

Figure 2-21 The simulated electric field in 40 pairs InGaAlAs/InAlAs DBRs. The penetration depth extends to 1/e of the magnitude of the incident light.

Chapter 3

Figure 3-1 Energy band diagram versus lattice constant

Chapter 4

Figure. 4.1 The structure of InGaN/GaN MQW

Figure. 4-2 HRXRD spectra of InGaN/GaN 5QWs with different well thickness.

Figure 4-3 (a) The PL spectra of all samples with different quantum-well thickness and the same In content

(b) The effects of MQW structure with various well thickness on the PL peak position and intensity measured at room temperature.

Figure 4-4 The dependence of the output power on the quantum well thickness, which is measured under the condition at 20 mA injection current at room temperature.

Figure 4-5 HRXRD results for the InGaN/GaN QWs depending on the number of QWs.

Figure 4-6 (a) The PL spectra of all samples with different quantum-well number and the same In content

(b) The dependence of PL peak position and intensity on the number of wells

Figure 4-7 The output power characterization results of LED samples with different well number at 20 mA.

Figure 4-8 The dependences of the PL intensity (filled square) and PL peakwavelength (filled circles) of InGaN/GaN MQW samples as a function of the SiH_4 flow rate in the range of 0.12-0.59 sccm.

Figure 4-9 The measured LED output power as a function of injection current.

It can seen clearly the relative output luminous intensity as a function of the SiH_4 flow rate in the range of 0.12-0.59 sccm.

Figure 4-10 Photonic band structure for a 1D PC that shows a photonic band gap (PBG) between frequency 0.288 *c/a* and 0.302 *c/a* (e.g. the region between the dash lines).

Figure 4-11 Comparison of the averaged theoretical and experimental transmittances as a function of wavelength. The calculated (dash-line) and measured transmittances (solid-line) are averaged for the unpolarized light with the incident angles every 5 ^{o} from 0 ^{o} to 85 ^{o}.

Figure 4-12 Schematic diagram of a GaInN blue LED chip containing an omnidirectional 1D PC fabricated at the bottom. The inset shows the SEM picture of the 1D PC.

Figure 4-13 Electroluminescence intensity–current (*L–I*) characteristics of the LED with and without 1D PC.flow rate in the range of 0.12-0.59 sccm.

Figure 4-14 (a) The SEM image of the MOCVD grown structure(b) The SEM image of the

overall VCSEL(c) The schematic diagram of the overall VCSEL structure

Figure 4-15 The reflectance spectrum of AlN/GaN DBRs and Ta_2O_5/SiO_2 DBRs.

Figure 4-16 PL emission of MOCVD grown structure and overall VCSEL structure.

Figure 4-17 The light emission intensity from the VCSEL as a function of the exciting energy.

Chapter 5

Figure 4-17 The light emission intensity from the VCSEL as a function of the exciting energy.

Figure 5-1 The simulated gain-wavelength and gain-carrier relationships for (a) InGaAlAs and (b) InGaAsP strained compensating quantum wells. The strain and thickness of the quantum wells are 1.5% and 5 nm, respectively and the strain and thickness of the barriers are –0.75% and 10 nm, respectively.

Figure 5-2 The simulated band diagrams under forward bias for (a) InGaAlAs and (b) InGaAsP multiple quantum wells. f_c and f_v are quasi-Fermi levels for conduction and valence bands under forward bias. Due to the larger conduction band offset for InGaAlAs system, the InGaAlAs lasers demonstrate superior high temperature characteristics over InGaAsP lasers.

Figure 5-3 (a) The epitaxial structure for 1550 nm FP lasers. (b) The schematic of band diagram corresponding to the laser structure shown in (a).

Figure 5-4 The SEM cross-sectional image of the 1550 nm laser ridge. The ridge width is 2 μm. An etching stop layer is added in order to precisely control the etching depth during ridge formation.

Figure 5-5 The temperature dependence of the threshold current for both 1310 nm and 1550 nm FP lasers. The characteristic temperature is estimated to be 80 K.

Figure 5-6 The dependence of the laser threshold current density on the amount of

compressive strain in quantum wells. The barriers are all tensely strained to compensate the strain in QW. The number of quantum wells is six. The threshold current is calculated when the laser operates without facet coating.

Figure 5-7 The X-ray diffraction patterns of different strain-compensated MQWs.

Figure 5-8 The effect of quantum well numbers on the laser threshold current and confinement factor. Two types of quantum wells are compared. The strain for structure I and structure II is 1.37% and 1.4%, respectively.

Figure 5-9 (a) The pit density of 10 pairs InP/InGaAlAs DBRs grown with different interruption time t_p. (b) The cross section the InP/InGaAlAs DBRs grown with 0.1-minute interruption time investigated by SEM.

Figure 5-10 The reflectivity curves of 10 pairs InP/InGaAlAs DBRs grown with different interruption time t_p.

Figure 5-11 The X-ray diffraction patterns of 10 pairs InP/InGaAlAs DBRs grown with different interruption time t_p.

Figure 5-12 The SIMS results of InP/InGaAlAs DBRs grown with t_p = 0.2 minute.

Figure 5-13 The interface conditions of InP/InGaAlAs DBRs examined by TEM with different growth interruption time; (a) interruption time t_p = 0.3 minute, (b) interruption time t_p = 0 minute.

Figure 5-14 (a) The I-V curves of InP/InGaAlAs DBRs and InAlAs/InGaAlAs DBRs with round mesas of 50 μm in diameter. (b) simulation of the equilibrium band diagrams of the InP/InGaAlAs and InAlAs/InGaAlAs DBRs when the n-type concentration was chosen to be 1×10^{18} cm^{-3}. The dashed line is the Fermi level.

Figure 5-15 The reflectivity curves of 35 pairs InP/InGaAlAs and InAlAs/InGaAlAs DBRs measured by spectrometer.

Figure 5-16 The reflectivity of three-pair of InP/airgap DBR structure with a fixed $\lambda/4$ InGaAs layer and different InP layer.

Figure 5-17 (a)Schematic diagram of the dry etched mesas. (b)Schematic cross section of the InP/airgap DBRs.

Figure 5-18 The cross section of the stable suspended InP/airgap DBRs captured by SEM.

Figure 5-19 The calculated and measured reflectivity curves of the InP/airgap DBRs. Peak reflectivity is 99.9% at 1.54 μm.

Figure 5-20 Schematic cross section of VCSELs.

Figure 5-21 (a) Reflectance spectrum of 35 pairs InGaAlAs/InP DBRs. (b) Reflectance spectrum of a half VCSEL structure. (c) PL spectrum of SCMQWs. (d) Reflectance spectrum of a complete VCSEL structure. (e) PL spectrum of a complete VCSEL structure.

Figure 5-22 Schematic setup of optical pumping.

Figure 5-23 The VCSEL output power versus input laser pumping power characteristics at room temperature. The inset shows the VCSEL emission spectrum at the pumping power above the threshold. Peak emission wavelength is 1562 nm.

Figure. 5-24 Schematics of monolithically grown electrically pumped LW-VCSELs with Selectively etched undercut apertures.

Figure 5-25 (a) Detailed descriptions of LW-VCSEL epitaxial structure preparing for ion-implantation. (b) Schematic of LW-VCSEL with Si-implanted current aperture.

Figure 5-26 The voltage (dash line) and emission light output (solid line) versus driving current characteristics for InP-based LW-VCSELs with Si-implantation.

Figure 5-27 The reflectivity and PL curves (solid line) are measured with only the half-cavity. The PL peak is 1547.4 nm with FWHM of 38.6 nm in comparisons to 108.3 nm for PL curve of the original MQW. The dashed line is the EL spectrum for the full cavity structure of the LW-VCSEL with Si-implantation.

Figure 5-28 (a) (b) Detailed descriptions of epitaxial structure for long wavelength LED with

tunnel junction. (c) Schematic of operation principal in tunnel junction under the reverse bias.

Figure 5-29 (a) Schematic of long wavelength LED structure with buried tunnel junction. (b) The cross-section SEM image of the buried tunnel junction after the regrowth process. (c) The top view of the long wavelength LED before and after electrical operations.

Figure 5-30 The voltage (dash line) and emission light output (solid line) versus driving current characteristics for the long wavelength LED with buried tunnel junction.

CHAPTER 1 Introduction

In the last decade, the vertical cavity surface-emitting laser (VCSEL) has established itself as a low-cost high-speed solution for data communication applications and interconnects and has stared to challenge the well-established edge-emitting lasers in the telecom and data storage applications. VCSEL-based modules, with speed up to 2.5 Gbit/s per channel for distances up tp 300 meters are now commercially available. However due the ever-increasing demand for bandwidth, devices operating at higher transmission rates (10 Gbit/s and more) and emitting at long wavelengths will be needed in the near future, in order to penetrate the telecommunication markets and metro-area network applications. After a brief introduction to semiconductor lasers, optical communications in Chapter1.1 and the main applications for VCSELs are presented in Chapter1.2, namely datacom, telecom, plastic optical fiber networks and high-density optical data storage.

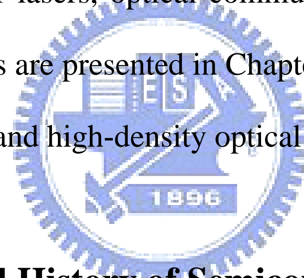
1896

1-1 The Background and History of Semiconductor lasers

Semiconductor laser

Since the first proposal of laser operation by Schawllow and Townes in 1958 [1] and first demonstration using a ruby crystal has al two years later [2], laser technology has had tremendous implications in every day life. Applications today include high precision medical surgery, industrial remote sensing, entertainment lightning, chemical spectroscopy, radar scanning, three-dimensional microscopy and many more, the list being constantly increased as new discoveries are made and technology improves [3-5]. The main advantages of lasers compared with other light sources such as light bulbs or neon tubes are that the emitted light is monochromatic, coherent, directional and that the small spot size can give very high density of energy. One of

the major breakthroughs in laser technology occurred in 1962 [6-7] with the invention of semiconductor lasers. Compared to other lasers such as gas or dry lasers, semiconductor lasers combine compactness, higher efficiency and reliability, lower cost, and ease of use.

One of the most important advantages of semiconductor lasers is that they can be directly modulated, i.e. one can readily obtain optical pulses as short as a few picoseconds by modulating the device current [8-9]. Such pulses may be used for time-resolved dynamical studies as well as carrying information at high bit rates in fiber and free-space optical communication systems [10-11]. Large gain bandwidth of semiconductor materials allows wavelength tunability [12] and the high light-current linearity of the lasers makes them suitable for modulation over a wide range of frequencies from DC to tens of GHz [13].

Optical communication

Apart from being widely used for optical data storage and retrieval, e.g. in CD or DVD players, to read/write digital information, semiconductor lasers have rapidly evolved into the most appropriate and widely used light sources for optical communication, the combined development of high speed microelectronics and semiconductor lasers, together with the invention of optical fiber [14] and fiber amplifier [15] made the information technology revolution possible, allowing the huge amounts of data to be transmitted almost instantly from one side of the world to the other. The never ending increased demand for bandwidth by today's applications such as video streaming through the internet is the main driving force behind the development of faster lasers.

Today, the most common devices for telecommunication applications are edge emitting lasers typically distributed feedback (DFB) lasers. The two most important

wavelengths are 1300nm, corresponding to minimum dispersion in single mode fibers and 1550nm, corresponding to minimum attenuation. The latter wavelength band is also the gain region for erbium doped fiber amplifiers (EDFA). In a DFB laser, the wavelength and mode selection is realized by horizontal gratings. Although this type of lasers exhibits high power, high side-mode suppression ratio (SMSR) narrow linewidth, it also results in high manufacturing costs. The last five years have seen the development of vertical-cavity lasers and their maturation for shorter wavelength (850 nm) Due to the combined advantages of low-cost, high-bandwidth and high-density, VCSELs are now used as the preferable light source for short distance communications (up to 300 m) such as access networks and local area networks (LANs). Recent achievements in Nitride-based materials, quantum dots and microelectromechanical technology also indicate that long wavelength VCSELs could start to challenge edge-emitting lasers in telecom and dense wavelength division multiplexing (DWDM) applications.

1-2 Vertical Cavity Surface Emitting lasers

Structure

As its name indicates, the fundamental difference between an edge-emitting and vertical cavity surface emitting laser is the fact that the laser oscillation as well as the out-coupling of the laser beam occur in a direction perpendicular to the epitaxial gain region and the surface of the laser chip. Figure 1.1 illustrates the typical differences between edge-emitting lasers and VCSELs. A VCSEL consists of an active medium, usually multiple quantum wells, placed between two DBR mirrors. The overall cavity length is mush shorter for a VCSEL, typically a few μm, as opposed to some hundreds of μm in the case of an edge-emitting laser, resulting in larger longitudinal

mode spacing and shorter gain region.

In order to compensate for the shorter gain region, the light has to travel back and forth more times before coupled out, therefore the mirror reflectivity has to be much higher. The reflectivity of an output facet for an edge-emitting laser, resulting from the change of refractive index at the cleaved interface semiconductor-air is typical around 30 %. Laser operation in VCSELs requires reflectivity higher than 99 %, using Bragg mirrors of alternating refractive index material. The first VCSEL structure was reported in 1965 by Melngailis consisting of an n^+-p-p^+ junction of InSb. When cooled to 10 K and subjected to a magnetic field to confine the carriers, the device emitted coherent radiation at a wavelength of around 5.2 μm. Later, other groups reported vertical lasers by using grating surface emission. Near IR vertical emission at around 1.5 μm was achieved by Iga in 1979 [16] at the Tokyo Institute of Technology. These early VCSEL devices utilized metallic mirrors which resulted in high threshold current densities (44 $kAcm^{-2}$) while cooled with liquid nitrogen. Epitaxial mirrors for the GaAs/AlGaAs VCSEL were first grown in 1983, with the first pulsed room temperature VCSEL produced in 1984 [17], and finally continuous wave (CW) operation at room temperature was achieved in 1989 [18].

Advantages and drawbacks

There are many reasons why VCSELs are becoming increasingly popular as light sources for applications such as datacom and optical interconnects. For the past 25 years VCSELs have been studied as a replacement for in-plane lasers due to their higher performance and reduced cost potential. Its design allows the lasers to be manufactured and tested on a single wafer using traditional semiconductor processing and testing technology. The VCSELs uniform, single mode beam profile and vertical emission simplifies coupling into optical fiber. This makes wafer-level *in situ* testing

before packaging possible and greatly reduces manufacturing costs [19]. Large two dimensional arrays of devices can now be created; making new types of optical interconnects possible. The use of DBRs eliminates the risk of catastrophic optical damage (COD) in the mirrors which can occur in edge-emitters where the active material close to the facets are depleted by surface recombination and thereby light absorbing. It also reduced the risk of the mechanical mirror damage. The extremely short resonator leads to a longitudinal mode spacing that is large compared with the gain bandwidth and leads to inherent single longitudinal mode operation. The small active volume and high mirror reflectivity contribute to the very low threshord observed in VCSELs, as low as a few microamperes [20], resulting in low power consumption and reduced heating of the device. This feature, combined with the absence of CODs, explains the remarkable reliability of VCSELs. Life-times of more than 10000 hours have been reported by several groups [21,22].

The surface emission and the small size make it possible to fabricate very dence two-dimensional arrays of VCSELs, suitable for multi-channels parallel transmission modules [23]. VCSELs don not need to be cleaved, it is therefore possible to integrate them monolithically with other optoelectronic components such as photodetectors, modulators or hetero-bipolar transistors [24] (HBT). Because of the circular symmetry of the VCSEL structure, the light is emitted with a circular beam and very low divergence. This results in high coupling into optical fibers, up to 90 % [25] and allows for relaxed tolerance in alignment, further reducing the cost of installation. For comparison, the output light emitted from an edge-emitting laser is elliptical with a transverse and lateral divergence of about 40 and 10 degrees, respectively, making it cumbersome to couple the light into an optical fiber without significant optical loss or advanced optics.

In addition, VCSEls have an inherent single-wavelength structure that is well suited for wavelength engineering, making it possible to process multi-wavelength array or tunable VCSEls. Although the manufacturing challenges are numerous, both types of devices have been demonstrated. By carefully designing the optical cavity, with the implementation of a small thickness variation in the bottom DBR, a record 140-wavelength VCSEL array has been reported [26]. The thickness gradient created a cavity thickness variation, which in turn led to laser wavelength variation, the overall wavelength span across the array being 43 nm. Large wavelength tunability can be achieved by mechanically varying the VCESL cavity length. This was demonstrated by placing a movable DBR on a microelectromechanical structure (MEMS) cantilever suspended over the VCSEL cavity, and by applying a voltage across the airgap. The electrostatic force, by attracting the top mirror, shortens the airgap, thus tuning the laser wavelength towards a shorted wavelength (blue shift). Wavelength tuning as high as 31.6 nm for a VCSEL operating at 950 nm was reported [27]. Finally, VCSELs have demonstrated modulation speed up to 21 GHz bandwidth [28], and have been used for transmission up to 20 Gbit/s through 200 m of MMF [29].

However, VCSEls also have some drawbacks compared to edge-emitters. The manufacturing tolerances on VCSEL growth are much tighter than for edge-emitting lasers, the layer thickness having to be controlled within 1%. The perhaps major disadvantage with VCSELs is the strong tendency to operate on multiple transverse modes, due to the large transverse dimensions of the optical cavity. This results in emission spectra with multiple emission wavelengths, which limits the maximum achievable distance due to chromatic dispersion effects. Most commercial VCSELs of today operate multimode and are mainly used in short distance multimode fiber based

optical data links [30], optical interconnects [31], optical storage [32] and laser printing [33]. A lot of efforts are made to produce high power single mode VCSELs. This includes oxide confined VCSELs with current aperture small enough to support only the fundamental mode, index-guided structures such as regrown or surface relief VCSELs, and spatial mode filtering in an external cavity or extended cavity. Although the first and last of these techniques have produced high single mode power, they are difficult to implement with high uniformity and yield. A more reliable technique is to combine a large-area oxidation (20 μm diameter aperture) with an etched shallow surface relief for mode selection. This implies only a small modification to the fabrication procedure but produces reasonably high single mode power (10 mW), with high uniformity and yield [34].

VCSEL applications

The datacom application also arose quite early from a very simple problem: the need for increased data rates in inexpensive fiber links. These links traditionally use light-emitting diodes (LEDs) as sources. In fact, very cheap links are almost defined by the use of a LED rather than a laser. These devices can easily be tested on wafer, and coupling into multi-mode fiber offers a wide alignment tolerance. Mass production of such devices can be implemented without the need for specialized human labor. However, a problem arises with the use of LEDs for the next generation of datacom links. Today, the fastest data rate reliably transmitted using LEDs is about 622 Mb/s. With the advent of the internet and multimedia applications, newer generation communication systems require much higher data rates. The vertical-cavity laser was perceived as a possible inexpensive high-speed source to replace LEDs. One can design a circular output beam with a low-divergence angle for ease of coupling. In addition, VCSELs can be tested directly on wafer just like an LED. For many

practical purposes the VCLs could be considered the new high-speed LEDs.

There remained, nonetheless, a problem with VCSELs in that they could not be fabricated to work well at the traditional wavelengths for fiber communication of 1.3-µm and 1.55-µm. In fact, it was only in 1995 that Dubravko Babic reported the first room-temperature cw operation of any long wavelength VCSEL. Whereas the shorter wavelength GaAs based VCSEL were setting record performances for semiconductor lasers, long-wavelength lasers were struggling even to operate at room temperature. In order to use vertical cavity lasers for fiber links, a new standard for fiber communication for short distances was set up to work at 850 nm (IEEE802.3z-Gigabit Ethernet). Thus VCSELs became the first choice for inexpensive high-speed, short-distance fiber communications.

Not surprisingly, with the new shorter wavelength laser, tradeoffs in certain performance criteria were made, the most important being the maximum transmission distance. This limitation still left a very strong demand for long wavelength VCSELs. ne reason for the limitation was that short-distance links were to run on inexpensive multi-mode fiber. Multi-mode fiber has an inherent transmission distance limitation due to inter modal dispersion. For standard 62.5 μm fiber the maximum distance one can transmit 1.25 Gb/s is 800 m due to the distance bandwidth product of the fiber. In reality, certain imperfections in installed fiber limit the distance to 200 m (IEEE 802.3z). At longer wavelengths, there is reduced dispersion so greater distances can be connected. For example, at 1.25 Gb/s with the same imperfect fiber one can go 500 m with a 1.3 μm laser versus 200 m using a 0.85 μm source. The distance difference between these two cases may make a strong marketing difference if the costs were similar. To further increase the maximum distance of transmission, one can use single-mode fiber which addresses the modal dispersion problem. This, of course,

significantly increases device packaging, connector, and fiber costs. Despite this, with the ever-increasing need for bandwidth, it is very likely that single-mode fiber will become the standard choice for new generation networks.

The implementation of single-mode fiber gives rise to another problem with the use of 850 nm sources. Standard telecommunications single-mode glass fiber (SMF) is designed for long-wavelength lasers so that it is no longer single-mode for 850 nm lasers. In fact, there are actually two modes for 850 nm light in standard SMF. 980 nm VCSELs, which can be fabricated as easily as 850 nm VCSELs, would be much better in this respect, but require InGaAs versus Si detectors. One has to use specially designed fiber if it is to be truly single mode at these wavelength. Using the shorter wavelengths for high-speed transmission, the distance bandwidth product of the link is severely degraded. The possible use of two different types of single-mode fiber results in issues of interoperability. Long-distance applications such as telecom or wide-area networks (WANs) will always use standard SMF fiber. Even if dispersion was not an issue, the transmission distance of 850 nm light in fiber is limited by the material loss so that it cannot be used for very long distances at any data rate. With 2 dB/km loss for 850 nm light versus 0.2 dB/km loss for 1.5 μm light, the minimum repeater distance for a long-wavelength link is an order of magnitude more than using a short-wavelength link. In addition, fiber amplifiers are also commercially available at 1.3 μm and 1.5 μm allowing the transmission distance to be increased by at least another order of magnitude. This leaves local area networks (LANs) with the choice of either installing 850 nm SMF fiber or standard SMF, when upgrading from MMF. With a strict definition of what is LAN versus a WAN (Wide Area Network), either is a reasonable choice. But a problem arises when the boundary between LAN and WAN is unclear. System design becomes much simpler when all components are

interoperable regardless of application. Thus the interoperability with existing fiber and components may become an important consideration when deciding on GaAs versus InP based lasers for LANs.

Although the LAN market offers great opportunity for long-wavelength VCSELs, an even bigger possible market for vertical-cavity lasers is the so-called fiber-to-the home (FTTH) or fiber-to-the-curb (FTTC) applications (also known as the access market). In such applications a transmitter-receiver pair is placed in every home of every subscriber. Such systems would allow private residences to have very high-speed internet access, as well as CATV and telephone service, delivered on a single fiber or fiber pair. There have been, however, many roadblocks to the implementation of such systems. Among them is the cost sensitivity of this application. The 1997 OITDA (Optoelectronic Industry and Technology Development Association) report stated that the goal for the complete ONU (Optical Network Unit) with transmitter, receiver, power supply, and package should be around $125 for FTTH applications. One great roadblock to this price target has been the high cost of the fiber-optic transmitters. In addition, due to the potentially large distances involved in such applications, SMF is necessary, increasing the components costs of the system. With the use of SMF, packaging of the lasers becomes a significant part of the transmitter cost. These costs must be minimized in order to allow for the mass production of such systems. To reduce costs some performance standards can be sacrificed, as long as some minimum standards are met so that the system can work reliably. These minimum standards must be meet in order for the devices to be considered commercially viable.

While copper coaxial cable and glass fiber, the traditional solutions to data communications are well suited to specific applications, they each have inherent

limitations for short range low cost applications. Copper unsuitable for high-speed data transmission because of its cost, a high attenuation at high frequencies and susceptibility to electromagnetic interference. The small diameter and fragility of glass carriers with it a high cost of installation and alignment. One alternative to the previous two solutions is plastic, in the form of optical fiber. Plastic optical fiber (POF) is a low-cost, easy-to-align, flexible and easy-to-use solution for short distance connections, and is already widely used in CD players, industrial electronics, PCs and car electronics. Mercedes and BMW now use POF in all the new car models for the communication system between all the multimedia applications, radio, navigation system, CD player, mobile phone system, and the safety features. The total amount of POF used is approximately 12 m and the typical data rate is around 10 Mbit/s [35]. Figure 1.2 shows the absorption spectrum of POF, with minimum attenuation at 590 and 650 nm. The high level of absorption (100 dB/km) limits the overall fiber length to 100 m. A number of different light sources are currently used, LEDs edge-emitting lasers, and more recently RCLEDs and VCSELs. While LEDs are cheap and reliable but slow, and edge-emitting laser exhibits high threshold currents and coupling limitations, RCLEDs present the combined advantages of improved directionality, speed, power, linewidth, and temperature stability [36]. Since then RCLEDs have been used at bit rates up to 500 Mbit/s but at higher speeds lasers are required, with VCSELs being the preferred choice. The typical 650 nm VCSEL is composed of alternate layers of high and low Al concentration AlGaAs layers to form the top and bottom quarter-wave mirrors, and a cavity based on AlGaInP with InGaP quantum wells. Recently 2 Gbit/s transmission using standard multimode fiber was achieved with an oxidized VCSEL [37].

The technological prospects for blue and near ultraviolet VCSELs and RCLEDs

are at an early and exciting research stage. A collaboration among Brown University, Sandia, and Agilent Technologies has demonstrated RT quasi-CW VCSEL operation in the 380-410 nm wavelength range using optical pumping at modest levels of excitation to generation the population inversion, which established a working optical design for blue VCSELs [38]. The first blue VCSEL operating at room temperature was demonstrated in 1999 [39]. By exploiting recent progress in crystal growth technology, an active region of InGaN quantum wells and mirror surfaces of gallium and aluminum nitrides were grown on a sapphire substrate to make disc-shaped cavities. Each one was only 18 μm in diameter. When the cavities were illuminated by a HeCd laser, light was emitted at a wavelength of 399 nm. The present challenge is to make the optical resonator structure compatible with electrical injection. The mirrors themselves are poorly conducting, so carriers must to be laterally fed into the active optical volume defined by the mirrors. The problem is especially severe on the p-side of the junction due to the low conductivity of p-side GaN. Song and co-workers at Brown University have solved the problem by inserting a thin transparent conductive layer of indium tin oxide within the optical cavity to enhance the lateral "current spreading". Devices with this layer have been operated to date as robust RCLEDs. Although laser operation in these structures has yet to be observed, further developments of high-efficiency blue light emitters are expected in the near future. While many technical improvements and an increased fundamental understanding will be required to bring the present blue and violet lasers into full technological bloom, it is clear that these devices are destined to fill an important role in future optoelectronics applications. Two-dimensional arrays of blue VCSELs could drastically reduce the read-out time in high-density optical data storage (for example, in CDs and DVDs) and increase the scan speed in laser printing technology. Blue

GaN VCSELs have great potential in a an other market sector unrelated to telecom, commercial lighting and display applications, because the cost of manufacturing enable them to compete with the traditional solutions such as LEDs and RCLEDs.

1-3 Overview of this Thesis

In this study, we focused on the fabrication of long wavelength and short wavelength vertical cavity surface emitting lasers (VCSELs) by metal organic chemical vapor deposition (MOCVD). For InGaN/GaN-based VCSELs, we investigated the optimized conditions of the InGaN/GaN active layers, fabricated high extraction efficiency of InGaN LEDs with an omnidirectional One-dimensional Photonic Crystals (1D PC) incorporated into the bottom of InGaN blue LED chips, and demonstrated the optically pumped GaN-based VCSELs structure grown by MOCVD. For InP-based VCSELs, we found out the optimized conditions of the active layers, fabricated InP/InGaAlAs-based DBR with excellent electrical and optical properties using MOCVD and the growth interruption technique, and demonstrated the optically pumped GaN-based VCSELs structure grown by MOCVD. We also fabricated electrically driven continuous wave LW-VCSELs by using selectively etched undercut apertures technique, Si-implant technique, regrowth technique.

Chapter 2 reviews fundamentals in semiconductor lasers at beginning. The origin of differences between EELs and VCSELs will be discussed. Then, general operation principles of VCSELs including light-current characteristics, the relationship between gain and current, the gain peak and cavity mode alignment, the characteristics of DBRs, the analysis of the heat flow will be introduced and characterized with the use of simulation software.

Chapter 3 mainly reviews recent progress in short wavelength and long wavelength VCSELs With specific conditions in requirement of VCSELs, the fundamental issues in design of VCSELs will be discussed at this chapter.

The optimum characteristics of InGaN/GaN active layer for GaN-based VCSEL have been discussed at the beginning of chapter 4. We fabricated high extraction efficiency of InGaN LEDs with an omnidirectional One-dimensional Photonic Crystals (1D PC) incorporated into the bottom of InGaN blue LED chips, and demonstrated the optically pumped GaN-based VCSELs structure grown by MOCVD.

Chapter 5 reports several different fabrication methods for DBRs used in long wavelength range. The optical and electrical properties of different DBRs will also be studied. Followed by the comparisons of novel InP/InGaAlAs and conventional InAlAs/InGaAlAs DBRs, the extremely high reflectivity mirror made by InP/Air-gap DBRs will be discussed. We report the structures of LW-VCSELs for optical pumping, including the InP-lattice-matched and wafer-fused structures. Chapter 5 also reports several different approaches to make electrically driven LW-VCSELs including selectively etched undercut apertures technique, Si-implant technique, regrowth technique to make current apertures in devices.

Chapter 6 is the briefly summary for this thesis.

References

[1] A. L.Schawlow and C. H. Townes, Phys. Rev., 112, 1940 (1958)

[2] T. H. Maiman, Nature, 187, 493 (1960)

[3] J. M. Vaughan, K. O. Steinvall, C. Werner and P. H. Flamant, Proc. Of the IEEE, 84, 205 (1996)

[4] D. E. Cooper and R. U. Rartinelli, Laser Focus World, 133 (1992)

[5] Opto&Laser Eorope, 83, 19, April (2001)

[6] M. I. Nathan, W. P. Dumke, G. Burns, F. H. Dill and G. Lasher, Appl. Phys. Lett., 1, 62 (1962)

[7] R. N. Hall, G. E. Fenner, J. D. Kingsley, T. J. Soltys and R. O. Carlson, Phys. Rev. Lett., 9, 366 (1962)

[8] D. Bimberg, K. Ketterer, H. E. Scholl and H. P. Vollmer, Electron. Lett., 20, 343 (1984)

[9] R. Stevens, Light output dynamics in modulated semiconductor laser diodes, M. Sc. Thesis, National University of Ireland, University College Cork, Aug. (1996)

[10] O. N. Makeyev, Y. A. Zarkevitch and V. I. Smirnov, Telecommun. And Radio Engi., 45, 41 (1990)

[11] G. C. Brooks, Telecommun. I., 58, 88 (1988)

[12] P. J. Rigole, S. Nilsson, L. Backbom, T. Klinga, J. Wallin, B. Stalnacke, E. Berglind and B. Stolz, IEEE Phot. Tech. Lett., 7, 697 (1995)

[13]O. Kjebon, R. Schartz, S. Lourdudoss, S. Nilsson, B. Stalnacke and L. Backbom, Ellectron. Lett., 33, 488 (1997)

[14] K. C. Kao and G. A. Hockman, IEE Proceedins J., 133, 1151 (1966)

[15] R. J. Mears, L. Reekie, I. M. Jauncey and D. N. Payne, Electron. Lett., 23, 1026

(1987)

[16] H. Soda, K. Iga and Y. Suematsu, Jpn. J. Appl. Phys., 18, 2329 (1979)

[17] K. Iga, S. Ishikawa, S. Ohkouchi and T. Nishimura, Appl. Phys. Lett., 45, 348 (1984)

[18] F. Koyama, S. Kinoshita and K. Iga, Appl. Phys. Lett., 55, 221 (1989)

[19] K. S. Giboney, L. R. Aronson, and B. E. Lemoff, " *IEEE Spectrum*, vol. 35, pp. 43-53, 1998.

[20] G. M. Yang, M. H. MacDougal and P. D. Dapkus, Electron. Lett., 31, 886 (1995)

[21] J. K. Guenter, J. A. Tatum, A. Clark, R. S. Penner, R. H. Johnson, R. A. Hawthorne, J. R. Biard, Y. Liu, invited paper, Proceedings of SPIE's Otoelectronics 2001, 4286, 1-14 (2001)

[22] J. S. Span, Y. S. Lin, C. F. Li, C. H. Chang, J. C. Wu, B. L. Lee, Y. H. Cuang, S. L. Tu, C. C. Wu, invited paper, Proceedings of SPIE's Otoelectronics 2001, 4286, 15-21 (2001)

[23] A. V. Krishnamoorthy, K. Lopata, J. A. Walker, L. A. D'Asaro, IEEE Photon. Technol. Lett., 12, 1073 (2000)

[24] U. Eriksson, P. Evaldsson and K. Streubel, CLEO Pacific Rim '97, Chiba, Japan, paper PD2.8, July (1997)

[25] K. Tai, G. Hasnai, J. D. Wyn, R. J. Fisher, Y. H. Hang, B. Weir, J. Gamelin and A. Y. Cho, Electron. Lett., 26, 1628 (1990)

[26] C. J. Chang-Hasnain, J. P. Habison, C. E. Zah, M. W. Maeda, L. T. Florez, N. G. Stoffel, and T. P. Lee, IEEE J. Quantum Elecrtron., 27, 1368 (1991)

[27] M. Y. Li, W. Yuan, G. S. Li and C. J. Chang-Hasnain, IEEE Photon. Technol. Lett., 10, 18 (1998)

[28] K. L. Lear, V. M. Hietala, H. Q. Huo, M. Ochiai, J. J. Banas, B. E. Hammons, J. C. Zolper and S. P. Kilcoyne, Optical Society of America, Trends in Optics and Photonics Series (OAS TOPS), 15, 69 (1997)

[29] D. M. Kuchta, P. Pepeljugoski, K. Young, Advanced Semiconductor Lasers and Applications, LEOS Summer Topical Meetings, 49 (2001)

[30] U. Fiedler, G. Reiner, P. Schnitzer and K. J. Ebeling, IEEE Photon. Technol. Lett., 8, 746 (1996)

[31] M. W. Haney, M. P. Christensen, P. Milojkovic, J. Ekman, P. Chandramani, R. Rozier, F. Kiamilev, Y. L. Liu and M. Hibbs-Brenner, Appl. Opt., 38, 6190 (1999)

[32] K. Goto, Jpn. J. Appl. Phys., 37, 2274 (11998)

[33] R. L. Thrnton, Proc. SPIE, 3003, 112 (1997)

[34] H. Martinsson, J. A. Vukusic, M. Grabherr, R. Michalzik, R. Jager, K. J Ebeling and A. Larsson, IEEE Photon. Technol. Lett., 11, 1536 (1999)

[35] Opto-Laser Europe, 38, September (2001)

[36] K. Streubel, U. Helin, V. Oskarsson, E. Backlin and A. Johansson, IEEE Photon. Technol. Lett., 10, 1685 (1998)

[37] C. Risberg, M. Runnstrom, M. Dubois, R. Marcks Von Wurtemberg, M. Ghisoni, B. Kronlond and R. Stevens, Confeence on Lasers and Electro-Optics (CLEO) Europe, Sept. (2000)

[38] Hailong Zhou, M. Diagne, E. Makarona, A. V. Nurmikko, J. Han, K. E. Waldrip and J. J. Figiel, Electron. Lett., 36, 1777 (2000)

[39] T. Someya, Y. Arakawa, R. Werner and A. Forchel, Confeence on Lasers and Electro-Optics (CLEO), May (1999)

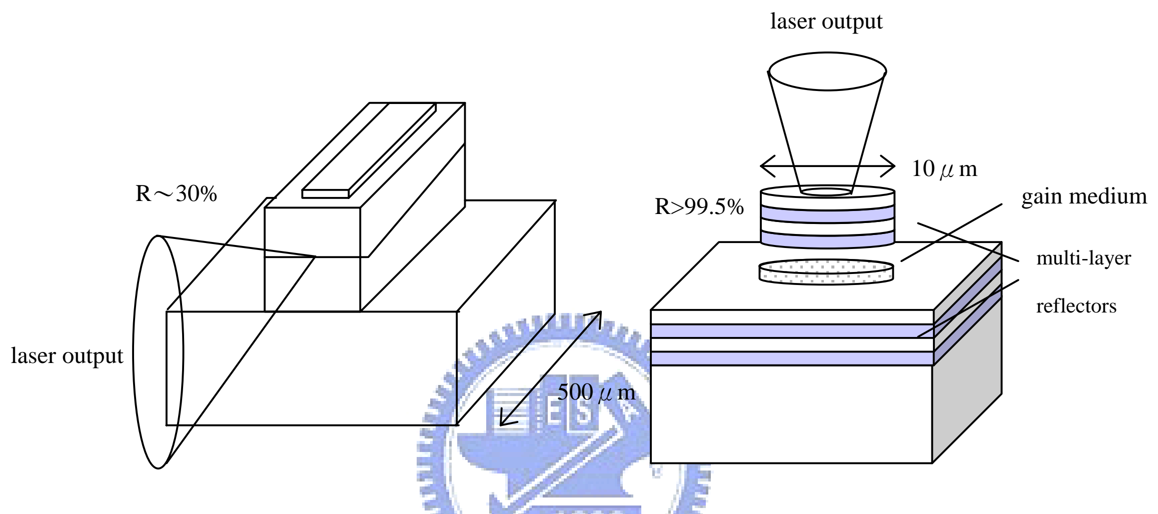

Fig. 1-1 Schematic illustration of edge-emitting lasers and VCSELs

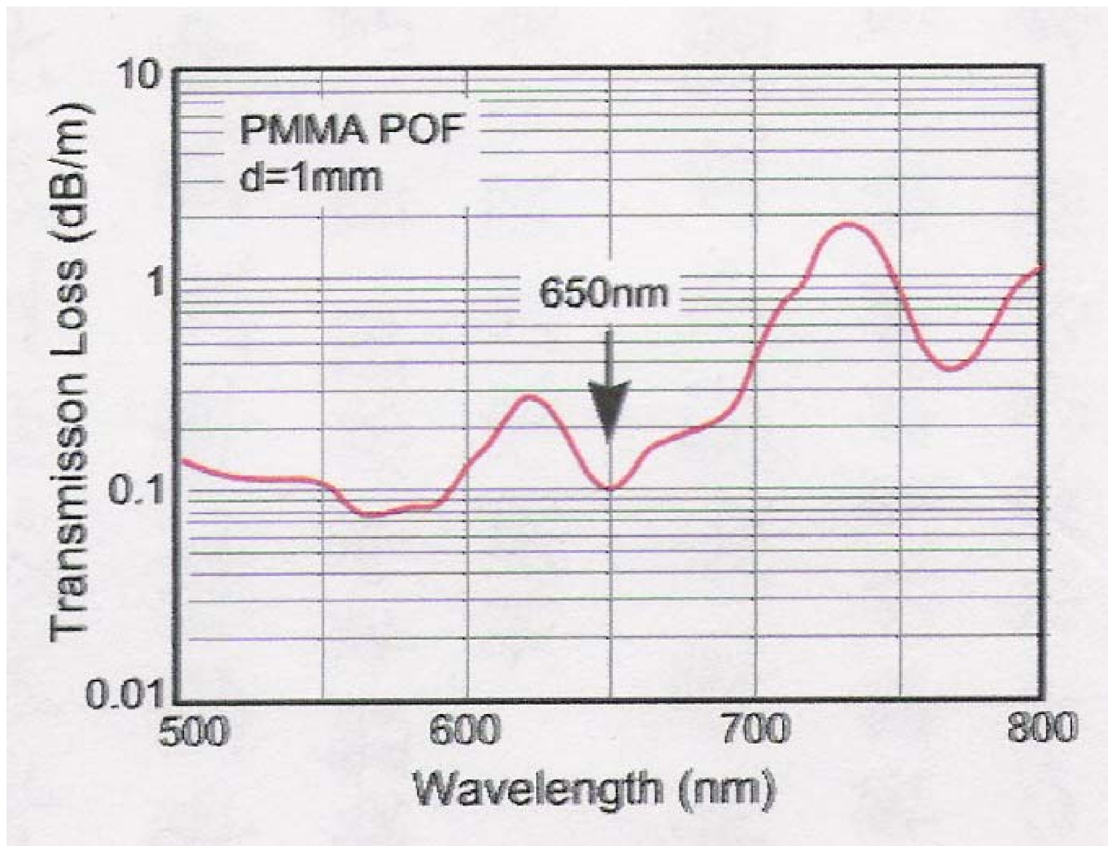

Fig. 1-2 The absorption spectrum of plastic optical fiber (POF).

CHAPTER 2

Fundamental of Vertical Cavity Surface Emitting Lasers

This chapter reviews fundamentals in semiconductor lasers at beginning. The origin of differences between edge emitting lasers (EELs) and vertical cavity surface emitting lasers (VCSELs) will be discussed. Then, general operation principals of VCSELs including light-current characteristics, the relationship between gain and current, the gain peak and cavity mode alignment, the characteristics of distributed Bragg reflectors (DBRs), the analysis of the heat flow will be introduced and characterized with the use of simulation software.

2-1 General Characteristics in Semiconductor Lasers

Semiconductor Laser Oscillation Conditions

The typical EELs shown in Figure 2-1(a) are Fabry-Perot (FP) lasers with double-heterojunction (DH) structures. The EELs, with small enough cross-section, may be initially modeled by considering a resonator, which contains plane optical waves travelling back and forth along the length of the lasers. The natural cleaved facets provide optical feedback for the laser cavity associated with the refractive index of the active layers. If the refractive index of the active layer is n_r, for the normal incident light, the reflectivity of the cleaved facet is

$$r^2 = R = \left(\frac{n_r - 1}{n_r + 1}\right)^2 \qquad (2\text{-}1)$$

Assumed an electromagnetic wave travelling back and forth in the laser cavity as shown in Figure 2-1(c), the amplitude decays or grows with distance because the wave suffers scattering and other fixed losses α_i per unit length, but also experiences a material optical gain γ per unit length provided by the electrons and holes

recombining at a rate which increases with the injected carrier density. The laser cavity length is L and the wave field at point (1) can be expressed as:

$$I_1 = I_o e^{jkz_o} \tag{2-2}$$

After the wave travels through point (2), (3), (4) and backs to point (1), the wave field cab be expressed as:

$$I_4 = R_1 R_2 I_o e^{2(\gamma - \alpha_i)L} e^{jk(z_o + 2L)} \tag{2-3}$$

The equilibrium wave field after one round trip must achieve for the occurrence of laser oscillation. Two oscillation conditions are obtained when I_1 equals to I_4. One is the amplitude condition:

$$R_1 R_2 I_o e^{2(\gamma - \alpha_i)L} = I_o \tag{2-4}$$

The other one is phase condition:

$$e^{jk(z_o + 2L)} = e^{jkz_o} \tag{2-5}$$

$$k \cdot 2L = q \cdot 2\pi \tag{2-6}$$

where q is an integer.

From the amplitude condition (2-4), the threshold condition can be obtained:

$$\gamma_{th} = \alpha_i + \frac{1}{2L} \ln \frac{1}{R_1 R_2} \tag{2-7}$$

which explains that the threshold gain is the summation of the internal loss and the mirror loss. However, the optical wave travelling in the laser cavity does not passes all the gain region, the confinement factor, Γ, has to added to modified the threshold condition:

$$\Gamma \gamma_{th} = \alpha_i + \frac{1}{2L} \ln \frac{1}{R_1 R_2} = \alpha_i + \alpha_m \tag{2-8}$$

If a linear gain approximation is assumed, the relationship between gain and carrier density can be expressed as:

$$\gamma_{th} \equiv a(n_{th} - n_{tr}) \tag{2-9}$$

where a is the differential gain, n_{tr} is the transparent current density. Assumed that thickness of the active layer is d, the threshold condition becomes:

$$\gamma_{th} = \frac{1}{\Gamma}(\alpha_i + \frac{1}{2L}\ln\frac{1}{R_1R_2}) = a(\frac{J_{th}\tau_n}{ed} - \frac{J_{tr}\tau_n}{ed})$$
$$J_{th} = \frac{d}{b\Gamma}(\alpha_i + \frac{1}{2L}\ln\frac{1}{R_1R_2}) + dJ_o \quad (2\text{-}10)$$
$$b \equiv \frac{a\tau_n}{e}, \quad J_o \equiv \frac{J_{tr}}{d}$$

where τ_n is the carrier lifetime, J_{tr} is the transparent current density. If the internal quantum efficiency is smaller than 1, the equation (2-10) should be modified as:

$$J_{th} = \frac{d}{\eta_i b\Gamma}(\alpha_i + \frac{1}{2L}\ln\frac{1}{R_1R_2}) + \frac{dJ_o}{\eta_i} \quad (2\text{-}11)$$

To further explain the characteristics of laser output, the analytical rate equations have been used. Assumed the photon density in the laser cavity is n_{ph}, and the effective refractive index of the waveguide is n_r, the rate equations for carrier density, n, and the photon density, n_{ph}, can be expressed as:

$$\frac{dn}{dt} = \frac{\eta_i J}{ed} - \frac{n}{\tau_n} - g \cdot n_{ph} \quad (2\text{-}12)$$

$$\frac{dn_{ph}}{dt} = \Gamma \cdot g \cdot n_{ph} - \frac{n_{ph}}{\tau_p} + \Gamma \cdot \beta \cdot \frac{n}{\tau_n} \quad (2\text{-}13)$$

and

$$g \equiv \gamma \cdot (\frac{c}{n_r}) = a \cdot (\frac{c}{n_r}) \cdot (n - n_{tr}) \quad (2\text{-}14)$$

where c is the speed of light, τ_p is the photon lifetime, and β is the spontaneous emission factor. Spontaneous emission factor represents the ratio that spontaneous emission modes contribute to the stimulated emission modes. The value of β is very small that the last term of the equation (2-13) can be neglect. At the steady state, from equation (2-13),

$$\tau_p = (\frac{1}{g}) = \frac{n_r}{c} \cdot \frac{1}{\alpha_i + \frac{1}{2L}\ln(\frac{1}{R_1R_2})}$$

(2-15)

When the operation condition approaches threshold, the photon density still can be seen as zero, the equation (2-13) becomes:

$$\frac{J_{th}}{ed}=\frac{n_{th}}{\tau_n} \tag{2-16}$$

which is identical to equation (2-11). When the operation condition is above the threshold, the carrier density pins at n_{th}, and the equation (2-13) becomes:

$$\frac{n_{ph}}{\tau_p}=\frac{J-J_{th}}{ed} \tag{2-17}$$

If the laser active volume is *V*, which is the product of the cross-section area *A* and thickness of active layer *d*. Let equation (2-17) time V at both sides of equation. Then, the power generated by stimulated emission inside the laser cavity can be expressed as:

$$P_s=(\frac{n_{ph}\cdot V}{\tau_p})\cdot h\nu=\eta_i\cdot\frac{h\nu}{e}\cdot(I-I_{th}) \tag{2-18}$$

Since the laser power out of the laser cavity is termed as the mirror loss, the output power can be expressed as:

$$P_o=\eta_i\cdot\frac{h\nu}{e}\cdot(I-I_{th})\cdot(\frac{\frac{1}{2L}\ln(\frac{1}{R_1R_2})}{\alpha_i+\frac{1}{2L}\ln(\frac{1}{R_1R_2})}) \tag{2-19}$$

As shown in Figure (2-2), the slope efficiency defined as the ratio between output power over injected current is expressed as:

$$\eta_s=P_o/(I-I_{th})=(\frac{h\nu}{e})\cdot\eta_d \tag{2-20}$$

where η_d is the differential quantum efficiency, which is the ratio between number of the increased photons over number of the injected electrons.

From the phase condition (2-4), the threshold condition can be obtained:

$$k\cdot 2L=q\cdot 2\pi$$

$$L=q\cdot(\frac{\lambda_o}{2n_r}) \tag{2-21}$$

Equation (2-21) shows that the laser oscillation wavelength is determined by cavity length. For a typical EEL, the line width of the gain spectrum is larger than the mode spacing as shown in Figure 2-3. The allowed laser modes, or longitudinal modes can be several. The mode spacing between longitudinal modes derived from equation (2-21) can be expressed as:

$$\Delta\lambda = \frac{\lambda^2}{2n_r L\left(1-\frac{\lambda}{n_r}\left(\frac{\partial n_r}{\partial \lambda}\right)\right)} \tag{2-22}$$

Figure 2-4 shows schematic of standing waves inside the laser cavity. Also shown in Figure 2-4 also shows that the laser output beam exhibits an elliptic shape due to the waveguide structure inside the laser cavity. The waveguide structure defines not only the optical confinement but also the carrier confinement. The optical confinement factor can be taken apart into three directions:

$$\Gamma = \Gamma_x \cdot \Gamma_y \cdot \Gamma_z \tag{2-23}$$

For typical EELs, Γ_z and Γ_y approaches unity and Γ_x ranges from 3% to 15%. Due to different confinement effect and field size in the transverse plane, the output beam shows different divergence angles in x and y direction.

General Characteristics of VCSELs

The operation of a VCSEL, like above descriptions, can be understood by analyzing the flow of carriers into active regions, the generation of photons due to the recombination of some of these carriers, and the transmission of some of these photons out of the laser cavity. Consider a generic VCSEL illustrated in Figure 2-5 with an active layer radius of *a* and active and effective cavity lengths of L_a and L, respectively. The threshold condition can be written as:

$$g_{th} = \alpha_a + \alpha_p\left(\frac{1}{\Gamma}-1\right) + \frac{1}{\Gamma \cdot L_a}\ln\left(\frac{1}{R_1 R_2}\right) + \alpha_d \tag{2-24}$$

where α_a and α_p are the absorption loss in the active and passive layers, respectively, R_1 and R_2 are the reflectivities of two mirrors, and α_d is the diffraction loss. The confinement factor is expressed as the product of the longitudinal confinement factor Γ_z and the transverse factor Γ_{xy}, which is nearly unity for VCSELs. The longitudinal confinement factor Γ_z is expressed as:

$$\Gamma_z = \frac{L_a}{L} \cdot \xi \quad \Gamma_z = \frac{L_a}{L} \cdot \xi \tag{2-25}$$

The last factor, ξ, is referred to as the axial enhancement factor, because it enhances the normally expected fill factor L_a/L in the axial confinement factor. When the field is approximated as a sinusoid enveloped by a decaying exponential in the DBRs, ξ reduces to [1, 2]

$$\xi = e^{-z_{DBR}/L_{DBR}} (1 + \cos(2\beta z_s) \cdot \frac{\sin \beta L_a}{\beta L_a}) \tag{2-26}$$

where $\beta = 2\pi n_r/\lambda$ is the axial propagation constant, z_s is the shift between the active layer center and the standing-wave peak, and the exponential pre-factor accounts for placement of the active region within the DBR mirror. In this, z_{DBR} is the distance to the active material measured from the cavity-DBR interface and L_{DBR} is the penetration depth of optical energy into the DBR. If the active region is placed between the mirrors, z_{DBR} is zero, and the pre-factor is unity. If a thin active layer is centered on the standing-wave peak in the cavity, ξ can be as large as 2. If the active layer is thick enough, ξ is unity. If a thin active layer is placed at a null ($2\beta z_s = \pi$), ξ can be near zero.

Table 2-1 lists the calculations of equation (2-8) and (2-24) for EEL and VCSEL threshold conditions, respectively. For VCSEL operations, the reflectivity, R, has to be greater than 99.8% to reach threshold gain of 0.1 μm^{-1}. In order to reduce the threshold gain, it's better to have smaller absorption in the passive layers. In addition, reducing the thickness of cladding layers and the penetration depths of DBRs are

effective ways to lower the chance of absorption.

Typically, the cavity length of VCSELs is on the order of half operating wavelength. In such a short cavity device, the width of mode spacing is larger than the line-width of a typical semiconductor gain medium as shown in Figure 2-6. As a result, VCSEL operates with a single longitudinal mode. Since there's only one longitudinal mode within gain curve, the alignment between gain peak and cavity mode needs to be paid attention. Typically, the gain peak will red-shift as the temperature increases due to the band-gap shrinkage. At the same time, the cavity mode will also red-shift as the temperature increases due to the effective increase of the refractive index with the slower movement speed. Device engineers need to take into account the operation temperature to decide the best gain peak offset. Typically, for a commercial 850 VCSEL, the gain peal offset is set to be zero to few nanometers to assure proper operation during –10 to 85 degree Celsius.

Transverse Modes in VCSELs

Although VCSELs operate with single longitudinal mode, several transverse modes existed in VCSELs for typical aperture size ranging from 5 μm to 30 μm in diameter. Take a VCSEL with oxidized aperture for example shown in Figure 2-8. Due to the complex 3-D structure for oxide VCSEL, the analysis of transverse mode can be assumed an optical waveguide using effective index model [3]. The effective refractive index of core region can be calculated as n_1, while that of outer region is n_2. The simplest rule for single transverse mode operation is:

$$V_n = \frac{2\pi}{\lambda_o} \cdot a \cdot \sqrt{2 \cdot \Delta n \cdot n_1} < 2.405 \qquad (2\text{-}27)$$

where

$$\frac{\Delta n}{n_1} = \frac{\Delta \lambda_o}{\lambda_o} \qquad (2\text{-}28)$$

$$\Delta n = \frac{n_1 - n_2}{n_1} \qquad (2\text{-}29)$$

and λ_o is the operating wavelength and V_n is the normalized frequency. The index difference of oxide VCSEL originates from the built-in oxidized layer with lower refractive index in comparison to periphery semiconductor materials. Due to the accurate position of oxidized aperture, tightly defining the injected carriers into the active regions and the built-in index guiding provided by the oxidized layer, the oxide-confined VCSELs have shown superior threshold current, efficiency and modulation speed in comparison to the proton implanted VCSELs [4]. However, the good transverse optical confinement results in multimode emission even in small aperture devices. Furthermore, the presence of the oxidized aperture and the inherent three-dimensional structure of the VCSEL have become a great challenge for researchers attempting to analyze and simulate the oxide-confine VCSELs [5]. Numerous works have been done in the study of the transverse emission mode patterns of the oxide-confined VCSELs to determine the mechanism of the transverse mode formation and evolution [6-12]. We report the investigation of the spontaneous emission patterns of oxide-confined VCSELs at the subthreshold condition using spectrally resolved near-field microscopy. Figure 2-9 shows the example of transverse modes in oxide VCSELs [13]. Not only the spontaneous emission patterns with similar mode structures as the stimulated emission patterns are observed, but also the high order Hermite-Gaussian and Laguerre-Gaussian modes are easily seen. We've also observed coexistence of two sets of identical lower order Hermite-Gaussian modes with different spot sizes, implying two cavity configurations in oxide-confined VCSELs and complex mechanism responsible for formation of laser modes in oxide-confined VCSELs.

2-2 Modeling the Gain Mediums

Optical Gain in Semiconductors

As shown in Figure 2-10, parabolic band structure approximation is used for conduction and valence band E-K relationship. The density of states for the combined system involving transition between E_2 and E_1 can be written as:

$$N_r(E) = (\frac{1}{2\pi^2}) \cdot (\frac{2m_r^*}{\hbar^2})^{3/2} \cdot (h\nu - E_g)^{1/2} \tag{2-30}$$

where the reduced effective mass is:

$$\frac{1}{m_r^*} = \frac{1}{m_c^*} + \frac{1}{m_v^*} \tag{2-31}$$

m_c^* and m_v^* is the effective mass for electron and hole, respectively, and $h\nu$ is the emission photon energy.

Assumed:

(1) The Einstein coefficient, B, is the same for semiconductor,

(2) Photon energy density is $\rho(\nu)d\nu = n_p \cdot h\nu$,where n_p is the photon density,

(3) Density of states is expressed as $N_r(\nu)$,

The transition rate between E_2 and E_1 can be written as:

- Stimulated absorption: $R_{1->2} = B_{12}\rho(\nu)d\nu \cdot N_r(\nu) \cdot [f_v(E_1)(1 - f_c(E_2))]$ (2-32)
- Stimulated emission: $R_{2->1} = B_{21}\rho(\nu)d\nu \cdot N_r(\nu) \cdot [f_c(E_2)(1 - f_v(E_1))]$ (2-33)

The net stimulated emission rate is:

$$R_{st} = R_{2->1} - R_{1->2} = B\rho(\nu)d\nu \cdot (f_2 - f_1) \tag{2-34}$$

where

$$f_2 = \frac{1}{e^{(E_2 - E_{fc})/kT} + 1} = f_c(E_2), \quad f_1 = \frac{1}{e^{(E_2 - E_{fv})/kT} + 1} = f_v(E_1) \tag{2-35}$$

If $f_2 - f_1 > 0$ or < 0, the stimulated emission or absorption occurs. If $f_2 - f_1$ equals to zero, the transparent condition occurs. Thus, the condition for net stimulated emission is:

$$E_g \le E_2 - E_1 < E_{fc} - E_{fv} \tag{2-36}$$

The gain is defined as the ratio of net power emitted per unit volume over the power crossing per unit area. As shown in Figure 2-11,.an incident light pass the distance of *dz* and gains the amount of power *ΔI*. The speed of light is v_g, where $dz = v_g * \Delta t$. The power of light can be express as: $I(\nu) = [\rho(\nu)d\nu]*v_g$. The optical gain coefficient is written as:

$$\begin{aligned}\gamma(\nu) &= \frac{R_{st} \cdot h\nu}{\rho(\nu)d\nu \cdot v_g} \\ &= B(\frac{h\nu}{v_g})N_r(\nu)(f_2 - f_1) \\ &= B(\frac{h\nu}{v_g})hN_r(E)(f_2 - f_1) \quad (cm^{-1})\end{aligned} \tag{2-37}$$

After the introduction to the concept of gain in a relative macroscopic point of view, the detail behavior and interaction between light and atomic system require quantum mechanical analysis. If we consider an atom with two-level energy system, the electron under light interaction has the Hamiltonian expressed by:

$$H = \frac{1}{2m}(\mathbf{p} + e\mathbf{A})^2 + V(r) \tag{2-38}$$

where A is the vector potential. The above equation can be expanded as:

$$\begin{aligned}H &= \frac{\mathbf{p}^2}{2m} + \frac{e}{2m}[\mathbf{p}\cdot\mathbf{A} + \mathbf{A}\cdot\mathbf{P}] + \frac{e^2}{2m}\mathbf{A}^2 + V(r) \\ &= \{\frac{\mathbf{p}^2}{2m} + V(r)\} + \{\frac{e}{m}[A\hat{\mathbf{e}}\cdot\mathbf{P}]\} \\ &= H_o + H'\end{aligned} \tag{2-39}$$

The term, *H'*, can be viewed as a time-dependent perturbation to the original Hamiltonian, H_o. This perturbation term is the driving force for transitions between the conduction and valence bands. From solutions of time-dependent Schrodinger's equation, the transition rate for semiconductors can be obtained as:

$$R_{21} = \frac{2\pi}{\hbar} |H'_{21}|^2 N_r(E_{21}) \delta(E_{21} - \hbar w) \quad (2\text{-}40)$$

where

$$H'_{21} = \int \varphi_2^* H' \varphi_1^* d^3 r = < 2 | H' | 1 > \quad (2\text{-}41)$$

Equation (2-40) is known as Fermi's Golden Rules. Compared with equation (2-33) and (2-40), and substituted Einstein coefficient, B, with matrix element, $|H'_{21}|$, the gain expression can be rewritten as:

$$\gamma(\nu) = \frac{2\pi}{\hbar} \cdot |H'_{21}|^2 \cdot (\frac{1}{v_g n_{ph}}) \cdot N_r(E) \cdot (f_2 - f_1) \quad (2\text{-}42)$$

The matrix element, $|H'_{21}|$, determines the strength of interaction between two states. In semiconductors, φ_2 and φ_1 in equation (2-41) are expressed as:

$\varphi_1 = F_1(r)*u_v(r)$ for valence band, (2-43)

$\varphi_2 = F_2(r)*u_c(r)$ for conduction band, (2-44)

where:

(1) $u_v(r)$ and $u_c(r)$ are Bloch functions of parabolic potential with atomic scale,

(2) $F_1(r)$ and $F_2(r)$ are envelope functions of macroscopic potential, satisfying Schrodinger's equation in such as quantum wells, quantum dots. The bulk, quantum-well, and quantum-wire envelope functions take the following form:

$$F(r) = \frac{1}{\sqrt{V}} \cdot e^{jk \cdot r} \quad \text{(bulk)} \quad (2\text{-}45)$$

$$F(r) = \frac{1}{\sqrt{A}} \cdot e^{jk \cdot r_{\|}} \quad \text{(quantum well)} \quad (2\text{-}46)$$

$$F(r) = \frac{1}{\sqrt{L}} \cdot e^{jk_z \cdot z} \quad \text{(quantum wire)} \quad (2\text{-}47)$$

If we define:

$$\mathbf{A} = \hat{\mathbf{e}} \frac{1}{2} [| A_o(r) | e^{jk \cdot r} + | A_o(r) |^* e^{-jk \cdot r}] \quad (2\text{-}48)$$

The H' can be written as:

$$H' = \frac{eA_o}{2m_o} (\hat{\mathbf{e}} \cdot \mathbf{P}) \quad (2\text{-}49)$$

Then,

$$
\begin{aligned}
H'_{21} &= \int \varphi_2^* H' \varphi_1 d^3 r \\
&= \frac{e}{2m_o} \int \varphi_2^* (A_o \hat{\mathbf{e}} \cdot \mathbf{p}) \varphi_1 d^3 r \\
&= \frac{e}{2m_o} \int F_2^* u_c^* (A_o \hat{\mathbf{e}} \cdot \mathbf{p}) F_1 u_v d^3 r \\
&= \frac{e}{2m_o} [\int F_2^* u_c^* u_v (A_o \hat{\mathbf{e}} \cdot \mathbf{p}) F_1 d^3 r \qquad \Rightarrow (u_c^* u_v = 0), \\
&\quad + \int [F_2^* (A_o) F_1][u_c^* (\hat{\mathbf{e}} \cdot \mathbf{p}) u_v] d^3 r] \\
&= \frac{eA_o}{2m_o} \int [F_2^* F_1][u_c^* (\hat{\mathbf{e}} \cdot \mathbf{p}) u_v] d^3 r \\
&= \frac{eA_o}{2m_o} \underbrace{< u_c | \hat{\mathbf{e}} \cdot \mathbf{p} / u_v >}_{\text{Overlap of Bloch function}} \underbrace{< F_2 | F_1 >}_{\text{Envelope function overlap integral}} \equiv (\frac{eA_o}{2m_o}) | \mathbf{M_T} |
\end{aligned} \tag{2-50}
$$

where $|\mathbf{M_T}|$ is known as transition matrix element. Since photon energy density is $n_{ph}*h\nu$, and electromagnetic wave energy density = $1/2*n_r^2 \xi_o |E|^2$, the A_o can be derived as:

$$
\begin{aligned}
&E = -jwA_o; \\
&|E|^2 = w^2 |A_o|^2; \\
&n_{ph} \cdot h\nu = \frac{1}{2} n_r^2 \cdot \varepsilon_o \cdot w^2 |A_o|^2; \\
&|A_o|^2 = (\frac{2\hbar}{n_r^2 \varepsilon_o w}) \cdot n_{ph}
\end{aligned} \tag{2-51}
$$

And the equation (2-42) can be rewritten as:

$$
\begin{aligned}
\gamma(\nu) &= (\frac{e^2 h}{2\varepsilon_o n_r c m_o^2 h\nu}) \cdot |\mathbf{M_T}| \cdot N_r(E) \cdot (f_2 - f_1) \\
&= \gamma_{\max} \cdot (f_2 - f_1)
\end{aligned} \tag{2-52}
$$

Optical Gain in Quantum Well Structures

We specially pay attention to the optical gain for quantum well structures, since the active mediums for all the devices in this study have quantum wells (QW). If we

assume the potential confinement is along the z direction, the envelope function overlap integral can be expressed as:

$$
\begin{aligned}
&< F_2 \mid F_1 >= \frac{1}{A}\int F_2^*(z)e^{jk_2\cdot r_\parallel}F_1(z)e^{-jk_1\cdot r_\parallel}d^3r; \\
&\text{for} \quad k_2 = k_1; \\
&< F_2 \mid F_1 >= \frac{1}{A}\int F_2^*(z)\cdot F_1(z)dz
\end{aligned}
\tag{2-53}
$$

Due to orthogonality between the quantum-well wave-function solutions, the overlap integral in equation (2-53) reduces to the following rule for sub-band transitions:

$$
|< F_2 \mid F_1 >|^2 \cong \delta_{n_c,n_v} \tag{2-54}
$$

This means that transitions can only occur between quantum-well sub-bands which have the same quantum number, $n_c = n_v$. These are referred to as allowed transitions. Transitions between sub-bands with dissimilar quantum numbers are forbidden transitions. Both are illustrated in Figure 2-12.

Except for the envelope function overlap integral; the other term in transition matrix element is the overlap of Bloch function, which is also known as momentum matrix element $|\mathbf{M}|^2$:

$$
|\mathbf{M_T}|^2 = |\mathbf{M}|^2 \cdot |< F_2 \mid F_1 >|^2 \tag{2-55}
$$

The momentum matrix element, which is polarization dependent, determines the transition probability between conduction band and valence band. To further define the Bloch functions of the various energy bands, the corresponding atomic orbitals have to be taken into account. The Bloch function, u_s, corresponding to the isotropic s atomic orbital in conduction band remains the same. However, the Bloch functions u_x, u_y and u_z corresponding to three p atomic orbitals for valence bands: p_x, p_y and p_z, interact with each other along with the spin up and down. Using the kp theory, the modified valence bands are shown in Figure 2-13. The three valence bands are commonly known as the heavy-hole (HH), light-hole (LH), and split-off hole (SO)

bands. Since the constant $|\mathbf{M}|^2$ can be determined experimentally, Table 2-2 has listed the reported values for several important materials. Table 2-3 summaries the results for bulk and quantum-well materials for either transverse electric (TE: electric field in the quantum-well plane) or transverse magnetic (TM: electric field perpendicular to quantum-well plane) polarizations.

Nonradiative Transitions

Nonradiative transition is relatively important when considering the overall carrier recombination process. Three major types of nonradiative transitions are depicted in Figure 2-14. The first type of nonradiative recombination happens when existing an energy level in the middle of the gap, which serves to trap an electron from the conduction band temporarily before releasing it to the valence band. Defects in the lattice structure are one source of traps. The recombination rate, also referred as Schockley-Read-Hall recombination, takes the form:

$$R_d = \frac{NP - N_i^2}{(N^* + N)\tau_h + (P^* + P)\tau_e} \tag{2-56}$$

where N_i is the intrinsic carrier concentration, τ_e is the time required to capture an electron from the conduction band assuming all traps are empty, τ_h is the time required to capture a hole from the valence band assuming all traps are full, and N^* and P^* are the electron and hole densities that would exist if the Fermi level was aligned with the energy level of the trap. For the laser applications, equation (2-56) can be simplified with the high-level injection regime:

$$R_d = \frac{N}{\tau_h + \tau_e} \tag{2-57}$$

The second type of nonradiative recombination in Figure 2-13 depicts electrons recombining via surface states of the crystal. The surface recombination rate under

$$R_s = \frac{a_s}{V} v_s N$$

high level injection in the active region can be expressed as:

(2-58)

where a_s is the exposed surface area, V is the volume of the active region, and v_s is the surface recombination velocity. Surface recombination is most damaging when the exposed surface-to-volume ratio is large. In addition, devices when make use of regrowth technique can suffer from poor interfaces and hence high interface recombination. Surface recombination is also material dependent. The recombination velocity of short-wavelength GaAs system is one order greater than that of long-wavelength quaternary InGaAsP system.

The last type of nonradiative recombination depicted in Figure 2-14 is basically a collision between two electrons, which knocks one electron down to the valence band and the other to a higher energy state in the conduction band. An analogous collision can occur between two holes in the HH band and either SO or LH band. The above three types of collision are refereed to as Auger processed. In laser applications with high injection level, the Auger recombination rate can be expressed as:

$$R_A = CN^3 \tag{2-59}$$

where C is a generic experimentally determined Auger coefficient. In long wavelength InGaAsP materials, the Auger coefficient is one order lager than GaAs systems since the smaller band-gap in InGaAsP materials enhances the probability of momentum conservation. The reduced material dimensionality, such as quantum well, appears to reduce the Auger process due to the modification of band structures. Another possible method of minimizing Auger recombination is to use strained materials in active layers.

Optical Gain in Strained Quantum Wells

Strained QWs use a material, which has different native lattice constant than the surrounding lattice constant. As shown in Figure 2-15, if the QWs native lattice constant is larger than the surrounding lattice constant, the QW lattice compress in the plane, and the lattice is said to be under compressive strain. If the opposite is true, the QW is under tensile strain. However, in any lattice-mismatched system, it is important to realize that there is a critical thickness beyond which the strained lattice will begin to revert back to its native state, causing high densities of lattice defects. For typical applications, this critical thickness is on the order of a few hundred angstroms, thus limiting the number of strained QWs in active layers.

Because the energy gap of a semiconductor is related to its lattice spacing, distortions in the crystal lattice should lead to alterations in the bandgap of the strained layer. There are two types of modifications. The first effect produces an upward shift in the conduction band as well as a downward shift in both valence bands, increasing the overall bandgap by an amount, *H* (which is positive for compressive strain and negative for tensile strain). The *H* indicates that this shift originate from the hydrostatic component of the strain. The second important effect separates the HH and LH bands, each being pushed in opposite directions from the center by an amount, *S*. The *S* indicates that this shift originates from the shear component of the strain. Figure 2-16 illustrates the energy shifts of the bands for biaxial strains. No only the energy shift, the band curvatures will be modified due to the strain effect. For a quantum-structure such as an $In_{1-x}Ga_xAs$ layer sandwiched between InP barriers, the band structures are shown in Figure 2-17 for (a) a compressive strain ($x < 0.468$), (b) no strain ($x = 0.468$), and (c) a tensile strain ($x > 0.468$) [18]. The left-hand side shows the quantum-well band structures in real space

vs. position along the growth (z) direction. The right-hand side shows the quantized subband dispersions in momentum space along the parallel (k_x) direction in the plane of the layer. These dispersion curves show the modification of the effective masses or the densities of states due to both the quantization and strain effects.

The above characteristics provide some advantages in using strained materials over unstrained materials. First, the bandgap can be adjusted to obtain certain emission wavelength. Next, the reduction in hole masses leads to lower threshold lasing and lower Auger recombination rate. Then, the applied strain can allow laser emission with tailored polarization. Finally, the built-in strain may suppress defect migration into the active region.

2-3 Characteristics of Distributed Bragg Reflectors

From the discussions in chapter 1, the high-reflectivity DBRs are extremely important components in VCSELs. In this section, we'd like to discuss the characteristics of DBRs. We start this section with the transfer matrix method in stacks of thin films. We construct a computational simulation program for the transfer matrix. Then, based on the simulation, we'll discuss the reflectance, transmittance, absorption, phase delay, and penetration depth for the DBRs.

Transfer Matrix Method

A thin film is shown in Figure 2-18(a) [19]. The direction of the incident wave is denoted by the symbol + (that is, positive-going) and waves in the opposite direction is – (that is, negative-going). Since there is no negative-going wave in the substrate and the waves in the film can be summed into one resultant positive-going wave and one resultant negative-going wave. At this interface b, then, the tangential

$$E_b = E_{1b}^{+} + E_{1b}^{-}$$
$$H_b = \eta_1 E_{1b}^{+} - \eta_1 E_{1b}^{-}$$

components of E and H are:

(2-60)

(2-61)

where η is the optical admittance of the film. Different polarizations have different forms:

for s-polarization (TE): $\eta_s = n\cos\theta\sqrt{\varepsilon_o/\mu_o}$ (2-62)

for p-polarization (TM): $\eta_s = n\sqrt{\varepsilon_o/\mu_o}/\cos\theta$ (2-63)

Hence

$$E_{1b}^{+} = \frac{1}{2}(H_b/\eta_1 + E_b) \quad (2\text{-}64)$$

$$E_{1b}^{-} = \frac{1}{2}(-H_b/\eta_1 + E_b) \quad (2\text{-}65)$$

$$H_{1b}^{+} = \eta_1 E_{1b}^{+} = \frac{1}{2}(H_b + \eta_1 E_b) \quad (2\text{-}66)$$

$$H_{1b}^{-} = -\eta_1 E_{1b}^{-} = \frac{1}{2}(H_b - \eta_1 E_b) \quad (2\text{-}67)$$

The field at the other interface a at the same instant and at a point with identical x and y coordinates can be determined by altering the phase factors of the waves to allow for a shift in the z coordinate from 0 to $-d$. The phase factor of the positive-going wave will be multiplied by exp(iδ) where

$$\delta = 2\pi n_1 d\cos\theta_1/\lambda \quad (2\text{-}68)$$

and θ_1 may be complex, while the negative-going phase factor will be multiplied by exp(-iδ). There the values of E and H at the interface are:

$$E_{1a}^{+} = E_{1b}^{+}e^{i\delta} = \frac{1}{2}(H_b/\eta_1 + E_b)e^{i\delta}$$

$$E_{1b}^{-} = E_{1b}^{-}e^{-i\delta} = \frac{1}{2}(-H_b/\eta_1 + E_b)e^{-i\delta}$$

$$H_{1b}^{+} = H_{1b}^{+}e^{i\delta} = \frac{1}{2}(H_b + \eta_1 E_b)e^{i\delta}$$

$$H_{1b}^{-} = H_{1b}^{-}e^{-i\delta} = \frac{1}{2}(H_b - \eta_1 E_b)e^{-i\delta}$$

So that

$$E_a = E_{1a}^{+} + E_{1a}^{-} = E_b \cos\delta + H_b \frac{i\sin\delta}{\eta_1}$$

$$H_a = H_{1a}^{+} + H_{1a}^{-} = E_b i\eta_1 \sin\delta + H_b \cos\delta$$

This can be written in matrix notation as:

$$\begin{bmatrix} E_a \\ H_a \end{bmatrix} = \begin{bmatrix} \cos\delta & (i\sin\delta)/\eta_1 \\ i\eta_1 \sin\delta & \cos\delta \end{bmatrix} \begin{bmatrix} E_b \\ H_b \end{bmatrix} \tag{2-69}$$

The 2×2 matrix on the right-hand side of equation (2-69) is known as the characteristic matrix of the thin film. Let another thin film be added to the single film so that the final interface is now denoted by c, as shown in Figure 2-18(b). The characteristic matrix of the film nearest the substrate is:

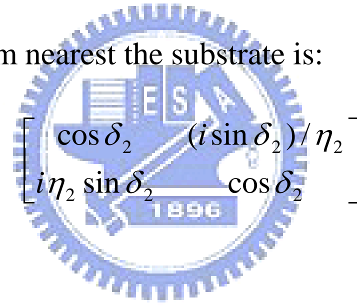

$$\begin{bmatrix} \cos\delta_2 & (i\sin\delta_2)/\eta_2 \\ i\eta_2 \sin\delta_2 & \cos\delta_2 \end{bmatrix}$$

And from equation (2-69):

$$\begin{bmatrix} E_b \\ H_b \end{bmatrix} = \begin{bmatrix} \cos\delta_2 & (i\sin\delta_2)/\eta_2 \\ i\eta_2 \sin\delta_2 & \cos\delta_2 \end{bmatrix} \begin{bmatrix} E_c \\ H_c \end{bmatrix}$$

and

$$\begin{bmatrix} E_a \\ H_a \end{bmatrix} = \begin{bmatrix} \cos\delta_1 & (i\sin\delta_1)/\eta_1 \\ i\eta_1 \sin\delta_1 & \cos\delta_1 \end{bmatrix} \begin{bmatrix} \cos\delta_2 & (i\sin\delta_2)/\eta_2 \\ i\eta_2 \sin\delta_2 & \cos\delta_2 \end{bmatrix} \begin{bmatrix} E_c \\ H_c \end{bmatrix}$$

If we define a characteristic matrix of the assembly, the above equation becomes:

$$\begin{bmatrix} B \\ C \end{bmatrix} = \begin{bmatrix} \cos\delta_1 & (i\sin\delta_1)/\eta_1 \\ i\eta_1 \sin\delta_1 & \cos\delta_1 \end{bmatrix} \begin{bmatrix} \cos\delta_2 & (i\sin\delta_2)/\eta_2 \\ i\eta_2 \sin\delta_2 & \cos\delta_2 \end{bmatrix} \begin{bmatrix} 1 \\ \eta_3 \end{bmatrix}$$

This result can be immediately extended to the general case of an assembly of q layers, when the characteristic matrix is simply the product of the individual matrices

taken in the correct order, i.e.

$$\begin{bmatrix} B \\ C \end{bmatrix} = \left(\prod_{r=1}^{q} \begin{bmatrix} \cos\delta_r & (i\sin\delta_r)/\eta_r \\ i\eta_r \sin\delta_r & \cos\delta_r \end{bmatrix} \right) \begin{bmatrix} 1 \\ \eta_m \end{bmatrix} \tag{2-70}$$

where we have now used the suffix m to denote the substrate or exit medium. If θ_o, the angle of incidence, is given, the values of θ_r can be found from Snell's law. So the reflectance, transmittance and absorptance can be expressed as [19]:

$$R = \left(\frac{\eta_o B - C}{\eta_o B + C}\right)\left(\frac{\eta_o B - C}{\eta_o B + C}\right)^* \tag{2-71}$$

$$T = \frac{4\eta_o \operatorname{Re}(\eta_m)}{(\eta_o B + C)(\eta_o B + C)^*} \tag{2-72}$$

$$A = \frac{4\eta_o \operatorname{Re}(BC^* - \eta_m)}{(\eta_o B + C)(\eta_o B + C)^*} \tag{2-73}$$

The phase change on reflection can be expressed as:

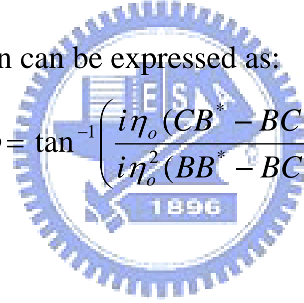

$$\phi = \tan^{-1}\left(\frac{i\eta_o (CB^* - BC^*)}{i\eta_o^2 (BB^* - BC^*)} \right) \tag{2-74}$$

Reflection Delay and Penetration Depth of DBRs

Since we are interesting in Bragg mirrors (quarter-wave mirrors) with incident light normal to the interfaces, the above equations can be much simplified. Due to the distributed nature of quarter-wave stack, these mirrors exhibit phase dispersion and a finite delay upon reflection [20]. The dispersion is responsible for pulse broadening and distortion [21], whereas the reflection delay adds to the laser cavity round-trip time. The storage of electromagnetic energy in a distributed reflector is also a factor of interest in the case of small-cavity structures where the cavity volume and the cavity round-trip time are of comparable magnitude as the mirror storage and the reflection delay. It has been common practice [22] to account for both the reflection

delay time and the energy storage in distributed laser mirrors by defining a quantity called penetration depth as the depth inside the mirror at which the optical pulse appears to reflect, or the energy falls off to $1/e$ of its initial value. The sum of the physical cavity length and the mirror penetration depth gives the effective cavity length.

Figure 2-19 shows the simulation results of InGaAlAs/InAlAs DBRs with center wavelength at 1550 nm for 10, 20, 30 and 40 pairs. Figure 2-19(a), (b) and (c) demonstrate the reflectivity, phase and delay time, respectively. Figure 2-20 illustrates the interpretation of penetration depth: a wave is incident from a medium with refractive index n onto a DBR with linear phase. Its reflection is delayed by τ and scaled by the value of the reflectivity. The equivalent model for the DBR is realized by extending the incident medium beyond the reference plane and by placing a fixed-phase mirror at depth L_{DBR}. To the observer placed to the left of the reference plane, the mirrors will appear equivalent if the reflectivity and the phase characteristics of the two cases are equal. The effective length and phase can be expressed as:

$$L_{DBR} = \frac{c\tau}{2n} \qquad \theta_o = \omega_o \tau \tag{2-74}$$

where the reflection delay is:

$$\tau = -\frac{\partial \phi(\omega)}{\partial \omega} \tag{2-75}$$

and L_{DBR} is the penetration depth. Figure 2-21 shows the simulated electric field in a 40 pairs InGaAlAs/InAlAs DBRs. The intensity of the electric field decreases from the incident plane. The distance from the incident plane to 1/e of the magnitude of the incident intensity represents the penetration depth. This depth needs to be considered in the determination of cavity mode wavelength in FP lasers and longitudinal confinement factor in VCSELs. The confinement factor is given by the ratio of

electromagnetic energy in the active region of length L_a and the total energy present in the cavity:

$$\Gamma_L = \frac{L_a}{L_{FP} + 2L_{DBR}} \tag{2-76}$$

From equation (2-76), the longer penetration depth will lower the confinement factor. If the absorption is taken into account, the longer traveling path will increase more loss. Table 2-4 lists various kinds of material combination for making DBRs with center wavelength at 1550 nm. The larger refractive index difference between the DBR layers leads to a smaller number of pairs to reach 99.9% reflectivity and a shorter penetration depth.

2-4 Analysis of the Heat Flow

It is well known that the heating effect is very important for semiconductor lasers in almost all applications. For VCSELs with relatively small device volume, the heat dissipation is one of the major limitations for continuous-wave (CW) operations. Long wavelength VCSELs especially suffer from the temperature effect due to the insufficient gain at high temperature. We'd like to develop a thermal model by using finite element analysis (FEA) software to simulate the heat flow in VCSELs.

Typically, the VCSEL structure is cylindrical symmetry. The coordinates in thermal model can be transformed to longitudinal, z, and axial, r, directions. The input parameters for the thermal model include the geometry, the thermal conductivity $k(\mathrm{T}, r, z)$ of the materials, and the heat source distribution $\mathrm{P}(r, z)$. The heat sources mainly originate from the Joule heat in conducting materials, nonradiative recombination and absorptions in active layers. The heat-transferred modal for the cylindrical symmetry can be expressed as:

$$\frac{\partial}{\partial r} k_r \frac{\partial T}{\partial r} + \frac{1}{r} k_r \frac{\partial T}{\partial r} + \frac{\partial}{\partial z} k_z \frac{\partial T}{\partial z} = -\frac{\partial P}{\partial V}(r, z) \tag{2-77}$$

where T is temperature and $\partial P/\partial V$ is the heat power density. If we assumed anisotropic thermal conductivity in DBR layers, then:

$$k_r = \frac{d_1 k_1 + d_2 k_2}{d_1 + d_2} \quad \text{and} \quad k_z = \frac{d_1 + d_2}{d_1 / k_1 + d_2 / k_2} \tag{2-78}$$

where k_1 and k_2 are thermal conductivities for bulk materials and d_1 and d_2 are the DBR layer thicknesses. The partial differential equation (2-77) can be easily solved by FEA software [23]. The visualized outputs contain the temperature distribution and heat flow. The thermal resistance can be calculated from the temperature distribution T(r, z) with uniform heat source in the active region:

$$R_{th} = \Delta T_{\max} / P_{heat} \tag{2-79}$$

Although heat flow in a VCSEL can be solved with the FEA software, the average device temperature can be easily evaluated. The power dissipated in the laser is

$$P_D = P_{in} - P_O = P_{in}(1-\eta) \tag{2-80}$$

where η is the wall-plug efficiency, which is the ratio between the emitted optical power over the injected electrical power. Then, the temperature rise is:

$$\Delta T = P_D Z_T \tag{2-81}$$

where Z_T is the thermal impedance. For small VCSELs on a relatively thick substrate, a simple analytic expression for Z_T is useful [24]:

$$Z_T = \frac{1}{4 k_T a_{eff}} \tag{2-82}$$

where k_T is the thermal conductivity of the substrate beneath the heat generating disk, and a_{eff} is the effective device radius. In the uncovered etched-mesa case, a_{eff} is approximately equal to the radius of active region; in other cases it tends to be somewhat larger due to heat spreading in either surrounding epitaxial material or deposited heat spreaders. In contrast, if the VCSEL is flip-chip bonded to a heat sink, a quasi-one-dimensional heat flow results, and then

$$Z_T = \frac{h}{k_T A} \quad (2\text{-}83)$$

where A is the effective area of the heat flow, h is the distance to the heat sink and k_T is the thermal conductivity of the material between the source and heat sink.

References

[1] R. H. Yan, Z. M. Chuang, S. W. Corzine, and L. A. Coldren, *J. Appl. Phys.*, v67, p4387, 1990.

[2] E. R. Hegblom, D. I. Babic, B. J. Thibeault, and L. A. Coldren, *IEEE J. Sel. Topics Quantum Electron.,* v3, p379, 1997.

[3] G. R. Hadley, *Optics Lett.*, v20, no.13, p1483, 1995.

[4] K. L. Lear, R. P. Schneider, Jr., K. D. Choquette, and S. P. Kilcoyne, *IEEE Photonics Technol. Lett.*, v8, p740, 1996.

[5] J. S. Gustavsson, J. A. Vukusic, J. B. Bengtsson, and A. Larsson, *IEEE J. Quantum Electron.* v38, p203, 2002.

[6] C. Degen, I. Fischer and W. Elsaber, *Optics Express*, v5, p38, 1999.

[7] C. J. Chang-Hasnain, M. Orenstein, A V. Lehmen, L. T. Florez, J. P. Harbison, and N. G. Stoffel, *Appl. Phys. Lett.* v57, p218, 1990.

[8] L. Raddatz, I. H. White, H. D. Summers, K. H. Hahn, M. R. Tan, and S.-Y. Wang, *IEEE Photonics Technol. Lett.*, v8, p743, 1996.

[9] I. Horsch, R. Kusche, O. Marti, B. Weigl, and K. J. Ebeling, *J. Appl. Phys.*, v79, p3831, 1996.

[10] J. Kim, D. E. Pride, J. T. Boyd, and H. E. Jackson, *Appl. Phys. Lett.*, v72, p3112, 1998.

[11] J. Kim, J. T. Boyd, H. E. Jackson, and K. D. Choquette, *Appl. Phys. Lett.*, v76, p526, 2000.

[12] W. C. Bradford, J. D. Beach, R. T. Collins, D. W. Kisker, and D. Galt, *Appl. Phys. Lett.*, v80, p929, 2002.

[13] T. C. Lu, W. C. Hsu, Y. S. Chang, H. C. Kuo and S. C. Wang, manuscript submitted to *J. Appl. Phys.* and under revision, 2004.

[14] C. Hermann and C. Weisbuch, *Phys. Rev. B*, v15, p823, 1977.

[15] C. Hermann and C. Weisbuch, *Modern Problems in Condensed Matter Sciences Volume 8; Optical Orientation,* ed. V. M. Agranovich and A.A. Maradudin, North-Holland Co., p463, 1984.

[16] B. Jani, P. Gilbart, J. C. Portal, and R. L. Aulombard, *J. Appl. Phys.*, v58, p3481, 1985.

[17] R. J. Nicholas, J. C. Portal, C. Houlbert, P. Perrier, and T. P. Pearsall, *Appl. Phys. Lett.*, v34, p492, 1979.

[18] S. L. Chuang, *"Semiconductor Lasers" in Physics of Optoelectronic Devices*, John Wiley and Sons, Inc, p443, 1995.

[19] H. A. Macleod, *"Basic theory" in Thin-Film Optical Filters*, 2nd ed. McGraw-Hill, p35, 1989.

[20] D. I. Babic and S. W. Corzine, *IEEE J. Quantum Electron.,* v28, no.2, p514, 1992.

[21] P. Laporta and V. Magni, *Appl. Opt.* , v24, p2014, 1985.

[22] F. Koyama, Y. Suematsu, S. Arai, and T. Tawee, *IEEE J. Quantum Electron.,* vQE-19, p1042, 1983.

[23] *Partial Differential Equation Toolbox User's Guide*, The MathWorks, Inc., p2-57, 1996

[24] S. S. Kutateladze and V. M. Borishanski, *A Concise Encyclopedia of Heat Transfer*, Permagon, Oxford, 1966.

Table 2-1 Comparison of threshold conditions for EEL vs VCSEL.

	EEL	***VCSEL***
Active length, L_a	300 μm	0.01 μm
Confinement factor, Γ	0.03	1 (or 2)
$1/\Gamma L_a$	1/9 μm^{-1}	1/0.01 μm^{-1}
Mirror loss, ln(1/R)	1.2 (R ~ 0.3)	0.001 (R ~ 0.998)
Threshold gain, g_{th}	0.1 μm^{-1}	0.1 μm^{-1}

Table 2-2 Magnitude of $|M|^2$ for various material systems.

Material systems	***$2|M|^2/m_o$ in eV***	***Reference***
GaAs	28.8 ± 0.15	[14, 15]
$Al_xGa_{1-x}As$ (x < 0.3)	29.83+2.85x	[16]
$In_xGa_{1-x}As$	28.8-6.6x	[14, 15]
InP	19.7 ± 0.6	[14, 15]
$In_{1-x}Ga_xAs_yP_{1-y}$ (x=0.47y)	19.7+5.6y	[15, 17]

Table 2-3 Magnitude of $|M_T|^2/|M|^2$ for different transitions and polarizations. C-HH represents the transition from electron band to heavy hole band. C-LH represents the transition from electron band to light hole band

	Bulk		Quantum-well ($k_t \sim 0$)	
Polarization	C-HH	C-LH	C-HH	C-LH
TE	1/3	1/3	1/2	1/6
TM	1/3	1/3	0	2/3

.

Table 2-4 Various material combinations for making high reflectivity DBRs

DBR materials	$\Delta n/n_o$	Required pairs to reach R>99.9%	Penetration depth (L_{DBR})
InP/Air	1.038	4	0.11 μm
TiO_2/SiO_2	0.509	7	0.14 μm
GaAs/AlAs	0.153	27	0.79 μm
AlGaAsSb/AlAsSb	0.149	28	0.87 μm
InGaAlAs/InP	0.102	41	1.26 μm
InGaAlAs/InAlAs	0.090	47	1.45 μm
InGaAsP/InP	0.082	51	1.59 μm

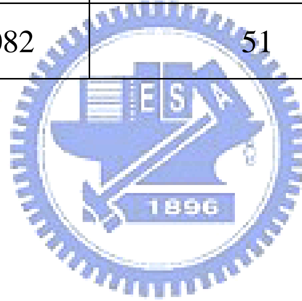

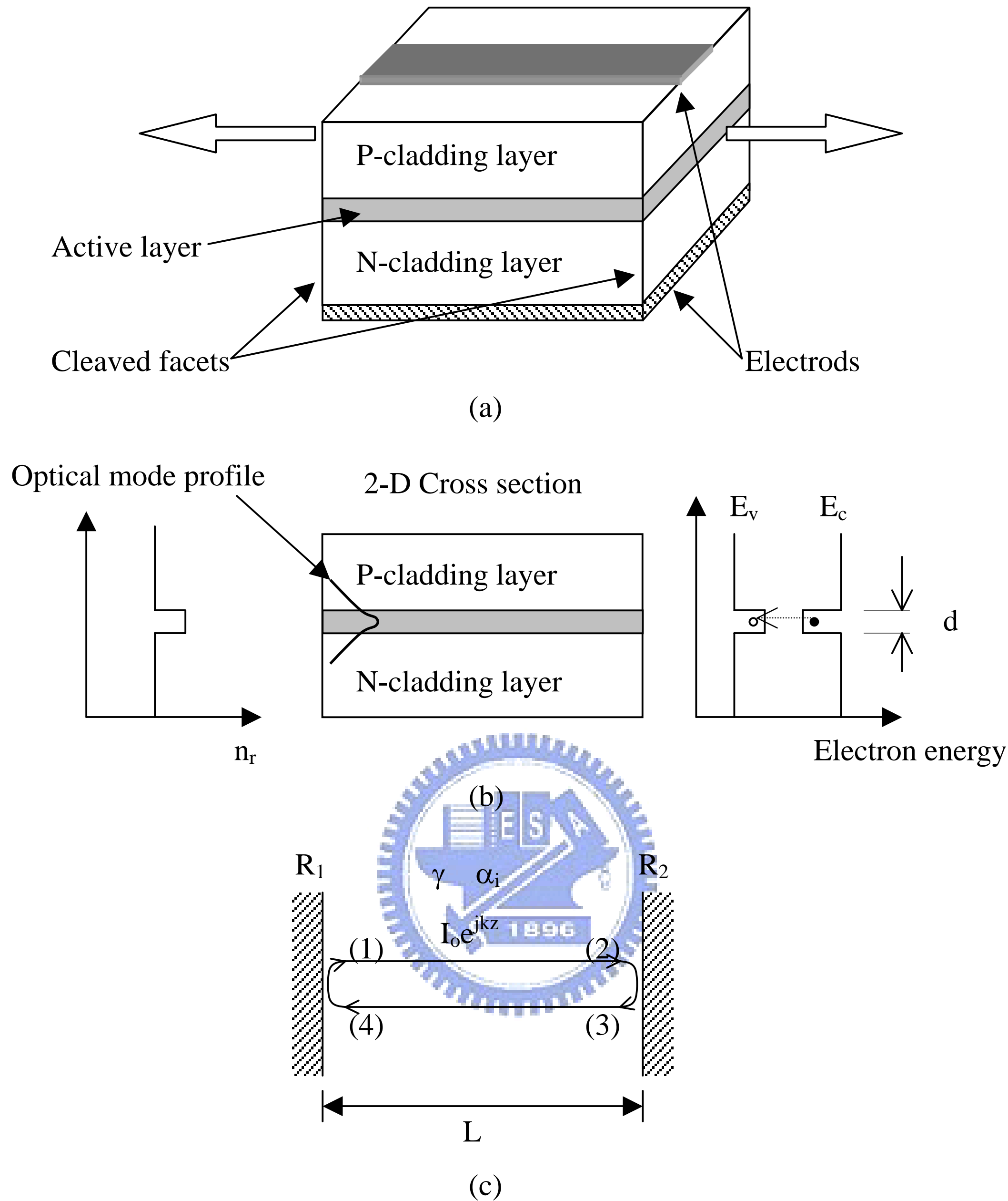

Figure 2-1 Schematics of edge emitting lasers. (a) The typical EELs with DH structures. The electrodes outside the P and N cladding layers provide the electrical current. The laser output goes out from both cleaved facets. (b) The 2-D cross-section of EELs. The refractive index profile shown on the left side have a high index value for the active region, which serves a natural optical waveguide for the laser mode. The conduction and valence band diagram for the EELs shown on the right side explains carrier confinement in DH structures. (c) Schematics of laser operation conditions with optical gain, γ, internal loss, α_i, cavity length, L, and mirror reflectivity, R.

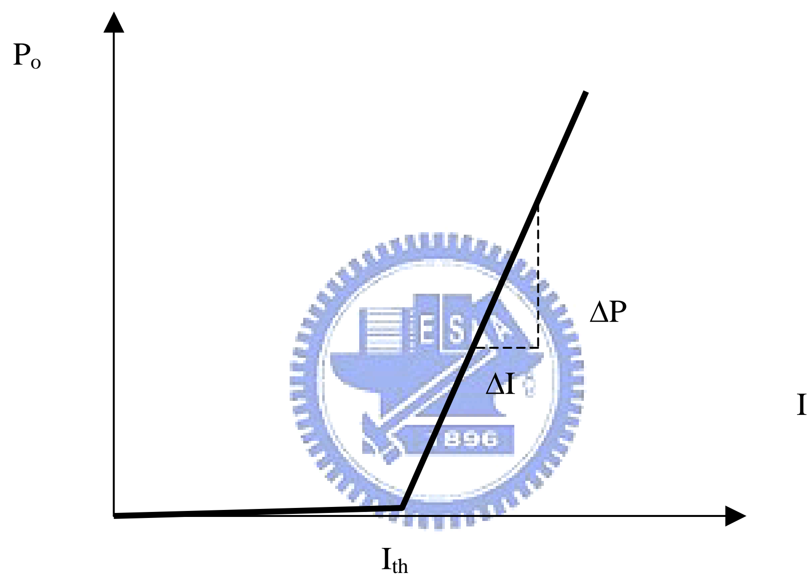

Figure 2-2 Typical semiconductor laser output power vs. injection current relation (L-I curve).

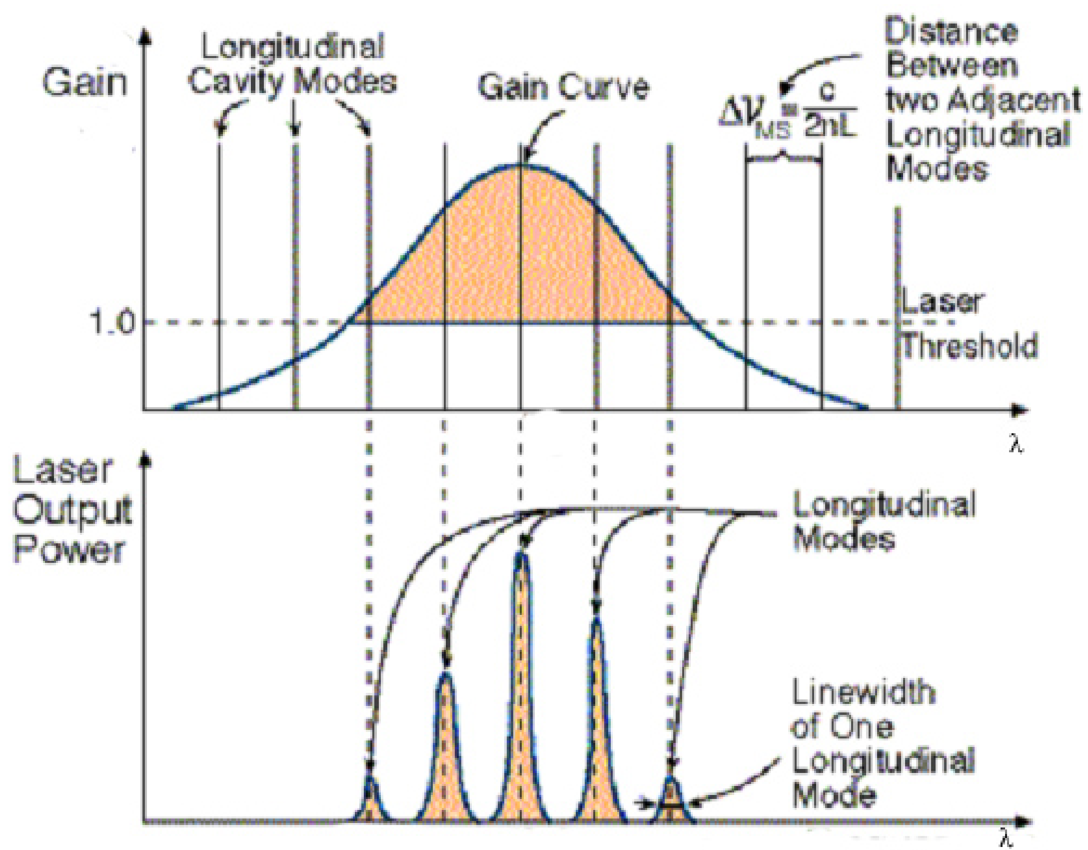

Figure 2-3 The gain, optical mode and power spectrum for a Fabry-Perot laser.

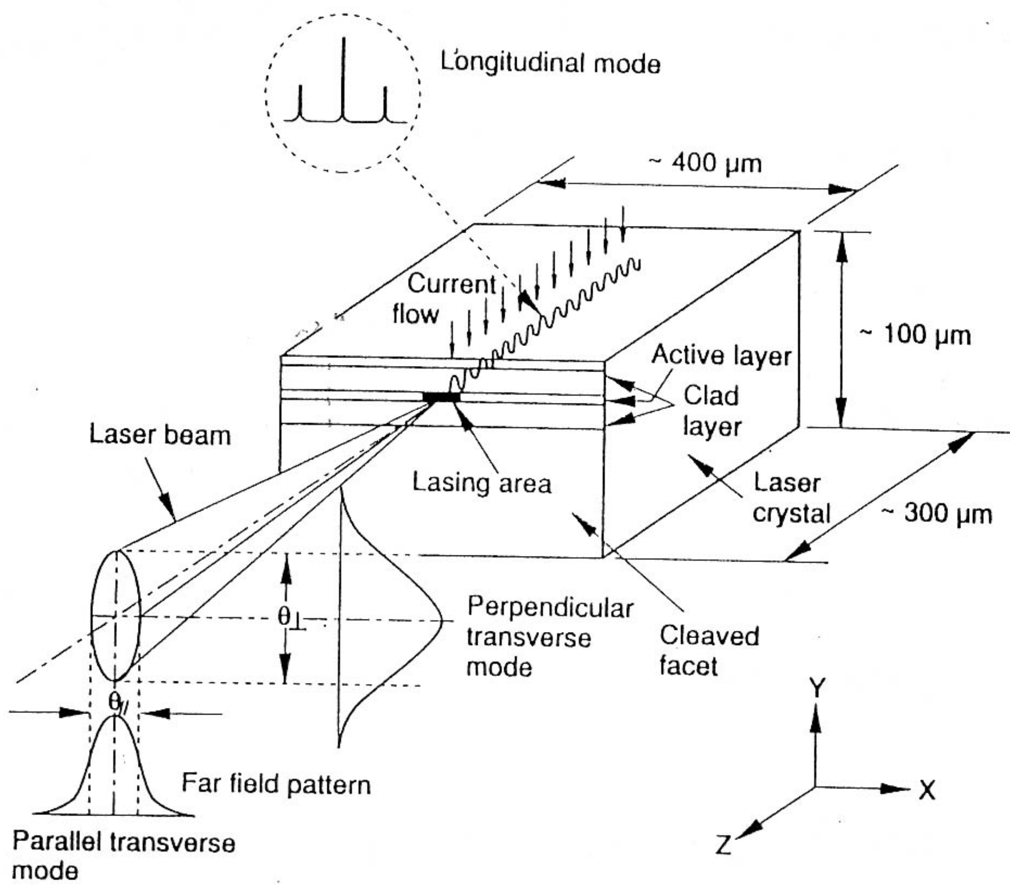

Figure 2-4 Operation of a Fabry-Perot laser.

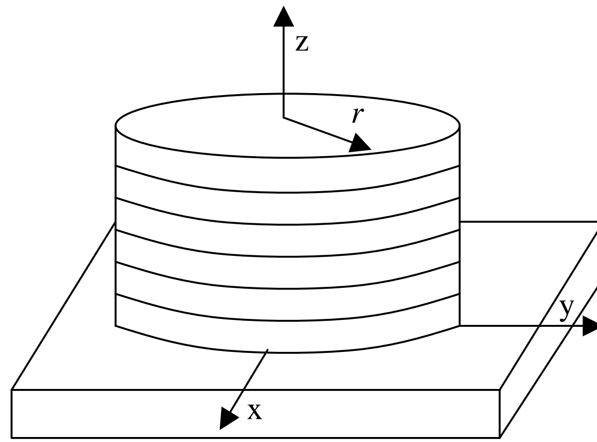

(a)

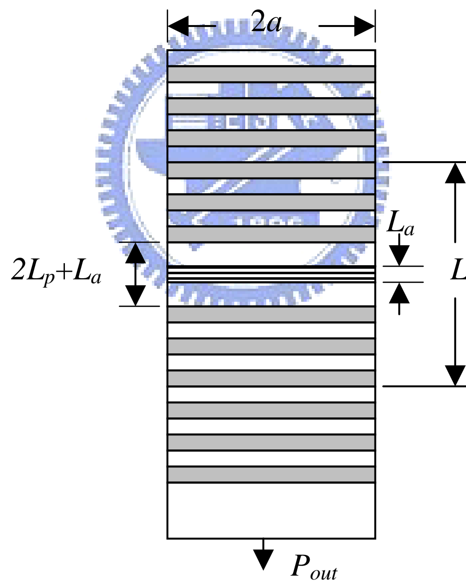

(b)

Figure 2-5 (a) General VCSEL schematic indicating coordinate system. (b) Cross-sectional schematic indicating active layer thickness, L_a, cladding layer thickness, L_p, and VCSEL effective cavity length, L.

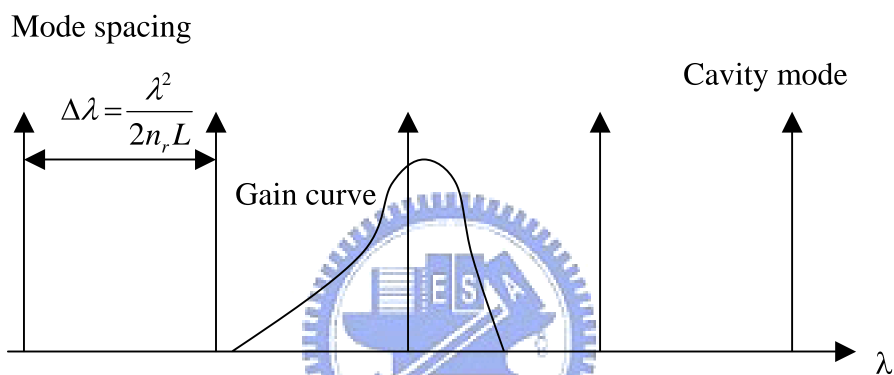

Figure 2-6 The gain and optical mode spectrum for a VCSEL. Since the effective cavity length of VCSEL is on the order of half wavelength, the longitudinal mode spacing is larger than linewidth for typical semiconductor gain medium. The property of short cavity makes VCSEL a single longitudinal device.

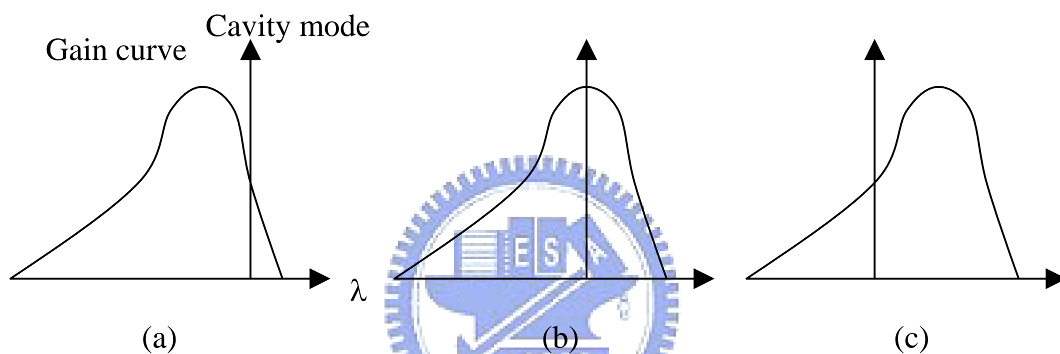

Figure 2-7 Schematics of alignment between gain and cavity mode peak at different temperature. Temperature increases as sequence as (a), (b) and (c). The gain peak red-shifts faster than the cavity mode as the temperature increases.

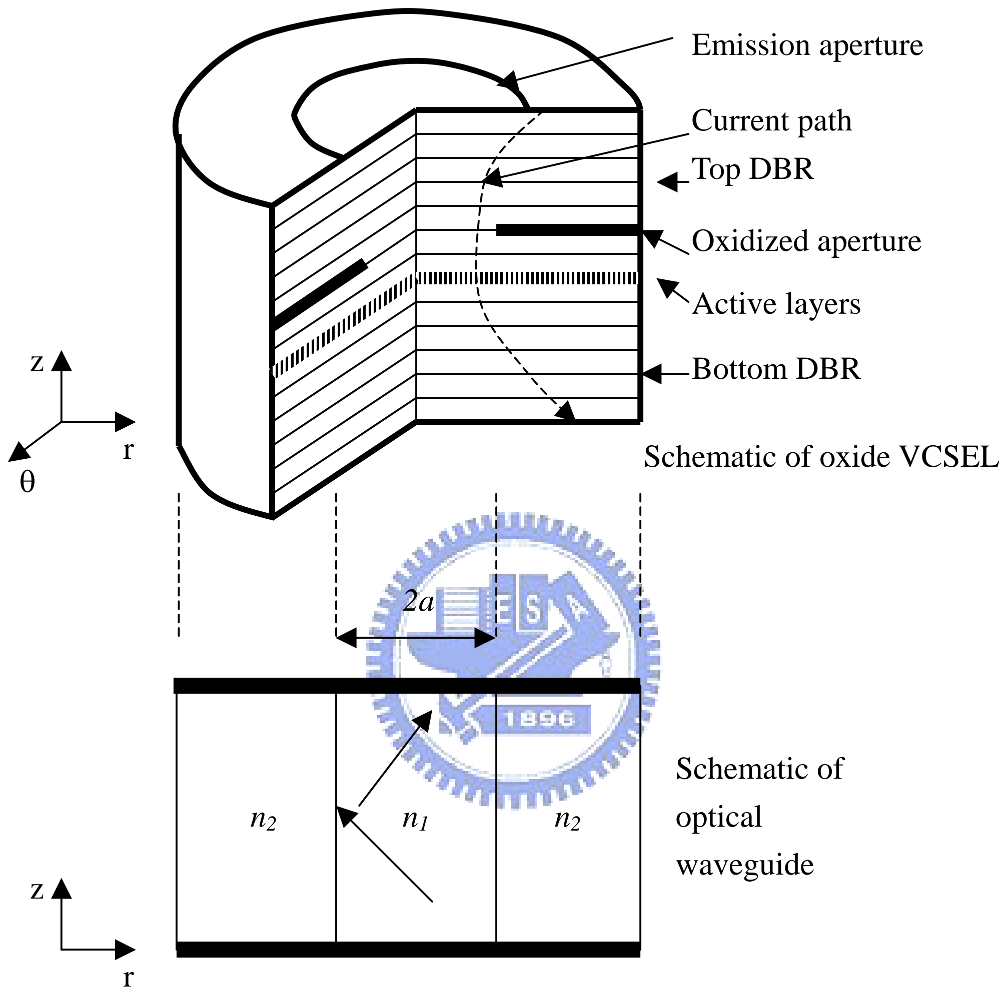

Figure 2-8 Schematics of optical waveguide for oxide VCSEL. Due to the complex 3-D structure for oxide VCSEL, the analysis of transverse mode can be assumed an optical waveguide using effective index model. The effective refractive index of core region can be calculated as n_1, while that of outer region is n_2.

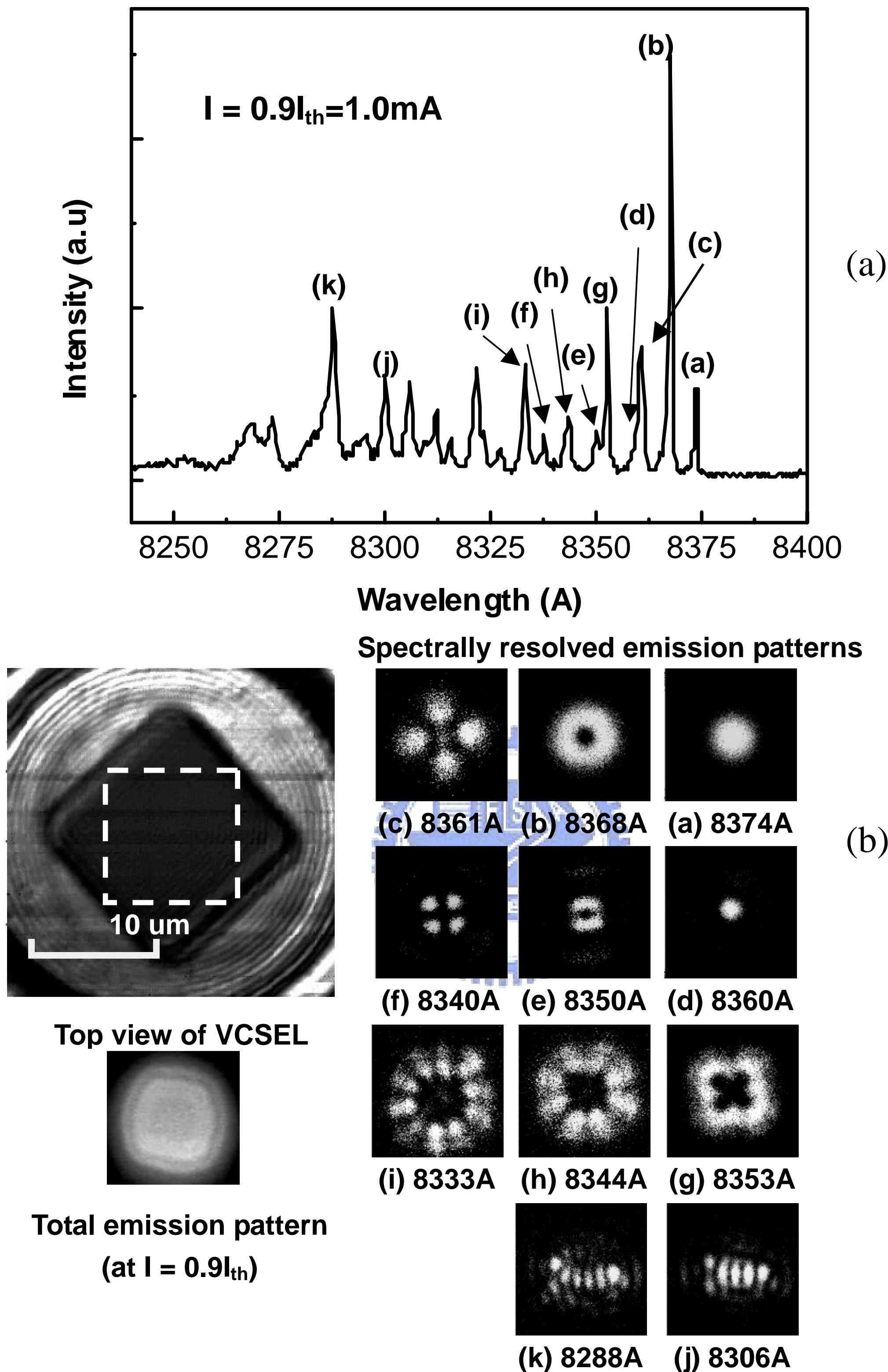

(a)

(b)

Figure 2-9 (a) The spectrum of the oxide-confined VCSEL with a 6x6 μm square aperture operated at 0.9 I_{th} (~1 mA). (b) The upper-left image is the top view of the VCSEL and the dash line indicates the scanning area. Below the top view of the VCSEL is the total spontaneous emission image observed directly from the microscope. On the other side is the spectrally resolved near field images corresponding to the emission peaks (a) to (k) labeled in the spectrum.

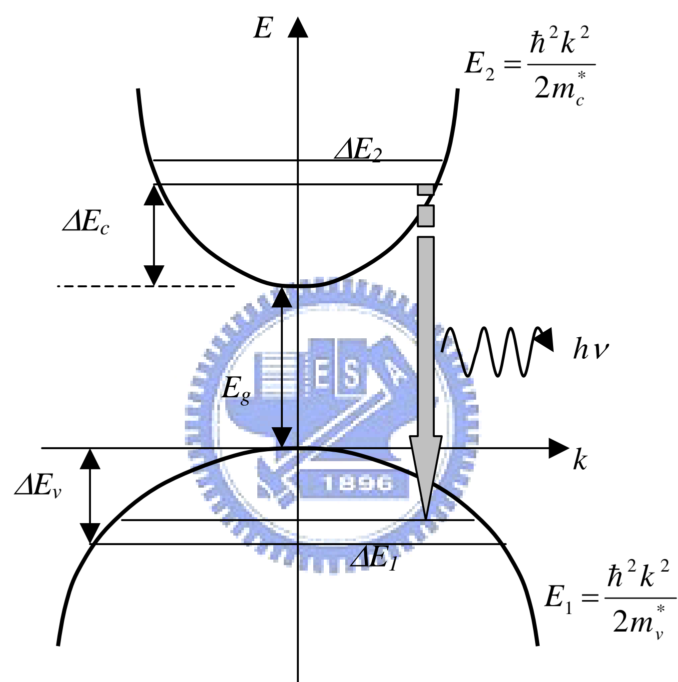

Figure 2-10 The relationship between energy and k-space and illustration of k-selected transition in parabolic shape band structure.

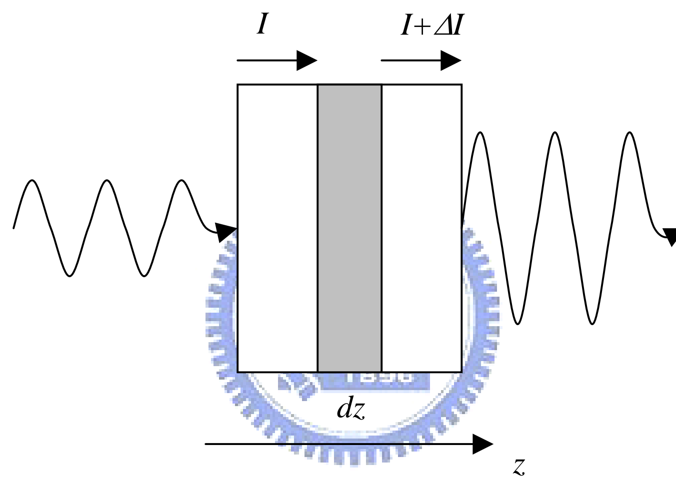

Figure 2-11 Illustration of an incident light gaining its power after passing through a portion of gain medium

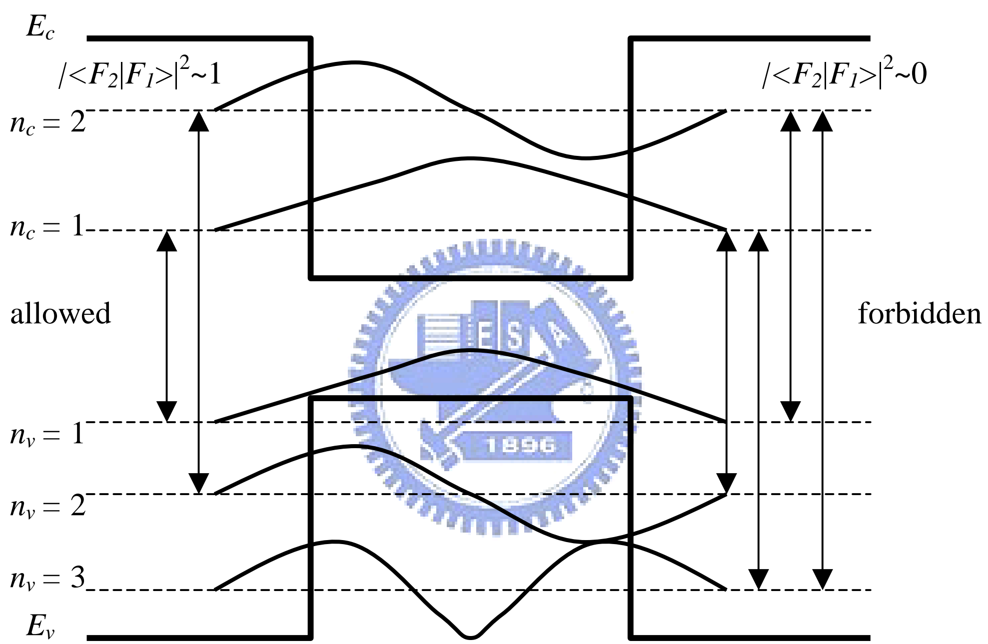

Figure 2-12 Allowed and forbidden transitions in a quantum well.

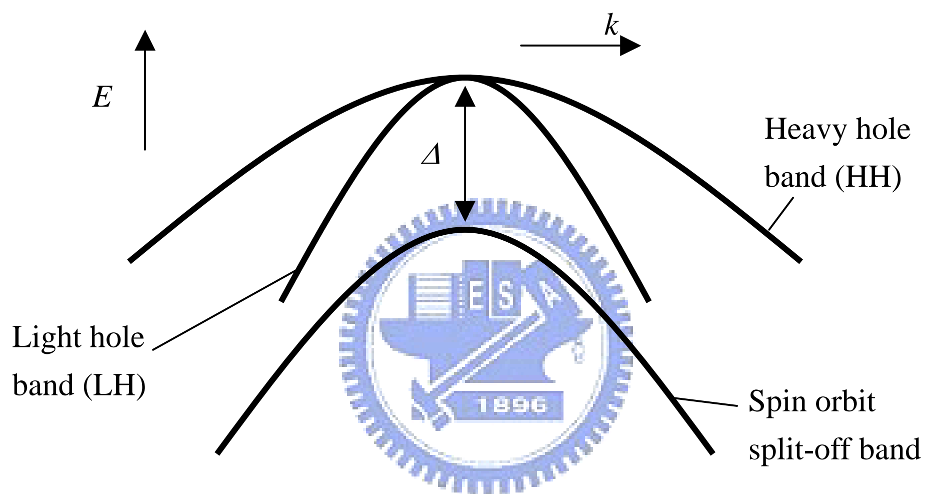

Figure 2-13 Valence band structures of unstrained bulk semiconductor such as GaAs

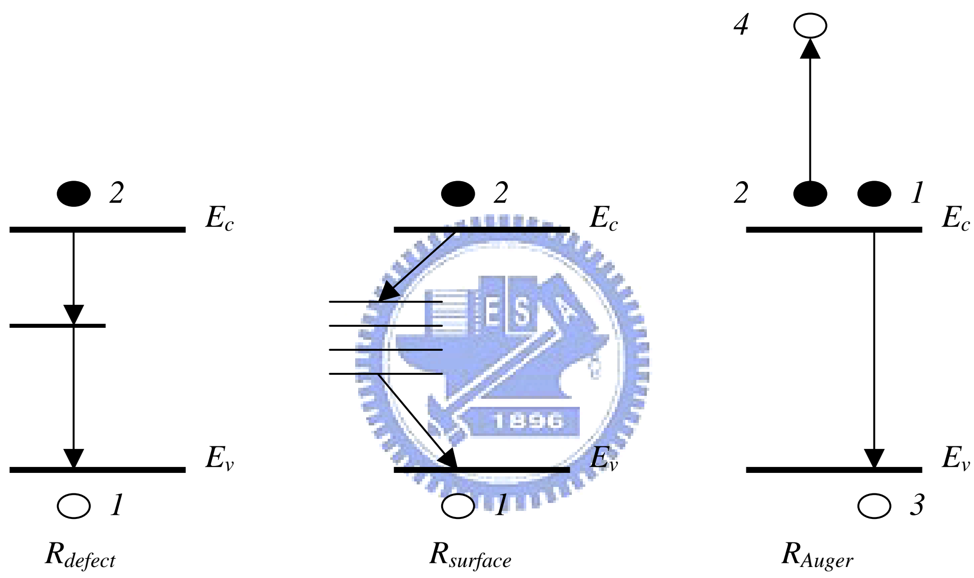

Figure 2-14 Three major types of nonradiative recombination paths

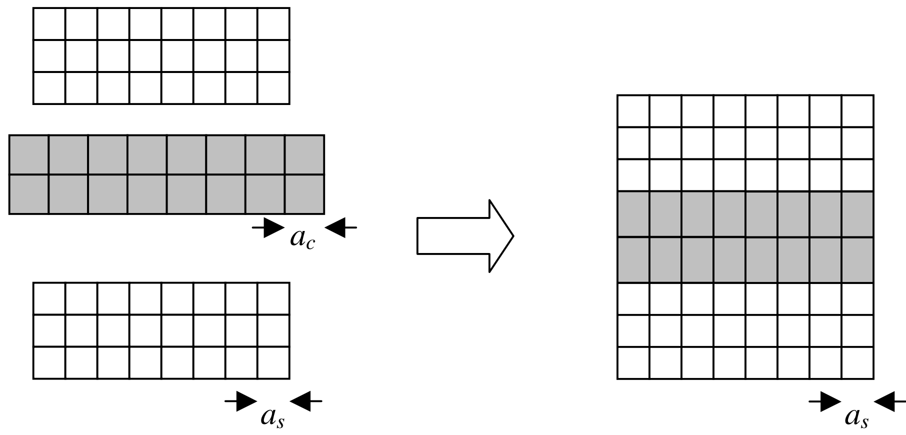

(a) Compressive strain

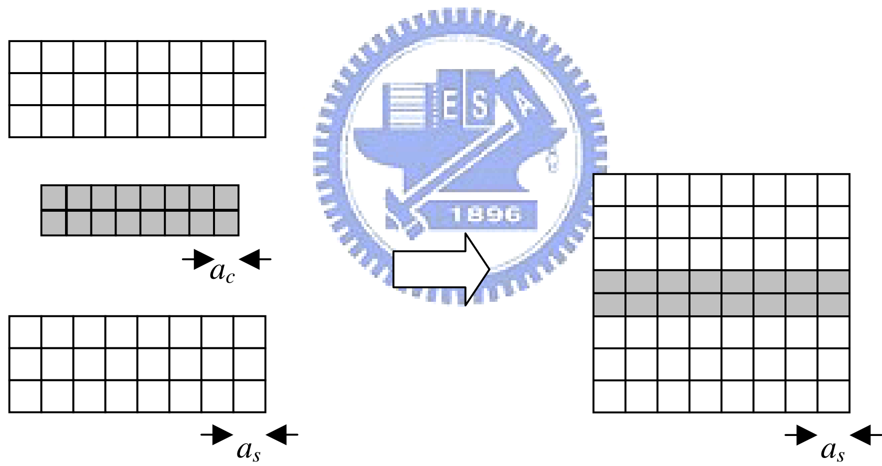

(b) Tensile strain

Figure 2-15 Illustration of thin epilayer of lattice constant a_c grown under biaxial (a) compression and (b) tension on substrate with lattice constant a_s.

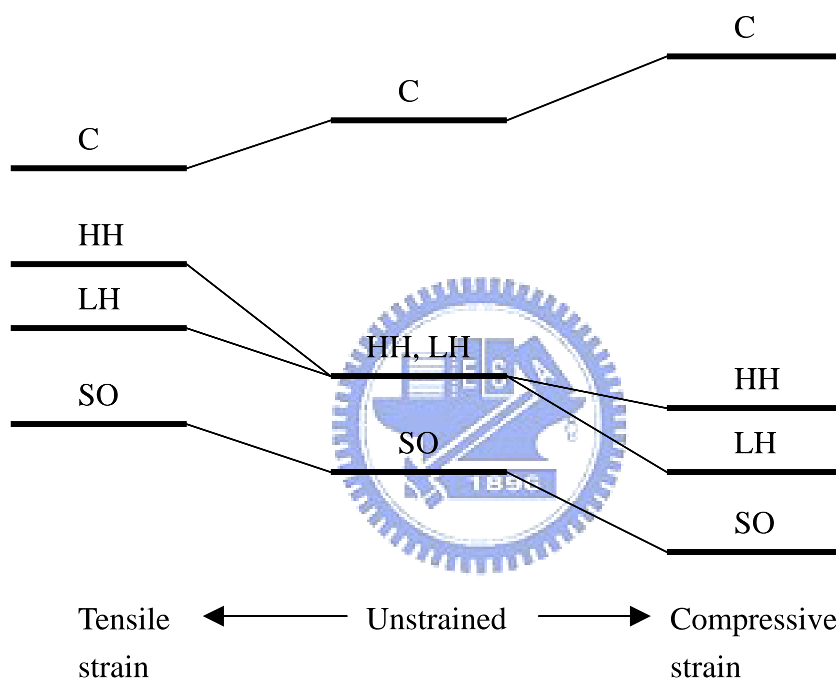

Figure 2-16 Qualitative band energy shift of the conduction band and three valence bands for biaxial compressive and tensile strain.

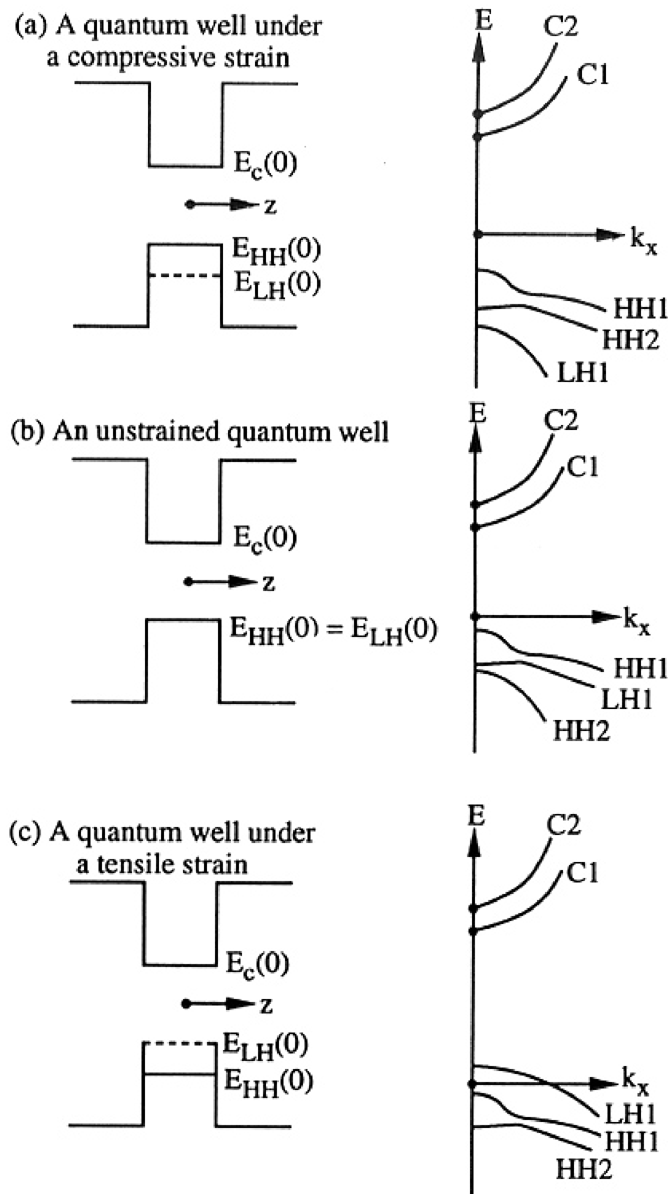

Figure 2-17 Band-edge profiles in real space along the growth (z) direction and the quantized subband dispersions in k space along the k_x direction (perpendicular to the growth direction) for a quantum well with (a) a compressive strain, (b) no strain, and (c) a tensile strain.

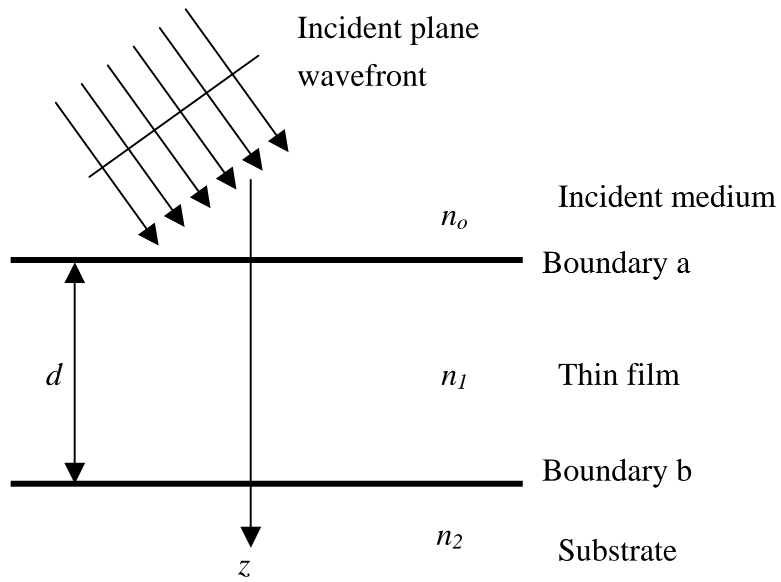

(a)

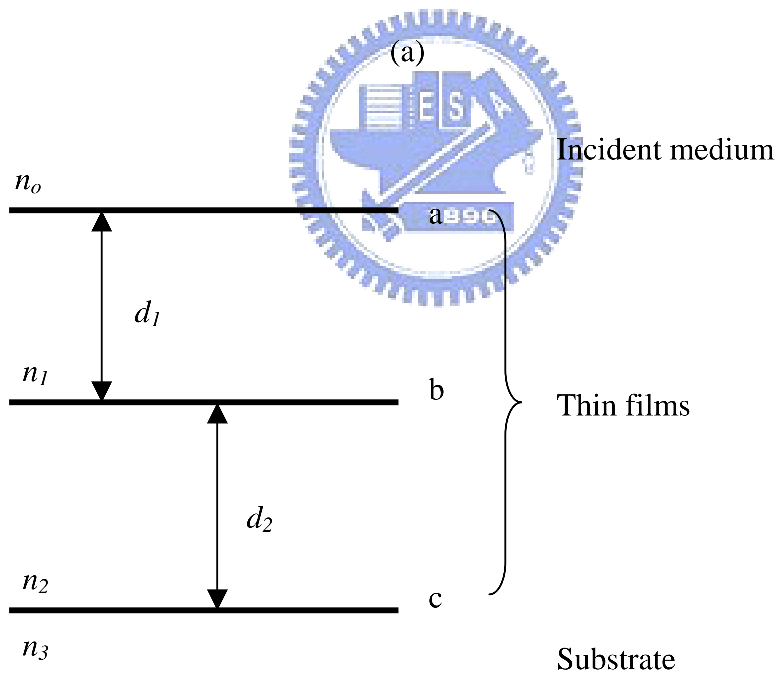

(b)

Figure 2-18 (a) Plane wave incident on a thin film, (b) Notation for two films on a substrate.

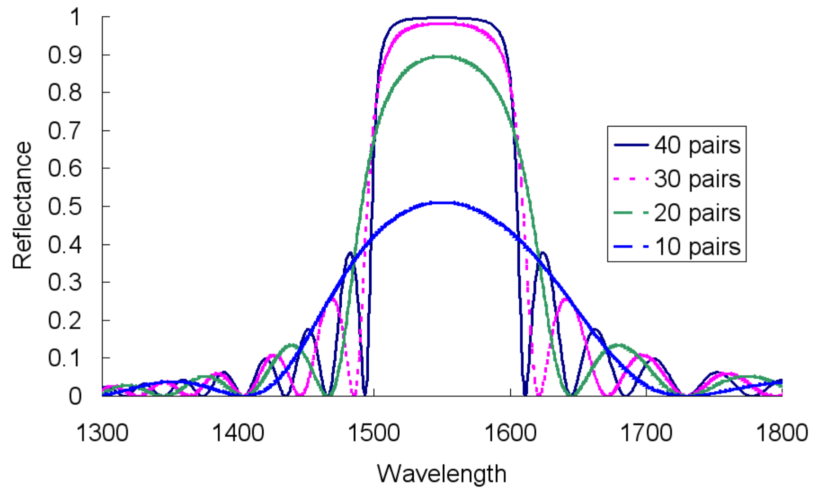

(a)

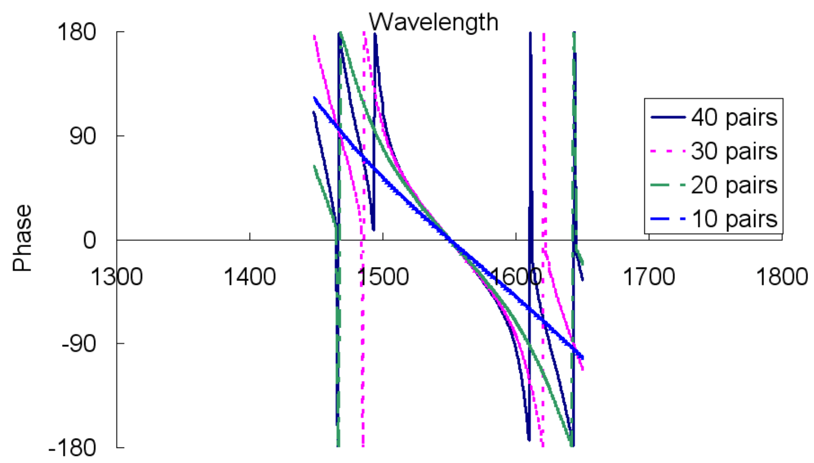

(b)

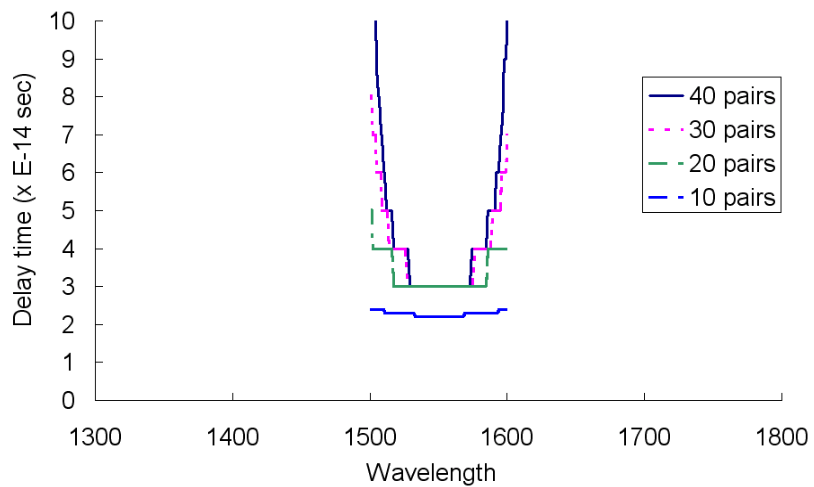

(c)

Figure 2-19 The simulated results for a stack of InGaAlAs/InAlAs DBRs with 10, 20, 30, and 40 pairs. (a) The reflectance, (b) The phase upon the reflection, (c) The delay time.

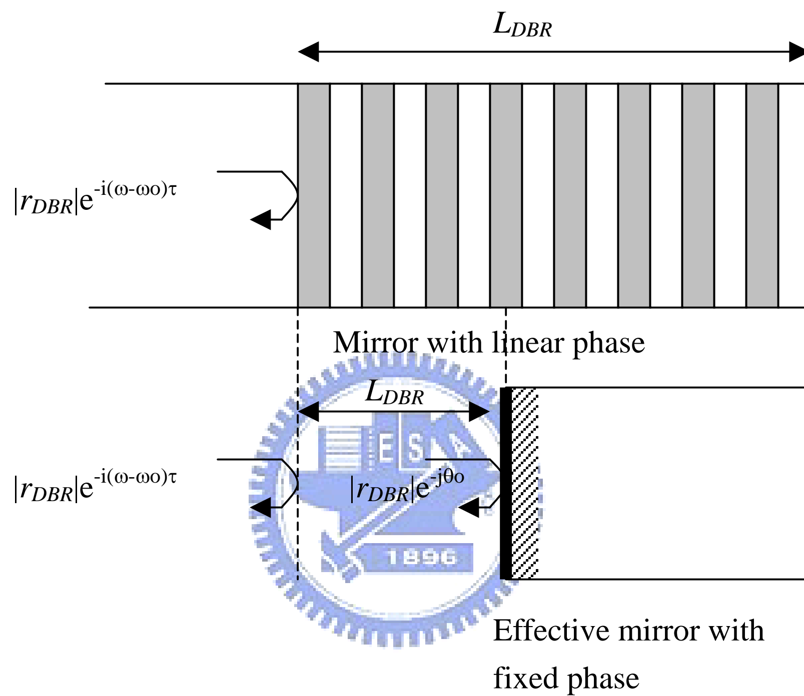

Figure 2-20 The illustration of the penetration depth concept. A linear phase mirror is replaced by a fixed phase mirror displaced by length L_{DBR}, into the mirror. The linear term in the phase characteristic is absorbed by the distance L_{DBR}, whereas the θ_o term assures that the phase of the equivalent and the original mirror match at the center frequency.

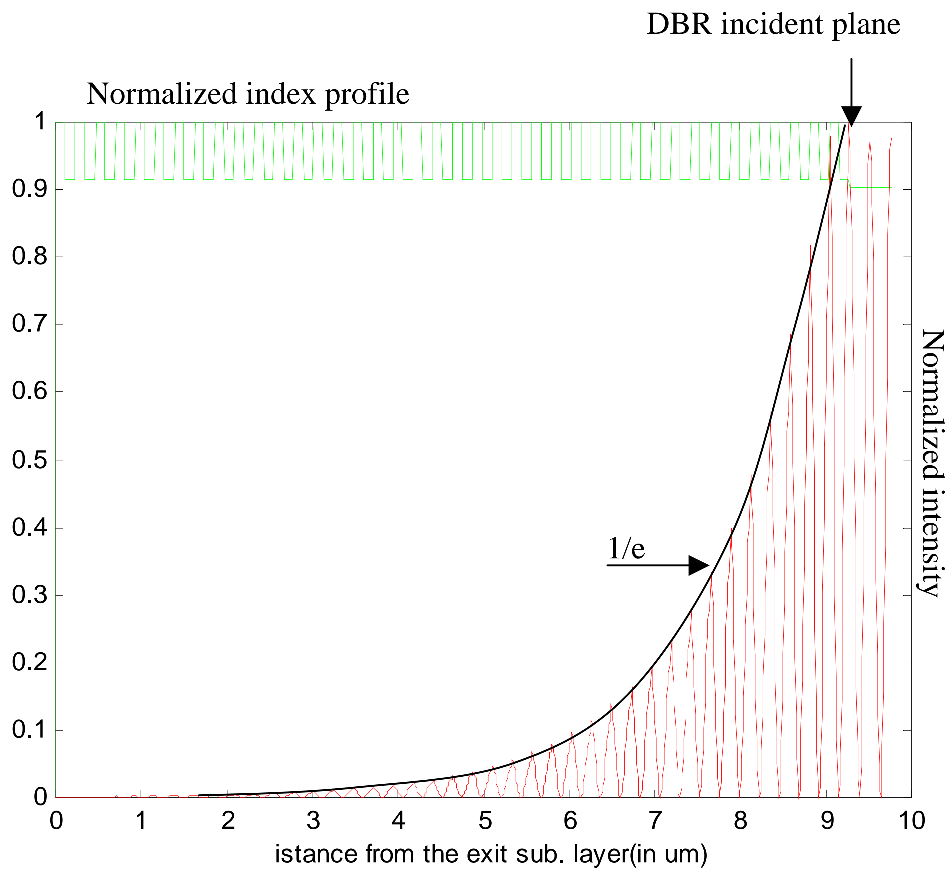

InGaAlAs/InAlAs DBRs. The penetration depth extends to 1/e of the magnitude of the incident light.

CHAPTER 3

Principal Issues in Design of Vertical Cavity Surface Emitting Lasers

Vertical cavity surface emitting lasers (VCSELs) are made by sandwiching a light emitting layer (i.e., a thin semiconductor of high optical gain such as quantum wells) between two highly reflective mirrors. The mirrors can be dielectric multilayered or epitaxial growth mirrors of distributed Bragg reflectors (DBRs) with reflectivity greater than 99.9%. Light is emitted normally from the surface of the mirrors. In this chapter, the most recent progress of VCSELs operating from infrared to ultraviolet is briefly described and the potential applications of VCSELs as light emitting sources in different commercial products are discussed. The reasons for the rapid commercialization of VCSELs and related products are also explained. The most recent progress of computational techniques and computer-aided design (CAD) tools used to analyze VCSELs are briefly described. Finally, the anticipated challenges in achieving high-speed and high-power VCSELs using novel structure and fabrication techniques are also explained.

3.1 Recent development of long wavelength VCSELs

VCSEL was first proposed and fabricated by K. Iga and his colleagues at the Tokyo Institute of Technology, Japan in the late 1970s. They indicated that in order to realize low threshold current, VCSELs should have (1) extremely small cavity volume, (2) high optical gain, and (3) mirrors with extremely high reflectivity (>95%) [1]. At that time, it was difficult to obtain high optical gain in bulk materials, and it was a challenge to obtain mirrors of such high reflectivity. Despite these difficulties, they

successfully demonstrated the first electrically pumped InGaAsP/InP VCSEL under pulse operation at 77 K in 1979 [2]. Several years later, they reported the achievement of an electrically pumped GaAs/AlGaAs VCSEL pulsing at room temperature [3,4]. Their early development of VCSELs usually involved a gold-based p-side reflector and n-side dielectric multilayered mirror (i.e., SiO_2/Si) in which light is emitted. However, further reduction of threshold current in GaInAsP/InP-based VCSELs was obstructed by the large Auger recombination and other nonradiative recombination inside such a small laser volume.

The realization of long-wavelength VCSELs using InP-based materials suffers from a significant drawback due to the (1) difficulty in obtaining highly reflective DBRs, (2) noticeable Auger recombination and inter-valence-band absorption, and (3) small conduction band offset. In addition, VCSELs with thick InGaAsP/InP DBRs (i.e., to produce high reflectivity) have high internal absorption loss and low thermal conductivity. In spite of these disadvantages, the 1300-nm InGaAsP VCSEL with n-type InGaAsP/InP mirror and SiO_2/Si mirror on the p side demonstrates a threshold current of 500 mA under pulsed operation at room temperature [5]. In fact, with appropriate n doping on InGaAsP/InP DBR, the corresponding electrical conductivity can be improved and the optical reflectivity can be maintained at 1500 nm [6]. Fabrication of 1550-nm InP QW VCSEL using n-type InGaAsP/InP DBRs on n-InP substrate has demonstrated 1-mW CW output power at room temperature [7]. Semiconductor/dielectric reflectors can be used as the high-reflectivity mirror on the p side of long wavelength VCSELs. In early-stage 1300- and 1550-nm InGaAsP/InP VCSELs, MgO/Si and Al_2O_3/Si amorphous dielectric mirrors were used to provide sufficient optical reflection [38]. Low-loss p-GaAs/Al_xO_y dielectric mirrors also used in the development of the 1500-nm optically pumped VCSEL have shown a low pumping threshold of 1.4 mW [9]. Although these dielectric mirrors have good

thermal conductivity and high reflectivity, they have a very high electrical resistance, making electrical excitation difficult and requiring a different injection method [10].

Fusion bonding of GaAs-based DBRs onto the AlGaInAs/InP or InGaAsP/InP QW active layer is an alternative method to realizing long-wavelength VCSELs [11-13]. Submilliampere and CW room-temperature operation of 1550-nm VCSELs can be easily obtained by wafer fusion of InGaAsP/InP QWs to two AlGaAs/GaAs DBRs [11]. This is because GaAs/AlGaAs DBR has high electrical and thermal conductivity. Double fusion of GaAs/AlAs DBRs to the AlGaInAs/InP QW active layer is also possible to fabricate for 1300- nm VCSELs [12]. The major drawback of using double fusion to produce long wavelength is the complicated fabrication procedures, which obstruct the commercialization of VCSELs because of the high production cost. The fusion technique can also been used to bond an AlGaAs/GaAs front DBR to an InGaAsP/InP half-cavity structure (i.e., n-doped InGaAsP/InP bottom DBR). VCSELs fabricated by this technique have demonstrated 1550-nm CW emission at 17℃ [13]. This method can reduce the time required for the fabrication procedure to half, but fusion bonding is still required in the process. The growth of high-quality GaAs/AlAs DBRs or GaAlAs/GaAs metamorphic DBRs on InP-based materials may be an alternative way to realize long-wavelength VCSELs other than the wafer fusion technique [14,15]. However, this method may have the reliability problems associated with the heavily dislocated metamorphics mirrors due to the lattice mismatch (see Fig. 3.1).

The technology of all-monolithic growth could be applied to fabricate long-wavelength VCSELs. In fact, it has been shown that using the InP lattice-matched AlGaInAs/InAlAs DBR system, all-monolithic growth VCSELs can be obtained [16,17]. This device consists of lattice-matched InGaAlAs/InAlAs n- and p-type DBRs grown on n-InP substrate. The n-type (typically ~ 43.5 periods) mirror is

usually doped with silicon, and the p-type (typically ~ 35 periods) mirror is doped with carbon in order to increase the electrical conductivity. AlGaInAs bulk [16] and AlInGaAs strain-compensated QWs [17] have been used as the active layer of this long wavelength VCSEL. The optimal threshold current and output power of the 1550-nm VCSEL at room temperature with aperture diameter of 25 μm are recorded to be ~ 6 mA and ~ 8 mW, respectively [17], and the corresponding differential efficiency is about 42%. This achievement of low threshold current is due to the high reflectivity of InGaAlAs/InAlAs DBRs at 1550 nm as the corresponding refractive index difference and characteristic temperature are about 0.31 $\pm$ 0.01 and 122 K, respectively.

It is also shown in Figure 3.1 that the lattice of AlGaAsSb/AlAsSb combination matches that of InP. This may represent an alternative choice of DBRs to realize monolithic growth VCSELs [18,19]. In addition, the AlGaAsSb/AlAsSb mirror has a contrast of refractive indices higher than that of the InGaAlAs/InAlAs mirror (i.e., the use of alternated pairs can be reduced by 20%) so that the corresponding thermal and electrical conductivities can be improved. This VCSEL can be grown by molecular beam epitaxy (MBE) on an n-doped InP substrate. The front mirror consists of 30 periods of $AlAs_{0.56}Sb_{0.44}/Al_{0.2}Ga_{0.8}As_{0.58}Sb_{0.42}$ $\lambda/4$ layers lattice-matched to InP plus a phase matching layer for the front gold contact (reflectivity >99.9%). The rear output DBR consists of the same material combination (reflectivity ~ 99.6%). The λ cavity active layer consists of five strain-compensated AlInGaAs QWs and a heavily doped tunnel junction sandwiched between the two mirrors [18]. This device, with an emission area of 25 μm diameter, demonstrates a threshold current of 7 mA and maximum output power of 2 mW at 17℃ under electrically pulsed operation. The performance of this device can be further improved by forming an aperture inside the active region.

Figure 3.1 shows that the GaInNAs system is lattice-matched with GaAs. This implies that GaAs-based DBRs can be used to realize long-wavelength VCSELs using the GaInNAs system as the active layer. One of the possible active layers consists of $(Ga_{0.7}In_{0.3})(N_{0.004}As_{0.996})$ wells and GaAs barriers. In order to obtain long-wavelength VCSELs, the active layer is sandwiched between p- and n-type AlAs/GaAs DBRs consisting of 21 and 25.5 layer pairs, respectively. Doping can be applied to increase the electrical conductivity of DBRs. This type of VCSEL has been demonstrated at room-temperature operation under electrically pulsed modulation emitting at 1180 nm [20]. The merit of using GaInNAs/GaAs QWs as the active region is due to the technology of fabricating AlAs/GaAs DBRs that can be adopted directly from GaAs-based VCSELs. However, the electrical and optical characteristics of GaInNAs/GaAs QWs are still not fully understood, and further exploration is required to fabricate more reliable GaInNAs QWs with controllable electrical and optical performance [21]. Room temperature CW operation of $Ga_{0.64}In_{0.36}N_{0.003}As_{0.997}$/GaAs QW VCSELs (with $Al_{0.7}Ga_{0.3}As$/GaAs DBRs and n-GaAs as substrate) has demonstrated maximum output power and threshold current of 1 mW and 2 mA, respectively, emitting at 1200 nm [22].

Another similar approach is to use $GaAs_{0.665}Sb_{0.335}$/GaAs QWs as the active layer, which is lattice-matched with AlAs/GaAs DBRs and n-GaAs substrate. This has also demonstrated the room-temperature CW operation of such an oxide aperture device emitting at 1.23 μm that has a threshold current of 0.7 mA [23]. Longer lasing wavelength can also be obtained by increasing the Sb content. GaAsSb VCSELs could be a viable low-cost light source for optical fiber data link systems. InGaAs/GaAs and InAs/InGaAs quantum dot (QD) active layers, which are lattice-matched with the GaAs-based materials, can be tuned to have maximum optical gain peak near 1300 nm [24]. This implies that long-wavelength VCSELs can

also be realized using GaAs-based QD materials. In fact, InAs QD VCSELs using AlAs/GaAs DBR on the p side and GaAs/AlO on the n side with n-GaAs substrate demonstrated 1300-nm emission under pulsed operation at 20℃ [24]. Therefore, it can be concluded that using GaInNAs/GaAs QWs, GaAsSb/GaAs QWs, or GaAs-based QDs with GaAs/AlAs DBRs may be promising methods of realizing long-wavelength VCSELs. This is because all-monolithic growth, predicable reliability, and low production cost can be maintained during the fabrication of long-wavelength VCSELs.

3.2 Recent development of short wavelength VCSELs

Short-wavelength VCSELs in the visible range is another attractive topic to be studied. This is because visible VCSELs can be found in wide-ranging applications such as laser printing and scanning, plastic-fiber-based communications, optical data storage (CD, DVD, etc.), and display applications. Using GaN and its material systems as the active layer can realize green to UV emitting lasers. Reports on the reliability performance of GaN-based LEDs and facet emitting lasers indicate that blue or shorter wavelength emission can also be realized in VCSELs [25].

However, the challenges to achieve blue/violet GaN-based VCSELs require high-reflectivity mirror materials and the fabrication of microcavity resonator structure. It is possible to fabricate monolithic growth VCSELs using AlGaN/GaN DBRs, but their small difference in refractive index requires a large number of layer pairs to achieve the required reflectivity. Hence, it is difficult to apply in situ epitaxial growth technique to form DBRs. Nonetheless, violet VCSELs with AlGaN/GaN DBRs emitting at 401 nm under photopumped room temperature has been reported [26]. On the other hand, it may be possible to replace AlGaN/GaN DBRs by dielectric

multilayered mirrors in blue/violet VCSELs. In fact, it has been shown that 10 pairs of SiO_2/HfO_2 dielectric layers can give more than 99% reflectivity between 400 and 450 nm [27,28]. The remaining challenge to realizing blue/violet VCSELs is the highly transparent carrier concentration (i.e., high threshold current density). This is because electron and hole masses of wide-bandgap materials are heavier than those of narrow-bandgap materials. In fact, transparent carrier concentration of wide-bandgap materials is reduced if the QW structure is used to realize the active region such as $GaN/Al_{0.1}Ga_{0.9}N$ QWs. Therefore, it is believed that low threshold current blue VCSELs can be realized using GaN QWs [29].

References

[1] K. Iga, "Surface emitting laser-its birth and generation of new optoelectronics field," *IEEE J Select. Topics Quantum Electron.*, Vol. 6, no. 6, pp. 1201-1215, 2000.

[2] H. Soda, K. Iga, C. Kitahara, and Y. Suematsu, "GaInAsP/InP surface emitting injection lasers," *Jpn. J. Appl. Phys.*, Vol 18., pp. 2329-2330, 1979.

[3] K. Iga, S. Ishikawa, S. Ohkouchi, and T. Nishimura, "Room temperature pulsed oscillation of GaAlAs/GaAs surface emitting injection laser," *Appl. Phys. Lett.*, Vol. 45, pp. 348-350, 1984.

[4] F. Koyama, S. Kinoshita, and K. Iga, "Room temperature continuous wave vertical cavity surface emitting laser and high-power 2D laser arrays," in *Tech. Digest, Conf. Lasers and Electro-Optics*, paper FC1, pp. 380-381, 1989.

[5] P. Salet, F. Gaborit, Ph. Pagnod-Rossiaux, A. Plais, E. Derouin, J, Pasquier, and J. Jacquet, "Room temperature pulsed operating of 1.3 μm vertical cavity lasers including bottom InGaAsP/InP multilayer bragg mirrors," *Electron. Lett.*, Vol. 33, no. 24, pp. 204-2049, 1997.

[6] I. F.L. Dias, B. Nabet, A. Kohl, J. ,L, Benchimol, and J. C. Harmand, "Electrical and optical characteristics of n-type doped distributed Bragg mirrors on InP," *IEEE Photon. Technol. Lett.*, Vol. 10, no. 6, pp. 763-765, 1998.

[7] J. Boucart, C. Starck, F. Gaborit, A. Plais, N. Bouche, E. Derouin, L. Goldstein, C. Fortin, D. Carpentier, P. Salet, F. Brillouet, and J. Jacquet, "1 mW CW-RT Monolithic VCSEL at 1.55 μm," *IEEE Photon. Technol. Lett.*, Vol. 11, no. 5, pp. 629-631, 1999.

[8] T. Baba, Y. Yogo, K. Suzuki, F. Koyama, and K. Iga, "Near room temperature continuous wave lasing characteristics of GaInAsP/InP surface emitting laser,"

Electron. Lett., Vol. 29, no. 10, pp. 913-014, 1993.

[9] H. W. Song, D. S. Song, L. Y. Han, C. K. Kim, H. Y. Ryu, and Y. H. Lee, "1.5 μm vertical cavity surface emitting lasers utilizing low loss Al*x*O*y*/GaAs irrors, *Electron. Lett.*, Vol. 35, no. 4, pp. 296-297, 1999.

[10] P. O. Vaccaro, H. Ohnishi, and K. Fujita, "Lateral junction vertical cavity surface emitting laser grown by molecular beam epitaxy on a GaAs (311) A oriented substrate," *Appl. Phys. Lett.*, Vol. 74, no. 25, pp. 3854-3856, 1999.

[11] N. M. Margalit, K. A. Black, Y. J. Chiu, E. R. Hegblom, P. Abraham, M. Anzlowar, J. E. Bowers, J. E. Hu, and K. Streubel, "Top emitting double fused 1.5 μm vertical cavity lasers," *Electron. Lett.*, Vol. 34, no. 3, pp. 285-287, 1998.

[12] Y. Qian, Z. H. Zhu, Y. H. Lo, H. Q. Hou, M. C. Wang, and W. Lin, "1.3 μm vertical cavity surface emitting lasers with double bonded GaAs/AlAs Bragg mirrors," *IEEE Photon. Technol. Lett.*, Vol. 9, no. 1, pp. 8-10, 1997.

[13] S. Rapp, F. Salomonsson, J. Bentell, I. Sagnes, H. Moussa, C. Meriadec, R. Raj, K. Streubel, and M. Hammer, "Near room temperature continuous wave operation of electrical pumped 1.55 μm vertical cavity lasers with InGaAsP/InP bottom mirror," *Electron. Lett.*, Vol. 35, no. 1, pp. 49-50, 1999.

[14] H. Gebretsadik, K. Kamath, K. K. Linder, X. Zhang, P. Bhattacharya, C. Caneau, and R. Bhat, "Growth of high quality GaAs/AlAs Bragg mirrors on patterned InP based quantum well mesa structures," *Appl. Phys. Lett.*, Vol. 71, no. 5, pp 581-583, 1997.

[15] J. Boucart, C. Starck, F. Gaborit, A. Plais, N. Bouche, E. Derouin, L. Goldstein, C. Fortin, D. Carpentier, P. Salet, F. Brillouet, and J. Jacquet, "1 mW CW-RT monolithic VCSEL at 1.55 μm," *IEEE Photon. Lett.*, Vol. 11, pp. 629-631, no. 6, 1999.

[16] C. Kazmierski, J. P. Debray, R. Madani, I. Sagnes, A. Ougazzaden, N. Bouadma, J. Etrillard, F. Alexandre, and M. Quillec, "+55℃ pulse lasing at 1.56 μm of all monolithic InGaAlAs/InP vertical cavity lasers," *Electron. Lett.*, Vol. 35, no. 10, pp. 811-812, 1999.

[17] J. K. Kim, E. Hall, O. Sjolund, G. Almuneau, and L. A. Coldren, "Room temperature, electrically pumped multiple active region VCSELs with high differential efficiency at 1.55 μm," *Electron. Lett.*, Vol. 35, no. 13, pp. 1084-1085, 1999.

[18] E. Hall, G. Almuneau, J. K. Kim, O. Sjolund, H. Kroemer, and L. A. Coldren, "Electrically pumped, single-epitaxial VCSELs at 1.55 μm Sb-based mirrors," *Electron. Lett.*, Vol. 35, no. 16, pp. 1337-1338, 1999.

[19] E. Hall, G. Almuneau, J. K. Kim, O. Sjolund, H. Kroemer, and L. A. Coldren, "Selectively etched undercut apertures in AlAsSb-based VCSELs," *IEEE Photon. Lett.*, Vol. 13, no. 2, pp. 97-99, 2001.

[20] M. C. Larson, M. Kondow, T. Kitatani, K. Nakahara, H. Inoue, and K. Uomi, "GaInNAs/GaAs long wavelength vertical cavity surface emitting laser diodes," *IEEE Photon. Technol. Lett.*, Vol. 10, no. 2, pp. 188-190, 1998.

[21] A. Wagner, C. Ellmers, F. Hohnsdorf, J. Koch, C. Agert, S. Leu, M. Hofmann, W. Stolz, and W. W. Ruhle, "GaInNAs/GaAs vertical cavity surface emitting laser with ultra-broad temperature operation range," *Appl. Phys. Lett.*, Vol. 76, no. 3, pp. 271-273, 2000.

[22] T. Kageyama, T. Miyamoto, S. Makino, Y. Ikenaga, N. Nishiyama, A. Matsutani, F. Koyama, and K. Iga, "Room temperature continuous wave operation of GaIn- NAs/GaAs VCSELs grown by chemical beam epitaxy with output power exceeding 1 mW," *Electron. Lett.*, Vol. 37, no. 4, pp 225-226, 2001

[23] M. Yamada, T. Anan, K. Kurhara, K. Nishi, K. Tokutome, A. Kamei, and S.

Sugou, "Room temperature low-threshold CW operation of 1.23 μm GaAsSb VCSELs on GaAs substrates," *Electron. Lett.*, Vol. 36, no. 7, 637-638, 2000.

[24] J. A. Lott, N. N. Ledentsov, V. M. Ustinov, N. A. Ustinov, M. A. Maleev, A. E. Zhukov, A. R. Kovsh, M. V. Maximov, B. V. Volovik, Zh. I. Alferov, and D. Bimberg, "InAs-InGaAs quantum dot VCSELs on GaAs substrates emitting at 1.3 μm," *Electron. Lett.*, Vol. 36, no. 16, pp. 1384-1385, 2000.

[25] S. Nakamura, M. Senoh, S. Nagahama, N. Iwasa, T. Yamada, T. Matsushita, H. Kiyoku, Y. Sugimoto, T. Kozaki, H. Umemoto, M. Sano, and K. Chocho, "High power, long lifetime InGaN/GaN//AlGaN based laser diodes grown on pure GaN substrates," *Jpn. J. Appl. Phys.*, Vol. 37, pp. L309-L312, 1998.

[26] I. L. Krestnikov, W. V. Lundin, A. V. Sakharov, V. A. Semenov, A. S. Usikov, A. F. Tsatul'nikov, and Zh. I. Alferov, "Room temperature photopumped InGaN/ GaN/AlGaN vertical cavity surface emitting laser," *Appl. Phys. Lett.*, Vol. 75, no. 9, pp. 1192-1194, 1999.

[27] Y. K. Song, H. Zhou, M. Diagne, I. Ozden, A. Vertikov, C. Certer-Coman, R. S. Kem, F. A. Kish, and M. R. Krames, "A vertical cavity light emitting InGaN quantum well heterostructure," *Appl. Phys. Lett.*, Vol. 74, no. 23, pp. 3441-3443, 1999.

[28] Y. K. Song, H. Zhou, M. Diagne, A. V. Nurmikko, R. P. Schneider, Jr., C. P. Kuo, M. R. Krames, R. S. Kern, C. Carter-Coman, and F. A. Kish, "A quasicontinuous wave, optically pumped violet vertical cavity surface emitting lasers," *Appl. Phys. Lett.*, Vol. 76, no. 13, pp. 1662-1664, 2000.

[29] T. Shirasawa, N. Mochida, A. Inoue, T. Honda, T. Sakaguchi, F. Koyama, and K. Iga, "Interface control of GaN/AlGaN quantum well structures in MOCVD growth," *J. Cryst. Growth*, pp. 124-127, 1998.

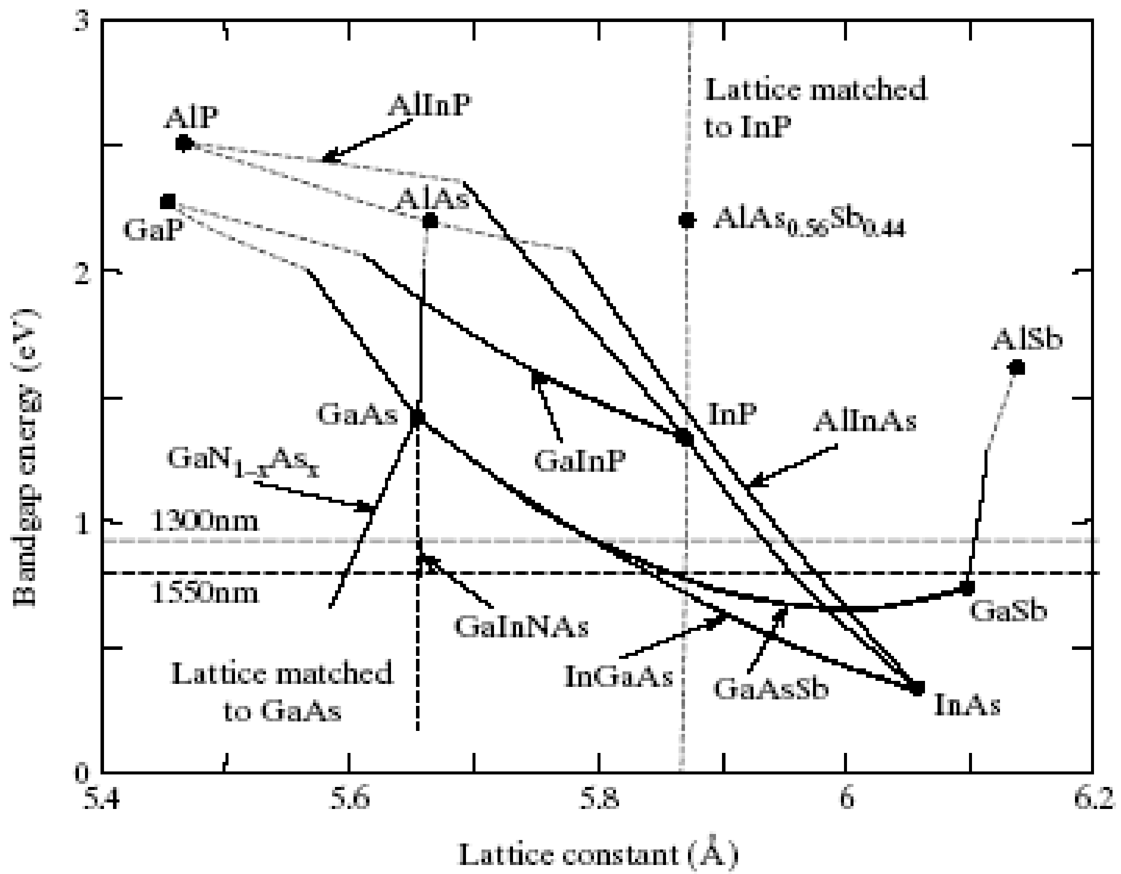

Figure 3-1 Energy band diagram versus lattice constant

CHAPTER 4

Fabrication of Short Wavelength Vertical Cavity Surface Emitting Lasers

This chapter mainly describes the fabrication equipments and procedures for short wavelength vertical cavity surface emitting lasers. Metal organic chemical vapor deposition (MOCVD) system is used for growing all the epitaxial structures through out this study. The growth process, fabrication process and characterization of short wavelength-VCSELs, will also be introduced in this chapter.

4-1 Optimization of the InGaN/GaN Active Layers

GaN and related materials have attracted much attention because of their potential for many applications such as light emitting diodes (LEDs), laser diodes (LDs), solar-blind ultraviolet detectors, and high power, high temperature electronic devices. In particular, $In_xGa_{1-x}N$ quantum wells (QWs) have attracted a tremendous interest since they form the active region in optoelectronic device such as LEDs and LDs working in the blue/violet region of the spectrum. The $In_xGa_{1-x}N$ active layer as been argued that presents some compositional fluctuations [1], and it has been argued that the luminescent centers in these devices were originating from localized states or quantum dots in the $In_xGa_{1-x}N$ QWs due to the presence of In rich fluctuations.

The Effect of thickness and number on InGaN quantum well

In recent years, InGaN/GaN-based optical devices such as light-emitting diodes (LEDs) and laser diodes (LDs) have considerably progressed. However, the emission mechanism that occurs in these devices is still not fully understood. So far, many articles have addressed this issue [1-8]. Two different radiative recombination mechanisms are generally accepted. One is based on spatial indium fluctuations

leading to indium-rich regions acting as quantum dots. The emission from the InGaN region may be assigned to the recombination of excitons localized at potential minima, i.e., so-called exciton-localization effect (ELE) [1-7]. Quantitative high-resolution transmission electron microscopy (HRTEM) proved the presence of spatial indium fluctuations [9-10]. Another model attributes the quantum-confined-Stark effect (QCSE) due to the presence of a large piezoelectric field in the quantum well, which arises from strain caused by the lattice mismatch between GaN and InGaN [11-15]. According with the QCSE model, the field causes the energy bands to "bend", thereby inducing charge separation and a red-shift of the emission. The ELE and QCSE are both related to the indium concentration, well numbers and well thickness. There are some reports that spatial In concentration fluctuations or ELE dominate the luminescent properties in samples with high indium concentrations in thinn wells, while QCSE dominate the recombination emission in wide QW structures [16-17]. This section investigates these two effects with regard to the well numbers and well thickness by means of photoluminescence (PL) and high-resolution x-ray diffraction (HRXRD) measurements. Finally, this section compares the different influences of these two effects on the performance of InGaN/GaN-based LEDs, which should be taken into account in designing InGaN/GaN optical devices such as high brightness LEDs, LDs and VCSELs.

The $In_{0.18}Ga_{0.88}N$/GaN MQW samples were grown on a (0001)-oriented sapphire substrates by low pressure metal-organic chemical vapor deposition (MOCVD) with a rotating-disk reactor (Veeco E300). Trimethylgallium (TMGa), Trimethylindium (TMIn), Trimethylaluminum (TMAl), and ammonia (NH_3) were used as the Ga, In, Al, and N precursors, respectively. Silane (SiH_4) and biscyclopentadienyl magnesium (Cp_2Mg) were used as the n- and p-type dopants. Hydrogen (H_2) and nitrogen (N_2) were used as a carrier gas. The substrate was firstly

treated in hydrogen ambient at 1050 ℃, followed by the growth of a 25 nm-thick GaN buffer layer at 550 ℃. After the high temperature annealing of a buffer layer, a 1.5 μm-thick undoped GaN layer was grown at 1040 ℃ and a 1.5 μm-thick n-type GaN layer was deposited. To investigate the properties of InGaN/GaN QWs, the QWs were grown as follows. First, the thickness of QWs was varied from 1.2 to 6.1 nm and the other conditions were held constant with well growth temperature at 750 ℃, five of the well number and 20nm-thick Si-doped barrier. Second, similar to the QWs grown at 750 ℃, the thickness of well and barrier layers was kept constant at 2.2 and 22 nm respectively, while the number of well was varied from five to eight. After the growth of active region, substrate temperature was elevated to 970 ℃ again to grow the Mg-doped p-$Al_{0.16}GaN$ cladding layer and the Mg-doped p-GaN cap layer. Fig 4.1 shows the structure of InGaN/GaN MQW. After the growth, the LEDs (300×300 μm^2) were fabricated using photolithographic patterning and dry etching. The metal contact layers, which include the transparent contact and pad layers, are patterned by a lift-off procedure and deposited onto samples using electron beam evaporation. Indium Tin oxide (ITO) is used for p-side transparent contact and Ti/Al/Ni/Au (20/150/20/200 nm) is used for n-type electrode. Finally, Ni/Au (20/1500 nm) is deposited onto both exposed transparent and n-type contact layers to serve as bonding pads. The current–voltage (I–V) characteristics were measured at room temperature (RT). RT electroluminescence (EL) and the luminous intensity of these fabricated LEDs were measured as functions of forward injection current between 0 and 20 mA.

The In composition, well number and barrier thickness were kept constant with varying well thickness from 1.2 to 6.0 nm. The well and barrier thickness and In composition were obtained through HRXRD measurement. The In composition and well number and barrier thickness are 18 %, 5, and 20 nm, respectively. HRXRD results are shown in figure 4.2 for the InGaN/GaN MQW depending on the thickness

of well. The strongest peak in each figure is due to the GaN epilayer. The spectra show a higher-order diffraction peak indicating good layer periodicity. In principle, the average In composition of the QW and the period can be determined from the relative positions of the zeroth- and higher-order peaks in the HRXRD patterns. The period (D) given by $D = n\lambda/2(\sin\theta_n - \sin\theta_{0th})$ is between 21.2 to 26.0 nm , where n is the order of the satellite peaks, θ_n is their diffraction angle and θ_{0th} the angle of the zeroth-order peak.. Figure 4.2 shows the HRXRD spectra of InGaN/GaN 5QWs with different well thickness. With increasing with thickness from 1.2 to 6.0 nm, the FWHM of the rocking curve for the zeroth- and 1st-order satellite peak in the QW with a 1.2 nm-thick well is broader than that in the other thick well samples and above the 3 nd-order peak, the profile is not clear in the QW with a 1.2 nm-thick well, implying that the crystal quality of the QWs improves with increasing well thickness.

For the optical properties, the PL intensity is another very important parameter. Here, we compare the PL intensity of all samples. Figure 4.3 (a) shows the PL spectra of all samples with different quantum-well thickness and the same In content. Each spectrum is dominated by a sharp emission peak accompanied by weak peaks on low–energy side and/or high-energy side except the sample with well thickness of ~1.2 nm. The emission energy of the samples shows a slight redshift with increasing quantum-well thickness. Figure 4.3 (b) shows effects of MQW structure on the PL peak intensity measured at room temperature. Generally, for the wider quantum-well structure, the transition matrix element is further decreased, i.e., the PL intensity is weakened by increasing quantum-well thickness except for the case of low In content [18]. However, the width increase of quantum wells did not have significant decrease on the PL intensity as shown in Fig. 4.3 (b). It suggested that these samples are consisted of low In content and the emission mechanism is dominated by the exciton localization effect. The enhancement of the exciton localization effect due to

increasing quantum-well thickness agrees with the previous report [19], in which the exciton localization effect can be observed only under the condition of the well thickness larger than a critical thickness for the samples with a lower indium concentration.

Next, we will compare the output power of LED samples with different well thickness. Figure 4.4 shows the dependence of the output power on the quantum well thickness, which is measured under the condition at 20 mA injection current at room temperature. In the case of 18% indium mole fraction, the output power increases with increasing well thickness up to 3.2 nm and then decreases with further increasing well thickness, which is in good agreement with the well thickness dependent PL intensity. Combined with Fig. 4.4, one can understand that the decrease of the output power with further increasing well thickness can be attributed to QCSE. Of course, if the QCSE is weak enough to be safely ignored, the performance of the LED can be improved by ELE.

Recently, the structural and optical properties of low-In-content InGaN/GaN multi-quantum wells (MQWs) have been examined with varying QW number. The photoluminescence (PL) peak was found to redshift and the emission peak intensity was found to increase with increasing well number up to six [20-24] and then decrease with further increasing well number. Figure 4.5 shows HRXRD results for the InGaN/GaN QWs depending on the number of QWs. The spectra show gradually better layer periodicity. The peak positions are almost stationary. This indicates one period (well and barrier) is constant. From the combined results of HRXRD analysis, the In composition in the well layer was about 18%, and the well and barrier thickness were 2.5 and 22 nm, respectively. PL peak positions of InGaN/GaN QWs with increasing well number reveal slightly redshift as shown in figure 4.6 (a). Figure 4.6 (b) shows dependence of PL peak position and intensity on the number of wells. PL

peak intensity increases with increasing well number up to six and decreases with further increasing well number. The results are consistent with some earlier reports. Figure 4.7 is output power characterization results of LED samples with different well number. It can seen clearly that the EL output power at 20 mA of LED sample with six-wells is higher than that of LED samples with five and eight-wells, which is in good agreement with the well number dependent PL intensity.

In summary, we have investigated low-In-content $In_xGa_{1-x}N/GaN$ (x~0.18) QWs by MOCVD with various well thickness and number by means of photoluminescence (PL) and high-resolution x-ray diffraction (HRXRD) measurements. Finally, this section also compares the different influences of these different growth conditions on the performance of InGaN/GaN-based LEDs.

The Effect of Si-doped barrier

Growth of high efficient InGaN active layer is main issue in the fabrication of high brightness ultra violet (UV) light emitting diodes and high power short wavelength laser diodes. Delta doping process has been recognized as an effective way to improve internal quantum efficiency by carrier injection layer, lower the transparency current density and increase the modulation bandwidth in the study of III-V arsenide and phosphide based optoelectronic devices. And it also improves the thermal stability related in the electronic and optoelectronic performance [25-27]. Recently, the effects of Si doping on the optical properties of GaN epilayers [28-29], InGaN/GaN QWs [30-33], and GaN/AlGaN QWs [34] have been reported. Cho et al [30] observed the reduced Stokes shift, the decrease in radiative recombination lifetime, and the increase in the interface quality with increasing Si doping concentration. They concluded that Si doping results in a decrease in carrier localization at potential fluctuations due to the In alloy fluctuations, thickness

variations, and/or defects in the QWs. However, Wang et al [31] reported that an obvious localization effect is found in slight Si doping QW structures, but the localization effect vanishes when the Si doping level increases. Furthermore, when the localization effect is stronger, the mobility is higher. Dalfors et al [32] suggested that the large blueshift in energy with increasing Si doping concentration can only be explained by the screening of the potential fluctuations and only partly be explained by the screening of the piezoelectric field. In this communication, we report the Si doping effect in the cw photoluminescence (PL) and of $In_{0.18}Ga_{0.88}N$/GaN MQW structures. High-resolution x-ray diffraction (HRXRD) was employed to study the structural properties of MQWs. We also discuss the RT electroluminescence (EL) and the luminous intensity dependence of these fabricated LEDs with various Si flow rates.

The $In_{0.18}Ga_{0.88}N$/GaN MQW structures used in this study were grown on a (0001)-oriented sapphire substrates by low pressure metal-organic chemical vapor deposition (MOCVD) with a rotating-disk reactor (Veeco E300). Trimethylgallium (TMGa), Trimethylindium (TMIn), Trimethylaluminum (TMAl), and ammonia (NH_3) were used as the Ga, In, Al, and N precursors, respectively. Silane (SiH_4) and biscyclopentadienyl magnesium (Cp_2Mg) were used as the n- and p-type dopants. Hydrogen (H_2) and nitrogen (N_2) were used as a carrier gas. The substrate was firstly treated in hydrogen ambient at 1050 ℃, followed by the growth of a 25 nm-thick GaN buffer layer at 550 ℃. After the high temperature annealing of a buffer layer, a 1.5 μm-thick undoped GaN layer was grown at 1040 ℃ and a 1.5 μm-thick n-type GaN layer was deposited. InGaN/GaN MQW samples were subsequently grown at a low temperature of 750 ℃, which consisted of 5 periods of 20 nm GaN barriers and 2.5 nm $In_{0.18}Ga_{0.88}N$ wells. A set of samples was grown to study the effects of Si-doping in the GaN barriers on the characteristics of the InGaN/InGaN QWs. Three

samples have various Si flow rates of 0.12, 0.16, 0.19, 0.37 and 0.59 sccm, respectively. After the growth of active region, substrate temperature was elevated to 970 ℃ again to grow the Mg-doped p-$Al_{0.16}GaN$ cladding layer and the Mg-doped p-GaN cap layer. After the growth, the LEDs (300x300 μm^2) were fabricated using photolithographic patterning and dry etching. The metal contact layers, which include the transparent contact and pad layers, are patterned by a lift-off procedure and deposited onto samples using electron beam evaporation. ITO is used for p-side transparent contact and Ti/Al/Ni/Au (20/150/20/200 nm) is used for n-type electrode. Finally, Ni/Au (20/1500 nm) is deposited onto both exposed transparent and n-type contact layers to serve as bonding pads. The current–voltage (I–V) characteristics were measured at room temperature (RT). RT electroluminescence (EL) and the luminous intensity of these fabricated LEDs were measured as functions of forward injection current between 0 and 20 mA.

Figure 4.8 shows the dependences of the PL intensity (filled square) and PL peak wavelength (filled circles) of InGaN/GaN MQW samples as a function of the SiH_4 flow rate in the range of 0.12-0.59 sccm. As SiH4 flow rate increases from 0.12 to 0.19 sccm, PL intensity of MQW samples significantly increases. The SiH_4 flow rate for the maximum PL intensity was 0.19 sccm, where the PL intensity at the main peak position was 13 times higher than that of the MQW samples without Si doping. In the previous work, Si doping process has been recognized as a method for introducing a potential well having high electron density and higher hole confinement by higher valance band offset . The increase in PL intensity may be attributed to the effective supply of electrons captured in potential well produced by Si doping in the GaN barrier layers into the InGaN well layer and enhancement of hole capturing by higher valance band offset [25,27]. However, as SiH_4 flow rate beyond 0.19 sccm further increases till 0.59 sccm, the PL intensity is decreased. It is resulted from the

decrease of electron tunneling process because the energy level in the potential well of Si-doped barrier is not properly aligned with the InGaN well layer at a higher Si doping level.

The Si-doping of the GaN barrier layers also affected the structural properties of 5 period InGaN/GaN MQWs. HRXRD shows ω-2θ spectra of MQW samples with various SiH_4 flow rate. As increasing Si-doping of the barriers, high resolution X-ray di¤raction measurements revealed a significant narrowing of the full-width at half-maximum (FWHM) of the first and second order superlattice (SL) peaks. From these, it is found that the crystal quality of InGaN/GaN MQW structures is improved by impurity doping. This is consistent with previous reports that Si doping promotes the surface and interface smoothness of InGaN/GaN MQWs[35-36].

Fig. 4.9 shows the measured LED output power as a function of injection current. It can seen clearly that the EL intensity of LED with SiH_4 flow rate of 0.19 is approximately ~20 % of magnitude higher than that of LED with SiH_4 flow rate of 0.12 at 20 mA and presents the relative output luminous intensity as a function of the SiH_4 flow rate in the range of 0.12-0.59 sccm. The much larger output power at 20 mA could be also attributed to the improved crystal quality and thermal stability of MQW structures due to Si incorporate into column-III sites to prevent formation of the Ga vacanies[37].

In summary, we have studied the effect of Si doping on the GaN barriers. As increasing Si doping in the barriers, the PL shows an increase of emission intensity and a blueshift of peak energy. With the same MQW emission peak at about 460 nm and driving current of 20 mA, it is found that the light output power of the LED with Si flow rate of ~ 0.19 sccm is ~20 % of magnitude higher than that of LED with Si flow rate of ~ 0.12sccm. This result shows that PL intensity and LED output power of the MQW samples with Si-doped barrier layers are dramatically increased. The

increases in internal quantum efficiency of the MQW samples can be attributed to the effective injection of electrons from the Si-doped barrier layers into QW layers, an increase of hole accumulation by higher valance band offset, and the improved crystal quality and thermal stability of MQW structures.

4-2 Enhanced Light Output in InGaN-based Light-Emitting Diodes with Omnidirectional One-dimensional Photonic Crystals

GaN-based materials have attracted considerable interest in optoelectronic devices such as light emitting diodes (LEDs) and laser diodes (LDs) [38-41]. Recently, as the brightness of GaN-based LEDs has increased, applications such as displays, traffic signals, backlight for cell phone, exterior automotive lighting, and printer have become possible. However, there is still a great need for improvement of the internal quantum efficiency as well as extraction efficiency. The LEDs are inherently inefficient because photons are generated through a spontaneous emission process and emit in all directions. A large fraction of light emitted downward toward the substrate and to the side does not contribute to useable light output. Most commercially packaged GaN-based LEDs incorporate a reflector cup to redirect bottom-emitting light upwards. However, there are significant losses experienced at each interface, especially at the adhesive bond between the backside of the LED chip and the cup. Some applications requiring surface-mounted LEDs make such reflectors impractical. Metals with high visible reflectance, such as Al and Ag, exhibit an average reflectance of around 90% or better across that wavelength range [42]. To achieve consistent adhesion to the sapphire substrate, an intermediate binding layer of Cr must be employed; however, this results in a much lower reflectance value of ~55% [43]. Recently, Zhao et al. proposed a method to use a distributed Bragg reflector (DBR) mirror deposited directly on the back surface of GaN based LED chip to enhance

extraction efficiency [44]. A wide reflectance bandwidth in the blue and green wavelength regions was obtained using a double quarter-wave stack design composed of TiO_2 and SiO_2 layers. More than 65% enhancement in extracted light intensity was demonstrated for a blue LED measured at the chip level. However, the reflectance bandwidth of a DBR mirror is determined for the light at a certain incident angle. The reflectance bandwidth will shift when the incident angle changes or if the polarization of the incident light is different. In other words, the high reflectance of a DBR mirror is limited by the incident angle and polarization of light. More recently, a new kind of omnidirectional reflector (ODR) composed of metallic and dielectric materials was reported and applied to GaInN LEDs [45]. Higher reflectance and higher insensitivity to the incident angle make such kind of conducting ODR a good candidate to reflect light upward for a flip-chip type LED.

Photonic crystals (PCs) have unique energy dispersion due to coupling between periodic dielectric (or metallic) materials and electromagnetic waves. Particularly, the strong energy dispersion of the propagating modes of PCs has attracted much interest because of the formation of electromagnetic stop bands or so called photonic band gaps (PBGs) [46,47]. Although the high reflectance of a DBR mirror has been studied for a long time, it is just recently shown that one-dimensional photonic crystals (1D PCs) can exhibit the property of omnidirectional reflection provided the reflective indices of the materials and geometry of the structure are chosen appropriately [48.49]. The use of omnidirectional 1D PCs, enables the control of the light spectrum emitted from the LED chip, and compared with a DBR mirror, a substantially higher reflectance can be achieved at any incident angle and any polarization of light within the desired range of wavelengths determined by the PBG.

In this section, an omnidirectional 1D PC is designed and incorporated into the bottom of GaInN blue LED chips. The designed omnidirectional 1D PC composed of

two different transparent optical materials TiO_2 and SiO_2 layers stacked alternately to possess a PBG within the blue regime of interest. It is shown that the omnidirectional 1D PC has a higher reflectance and a wider reflection angle than a conventional DBR. Furthermore, an up to 80% enhancement in the extracted light intensity is demonstrated for a blue PC-LED around 450 nm.

Our GaN LED samples are grown by metal-organic chemical vapor deposition (MOCVD) with a rotating-disk reactor (Emcore) on a c-axis sapphire (0001) substrate at the growth pressure of 200 mbar. Trimethylgallium (TMG), Trimethylaluminum (TMA) ammonia, CP_2Mg and Si_2H_6 are used as Ga, Al, N, Mg, and Si sources, respectively. The LED structure consists of a 30-nm-thick GaN low temperature buffer layer, a 4.0-μm-thick highly conductive Si-doped GaN layer (grown at 1050°C), an undoped multiple quantum wells (MQW) active region consisting of five periods of 2/5-nm-thick $In_{0.21}Ga_{0.79}N$/GaN multiple quantum wells (grown at 750°C), a 50-nm-thick Mg-doped AlGaN layer (grown at 1050°C), and a 0.1-μm-thick Mg-doped GaN (grown at 1050°C). Finally, a p-AlInGaN–GaN double-cap layer is grown at 800°C with nano-roughened surface for enhanced light extraction [50]. The LED chips are fabricated using standard process (4 mask steps) with a mesa area of 300×300 μm^2. The 0.5 μm SiO_2 is deposited onto the sample surface using plasma enhanced chemical vapor deposition (PECVD). By means of photo-lithography, the mesa pattern is defined after wet etching SiO_2 by buffer oxide etching solution. Mesa etching is then performed with Cl_2/Ar as the etching gas in an ICP-RIE system (SAMCO ICP-RIE 101iPH), and with the ICP source power and bias power operating at 13.56 MHz. The metal contact layers, which include the transparent contact and pad layers, are patterned by a lift-off procedure and deposited onto samples using electron beam evaporation. ITO is used for p-side transparent contact and Ti/Al/Ni/Au (20/150/20/200 nm) is used for n-type electrode. Finally, Ni/Au (20/1500 nm) is

deposited onto both exposed transparent and n-type contact layers to serve as bonding pads. After front-end process, an omnidirectional 1D PC is incorporated into the bottom of GaInN blue LED chips and the design is described as following.

Conventionally, a white light LED device comprises of a blue LED chip and a layer of yellow phosphor grains. To increase the luminance of a white light LED device by enhancing the extraction efficiency of the blue light generated inside the chip is the most promising way. Therefore, we design an omnidirectional 1D PC having a PBG at around 450 nm and incorporate the 1D PC onto the bottom of a GaInN blue LED chip. The transparent optical materials we chose are TiO_2 and SiO_2 with thickness given respectively by 0.455 and 0.545 times the lattice constant *a* of the photonic band structure, and with reflective indices 2.42 and 1.47, respectively, around wavelength 450 nm. Fig. 4.10 shows the photonic band structures for this designed 1D PC which exhibits a PBG between frequency 0.288 *c/a* and 0.302 *c/a* (e.g. the region with dash line), which correspond to wavelengths of 458 nm and 437 nm, respectively, if a = 132 nm is chosen. For a finite structure with 14 periods, the result in Fig. 4.10 shows the comparison of the average theoretical and experimental transmittances as a function of wavelength. The calculated and measured transmittances are averaged for the unpolarized light with the incident angles every 5° from 0° to 85°. Fig. 4.11 shows a close agreement between theoretical and experimental results. The transmittance goes down to 0.5 % between 438 nm and 460 nm for the theoretical result, which matches the expectation of the PBG in Fig.4.9. The experimental result shows a wider PBG that is between 437 nm and 469 nm because of the absorption from the substrate and slightly different reflective indices for the fabricated TiO_2 and SiO_2. Fig.4.12 shows the schematic of a GaInN blue LED chip containing an omnidirectional 1D PC, and the insertion is the scanning electron micrograph (SEM) image of the cross section of our 1D PC. We incorporate this

omnidirectional 1D PC onto the bottom of our GaInN blue LED chip with emitting peak at 454 nm and FWHM about 20 nm (e.g. between 444 nm and 464 nm) so that the PBG is wide enough to omnidirectionally reflect downward blue light back to the upward side to increase the extraction efficiency.

In the electroluminescence (EL) measurement, a continuous current is injected into the device at room temperature. The light output is detected by a calibrated large area Si photodiode placed 5 mm above the top of the device. This detecting condition captures almost all the power emitting from the LED. It is found that the 20-mA forward voltages of the conventional LED and the present LED were 3.25 and 3.26 V, respectively; indicating that the processing associated with the additional 1D PC structure did not change the electrical properties. Fig.4.13 shows the comparison of the intensity–current (*L–I*) characteristics of the LED with and without an omnidirectional 1D PC. It can be seen that the EL intensity of our present LED is larger than that observed from the conventional LED. At an injection current of 20 mA, it is found that the MQW emission peaks of these two devices are both about 450 nm and the light output powers of the LED with and without 1D PC are about 11.7 mW and 6.5 mW, respectively. In other words, we can enhance the output power by a factor of 1.8 for the InGaN–GaN MQW LED with an omnidirectional 1D-PC. This demonstrates that the LED with 1D PC has a higher light extraction efficiency.

In summary, a GaN-based LED with an omnidirectional 1D PC is designed and fabricated. The omnidirectional 1D PC composed of alternately stacked TiO_2 and SiO_2 layers possesses a PBG within the blue regime of interest. With the same MQW emission peak at about 450 nm and driving current of 20 mA, it is found that the light output powers of the LED with and without 1D PC are about 11.7 mW and 6.5 mW, respectively. This result shows that the omnidirectional 1D PC has a higher reflectance and a wider reflection angle than the conventional DBR. Our finding has

promising potential for the enhancement of output powers of commercial light emitting devices.

4-3 Optically Pumped short-wavelength VCSELs

Gallium nitride is a direct wide bandgap semiconductor, which has attracted considerable interest in its application in blue, green and ultraviolet light-emitting diode and laser diodes [51]. With the demonstration and commercialization of GaN-based edge-emitting laser diodes earlier [52], the research interest has gradually shifted to the fabrication and demonstration of GaN-based vertical cavity surface emitting laser (VCSEL) structures and GaN Resonant-Cavity Light-Emitting Diodes (RC-LED). An important requirement for the realization of GaN-based VCSEL is the fabrication of high reflectance mirrors with large band width, usually in the form of distributed Bragg reflectors (DBRs). In the case of wide band-gap nitride semiconductors, both InGaN-based RCLEDs and optically pumped VCSELs [53-55] incorporating GaN/AlGaN Bragg mirrors [56-59] have been reported. H. M. Ng *et. al.* report the peak reflectance up to 99% centered at 467 nm with a bandwidth of 45 nm based on AlN/GaN quarterwave layers have been grown by electron cyclotron resonance plasma-assisted molecular-beam epitaxy. M. Diagne et. al. [60] was demonstrate the dominant mode at 413 nm, which coincides with the high reflectivity region of the DBR and the peak of the QW PL emission, has a spectral linewidth of ~0.6 nm. The AlN/GaN based DBR grown by MOCVD was reported by T. Shirasawa et.al. [61] with a peak reflectance of about 88%. In this section, we report the growth of high reflectivity and large stopband width AlN/GaN DBR structures by MOCVD system, and demonstration of GaN-based VCSEL with AlN/GaN DBR structure.

Fabrication of GaN-based VCSEL

The structure of the GaN-based VCSEL was grown in a vertical-type MOCVD system (EMCORE D-75) with a fast rotating disk, which can hold one 2-inch wafer. The polished optical-grade C-face (0001) 2-inch-diameter sapphire was used as substrate for the epitaxial growth of the VCSEL structure. Trimethylindium (TMIn), Trimethylgallium (TMGa), Trimethylaluminum (TMAl), and ammonia (NH_3) were used as the In, Ga, Al, and N sources, respectively. Initially, a thermal cleaning process was carried out at 1080°C for 10 minutes in a stream of hydrogen ambient before the growth of epitaxial layers. After depositing a 30-nm-thick GaN nucleation layer at 530°C, the temperature was raised up to 1045°C for the growth of a 1-μm-thick GaN buffer layer. Then a 25-pairs AlN/GaN DBR structure was grown at 1040°C under the fixed chamber pressure of 100 Torr similar to the previous reported growth condition. Then a 380-nm-thick n-type GaN, followed by a ten pairs $In_{0.2}Ga_{0.8}N$ MQW and a 100-nm-thick p-type GaN were grown to form a 3 λ cavity. Finally, an eight pairs Ta_2O_5/SiO_2 dielectric mirror was deposited by the E-gun as the top DBR reflector. The SEM image of the MOCVD grown structure and the overall VCSEL structure are shown in the Fig 4.14 (a) and (b). The schematic diagram of the overall VCSEL structure is shown in Fig. 4.14 (c).

Reflectance Spectrum and Photoluminescence

The structure of GaN-based VCSEL is fabricated as discussed previously. The reflectance spectrum of the 25 pairs of AlN/GaN DBR grown on the sapphire by the MOCVD and the 8 pairs of Ta_2O_5/SiO_2 DBR evaporated on the Si substrate by E-gun were measured by the n&k ultraviolet-visible spectrometer with normal incidence at room temperature. Figure 4.15 shows the reflectance spectrum of AlN/GaN DBRs and

Ta_2O_5/SiO_2 DBRs, respectively. The AlN/GaN mirror with 25 pairs of DBR can achieve the high reflectivity of 94% and the wide FWHM of reflectance spectrum about 33nm. The Ta_2O_5/SiO_2 mirror with 8 pairs of DBR can achieve the high reflectivity of 97.5% and the wide FWHM of reflectance spectrum about 115nm.

The photoluminescence (PL) emission was excited by a 325nm He-Cd laser with a spot size of about 2-μm-diameter. Figure 4.16 shows the PL emission of the MOCVD grown structure and overall VCSEL structure. The PL emission peak wavelength and the FWHM of emission spectrum of MOCVD grown structure were 448nm and 10.5nm, respectively. It is obviously that the PL emission peak wavelength of overall VCSEL structure was dominated by cavity mode and was centered at 448nm. The PL emission of and the FWHM of emission spectrum of overall VCSEL structure were 448nm and 1.4nm, respectively. The narrow FWHM of 1.4nm is attributed to the Febry-Perot cavity effect.

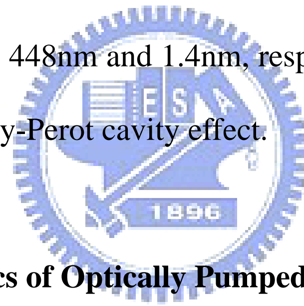

1896

The Characteristics of Optically Pumped GaN-based VCSEL

The optical pumping of the sample was performed using a frequency-tripled Nd:YVO_4 355-nm pulsed laser with a pulse width of ~ 0.5 ns at a repetition rate of 1 kHz. The pumping laser beam with a spot size of 60 μm was incident normal to the VCSEL sample surface. By using the microscopy system (WITec, alpha snom), the light emission from the VCSEL sample was collected into a spectrometer/CCD (Jobin-Yvon Triax 320 Spectrometer) with a spectral resolution of ~0.1nm for spectral output measurement. The stimulated emission of fabricated GaN-based VCSEL was achieved and observed by using the optical pumping system mentioned above. The light emission intensity from the VCSEL as a function of the exciting energy is shown in Fig 4.17. A distinct threshold characteristic was observed at the threshold pumping

energy (E_{th}) of about 1.5μJ corresponding to an energy density of 53mJ/cm^2. Then the laser output increased linearly with the excitation energy beyond the threshold. The inset of the Fig 4.17 shows the excitation energy dependent emission spectrum. The GaN VCSEL emits 448nm blue wavelength with a linewidth of 0.25nm. It evidently expresses the behavior from spontaneous emission to stimulated emission.

In conclusion, the GaN-based Vertical-Cavity surface-Emitting Laser (VCSEL) structure grown by MOCVD were investigated. The 25 pair AlN/GaN DBR structure and 3 λ cavity layer were consisted in this VCSEL structure. The AlN/GaN mirror with 25 pairs of DBR can achieve the high reflectivity of 94% and the wide FWHM of reflectance spectrum about 33nm. The Ta_2O_5/SiO_2 mirror with 8 pairs of DBR can achieve the high reflectivity of 97.5% and the wide FWHM of reflectance spectrum about 115nm. The PL emission of and the FWHM of emission spectrum of overall VCSEL structure were 448nm and 1.4nm, respectively. The narrow FWHM of 1.4nm is attributed to the Febry-Perot cavity effect. The stimulated emission of fabricated GaN-based VCSEL was achieved and observed by using the optical pumping system. The GaN VCSEL emits 448nm blue wavelength with a linewidth of 0.25nm. It evidently expresses the behavior from spontaneous emission to stimulated emission.

References

[1] P. A. Crowell, D. K. Yong, S. Keller, E. L. Hu, and D. D. Awschalom, Appl. Phys. Lett. **72**, 927 (1998).

[2] P. G. Eliseev, P. Perlin, J. Lee, and M. Osinski, Appl. Phys. Lett. **71**, 569 (1997).

[3] M. S. Minsky, S. B. Fleischer, A. C. Abare, J. E. Bowers, E. L. Hu, S. Keller, and S. P. Denbaars, Appl. Phys. Lett. **72**, 1066 (1998).

[4] K. L. Teo, J. S. Colton, P. Y. Yu, E. R. Weber, M. F. Li, W. Liu, K. Uchida, H. Tokunaga, N. Akutsu, and K. Matsumoto, Appl. Phys. Lett. **73**, 1697 (1998).

[5] P. Perlin, C. Kisielowski, V. Iota, B. A. Weinstein, L. Mattos, N. A. Shapiro, J. Kruger, E. R. Weber, and J. Yang, Appl. Phys. Lett. **73**, 2778 (1998).

[6] T. Wang, D. Nakagawa, M. Lachab, T. Sugahara, and S. Sakai, Appl. Phys. Lett. **74**, 3128 (1999).

[7] T. Wang, H. Saeki, J. Bai, M. Lachab, T. Shirahama, and S. Sakai, Appl. Phys. Lett. **76**, 1737 (2000).

[8] J. Bai, T. Wang, and S. Sakai, J. Appl. Phys. **88**, 4729 (2000).

[9]C. Kisielowski, "Composition and Strain Fluctuations in InN/GaN/AlN Heterostructures: A Microscopic Glimpse below Surfaces", Proceedings of the 2nd International Symposium of blue Laser and Light Emitting Diodes, 321 (Ohmsha Ltd., 1998)

[10] C. Kisielowski, Semiconductors and Semimetals **57**, 306 (1999).

[11] T. Takeuchi, C. Wetzel, S. Yamaguchi, H. Sakai, H. Amano, and I. Akasaki, Appl. Phys. Lett. **73**, 1691 (1998).

[12] P. Perlin *et al.*, Appl. Phys. Lett. **73**, 2778 (1998).

[13] T. Takeuchi, S. Sota, M. Katsuragawa, M. Komori, H. Takeuchi, H. Amano, and I. Akasaki, Jpn. J. Appl. Phys., Part 2 **36**, L382 (1997).

[14] T. Takeuchi, C. Wetzel, S. Yamaguchi, H. Sakai, H. Amano, and I. Akasaki,

Appl. Phys. Lett. **73**, 1691 (1998).

[15] M. D. Nardell, K. Rapcewic, and J. Bernhol, Appl. Phys. Lett. **71**, 3135 (1997).

[16] Shapiro N A, Perlin P, Kisielowski C, Mattos L S, Yang J W and Weber E R 2000 MRS Internet J. Nitride Semicond Res. **1** 5

[17] Bai J, Wang T and Sakai S, J. Appl. Phys. **88**, 4729 (2000)

[18] T. Wang, J. Bai, S. Sakai and J. K. Ho, Appl. Phys. **78**, 2617 (2001).

[19] T. Wang, D. Nakagawa, M. Lachab, T. Sugahara, and S. Sakai, Appl. Phys. Lett. **74**, 3128 (1999)

[20] Kim D J, Moon Y T, Song K M, Choi C J, Ok Y W, Seong T Y and Park S J 2000 *J. Cryst. Growth* **368** 221

[21] Grandjean N, Massies J, Dalmasso S, Vennegnes P, Siozande L and Hirsch L 1999 *Appl. Phys. Lett.* **3616** 74

[22] Uchida K, Kawata M, Yang T, Toto S, Mishima T, Niwa A and Gotoh J 1999 *J. Electron. Mater.* **246** 28

[23] Cho H K, Lee J Y, Kim K K and Yang G M 2000 *Appl. Phys. Lett.* **77** 247

[24] Myung Goo Cheong, E-K Suh and H. J. Lee, Semicond. Sci. Technolo. **16**, 783-788 (2001)

[25] O. Buchinsky, M. Blumin, R. Sarfaty, D. Fekete, I. Samid, and M. Yust, Appl. Phys. Lett. **68**, 2043 (1996).

[26] O. Buchinsky, M. Blumin, R. Sarfaty, D. Fekete, I. Samid, and M. Yust, Appl. Phys. Lett. **72**, 1484 (1998).

[27] X. B. Zhang, R. D. Heller, M. S. Noh, R. D. Dupuis, G. Walter, and N. Holonyak, Jr., Appl. Phys. Lett. **82**, 4343 (2003).

[28] E.F. Schubert, I.D. Goepfert, W. Grieshaber, J.M. Redwing, Appl. Phys. Lett. **71** 921 (1997).

[29] E.S. Oh, C.S. Sone, O.H. Nam, H.S. Park, Y.J. Park, Appl. Phys. Lett. **76** 3242

(2000).

[30] Y.-H. Cho, J.J. Song, S. Keller, M.S. Minsky, E. Hu, U.K. Mishra, S.P. DenBaars, Appl. Phys. Lett. **73** 1128 (1998).

[31] T. Wang, H. Saeki, J. Bai, T. Shirahama, M. Lachab, S. Sakai, P. Eliseev, Appl. Phys. Lett. **76** 1737 (2000).

[32] J. Dalfors, J.P. Bergman, P.O. Holtz, B.E. Sernelius, B. Monemar, H. Amano, I. Akasaki, Appl. Phys. Lett. **74** 3299 (1999).

[33] M.S. Minsky, S. Chichibu, S.B. Fleischer, A.C. Abare, J.E. Bowers, E.L. Hu, S. Keller, U.K. Mishra, S.P. DenBaars, Jpn. J. Appl. Phys. **37** L1362 (1998).

[34]K.C. Zeng, J.Y. Lin, H.X. Jiang, A. Salvador, G. Popovici, H. Tang, W. Kim, H. Morkoc, Appl. Phys. Lett. **71** 1368 (1997).

[35]S. Keller, S. F. Chichibu, M. S. Minsky, E. Hu, U. K. Mishra, and S. P. DenBaars, J. Cryst. Growth **195**, 258 s1998d.

[36]Y.-H. Cho, J. J. Song, S. Keller, M. S. Minsky, E. Hu, U. K. Mishra, and S. P. DenBaars, Appl. Phys. Lett. **73**, 1128 s1998d.

[37] K. Kusakabe, T. Hara and K. Ohka, J. Appl. Phys. **97** 043503 (2005).

[38] S. Nakamura, M. Senoh, N. Iwasa, and S. Nagahama, “High-brightness InGaN blue, green and yellow light-emitting diodes with quantum well structures,” *Jpn. J. Appl. Phys.*, vol. **34**, p. L797, (1995).

[39] S. Nagahama, N. Iwasa, M. Senoh, T. Matsushita, Y. Sugimoto, H. Kiyoku, T. Kozaki, M. Sano, H. Matsumura, H. Umemoto, K. Chocho, T. Yanamoto, and T. Mukai, “GaN-based light-emitting-diodes and laser diodes, and their recent progress,” *Phys. Stat. Sol. (a)*, vol. **188**, no. 1, pp. 1–7, (2001).

[40] Y. C. Lin, S. J. Chang, Y. K. Su, T. Y. Tsai, C. S. Chang, S. C. Shei, S. J. Hsu, C. H. Liu, U. H. Liaw, S. C. Chen, and B. R. Huang, “Nitride-based light emitting diodes with Ni/ITO p-type ohmic contacts,” *IEEE Photon. Technol. Lett.*, vol. **14**,

pp. 1668–1670, (2002).

[41] C. C. Kao, H.C. Kuo, H. W. Huang, J. T. Chu, Y. C. Peng, Y. L. Hsieh, C. Y. Luo, S. C. Wang, C. C. Yu, and C. F. Lin, **“**Light-output enhancement in a nitride-based light-emitting diode with 22° undercut sidewalls,” *IEEE Photon. Technol. Lett.*, vol. **14**, pp. 19-21, (2005).

[42] R. V. Steele, “Overview of the high-brightness LED market”, *Proc. of SPIE, Solid-State Lighting and Displays,* vol. **4445**, pp1-4, (2001).

[43] R. A. Paquin, in *Handbook of Optics* (McGraw-Hill, New York. 1995), pp. 37.1-35.78

[44] Y. S. Zhao, D. L. Hibbard, H. P. Lee, K. Ma, W. So, and H. Liu, “Efficiency Enhancement of InGaN/GaN Light-Emitting Diodes with a “Back-Surface Distributed Bragg Reflector,” *Journal of Electronic Materials*, vol. **32**, pp1523-1526, (2003).

[45] Jong Kyu Kim, Thomas Gessmann, Hong Luo, and E. Fred Schubert, "GaInN light-emitting diodes with $RuO_2/SiO_2/Ag$ omni-directional reflector," *Appl. Phys. Lett.*, Vol. 84, No. **22**, pp. 4508-4510, (2004).

[46] E. Yablonovitch, "Inhibited spontaneous emission in solid-state physics and electronics," *Phys. Rev. Lett.*, Vol. 58, No. **20**, pp. 2059-2062, (1987).

[47] S. John, “Strong localization of photons in certain disordered dielectric superlattices,” *Phys. Rev. Lett.*, vol. **58**, pp. 2486-2489, (1987).

[48] Y. Fink, J. N. Winn, S. an, C. Chen, J. Michel, J. D. Joannopoulos, and E. L. Thomas, "A dielectric omnidirectional reflector," *Science,* vol. **282**, pp. 1679-1682, (1998).

[49] D. N. Chigrin, A. V. Lavrinenko, D. A. Yarotsky, and S. V. Gaponenko, "Observation of total omnidirectional reflection from a one-dimensional dielectric lattice," *Appl. Phys. A: Mater. Sci. Process*, vol. **68**, pp. 25-28, (1999).

[50] S. J. Chang, L. W. Wu, Y. K. Su, Y. P. Hsu, W. C. Lai, J. M. Tsai, J. K. Sheu, and C. T. Lee, “Nitride-Based LEDs With 800℃ Grown p-AlInGaN–GaN Double-Cap Layers,” *IEEE Photon. Technol. Lett.*, vol. **16**, pp. 1447, (2004).

[51] S. Nakamura, M. Senoh, S. Nagahama, N. Iwasa, T. Yamada, T. Matsushita, H. Kiyoku, and Y. Sugimoto, Jpn. J. Appl. Phys., Part 2 **35**, L74 (1996).

[52] S. Nakamura and G. Fasol, The Blue Laser Diode ,Springer, Berlin, (1997).

[53] T. Someya, K. Tachibana, J. Lee, T. Kamiya, and Y. Arakawa, Jpn. J. Appl. Phys., Part 2 **37**, L1424 (1998).

[54] I. L. Krestnikov, W. V. Lundin, A. V. Sakharov, V. A. Semenov, A. S. Usikov, A. F. Tsatsul’nikov, Z. I. Alferov, N. N. Ledentsov, A. Hoffmann, and D. Bimberg, Appl. Phys. Lett. **75**, 1192 (1999).

[55] Y.-K. Song, H. Zhou, M. Diagne, A. V. Nurmikko, R. P. Schneider, C. P. Kuo, M. R. Krames, R. S. Kern, C. Carter-Coman, and F. A. Kish, Appl. Phys. Lett. **76**, 1662 (2000).

[56] M. Diagne, Y. He, H. Zhou, E. Makaronp, A. V. Nurmikko, J. Han, K. E. Waldrip, J. J. Figiel, T. Takeuchi, and M. Krames, Appl. Phys. Lett. **79**, 3720 (2001).

[57] N. Nakada, M. Nakaji, H. Ishikawa, T. Egawa, M. Umeno, and T. Jimbo, Appl. Phys. Lett. **76**, 1804 (2000).

[58] F. B. Naranjo, S. Ferna`ndez, M. A. Sa`nchez-Garcia`, F. Calle, and E. Calleja, Appl. Phys. Lett. **80**, 2198 (2002).

[59] B. Roycroft, M. Akhter, P. Maaskant, P. De Mierry, S. Fernandez, F. B. Naranjo, E. Calleja, T. McCormack, and B. Corbett, Phys. Status Solidi A **192**, 97 (2002).

[60] M. Diagne, M. Y.He, H. Zhou, E. Makarona, A. V. Nurmikko, J. Han, K.E. Waldrip, J. J. Figiel, T. Takeuchi, and M. R. Krames, Appl. Phys. Lett. **79**, 3720 (2001).

[61] Tomoe Shirasawa, Noriaki Mochida, Akira Inoue, Tohru Honda, Takahiro

Sakaguchi, Fumio Koyama, and Kenichi Iga, J. of Crystal Growth **189**, p.124 (1998).

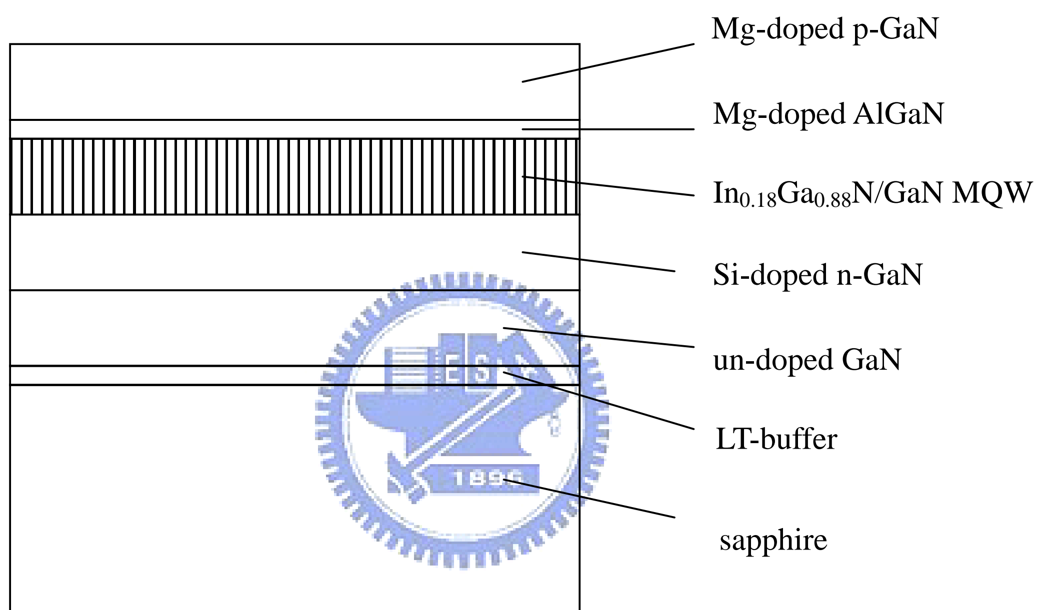

Fig. 4.1 The structure of InGaN/GaN MQW

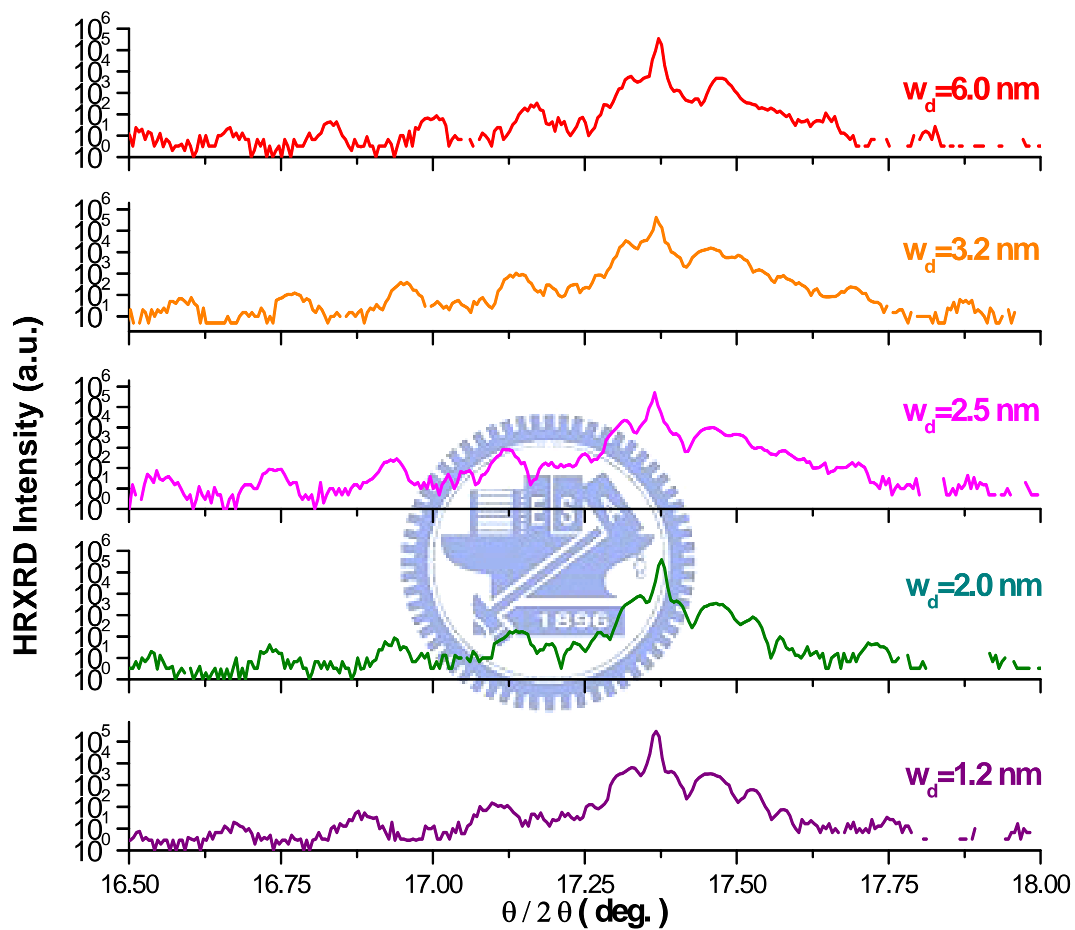

Fig. 4-2 HRXRD spectra of InGaN/GaN 5QWs with different well thickness.

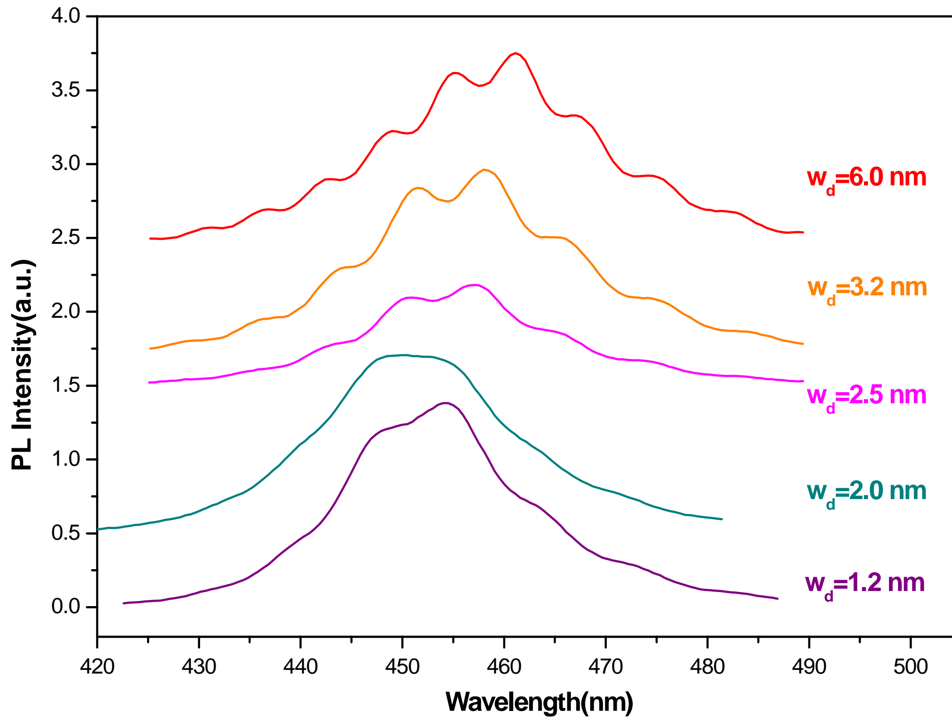

Figure 4-3 (a) The PL spectra of all samples with different quantum-well thickness and the same In content

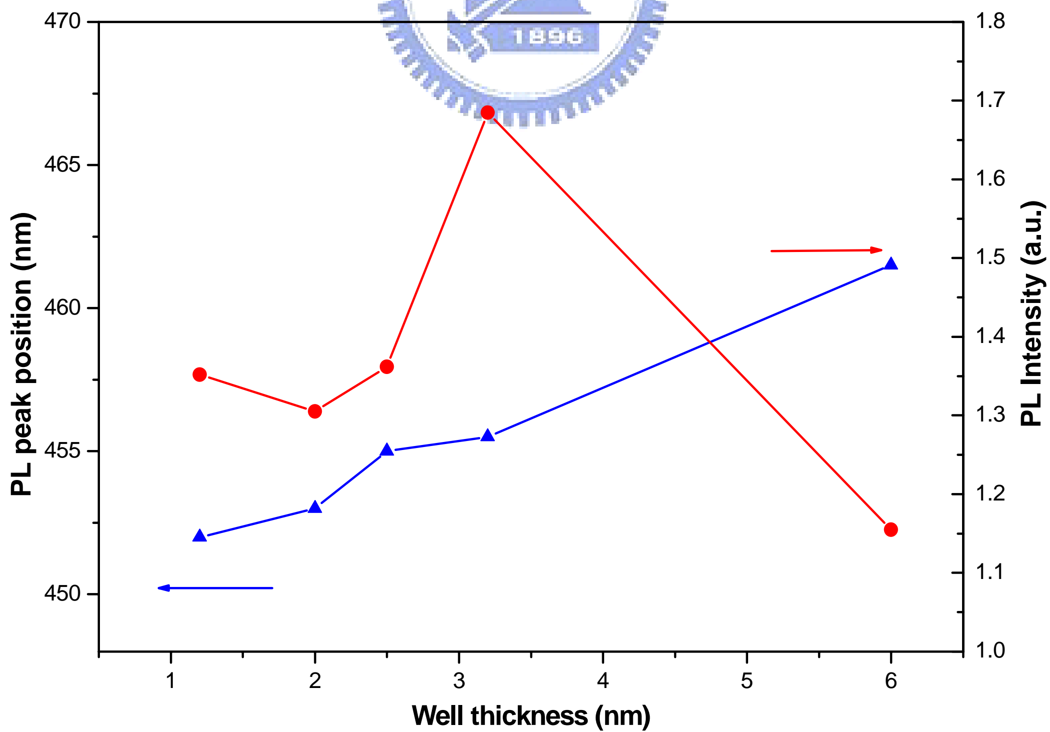

Figure 4-3 (b) The effects of MQW structure with various well thickness on the PL peak position and intensity measured at room temperature.

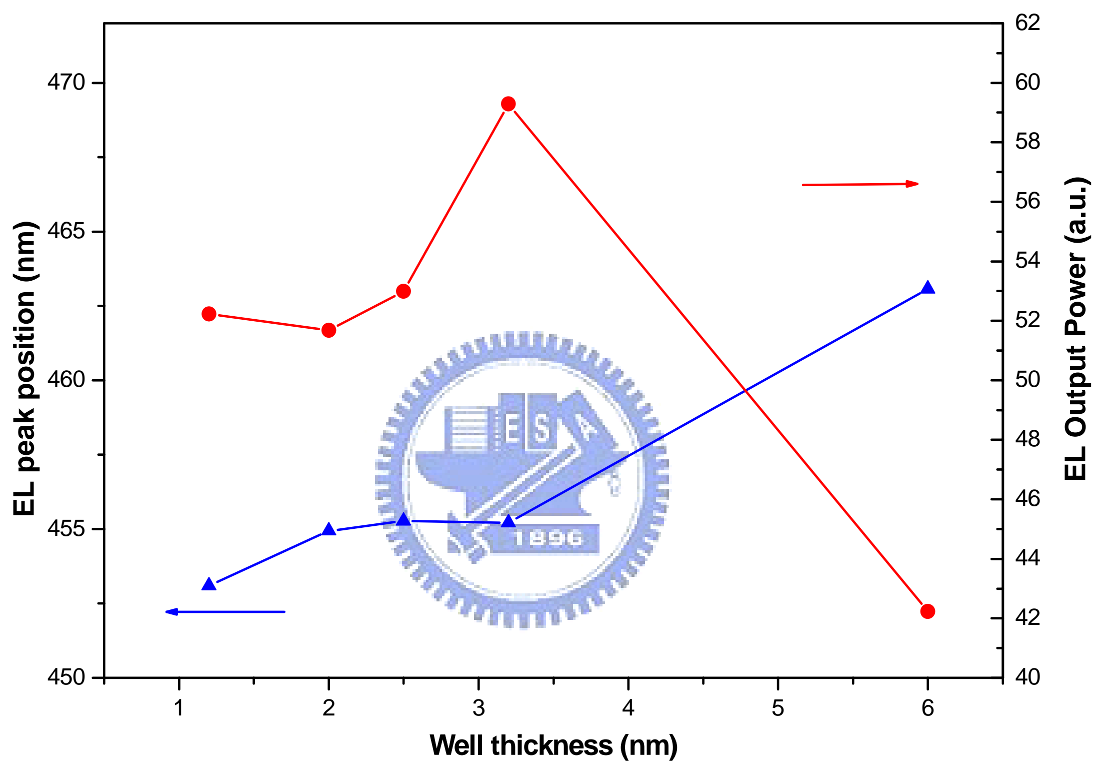

Figure 4-4 The dependence of the output power on the quantum well thickness, which is measured under the condition at 20 mA injection current at room temperature.

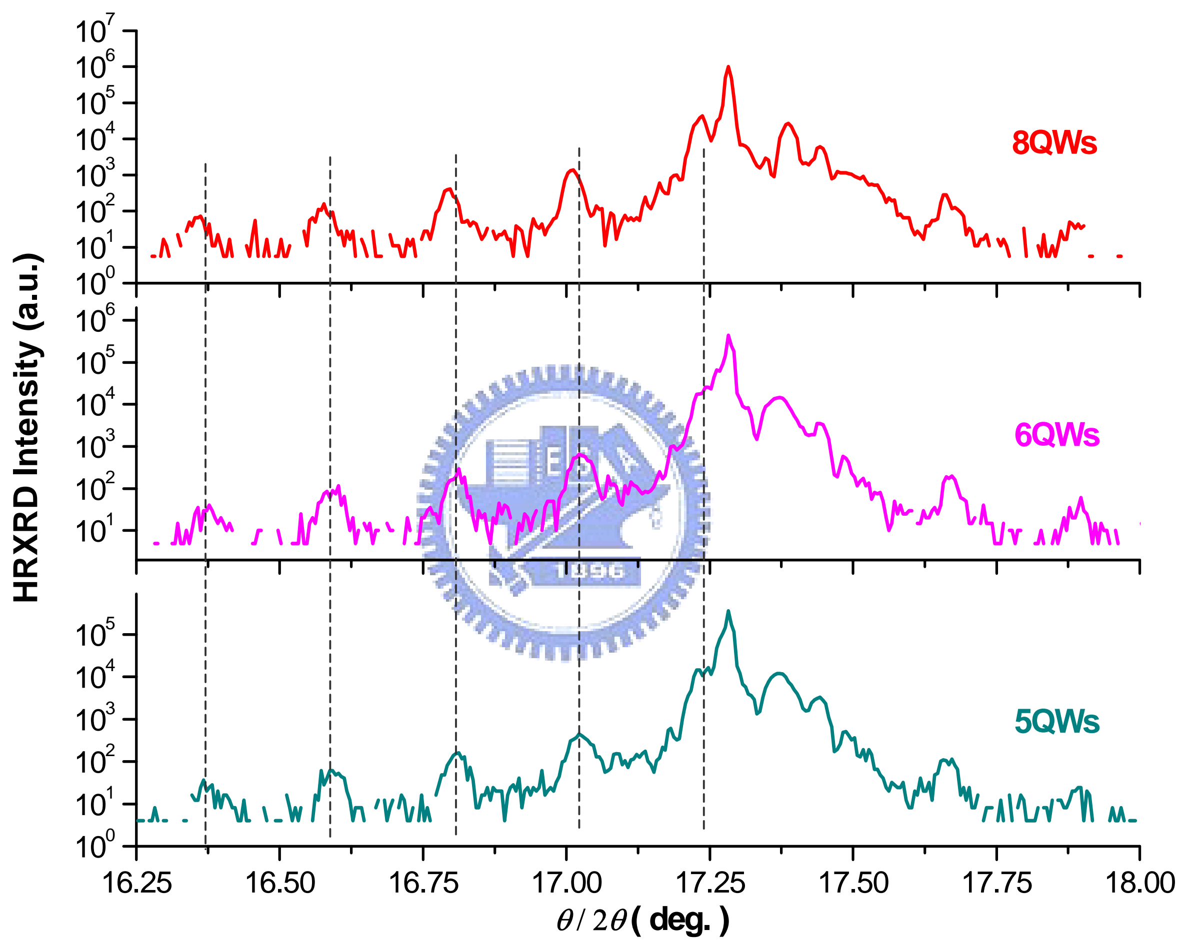

Figure 4-5 HRXRD results for the InGaN/GaN QWs depending on the number of QWs.

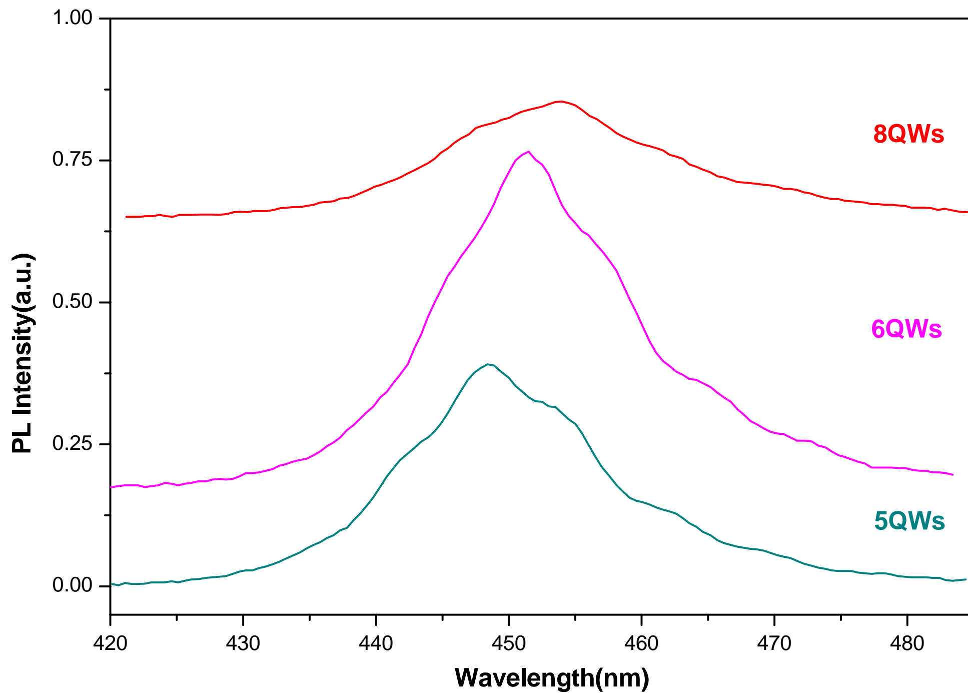

Figure 4-6 (a) The PL spectra of all samples with different quantum-well number and the same In content

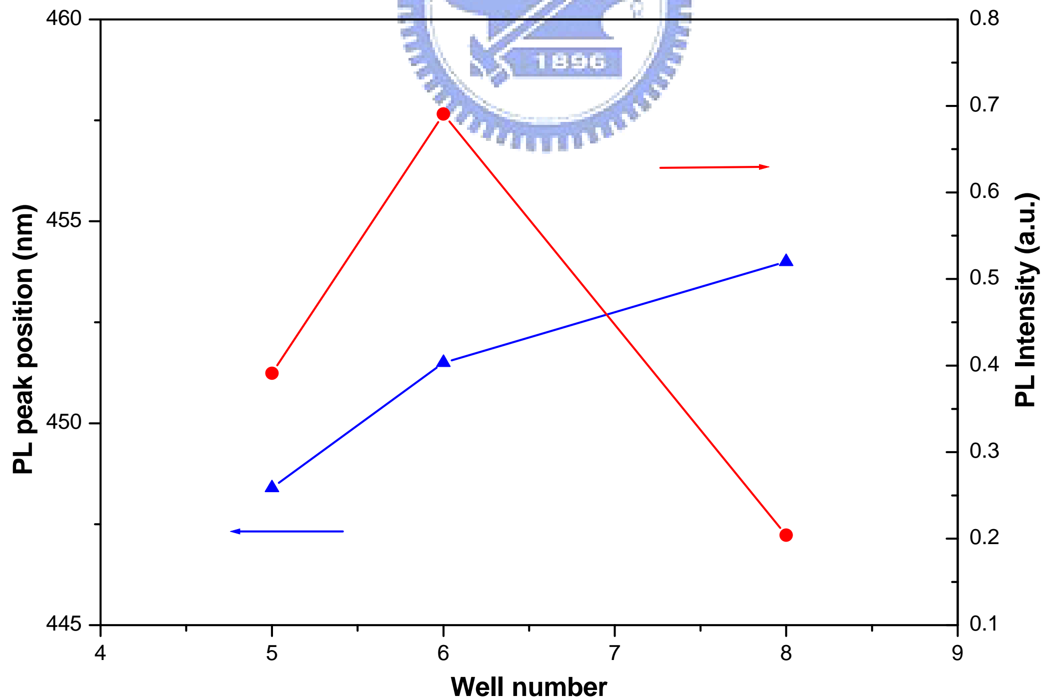

Figure 4-6 (b) The dependence of PL peak position and intensity on the number of wells

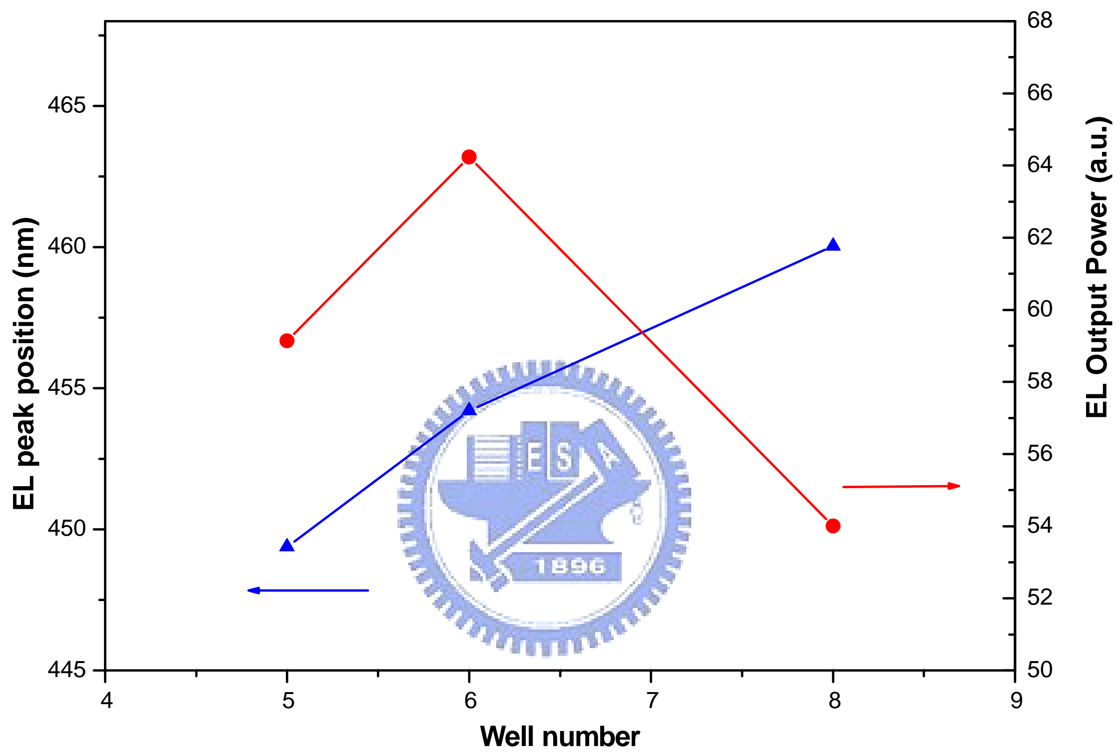

Figure 4-7 The output power characterization results of LED samples with different well number at 20 mA.

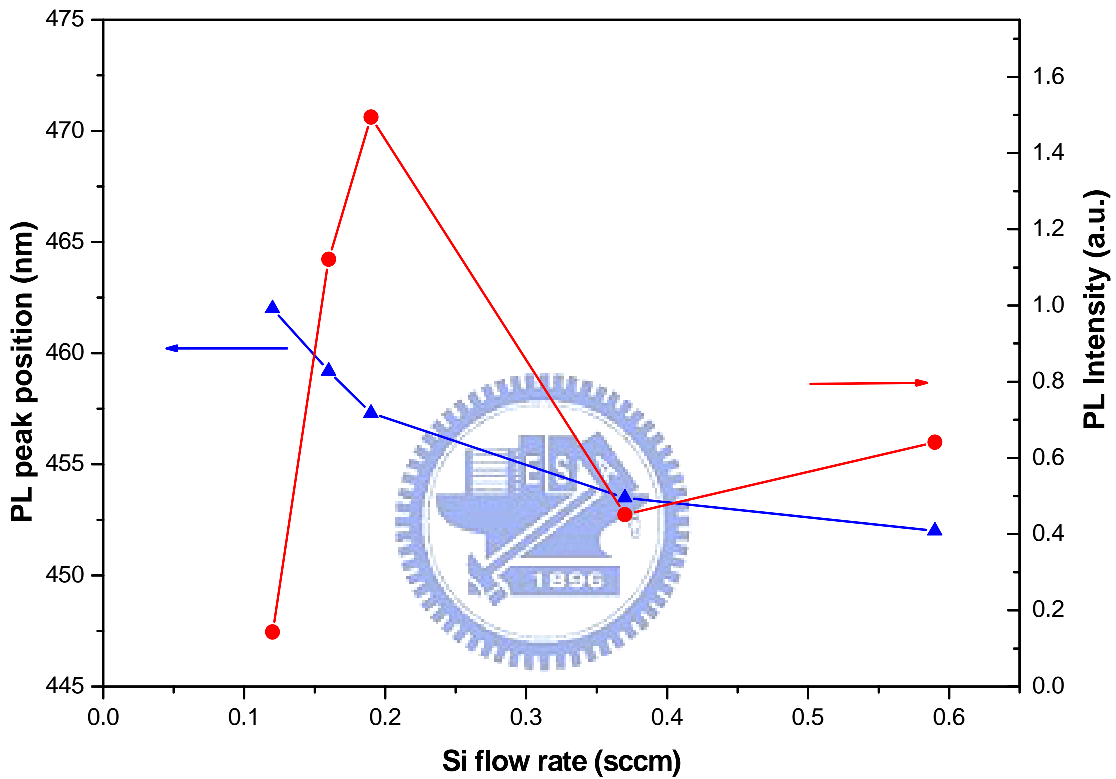

Figure 4-8 The dependences of the PL intensity (filled square) and PL peakwavelength (filled circles) of InGaN/GaN MQW samples as a function of the SiH_4 flow rate in the range of 0.12-0.59 sccm.

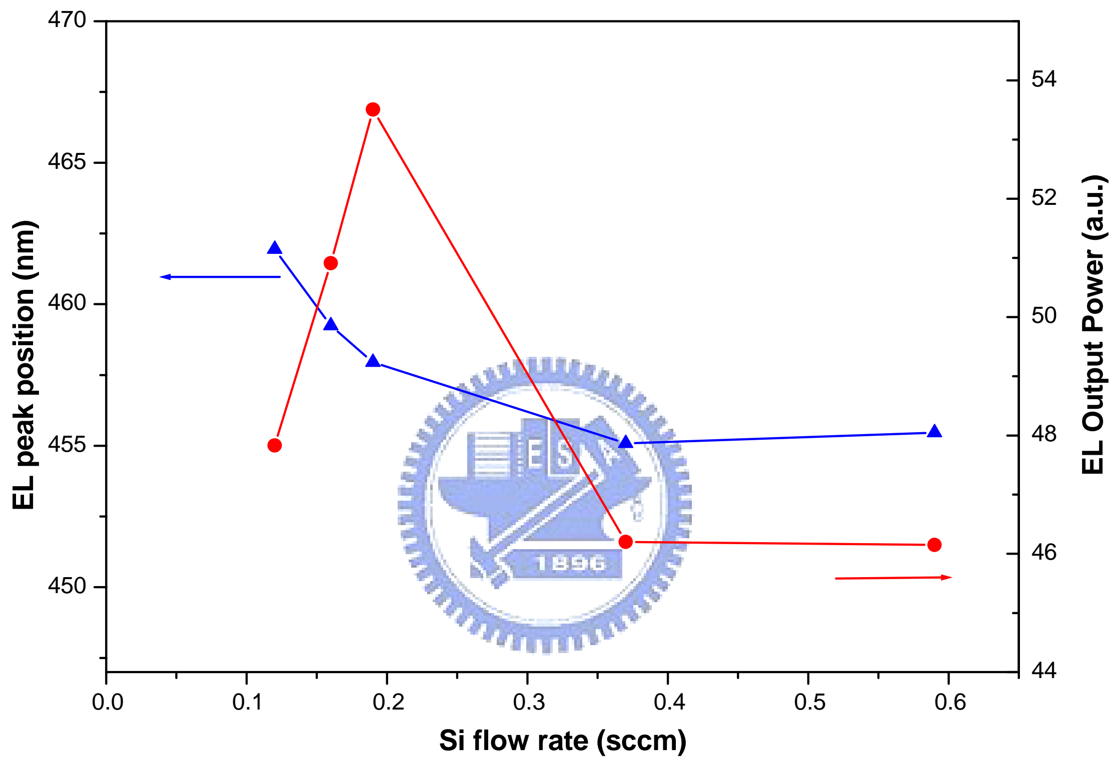

Fig 4-9 The measured LED output power as a function of injection Current. It can seen clearly the relative output luminous intensity as a function of the SiH_4 flow rate in the range of 0.12-0.59 sccm.

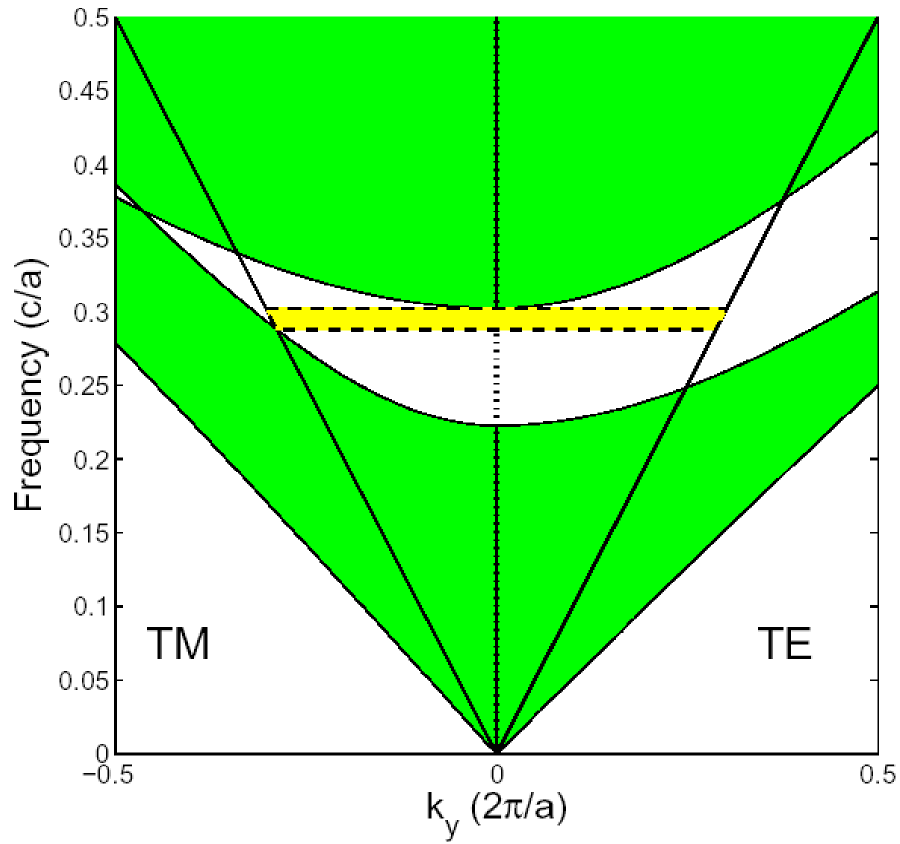

Fig 4-10 Photonic band structure for a 1D PC that shows a photonic band gap (PBG) between frequency 0.288 *c/a* and 0.302 *c/a* (e.g. the region between the dash lines).

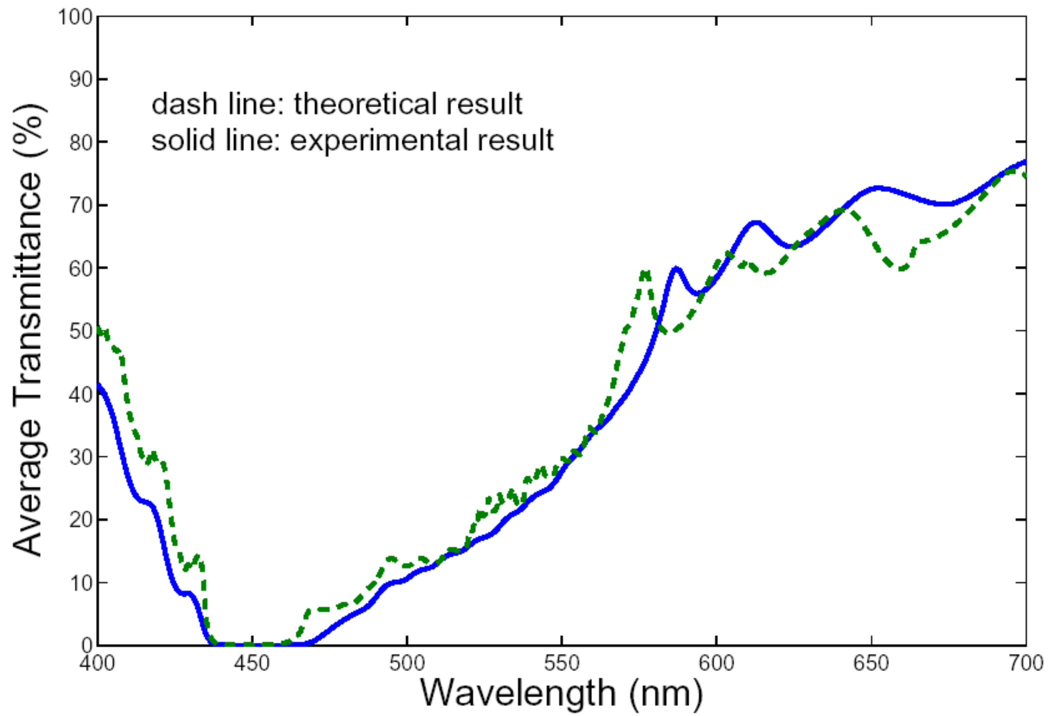

Fig 4-11 Comparison of the averaged theoretical and experimental transmittances as a function of wavelength. The calculated (dash-line) and measured transmittances (solid-line) are averaged for the unpolarized light with the incident angles every 5 ^{o} from 0 ^{o} to 85 ^{o}.

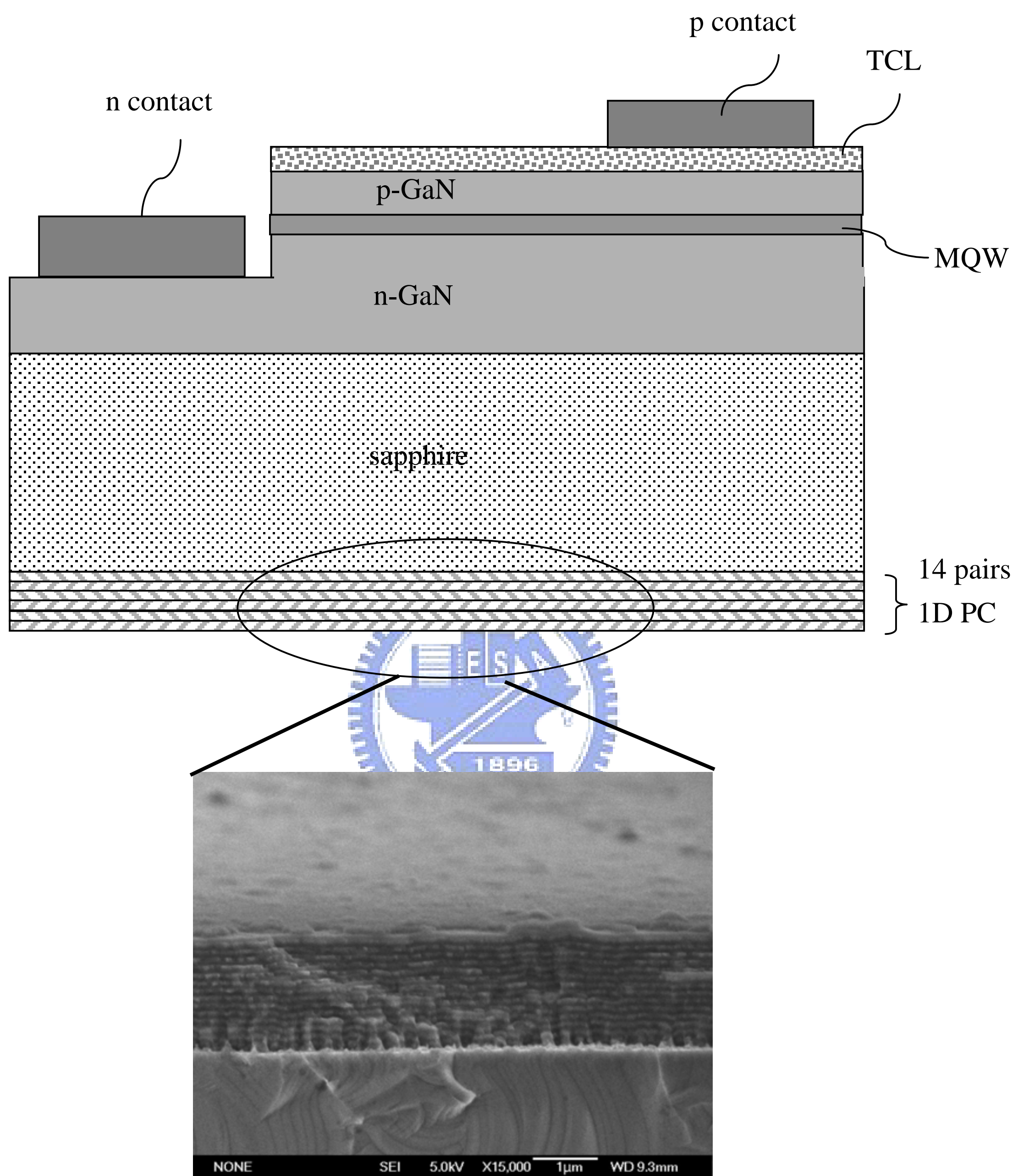

Fig 4-12 Schematic diagram of a GaInN blue LED chip containing an omnidirectional 1D PC at the bottom. The inset shows the SEM picture of the 1D PC.

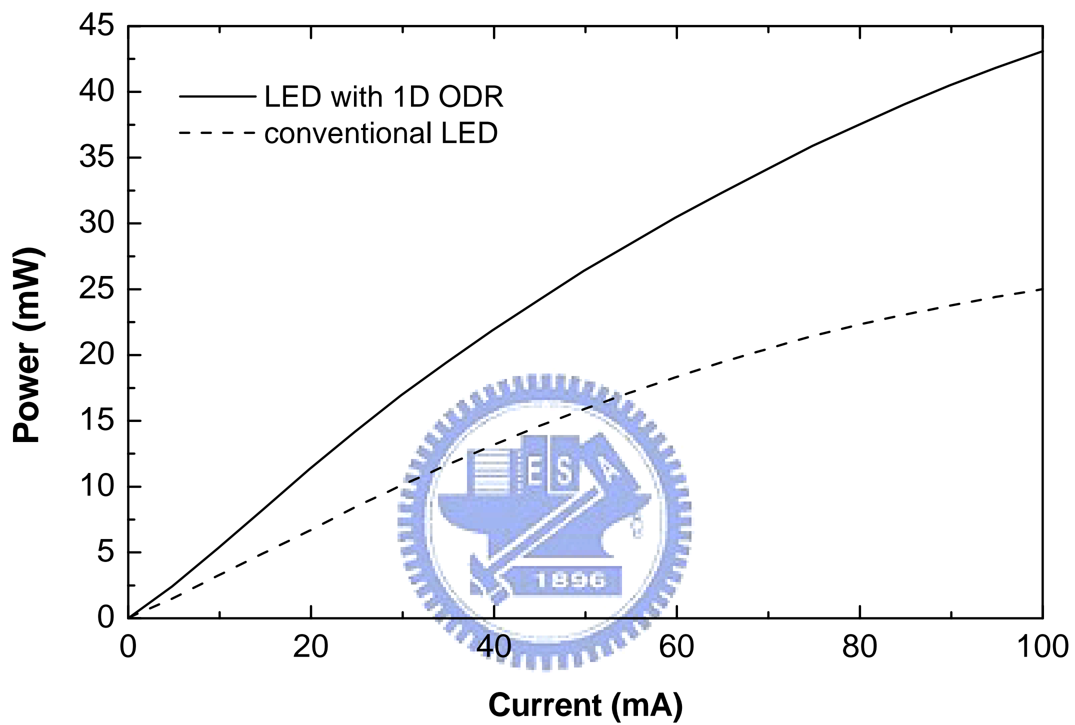

Fig 4-13 Electroluminescence intensity–current (L–I) characteristics of the LED with and without 1D PC.flow rate in the range of 0.12-0.59 sccm.

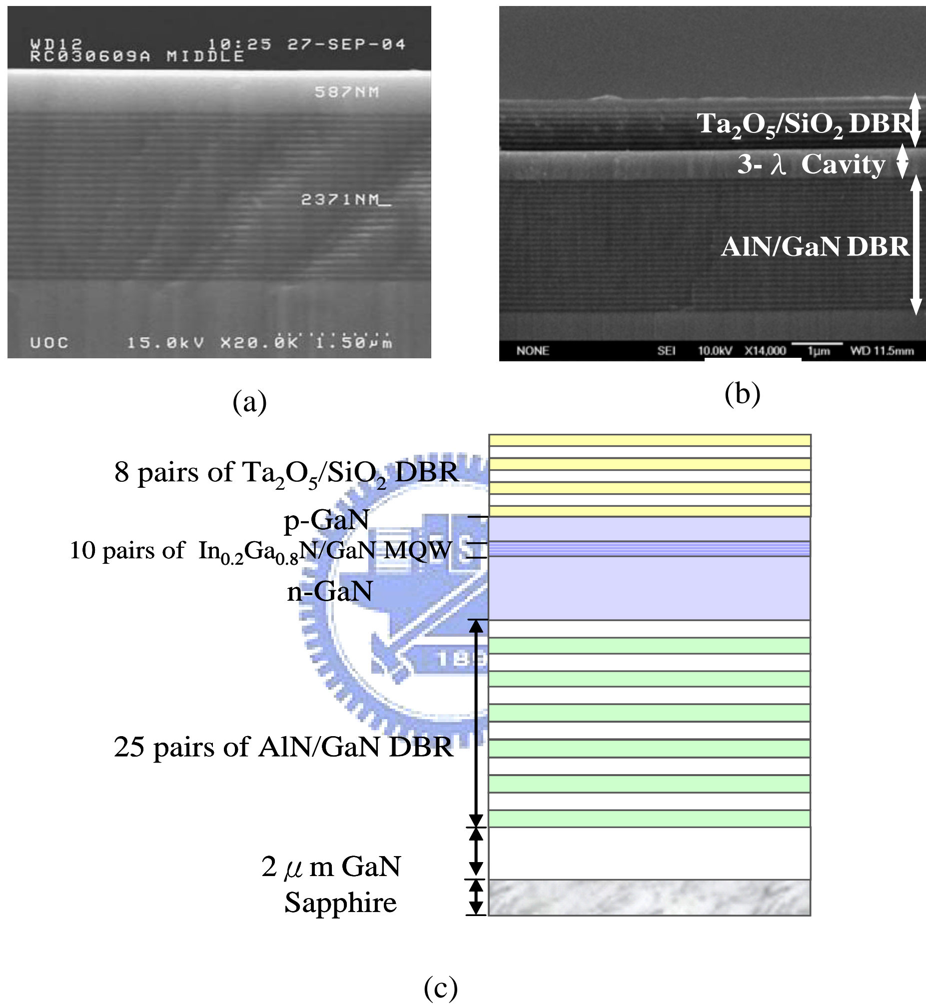

Figure 4-14 (a) The SEM image of the MOCVD grown structure
4-14 (b) The SEM image of the overall VCSEL
4-14 (c) The schematic diagram of the overall VCSEL structure

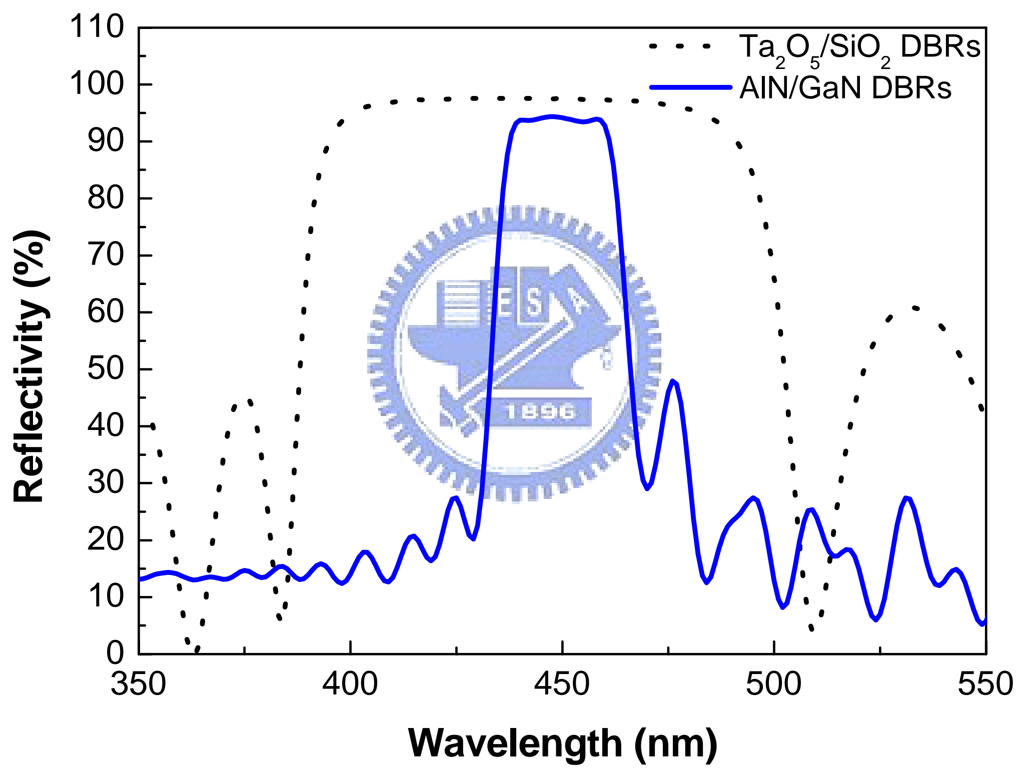

Figure 4-15 The reflectance spectrum of AlN/GaN DBRs and Ta_2O_5/SiO_2 DBRs.

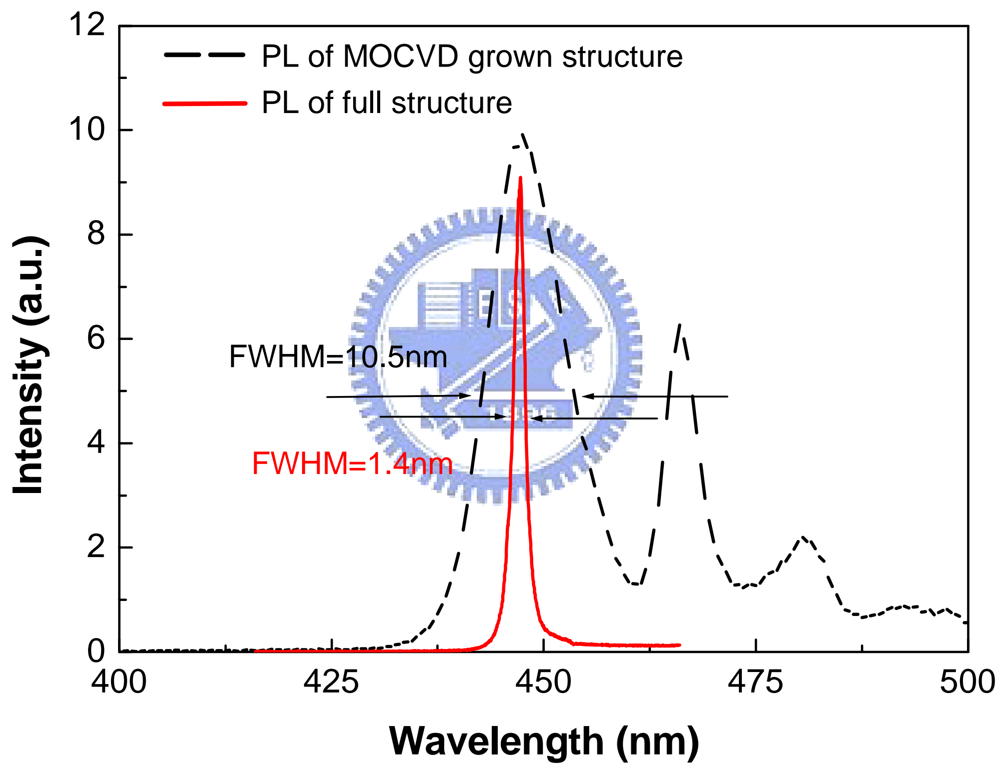

Figure 4-16 PL emission of MOCVD grown structure and overall VCSEL structure.

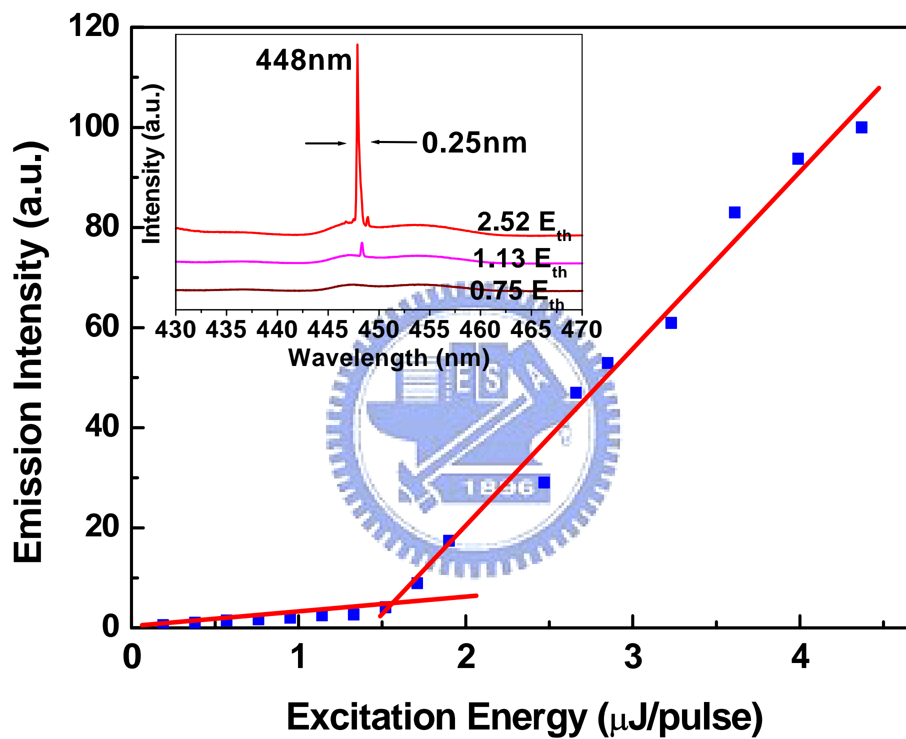

Fig 4-17 The light emission intensity from the VCSEL as a function of the exciting energy.

CHAPTER 5

Fabrication of Long Wavelength Vertical Cavity Surface Emitting Lasers

This chapter mainly describes the fabrication equipments and procedures for long wavelength vertical cavity surface emitting lasers (LW-VCSELs). The characteristics of gain medium suitable for long wavelength vertical cavity surface emitting laser (LW-VCSEL) have been discussed at the beginning of this chapter. By considering material quality and limitations of process equipment, the InGaAlAs system lattice-matched to InP has been chosen as the active layers in this study. Since the epitaxial equipment and process determine most of the characteristics of LW-VCSELs, detailed descriptions are given in this chapter. The growth process, and regrowth process will also be addressed. Wafer fusion technique, which is the other special and important process in fabrication of LW-VCSELs, will also be introduced in this chapter.

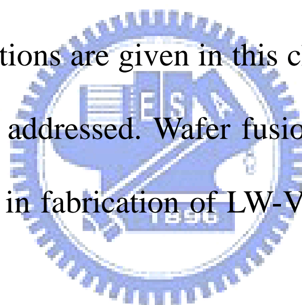

5-1 Characterization and Optimization of the Active Layers

InP-Based Gain Materials

The characteristics of gain medium suitable for long wavelength vertical cavity surface emitting laser (LW-VCSEL) have been discussed at the beginning of this chapter. By considering material quality and limitations of process equipment, the InGaAlAs system lattice-matched to InP has been chosen as the active layers in this study. The optimized layer structures have been determined by investigating performance of edge emitting lasers (EELs) with InGaAlAs multiple quantum wells (MQW) as the active layers.

Several kinds of material system can combine to emit light in long wavelength range. However, the most promising and conventional material systems lattice-match to InP substrate. As mentioned previously, the absence of high reflectivity distributed Bragg reflectors (DBRs) is the most challenge in making InP-based LW-VCSELs. The fundamental properties of the InP-based gain materials will also be discussed.

Monolithically grown DBRs lattice-matched to InP continued to attract interests due to the well existing highly efficient InGaAsP and InGaAlAs gain materials covered the wavelength window from 1.3 to 1.8 μm. The InGaAsP material systems have been applied for buried heterostructure (BH) type long wavelength EELs for a long time. The quaternary feature makes this material easy to tailor different strain and emission wavelength. The InGaAlAs material system, which developed later [1], also shows good performance in laser operations. We first compare the gain-spectrum and gain-carrier concentration relation between InGaAlAs and InGaAsP material for a single quantum well structure with a thickness of 5 nm and a compressive strain of 1.5 %. The emission wavelength is calculated to be 1.51 μm when considering the quantum size effect and strain splitting effect as mentioned in chapter 2. The barrier is 10 nm thick and 0.75% tensely strained for compensating the strain in quantum well. No additional loss and confinement factor are assumed. The carrier recombination and emission above the barrier are also neglected. The temperature for calculation is 300 K. The injected carrier density ranges from 1×10^{16} to 5×10^{18} cm^{-3}. The simulated gain spectrums for TE mode are shown on the left side of Figure 5.1 with the gain-carrier concentration relations shown on the right side. No big difference can be distinguished between these two materials from the intrinsic gain behavior at this point.

We then construct a Fabry-Perot (FP) laser structure containing these two

material systems for MQWs. The number of quantum wells and the amount of strain is the same for two material systems. The lower threshold current and higher slope efficiency for InGaAlAs system was obtained. The simulated band diagrams under forward bias and above the threshold conditions are shown in Figure 5.2. The band offset ratio between conduction band and valence band is 0.72 for InGaAlAs and 0.36 for InGaAsP. Due to the larger conduction band offset for InGaAlAs system, the electrons have fewer chance to jump out of the quantum wells to become leakage current The high potential barrier is very important for high temperature laser operations since the extra energy gained by the electrons increases the possibility for electron to over-ride the barrier potential. In contrast, the relatively large valence band offset in InGaAsP system prevents the holes with large effective mass and low mobility uniformly distributing over the multiple quantum wells [2], leading to enhanced losses and carrier wasting. The electrons and holes gather in the first quantum well near the p-type cladding layer as shown on the right side of Figure 4.2 (b). The increased carrier densities further worsen the laser performance due to the Auger recombination loss. The smaller conduction band offset and non-uniformity of carrier distribution for InGaAsP lasers lead to higher threshold current and lower slope efficiency in comparisons to InGaAlAs lasers.

Since the high temperature characteristic is essential in LW-VCSELs, we thereby choose the InGaAlAs system for gain mediums in this study. In this section, the structures of InGaAlAs multiple quantum wells will be optimized by investigating the performance of corresponding EELs.

Fabrication of Long Wavelength FP EELs

The typical laser structure is shown in Figure 5.3 (a). All the epitaxial layers

were grown by MOCVD on S doped n-type InP substrates with exact orientation to <100> direction. The laser structure consists of following layers: an 1 μm thick n-type InP layer, an 100 nm thick n-type InAlAs layer served as inner cladding, a pair of 100 nm un-doped $Al_xGa_{1-x}In_{0.48}P$ confinement layers with x graded from 0.49 to 0.25, active layers with six compressively strained InGaAlAs quantum wells separated by five tensile strained InGaAlAs barrier layers, a 50 nm thick p-type InAlAs layer also served as inner cladding, a 50 nm thick p-type InGaAsP barrier reducing layer with emission wavelength of 1.3 μm, and a 200 nm thick p-type InGaAs contact layer. The equivalent band diagram is illustrated in Figure 5.3 (b). The as-grown wafer with laser structure is then processed to form a simple ridge structure. The first step is ridge formation using dry or wet chemical etching. Then, the SiN_x was deposited to protect the top surface except for the contact layer above the ridge, followed by the metallization for top and bottom sides. The processed wafer was then cleaved into 300 μm by 300 μm chips with both facets coated. The reflectivity of front and rear coating is 30% and 85%, respectively. Finally, the chips were mounted to TO-56 packages for final testing.

The scanning electron microscope (SEM) is commonly used to examine the geometry of microelectronics. Figure 5.4 is the profile of the 1550 nm laser. In order to maintain single transverse mode, the ridge width is smaller than 3 μm. An additional etching stop layer is incorporated in order to precisely control the etching depth during ridge formation. Normally, the emission wavelength of the etching stop layer is shorter than the lasing wavelength to avoid the absorption causing the increase of the internal loss. The vertical position of the etching stop layer directly influences the threshold current by the amount of lateral diffusion current under the etching stop layer [3]. The precision control of the ridge depth by introducing the

etching stop layer in the laser structure assures highly uniformity of the laser characteristics over the entire wafer.

Figure 5.5 shows the high temperature performance of 1550 nm and 1310 nm lasers. The characteristic temperature can be calculated to be 80K, which is better than the performance of lasers with InGaAsP quantum wells (about 50 ~ 70K).

The Effect of Strain

The $In_xGa_{1-x}As$ layer can be directly used for quantum wells for laser operated in 1500 nm band. However, only one variable in composition of this alloy needs to adjust the quantum well thickness simultaneously to achieve our target lasing wavelength. For a 5 nm quantum well lasing in 1500 nm band, the percentage of In has to be 0.37 with a compressive strain of 0.67%. The thickness of quantum well has to be reduced to further obtained higher compressively strain or vise versa. Thin quantum wells place great challenges to epitaxial systems. The incorporation of Al in InGaAs system increases the freedom of combinations. The $In_{1-x-y}Ga_xAl_yAs$ system, with two variables in composition, allows us to have fixed thickness of quantum wells and emission wavelength but various values of strain.

Figure 5.6 demonstrates the performance of lasers with different amount of compressive strains in MQWs. All the barriers are tensely strained to compensate the strain in QWs. The threshold current density is calculated when the laser operates without facet coating. The threshold current density is decreased about 40% when increasing the strain in QWs from 0.6 % to 1.4 %. Figure 5.7 shows the X-ray diffraction patterns of different strain-compensated MQWs. The positions of the satellite peaks tell the strain amount in laser structures. If we check a little more in Figure 5.6, the slight increase of the threshold current has been observed with the

compressive strain more than 1.5 % in MQWs. We attributes that the product of this strain and QW thickness approaches the critical thickness. The induced defect and imperfection increase the non-radiative recombination in QWs, thus, degrade the laser performance. This implies that the strain in MQWs can't be increased further even the compensating scheme is introduced. Therefore, the strain of 1.4 % in MQWs becomes the best choice in our study.

The Effect of QW number

We have also fabricated 1550 nm lasers with different QW numbers. In typical EELs, the larger number of quantum wells will increase the confinement factor in the transverse direction and enhance the laser performance in high temperature operations. The calculated confinement factors with four to eight quantum wells are shown in Figure 5.8. The confinement factor has increased 50 % when the number of QWs increases from four to eight.

Two types of quantum wells have been fabricated and examined. For structure I, the thickness of the QW and barrier are 5.5 nm and 9.3 nm, and the strain of the QW and barrier are 1.37% and –0.6%, respectively. For structure II, the thickness of the QW and barrier are 6 nm and 7 nm, and the strain of the QW and barrier are 1.4% and –0.8%, respectively. The corresponding threshold current density with both facets coated has been shown in Figure 5.8. For quantum well structure I, the threshold current density has decreased about 26% with number of quantum wells from four to eight. The enhanced trend toward larger number of quantum wells seems to poise at eight or nine quantum wells. The relatively low enhancement in comparisons to the confinement factor might arise from the non-uniformity of the carrier distributions in quantum wells with more pairs.

Quantum well structure II, which contains larger strain amount in quantum wells, exhibits better performance when the number of quantum wells is six. However, the threshold current density increases a little when the number of quantum wells goes to eight. We try to explain this in terms of the net amount of strain. The strain effect will accumulate as the layer thickness increases. Thus, it's better to evaluate the net strain with summations of the product of strain and thickness for all layers. The net amount for structure II quantum well is 50% larger than that for structure I quantum well. Defects and imperfections might be easily introduced when the number of structure II quantum wells increases. Therefore, more delicate strain scheme has to be taken care in MQWs with pairs more than six.

5-2 Fabrication of the high reflectivity Distributed Bragg Reflectors

5-2-1 Comparisons of InP/InGaAlAs and InAlAs/InGaAlAs Distributed Bragg Reflectors

Introduction

Long wavelength (1.3-1.5 μm) vertical cavity surface emitting lasers (VCSELs) are considered the best candidate for the future light sources in fiber communications. The advantages of VCSELs include single longitudinal mode output, small divergence circular emission beam profile, low power consumption and low cost reliable productions. The absence of high refractive index contrast in InP-lattice-matched materials impeded the progress of the development of 1.3-1.5 μm VCSELs in comparison to the short wavelength (0.78-0.98 μm) VCSELs. Recently, long wavelength VCSELs have been successfully demonstrated with several different approaches. First, wafer fusion technique, that integrated the InP-based active layers

and GaAs-based DBRs together, had been successfully realized for high performance long wavelength VCSELs [4,5] but the capability of mass production is still questionable. Second, the InGaNAs 1.3 μm VCSELs grown on GaAs substrates have been demonstrated with excellent characteristics [6,7]. However, to extend the InGaNAs gain peak to beyond 1.5 μm is rather difficult.

Monolithically grown DBRs lattice-matched to InP continued to attract interests due to the well existing highly efficient InGaAsP and InGaAlAs gain materials covered the wavelength window from 1.3 to 1.8 μm. Metamorphic GaAs/AlAs DBRs lattice-matched to InP substrate have been applied to realize the long wavelength VCSELs [8,9] but the inherent dislocations in metamorphic layers have impacts on the reliability of the devices. The Sb-based DBRs have large refractive index contrasts Δn ranging from 0.43 to 0.44 and have been successfully applied in the VCSEL structures [10,11]. However, these DBRs have drawbacks such as the low thermal conductivity and relatively high growth complexity. The problem with the conventional InP-lattice-matched InP/InGaAsP and InAlAs/InGaAlAs is the small refractive index contrast (Δn = 0.27 for InP/InGaAsP and Δn = 0.3 for InAlAs/InGaAlAs) resulting in a larger number of DBR pairs required to obtain high reflectivity. In addition, using the conventional DBRs, not only the penetration depth will increase causing more absorption, but the heat dissipation is also a problem.

Recently, the DBRs based on relatively large refractive index contrast (Δn = 0.34) material combination of InP/InGaAlAs have also been demonstrated [12-14]. This material combination not only has larger refractive index contrast than the conventional InP/InGaAsP and InAlAs/InGaAlAs material systems, but it also has other benefits including the smaller conduction band discontinuity, which is good for n-type DBRs, and the better thermal conductivity due the binary alloy of InP.

However, the InP and InGaAlAs belong to different group V based materials. Problems like the As carry over, the transitional interface, and lateral uniformity will affect the quality of the epitaxial layers and the reflectivity of the DBRs. As a result, the challenge of growing this combination relies on perfect switching between InP and InGaAlAs.

The growth interruptions have been frequently used in the metal organic chemical vapor deposition (MOCVD) growth of the InGaAs/InP or InGaAs/InGaAsP quantum wells in order to obtain abrupt interface [15,16], but the growth of the InP/InGaAlAs DBRs using growth interruptions has not been investigated. In this paper, we report the effect of the growth interruptions on fabrication of the InP/InGaAlAs DBRs. The lateral uniformity and the reflectivity of the DBRs are very sensitive to the stabilization time of each terminated interface. We incorporated an in situ laser reflectometry while growing DBRs with thickness more than 8 μm to insure minimum fluctuation in the center wavelength of the stopband. The optically pumped 1.56 μm VCSELs with 35 pairs InP/InGaAlAs DBRs achieved stimulated emission at room temperature with the threshold pumping power of 30 mW.

Experimental Procedure

All structures were grown in a vertical type low pressure MOCVD system with a rotating disk. The disk rotated at 900 revolutions per minute to maintain the laminar gas flow. The growth pressure was 70 torr. The growth temperature was 625℃. V/III ratio was 150 for InP and 200 for InGaAlAs. The growth rate was 36.5 nm/min and 35 nm/min for InP and InGaAlAs, respectively. The alkyl sources were Trimethylindium, Trimethylgallium, and Trimethylaluminum, and the group V gases were AsH_3 and PH_3. The carrier gas was hydrogen. Si_2H_6 was used as the precursor of

the n-type dopant. The epitaxial layers were all grown on n-type (100) InP substrates. The growth interruption between the InP and InGaAlAs had been divided into three steps. In the first step, the gases flowing just after the growth were hydrogen and the group V source used in the previous layer but with half of the flow rate for different period of t_p minute. Then, the group V source was switched off. The hydrogen was kept flowing for 0.02 minute in the second step to remove the remaining group V source in the reactor. After that, the other group V source with the same flow rate used in the next layer was switched on with the hydrogen flowing for 0.01 minute in the third step to prepare the growth environment. Five different periods (t_p = 0, 0.1, 0.2, 0.3 and 0.4 minute) of interruption were examined.

The optical microscope with the magnification of 120 examined the as-grown wafers first to check the lateral uniformity. The spectrometer was used to determine the reflectivity of the DBRs. The reflectivity of the Au film was used as the reference. The crystal quality and the lattice mismatch of the DBRs were analyzed by the double crystal X-ray. The thickness of each layer and the vertically compositional profiles were investigated by the field emission scanning electron microscope (SEM) and the secondary ion mass spectrometry (SIMS). The high-resolution transmission electron microscope (TEM) was used to investigate the abruptness of the interface. The current-voltage (I-V) measurement was used to determine the resistance of the n-type doped DBRs.

Results and Discussion

The DBRs with ten pairs InP/InGaAlAs designed for 1.55 μm VCSELs were first grown and investigated. The quarter-wavelength thickness of InP and InGaAlAs was 122 nm and 110 nm, respectively. To avoid the absorption of DBRs while the

operating wavelength was 1.55 μm, the lattice matched $In_{0.53}Ga_{0.39}Al_{0.08}As$ was used with a band gap emission wavelength of 1.42 μm. Figure 5.9 (a) summarizes the surface conditions of 10 pairs InP/InGaAlAs DBRs grown with different interruption time t_p under the examinations by the optical microscope with the magnification of 120. When there was no interruption time (t_p = 0 minute), pits with diameter ranging from 0.5 μm to 2 μm appeared densely on the surface of the as-grown wafer. When t_p increased to 0.4 minute, the pits decreased to fewer than 100 per square centimeter. A DBR structure grown with 0.1-minute interruption time was investigated by SEM and the picture of the cross section is shown in Figure 5.9 (b). The arrow indicates the location where the pits occurred. Figure 5.10 shows the reflectivity curves of these samples measured by the spectrometer. The maximum reflectivity of DBRs increased when the interruption time t_p becomes larger. However, the center wavelength and the width of the stopband remained unchanged. Figure 5.11 shows the X-ray diffraction pattern of a set of samples grown with different interruption time. The value of lattice mismatch of all samples was within 200 ppm. Meanwhile, more intense satellite peaks are observed when the interruption time is longer. As far as the DBRs of the VCSELs are concerned, it is very critical to increase the reflectivity. The decrease of the reflectivity of the DBRs and the intensity of the satellite peak of the X-ray diffraction pattern with the shorter interruption time may be resulted from the scattering loss caused by the pits on the lateral interface. Nevertheless, the small differences in the width of the stopband in the reflectivity curves among five samples showed that the layer compositions in the vertical direction did not vary a lot indicating the abruptness between the interfaces was intact. The SIMS results of InP/InGaAlAs DBRs grown with t_p = 0.2 minute shown in Figure 5.12 suggest that the phenomena of As carry-over did not appear. Consequently, the degradation of the

reflectivity of InP/InGaAlAs DBRs mainly relates to the growth interruption time. After an InP or an InGaAlAs layer has grown, the surface needs time to stabilize under the atmosphere of previous group V gas. Then, the next layer with alternate group V source can continue to grow. This is the different case from growing the InAlAs/InGaAlAs or AlAs/GaAs material system. When the interruption time is shorter than 0.1 minute, the atom of the group V source cannot completely occupy the surface. Meanwhile the other group V source switches on and enters the vacant site. This lattice mismatch causes the formation of defects. The defects elongate upward to form the pits while the growth continues.

Figure 5.13 (a) and (b) show the interface conditions of the InP/InGaAlAs DBRs examined by TEM for two different growth interruption time. The growth sequence is indicated as the arrow direction. Figure 5.13 (a) is for the optimized growth condition with interruption time of 0.3 minute. As can be seen the interfaces between the InP and InGaAlAs are clear and abrupt. Figure 5.13 (b) shows the interfaces when the interruption time was 0 minute. Some dark clusters can be seen at the interface between the InGaAlAs and InP. However, the interface between InP and InGaAlAs did not contain these dark clusters. We attribute the dark clusters to the As carry-over effect when grown under the non-optimized growth condition. The lattice-mismatched InAsP formed at the interface and became defects. These defects elongated upward to form the pits while the growth continues and reduce the reflectivity of the DBRs. On the contrary, there is no need to consider the interface switching problems to grow the InAlAs/InGaAlAs DBRs. The abrupt interface can be obtained without the interruption time between consecutive layers. These results suggest that to grow the InP/InGaAlAs DBRs with high reflectivity, one need to add interruption time t_p more than 0.2 minute and make compromises between the total

growth time, the amount of source usage and the required high reflectivity.

The DBRs with seven pairs n-type InP/InGaAlAs and InAlAs/InGaAlAs designed for 1.55 μm VCSELs were then grown and investigated. The as-grown wafers were dry etched roughly 1.8 μm down to the n-type InP substrate to form a round mesa with the diameter of 50 μm. The periphery of the mesa was then passivated by SiN_x. After the thinning of the n-type InP substrate, the AuGe/Ni/Au contacts were deposited on the both sides of the wafers. Figure 5.14 (a) shows the I-V curves of the InP/InGaAlAs and InAlAs/InGaAlAs DBRs with round mesas of 50 μm in diameter. The resistance per DBR pair is calculated to be 1.2×10^{-5} Ωcm^2 and 2.2×10^{-5} Ωcm^2 for InP/InGaAlAs and InAlAs/InGaAlAs DBRs, respectively. The lower value of the resistance of the InP/InGaAlAs is due to the smaller conduction band discontinuity ($\Delta E_c = 0.15$ for InP/InGaAlAs and $\Delta E_c = 0.47$ for InAlAs/InGaAlAs [17]) between two layers. Figure 5.14 (b) shows the simulated equilibrium band diagrams of the InP/InGaAlAs and InAlAs/InGaAlAs DBRs for the n-type concentration of 1×10^{18} cm^{-3}. The results suggest that the voltage drop is mainly located at the interface to overcome the potential barrier. Further reduction in the resistance value can be achieved by modulation doping of the interfaces of the DBR structure to lower the potential barriers.

Next, two DBR structures with 35 pairs of $InP/In_{0.53}Ga_{0.39}Al_{0.08}As$ and 35 pairs of $In_{0.52}Al_{0.48}As/In_{0.53}Ga_{0.39}Al_{0.08}As$ were grown for comparisons. The interruption time t_p for growing $InP/In_{0.53}Ga_{0.39}Al_{0.08}As$ DBRs was chosen to be 0.4 minute. Fig. 5.15 shows the reflectivity curves of these two samples measured by the spectrometer. The measured reflectivity of samples was normalized to the reflectivity of the Au film. The maximum reflectivity of the $InP/In_{0.53}Ga_{0.39}Al_{0.08}As$ DBRs can reach over 99% and the width of the stopband is more than 100 nm, which is larger than the width of

the $In_{0.52}Al_{0.48}As/In_{0.53}Ga_{0.39}Al_{0.08}As$ DBRs.

In summary, we have grown the InP/InGaAlAs and the InAlAs/InGaAlAs DBRs with excellent electrical and optical properties using MOCVD and the growth interruption technique. The DBRs show low resistance with an estimated resistance per DBR pair of 1.2×10^{-5} Ωcm^2 and 2.2×10^{-5} Ωcm^2 for InP/InGaAlAs and InAlAs/InGaAlAs DBRs, respectively. The maximum reflectivity of both DBRs exceeds 99% with a stopband width of 110 nm for InP/InGaAlAs DBR and 100 nm InAlAs/InGaAlAs DBR. Although the InP/InGaAlAs DBRs have better optical and electrical properties, the InAlAs/InGaAlAs DBRs has much lower growth complexity. Both DBR structures should be applicable for fabrication of long wavelength VCSELs in 1.5~1.6 μm range.

5-2-2 Distributed Bragg Reflectors for Long Wavelength VCSELs using InP/Air-gap

Recently, using InP/airgap structure as DBR for 1.55 μm VCSELs using InGaAs as sacrificial layer was reported [18, 19]. This structure has largest refractive index contrast of $\Delta n = 2.16$ [20] and small optical loss in comparison to the conventional InP/InGaAsP and InAlAs/InGaAlAs material systems. The InP/airgap structure only requires 3 pairs to achieve high reflectivity of ~99.9 %. However in the reported InP/airgap DBR structures, the wet etching solution of $FeCl_3$ was used to etch the sacrificial InGaAs layer. The $FeCl_3$ solution has relatively low selectivity between InGaAs and InP layers which could cause the decrease in the reflectivity and shifting the stop bandwidth center of the DBR. These reports also did not measure the actual reflectivity of InP/airgap DBRs. In this section, we report the fabrication and

realization of a high reflectivity and rigid 1.55 μm InP/airgap DBR using a new etching technique based on the superior etching selectivity and high etching rate of H_2SO_4 solution for the InP/airgap DBR fabrication.

Design and Fabrication

For a rigid InP/airgap DBR with high reflectivity, a thicker InP layer is preferable. Our three–pair InP/airgap DBR structure has a λ/4 thick InGaAs sacrificial layer and a 5λ/4 thick InP layer based on the simulation results. Figure 5.16 showed the calculated reflectivity of a three-pair InP/airgap DBR structure with three different InP layer thickness of λ/4, 3λ/4, and 5λ/4 for a fixed thickness of λ/4 for the InGaAs layer. The result showed the peak reflectivity of three DBR structures has nearly the same high reflectivity value of 99.9 % around 1.55 μm while the stopband width gradually decreased with increasing InP layer thickness. For the 5λ/4 thick InP layer of DBR, the sopband still had a wide width of about 350 nm.

The 3-pair InP/InGaAs DBR structure with 615 nm (5λ/4) thick of InP layer and 387 nm (λ/4) thick of InGaAs layer was grown in a vertical type low pressure MOCVD system with a rotating disk. The disk rotated at 900 revolutions per minute to maintain the laminant gas flow. The growth pressure was 70 torr. The growth runs were carried out at a temperature of 625℃. V/III ratio was 160 for InP and 75 for InGaAs. The growth rate was about 34 nm/min and 36 nm/min for InP and InGaAs, respectively. The alkyl sources were Trimethylindium (TMIn), Trimethylgallium (TMGa), and Trimethylaluminum (TMAl), and the group V gases were AsH_3 and PH_3. Hydrogen was used as the carrier gas. The epitaxial layers were all grown on n-type (100) InP substrates. For growth of the InP and sacrificial InGaAs layers of DBR, the

growth interruption time technique with an interruption time of 0.4 minutes based on our previous results [18] was used by switching gas flow between different group V sources. The double crystal X-ray measurement of the grown InP/InGaAs DBR structure showed clear satellite peaks indicating excellent crystal quality of the grown DBR structure.

The basic processing procedures of the fabrication of InP/airgap DBR are shown in Figure 5.17 (a) and (b). The MOCVD grown InP/InGaAs DBR structure was deposited with SiO_2 as dry etching mask by using plasma enhanced chemical vapor deposition (PECVD). Conventional photolithography was employed to define a 40 μm width of square mesas for supporting the InP/airgap structure with a 10 μm spacing openings. The openings were then dry etched by reactive ion beam etching (RIE). The etching conditions were set at 300 W total power under a 20 mTorr pressure with 10 sccm CH_4 /40 sccm H_2 /15 sccm Ar gas mixtures. The corresponding etching rates of InP and InGaAs were about 45 nm/min and 7 nm/min respectively. The time required for etching the whole DBR structure of about 4 μm depth was about 200 minutes. To prevent the accumulation of polymer during the RIE dry etching which has a deposition rate of about 3 nm/mins, a 10-minute clean-etching step is conducted using O_2 plasma between every 30 minutes of the CH_4 /H_2 /Ar RIE process. The procedure is important for maintaining the constant RIE dry etching rate [21,22] for making the mesa with vertical sidewall. A vertical sidewall mesa is critical for uniform etching of the sacrificial InGaAs layers later and the formation of uniform airgap width to prevent any change in the reflectivity of InP/airgap DBR. After the mesa dry etching, the SiO_2 mask was removed by wet etching using HF solution.

The etching of InGaAs layers to form the air gap was conducted by wet chemical selective etching using a H_2SO_4: H_2O_2: H_2O=1:1:2 solution. The solution has a good

etching selectivity for InP and InGaAs and three times higher etching rate than the $FeCl_3$ solution. We used a spinning roller in the solution to increase wet etching uniformity and take away the reactant between the InGaAs layers. The airgap created by the wet etching process had a width of about 12.5 μm. The InP/airgap DBR structure was rinsed in D.I water and dried on the hot plate to clean up the residual water left in the air gap. Figure 5.18 depicts the SEM picture of the fabricated InP/airgap DBR structure. The DBR structure has a rigid and stable structure with uniform air gaps.

Optical Characterization

The reflectivity of the fabricated DBR structures was measured by the spectrometer using the reflectivity of the Au film as the reference. Since the Au film had a reflectivity of 95 % at 1.55 μm wavelength, all of the reflectivity of DBR was normalized to the reflectivity of the Au film. Figure 5.19 shows the reflectivity spectrum of the InP/airgap DBR structure. The dash line was the calculated curve and the solid line was the measured result. The peak reflectivity of 99.9 % at the wavelength of 1540 nm with a stopband width of about 200 nm was obtained. The measured stop-band width was narrower than the calculated width, which could be due to the limited etched airgap regions.

5-3 Optically Pumped LW-VCSELs

The feasibility of the active layers and DBRs discussed in previous two chapters is examined by the performance of optically pumped LW-VCSELs. This chapter reports the structures and the characteristics of LW-VCSELs for optical pumping, including the InP-lattice-matched and wafer-fused structures.

The Structure of LW-VCSEL

To further validate the viability of the DBR structures for long wavelength VCSELs, we have grown a laser structure based on the InP/InGaAlAs DBRs using the growth interruption technique. Figure 5.20 shows the laser structure. The epitaxial layers were grown on an n-type InP substrate. The first step was to grow the $5/4\lambda$ thick InGaAlAs and InP calibration layers followed by the 35 pairs InGaAlAs/InP DBRs. The interruption time was 0.2 minute. The laser reflectometry monitored the epitaxial growth. The $5/4\lambda$ thick InGaAlAs and InP calibration layers were first grown to check the growth rate and growth conditions before the entire DBRs were grown. The 2λ thick periodic gain cavity was grown in the second step. At the same time, another InP dummy wafer was loaded in MOCVD for photoluminescence (PL) measurement. The laser structure has InGaAlAs cladding layers of 2λ thick with a band edge emission peak at 1.1 μm. Three sets of strain compensated multi-quantum wells (SCMQWs) were placed at the anti-nodes of the electric standing wave field within the 2λ thick cavity to increase the enhancement factor of MQW active regions. Each set of SCMQWs consisted of five InGaAlAs (strain = 1.37%, thickness = 5.5 nm) quantum wells and four InGaAlAs (strain = -0.6%, thickness = 9.3 nm) barriers and the PL wavelength was tuned at 1.51 μm, which is 40 nm blue-shifted from the target emission wavelength to insure the proper operation of the VCSELs at room temperature [24]. Two InP space layers of half λ thickness grown on the top and the bottom of the cavity were served to protect the InGaAlAs layer from being oxidized during the post processing. Finally, the wafer was coated with 10 pairs SiO_2/TiO_2 top dielectric mirrors to form a complete VCSEL structure.

The Results of Optical Pumping

Figure 5.21 shows the reflectivity and PL measurements during every process step. All of the reflectivity results were normalized to the reflectivity of Au film. Figure 5.21 (a) shows the reflectivity curve of 35 pairs InGaAlAs/InP DBRs. The center wavelength of the stop-band is located at 1555 nm. Figure 5.21 (b) shows the reflectivity of the half cavity VCSEL. The PL spectrum of the active regions grown on the InP dummy wafer in the same run is shown in Figure 5.21 (c). The PL peak is 1510 nm and the full width half maximum (FWHM) is 54 nm. The peak of shorter wavelength was the signal belonged to the previous grown layers on the InP dummy wafer. Figure 5.21 (d) shows the reflectivity of the complete VCSEL structure and the Fabry-Perot dip is located at 1558 nm. Figure 5.21 (e) demonstrates the PL spectrum of the complete VCSEL structure. The peak wavelength is coincided with the Fabry-Perot dip and the FWHM is measured to be 3.3 nm. The equivalent quality factor, Q, is estimated about 470 in the vertical direction.

The complete VCSEL structure was placed in an optical pumping system as shown in Figure 5.22. The pumping source was a continuous wave operated Ti:sapphire laser. The wavelength of the Ti:sapphire laser was tuned at 990 nm although the pumping wavelength at slightly beyond 1.1 μm would be more desirable to avoid absorption of the InP ($\lambda g = 0.9$ μm) space layers and InGaAlAs ($\lambda g = 1.1$ μm) cladding layers. The diameter of the pumping beam entered from the top dielectric DBRs was estimated to be 30 μm. Figure 5.23 shows the pumping result of the VCSEL. The threshold pumping power is 30 mW at room temperature. The wavelength of the output beam is 1562 nm. The minimum linewidth above threshold is 1 nm limited by the resolution of the spectrometer. The red shift of the peak wavelength from the Fabry-Perot dip was attributed to the local heating caused

by the strong absorption. The equivalent threshold current density is calculated to be 2 kA/cm^2 when taking into account the absorption of the pumping light in the cladding layers and the reflection at the surface. Compared this number with the best threshold current density obtained in chapter 4, which is about 1.45 kA/cm^2 shown in Figure 4-11, the relatively large threshold current density might be attributed to two reasons. One is the non-optimized quantum well structure in terms of the amount of net strain in periodic gain structure. The other is the relatively large cavity loss such as the absorption of the pumping power by the 2λ thick cladding layers in the laser structure. All in all, the quality of the DBRs and the active region have been basically qualified in this demonstration for the first step in LW-VCSEL process.

5-4 Electrically Pumped LW-VCSELs

5-4-1 Selectively etched undercut apertures in InP-based LW-VCSELs

Unlike GaAs-based VCSELs, there is no natural oxidizable material in InP-based monolithic VCSEL from which an oxide aperture can be formed. In wafer-fused devices, an AlAs aperture placed in the GaAs-based mirror is typically used. In the InP-lattice-matched materials, there are been some reported on oxide apertures with AlInAs, but the lateral oxidation rate is low. We have demostrated an undercut aperture is employed instead of the oxide aperture, and this is formed by selectively etching an InGaAlAs-based active region with H_2SO_4 solution. An advatage of the undercut aperture is that this constrains current exactly into the desired area of the active region, and there is no current spreading between the current aperture and active region as can be seen in oxide aperture. Surface-recombination appears to be low in the 1.55 μm multiple quantum-well (MQW) active regions.

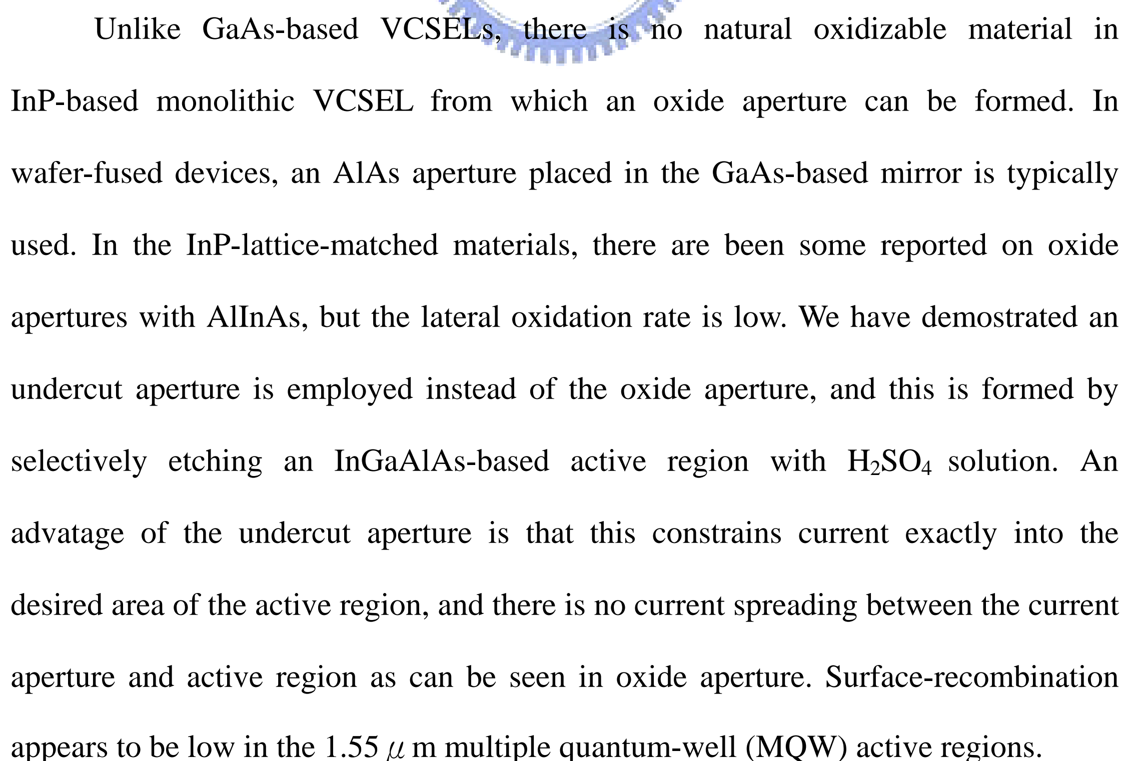

Based on the success of the optically pumped LW-VCSELs, a half

intracavity-contacted VCSEL with n-doped (Si) and p-doped (Zn) for electrically pumping was grown by MOCVD in a single step. A schematic of this structure is shown in Fig. 5.24. This structure is fabricated into devices of diameters 20 μm by CH_4 reactive ion beam etching (RIE). The mesas were selectively etched by H_2SO_4 solution. For these devices, a high etching selectivity existed between the active region and InP cladding layers. The undercut apertures could be controlled by different etching time. The top dielectric DBR was deposited with 5 pairs of an electron-beam-evaporated SiO_2/TiO_2 stack. The half intracavity-contacted VCSEL allow the VCSEL to utilize undoped top DBR, reducing free-carrier absorption in conventinal p-DBR. However, there was no lasing operation due to leakage currents in these selectively etched undercut devices.

5-4-2 Fabrication of LW-VCSELs by Ion-implantations

Implantation technique is a common approach for current confinement [25,26]. Ion-implantation has long been an easy and stable fabrication method in 850 nm VCSEL industry. In this section, we'd like to discuss the structure and experimental results of the InP-based LW-VCSEL with a Si-implantation current aperture.

The Structure of LW-VCSEL

Figure 5.25 (a) shows the laser structure. The epitaxial layers were grown on an n-type InP substrate. The first step was to grow 42 pairs InGaAlAs/InP DBRs. The interruption time was 0.2 minute. The quarter-wavelength thickness of InP and InGaAlAs was 122 nm and 110 nm, respectively. To avoid the absorption of DBRs while the operating wavelength was 1.55 μm, the lattice matched $In_{0.53}Ga_{0.39}Al_{0.08}As$ was used with a band gap emission wavelength of 1.42 μm. The laser reflectometry

in-situ monitored the epitaxial growth. Then, the 3/4λ thick n- and p-type InP spacers for phase matching were grown. The half-wavelength thick cavity was sandwiched between InP spacers. The cavity consisted of n- and p-type InAlAs inner cladding layers and strain compensated multiple quantum wells (SCMQWs). The SCMQWs consisted of seven InGaAlAs (strain = 1.4%, thickness = 6 nm) quantum wells and eight InGaAlAs (strain = -0.8%, thickness = 7 nm) barriers and the photoluminescence (PL) wavelength was 1551.5 nm with the FWHM of 108.3 nm. The wafer was then sent to ion-implantation with Si after aperture mask patterning. The diameter of the aperture was 28 μm. The Si ions can compensate the p-type dopant and even make the InP layer to become n-type outside the aperture to form current blocking regions. The energy of the implanting ions is 100 KeV. The peak concentration of the Si in InP spacer layer located at about 100 nm away from the wafer surface measured by the secondary ion mass spectrometry (SIMS). Next, the wafer was passivated with SiN_x and coated with metal contacts for both sides. The emission aperture was 10 μm in diameter. Finally, the wafer was coated with 10 pairs SiO_2/TiO_2 top dielectric mirrors to form a complete VCSEL structure. The schematic of LW-VCSEL structure with a Si-implanted current aperture is shown in Figure 5-25 (b).

Results and Discussion

The voltage and emission light output versus driving current characteristics are shown in Figure 5.26. The solid lines in Figure 5.27 are the reflectivity and PL curves measured with only the half-cavity, which is the as-grown structure shown in Figure 5.25 (a). The PL peak is 1547.4 nm with FWHM of 38.6 nm in comparisons to 108.3 nm for PL curve of the original MQW. The shrinkage of the FWHM demonstrated the

increased quality factor of the cavity provided by the high reflectivity bottom DBR. However, this device did not show stimulated emission under the continuous-wave (CW) operation. The emission output light saturated above 8 mA. The dashed line in Figure 7-3 is the electro luminance (EL) curve for the device. The FWHM of the EL spectrum is 36.9 nm with peak of 1518.0 nm for the full LW-VCSEL structure. The nearly unchanged FWHM and the quality factor of the full LW-VCSEL structure represented the ill function of the top mirror and large optical loss inhibiting the lasing operation. We have found that the top dielectric mirror degraded rapidly after the forward current applied. The degraded top dielectric mirror also changed the original phase matching condition in the half cavity structure, and thus the emission peak of EL spectrum for the full VCSEL structure has shifted. The relatively high operation voltage might arise from the poor p-type contact and caused more heat in the small aperture. To further modify this type of structure, we need to find more stable material conditions for dielectric DBRs to prevent the mirror degradation and improve the p-type contact by inserting a p-type InGaAs for contact layer to reduce the operation voltage.

5-4-3 Long Wavelength Light Emitting Diodes with Buried Tunnel Junctions

Introduction

The buried tunnel junctions have been applied in many opto-electronic devices, such as multi-junction solar cells [27], multi-layer GaAs lasers [28-31], vertical cavity surface emitting lasers [32] and GaN based blue light emitting diodes [33]. Introducing buried tunnel junctions in LW-VCSELs has two main advantages. First, the buried tunnel junction allows selective tunneling current injection and the areas

without the tunnel junction automatically serve as the current blocking function. In comparisons to the ion-implantation, the buried tunnel junction provides precise aperture location inside the LW-VCSEL structure. Second, the buried tunnel junction exhibits higher effective refractive index for the current aperture providing index-guiding effect as discussed in chapter 2. In this subsection, we'd like to discuss the initial attempt to fabricate the lone wavelength light emitting diodes (LEDs) with buried tunnel junctions before we fabricated the LW-VCSELs with tunnel junctions.

The Structure of Long Wavelength LEDs with Buried Tunnel Junctions

Figure 5.28 (a) shows the epitaxial structure. The epitaxial layers were grown on an n-type InP substrate. The half-wavelength thick cavity with the same structure as discussed in the previous subsection was sandwiched between InP spacers. The cavity consists of n- and p-type InAlAs inner cladding layers and SCMQWs. The PL wavelength was 1531.9 nm. After that, the half-wavelength thick p-type InP layer was grown followed by the p^{++}/n^{++} tunnel junction. The top layer was a thin n-type InP layer for protection. The tunnel junction layers consisted of an InGaAlAs (20 nm, λ_g = 1425 nm) heavily doped p^{++} layer and 2 period InGaAs/InP (4 nm/4 nm) modulation doped n^{++} layers as shown in Figure 5.28 (b). The tunnel junction is necessary to be in the nodes of the standing electromagnetic wave inside the VCSEL cavity to prevent large internal loss. The buried tunnel junction located on the top of the aperture serves as the window area assisting current flowing from p-type InP space layer to n-type InP contact layer. That is, both contacts of the device are n-type, except that the top contact is positively charged and the bottom contact is negatively charged. The schematic operation principal for the tunnel junction shown in Figure 5.28 (c) explains the electron flow under the reverse bias condition. The wafer was then sent back to MOCVD for regrowth after desired aperture mesa was etched. The

cross-section SEM image of the buried tunnel junction after the regrowth process with the smooth regrown surface is shown in Figure 5.29 (b). The diameter of the aperture was 30 μm. Next, the wafer was passivated with SiN_x and coated with metal contacts for both sides. The metal contact aperture was 50 μm in diameter. The schematic of lone wavelength light emitting diode structure with buried tunnel junction is shown in Figure 5.29 (a). The top view of the devices is shown in Figure 5.29 (c).

Results and Discussion

Figure 5.30 successfully demonstrates the light emission power and voltage versus current characteristics for the long wavelength light emitting diode with buried tunnel junction. However, this structure can be applied in LW-VCSELs before the operation voltage is lowered. The high operation voltage might arise from the low tunneling efficiency of the tunnel junction. Since the p-type dopant, Zn, is highly diffusive, the diffusion of Zn into heavily n-type doped area will compensate that area to form a graded junction. However, the abrupt junction interface is essential for tunneling current with low reverse bias voltage. Therefore, other p-type dopant with low diffusion characteristics, such as C, is more appropriate for heavily doping layer in tunnel junction. The C doping is relatively difficult in In-contained materials with percentage of In more than 50% [34]. The special epitaxial technique has to be established in the future.

References

[1] C. E. Zah, R. Bhat, B. N. Pathak, F. Favire, W. Lin, M. C. Wang, N. C. Andreadakis, D. M. Hwang, M. A. Koza, T. P. Lee, Z. Wang, D. Barby, D. Flanders, and J. J. Hsieh, *IEEE J. Quantum Electron.*, **30**, no.2, p511, (1994).

[2] J. Piprek, P. Abraham, and J. E. Bowers, *Appl. Phys. Lett.*, **74**, no.4, (1999).

[3] J. Piprek, P. Abraham, and J. E. Bowers, *IEEE J. Quantum Electron.*, **36**, no.3, p366, (2000).

[4] D. I. Babic, J. Piprek, K. Streubel, R. P. Mirin, N. M. Margalit, D. E. Mars, J. E. Bowers and E. L. Hu, *IEEE J. Quantum Electron.*, **33**, no.8, p1369, (1997).

[5] Y. Ohiso, C. Amano, Y. Itoh, H. Takenouchi and T. Kurokawa, *IEEE J. Quantum Electron.*, **34**, no.10, p1904, (1998).

[6] S. Sato, N. Nishiyama, T. Miyamoto, T. Takahashi, N. Jikutani, M. Arai, A Matsutani, F. Koyama and K. Iga, *Electron. Lett.*, **36**, no.24, p2018, (2000).

[7] G. Steinle, F. Mederer, M. Kicherer, R. Michalzik, G. Kristen, A. Y. Egorov, H. Riechert, H. D. Wolf and K.J. Ebeling, *Electron. Lett.*, **37**, no.10, p632, (2001).

[8] J. Boucart, C. Starck, F. Gaborit, A. Plais, N. Bouche, E. Derouin, J. C. Remy, J. Bonnet-Gamard, L. Goldstein, C. Fortin, D. Carpentier, P. Salet, F. Brillouet and J. Jacquet, *IEEE J. Sel. Topics Quantum Electron.*, **5**, no.3, p520, (1999).

[9] W. Yuen, G.S. Li, R.F. Nabiev, J. Boucart, P. Kner, R.J. Stone, D. Zhang, M. Beaudoin, T. Zheng, C. He, K. Yu, M. Jansen, D.P. Worland and C.J. Chang-Hasnain, *Electron. Lett.*, **36**, no.13, p1121, (2000).

[10] E. Hall, H. Kroemer and L.A. Coldren, *Electron. Lett.*, v35, no.5, p425, 1999.

[11] E. Hall, S. Nakagawa, G. Almuneau, J.K. Kim and L.A. Coldren, *Electron. Lett.*, **36**, no.17, p1465, (2000).

[12] I. Sagnes, G. Le Roux, C. Meriadec, A. Mereuta, G. Saint-Girons and M.

Bensoussan, *Electron. Lett.*, **37**, no.37, p500, (2001).

[13] M. Linnik and A. Christou, *IEEE Trans. Electron Devices*, **48**, no.10, p2228, (2001).

[14] M.H.M. Reddy, T. Asano, R. Koda, D.A. Buell and L.A. Coldren, *Electron. Lett.*, **38**, no.20, p1181, (2002).

[15] K. Streubel, J. Wallin, M. Amiotti, and G. Landgren, *J. Cryst. Growth.*, **124**, p541, (1992).

[16] K. Streubel, V. Harle, F. Scholz, and G. Landgren, *J. Appl. Phys.*, **71**, p3300, (1992).

[17] M.H.M. Reddy, T. Asano, R. Koda, D.A. Buell and L.A. Coldren, *Electron. Lett.*, **38**. no.20, p1181, (2002).

[18] E. Hall, S. Nakagawa, G. Almuneau,J. K. Kim, and L. A. Coldren, *Electron. Lett.*, **36**, no.17, p1465, (2000).

[19] N. Chitica, and M. Strassner, *Appl. Phys. Lett.*.,**78**, no.25, p3935, (2001).

[20] Seng-Ticng Ho, S. L. McCall, R. E. Slusher, L. N. Pfeiffer, K. W. West, A. F. Levi, G. E. Blonder, and J. L. Jeweil, Appl. Phys. Lett., **57**, no.14, p1387, (1990).

[21] T.C. Lu, J.Y. Tsai, and S.C. Wang, *J. Cryst. Growth*, **250**, p3-4, p305, (2003).

[22] K. Streubel, S. Rapp, J. André, and N. Chitica, *J. Mater. Sci. and Eng. B*; **44**, no.1-3, p364, (1997).

[23] A. Boyde, and P. Vesely, *1972 Proceedings of the Annual Scanning Election Microscopy Symposia, Chicago*, p266, (1972).

[24] J. Piprek, Y. A. Akulova, D. I. Babic, L. A. Coldren and J. E. Bowers, *Appl. Phys. Lett.*, **72**, no.15, p1814, (1998).

[25] C. Kazmierski, J. P. Debray, R. Madani, J. Sagnes, A. Ougazzaden, N. Bouadma,

J. Etrillard, F. Alexandre, and M. Quillec, “55 ℃ pulse lasing at 1.56 μm of all-monolithic InGaAlAs-InP vertical cavity lasers”, IEEE Electronics Letters Vol **35**, 811 (1999).

[26] J. Boucart, C. Starck, F. Gaborit, A. Plais, N. Bouche, E. Derouin, L. Goldstein, C. Fortin, D. Carpentier, P. Salet, F. Brillouet, and J. Jacquet, “1-mW CW-RT monolithic VCSEL at 1.55 μm”, IEEE photonics Technology Letters Vol **11**, 629 (1999).

[27] G. C. DeSalvo, *J. Appl. Phys.*, **74**, p4207, (1993).

[28] J. P. van der Ziel and W. T. Tsang, *Appl. Phys. Lett.*, **41**, p499, (1982).

[29] A. R. Sugg, E. I. Chen, T. A. Richard, S. A. Maranowki and N. Holonyak, Jr., *Appl. Phys. Lett.*, **62**, p2510, (1993).

[30] J. J. Wierer, P. W. Evans, and N. Holonyak, Jr., *Appl. Phys. Lett.*, **71**, p2286, (1997).

[31] J. C. Garcia, E. Rosencher, P. Collot, N. Laurent, J. L. Guyaux, J. Nagle and E. Chirlias, *J. Crystal Growth*, **201/202**, p891, (1999).

[32] J. J. Wierer, P. W. Evans, N. Holonyak, Jr. and D. A. Kellogg, *Appl. Phys. Lett.*, **71**, p3468, (1997).

[33] T. Takeuchi, G. Hasnain, S. Corzine, M. Hueschen, R. P. Schneider, Jr., C. Kocot, M. Blomqvist, Y.-l Chang, D. Lefforge, M. R. Krames, L. W. Cook and S. A. Stockman, *Jpn. J. Appl. Phys.*, **40**, pL861, (2001).

[34] N. Watanabe, S. Yamahata, and T. Kobayashi, *J. Cryst. Growth*, **200**, p599, (1999).

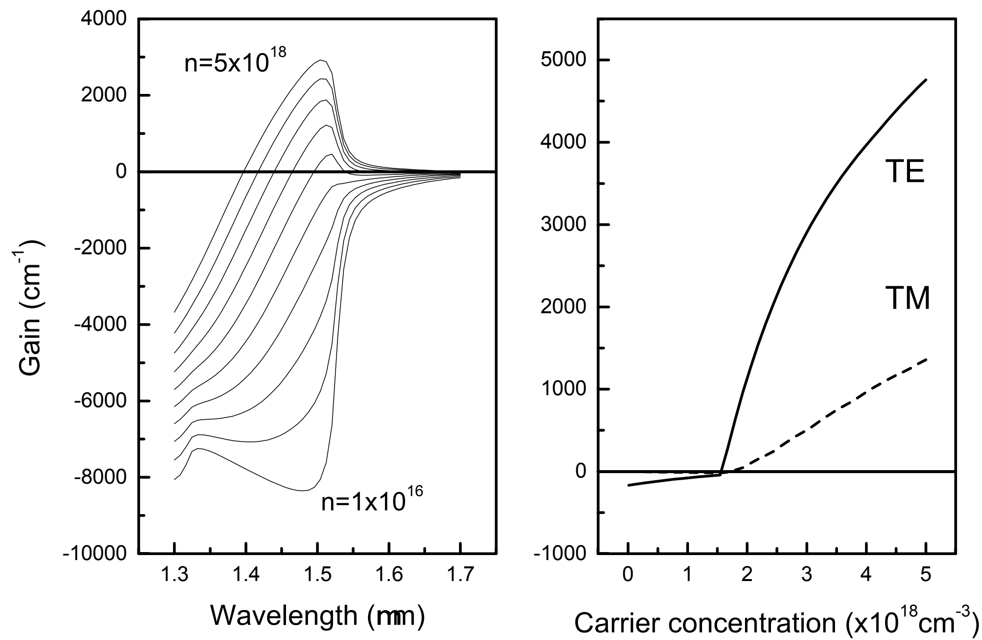

(a)

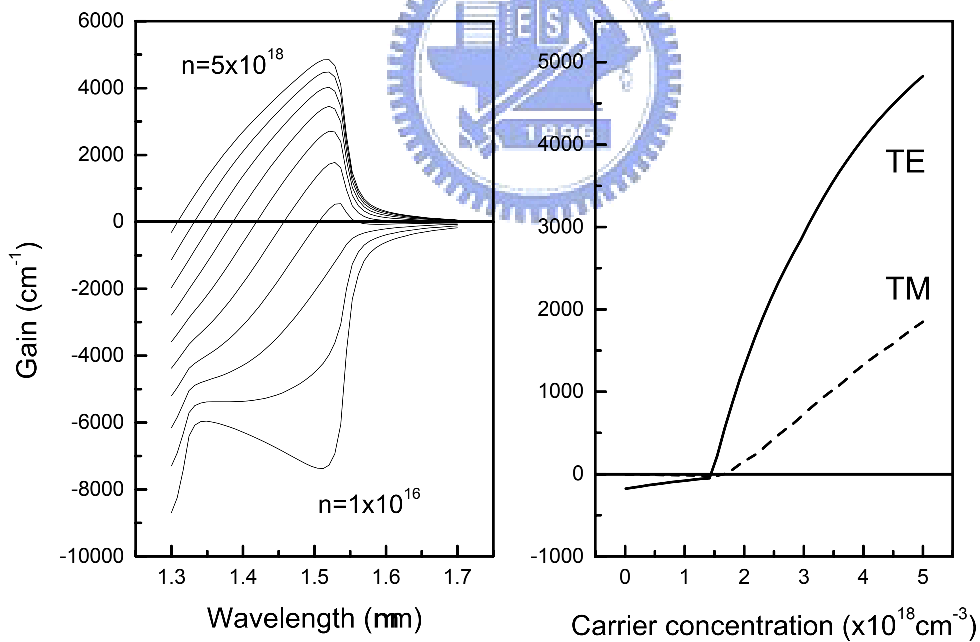

(b)

Figure 5-1 The simulated gain-wavelength and gain-carrier relationships for (a) InGaAlAs and (b) InGaAsP strained compensating quantum wells. The strain and thickness of the quantum wells are 1.5% and 5 nm, respectively and the strain and thickness of the barriers are –0.75% and 10 nm, respectively.

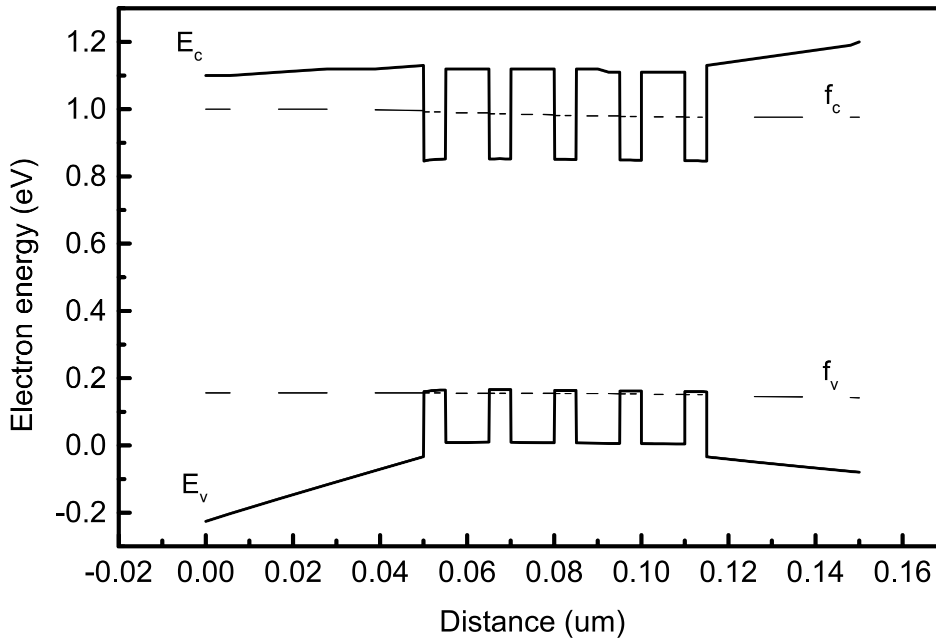

(a)

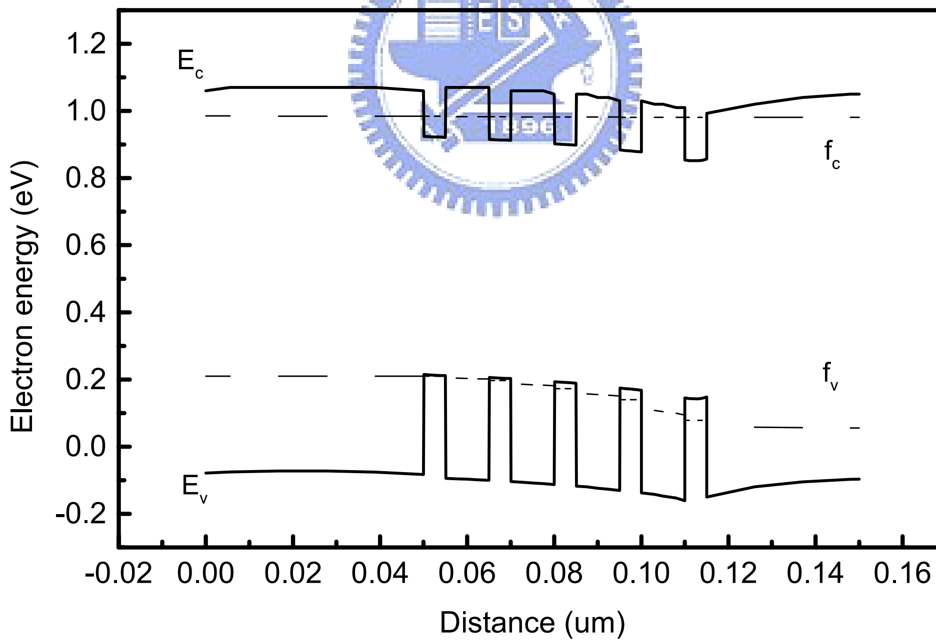

(b)

Figure 5-2 The simulated band diagrams under forward bias for (a) InGaAlAs and (b) InGaAsP multiple quantum wells. f_c and f_v are quasi-Fermi levels for conduction and valence bands under forward bias. Due to the larger conduction band offset for InGaAlAs system, the InGaAlAs lasers demonstrate superior high temperature characteristics over InGaAsP lasers.

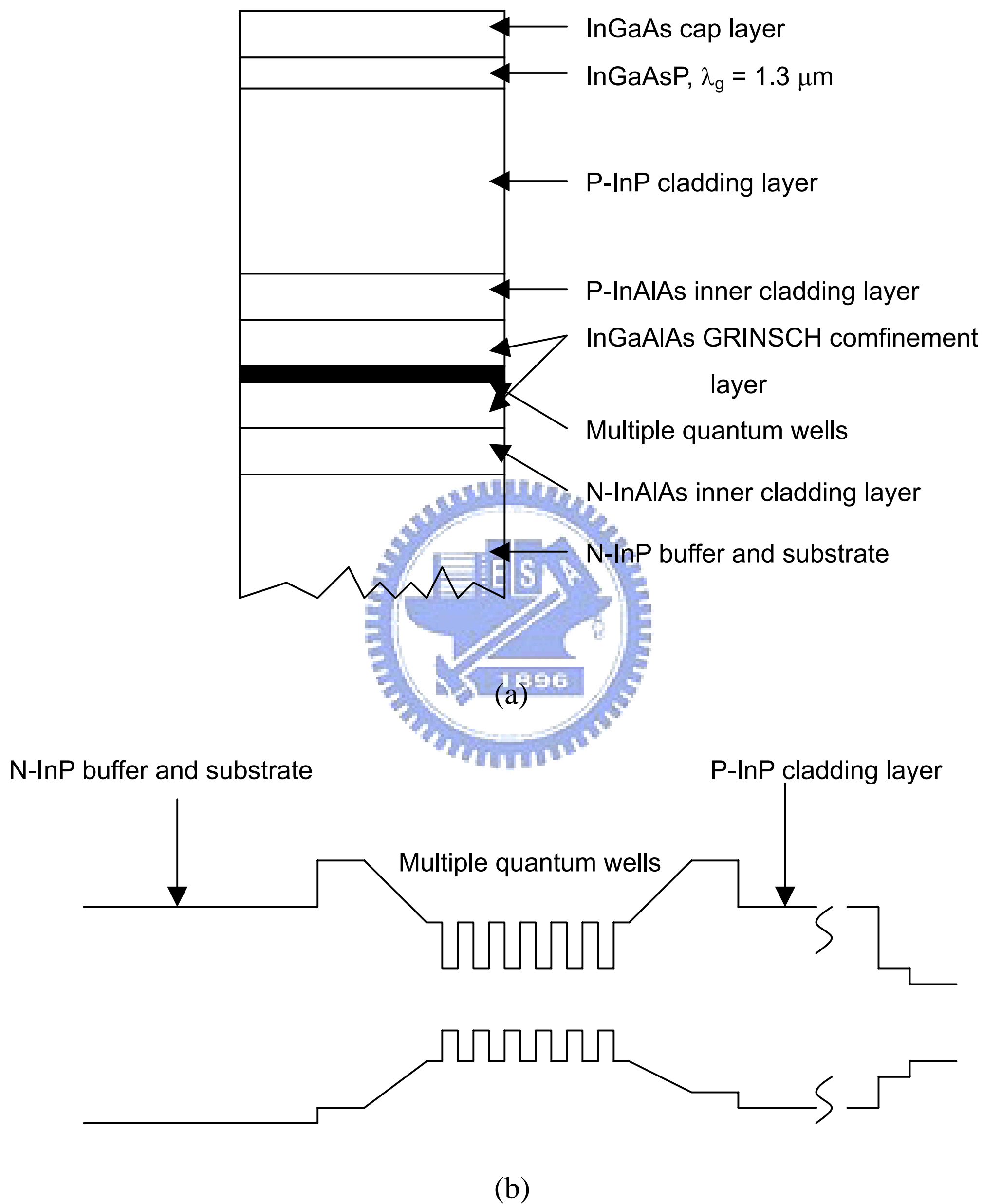

Figure 5-3 (a) The epitaxial structure for 1550 nm FP lasers. (b) The schematic of band diagram corresponding to the laser structure shown in (a).

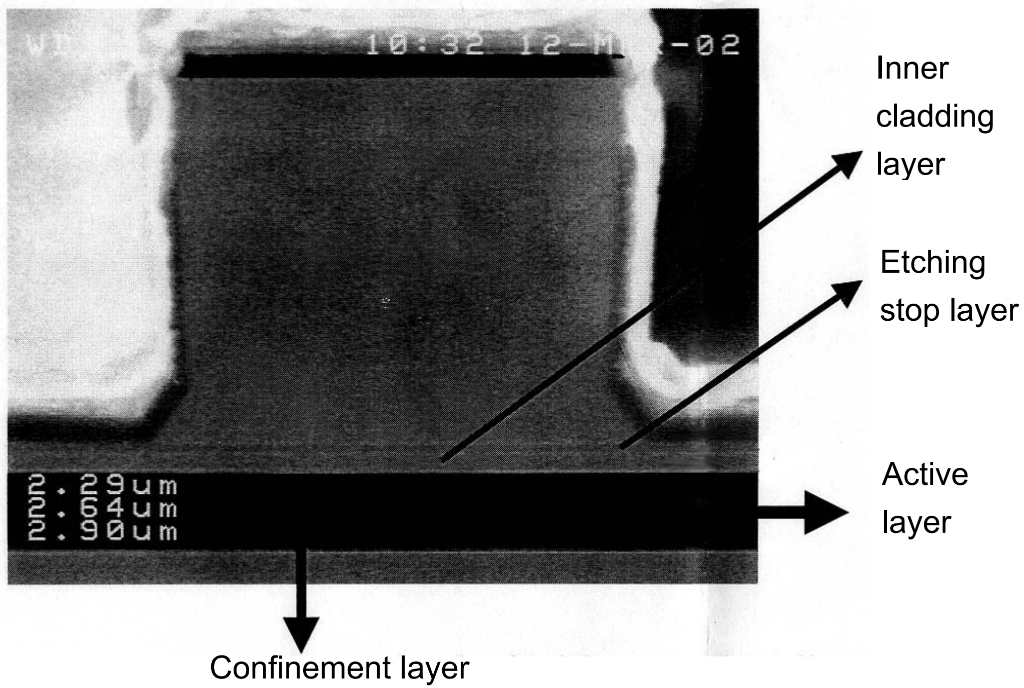

Figure 5-4 The SEM cross-sectional image of the 1550 nm laser ridge. The ridge width is 2 μm. An etching stop layer is added in order to precisely control the etching depth during ridge formation.

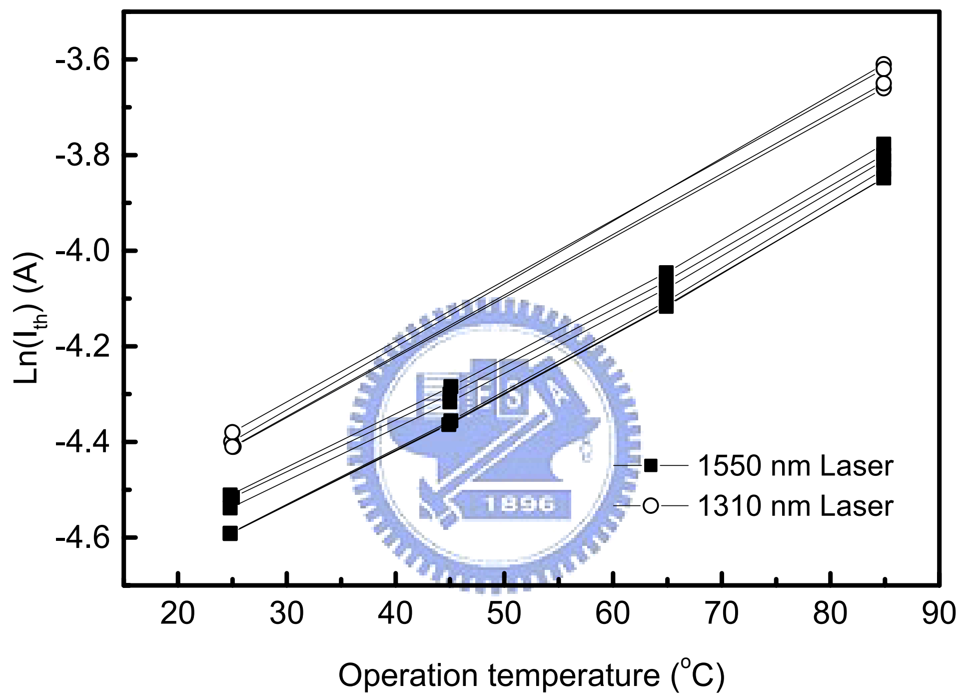

Figure 5-5 The temperature dependence of the threshold current for both 1310 nm and 1550 nm FP lasers. The characteristic temperature is estimated to be 80 K.

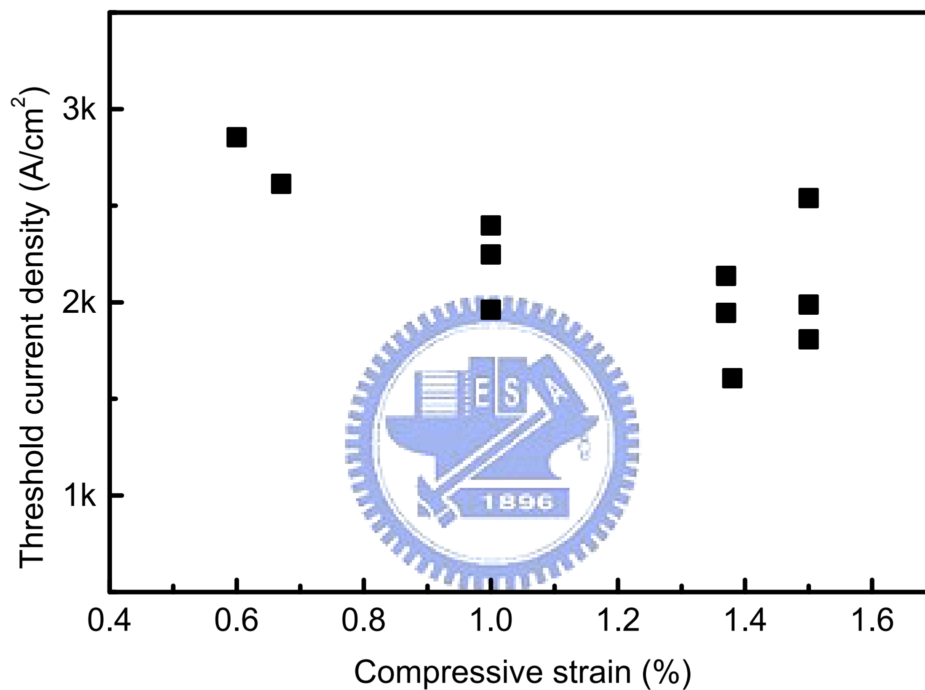

Figure 5-6 The dependence of the laser threshold current density on the amount of compressive strain in quantum wells. The barriers are all tensely strained to compensate the strain in QW. The number of quantum wells is six. The threshold current is calculated when the laser operates without facet coating.

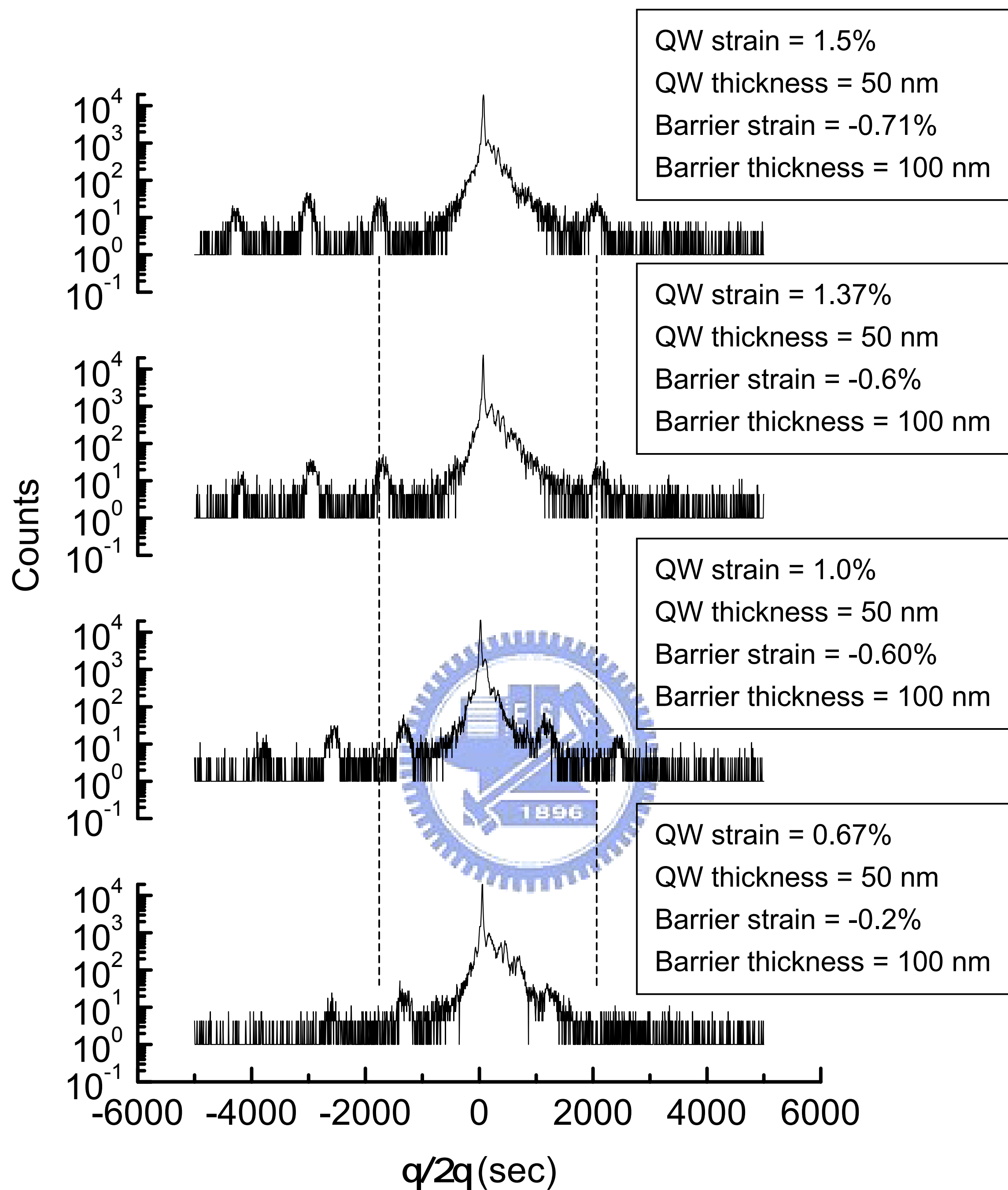

Figure 5-7 The X-ray diffraction patterns of different strain-compensated MQWs.

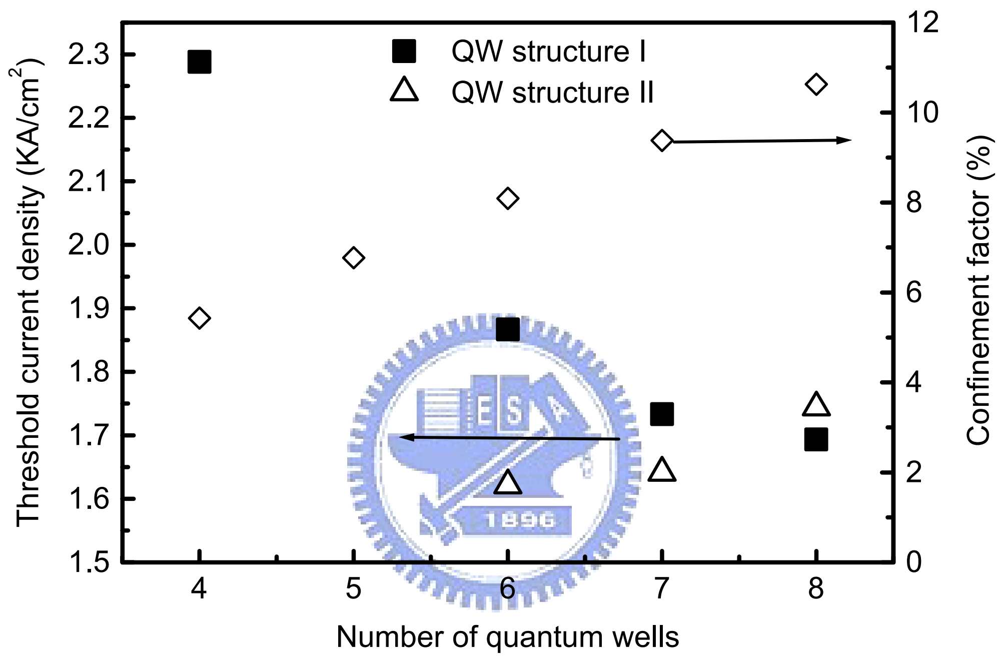

Figure 5-8 The effect of quantum well numbers on the laser threshold current and confinement factor. Two types of quantum wells are compared. The strain for structure I and structure II is 1.37% and 1.4%, respectively.

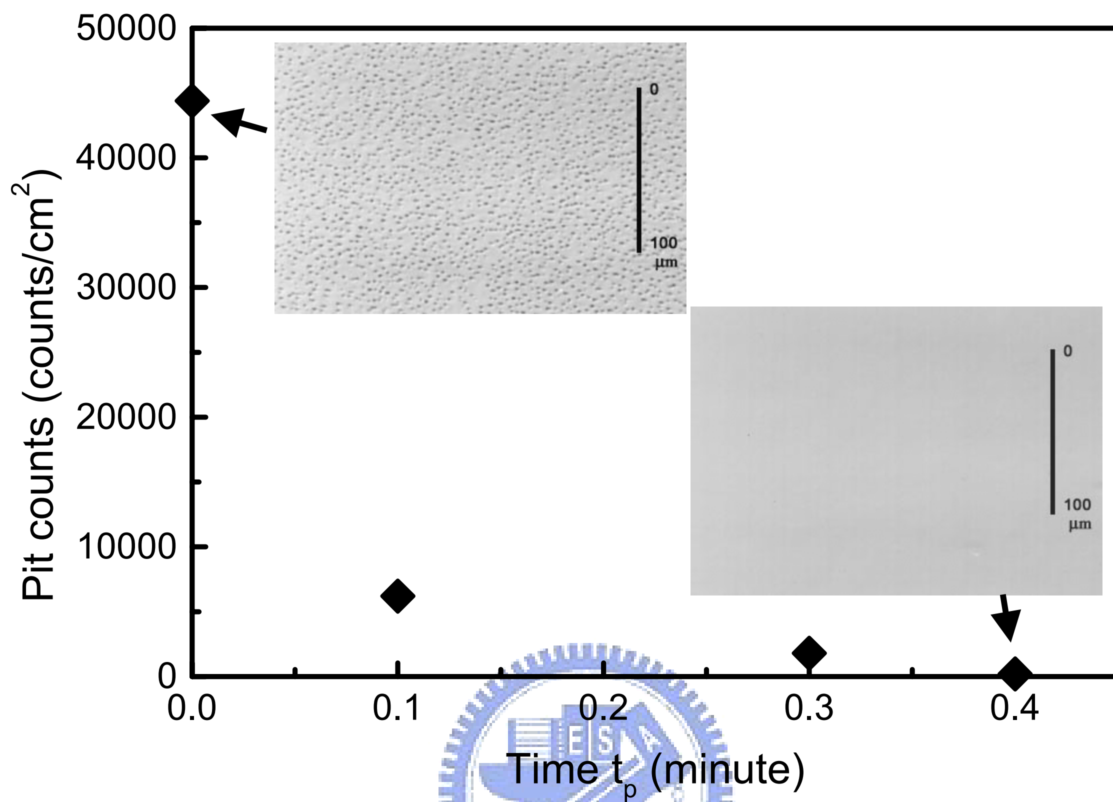

(a)

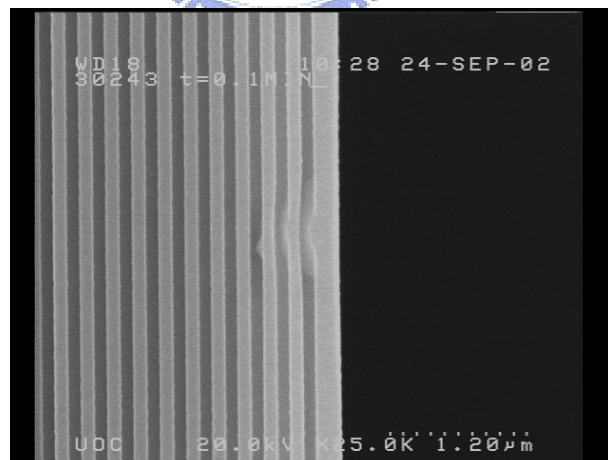

(b)

Figure 5-9 (a) The pit density of 10 pairs InP/InGaAlAs DBRs grown with different interruption time t_p. (b) The cross section the InP/InGaAlAs DBRs grown with 0.1-minute interruption time investigated by SEM.

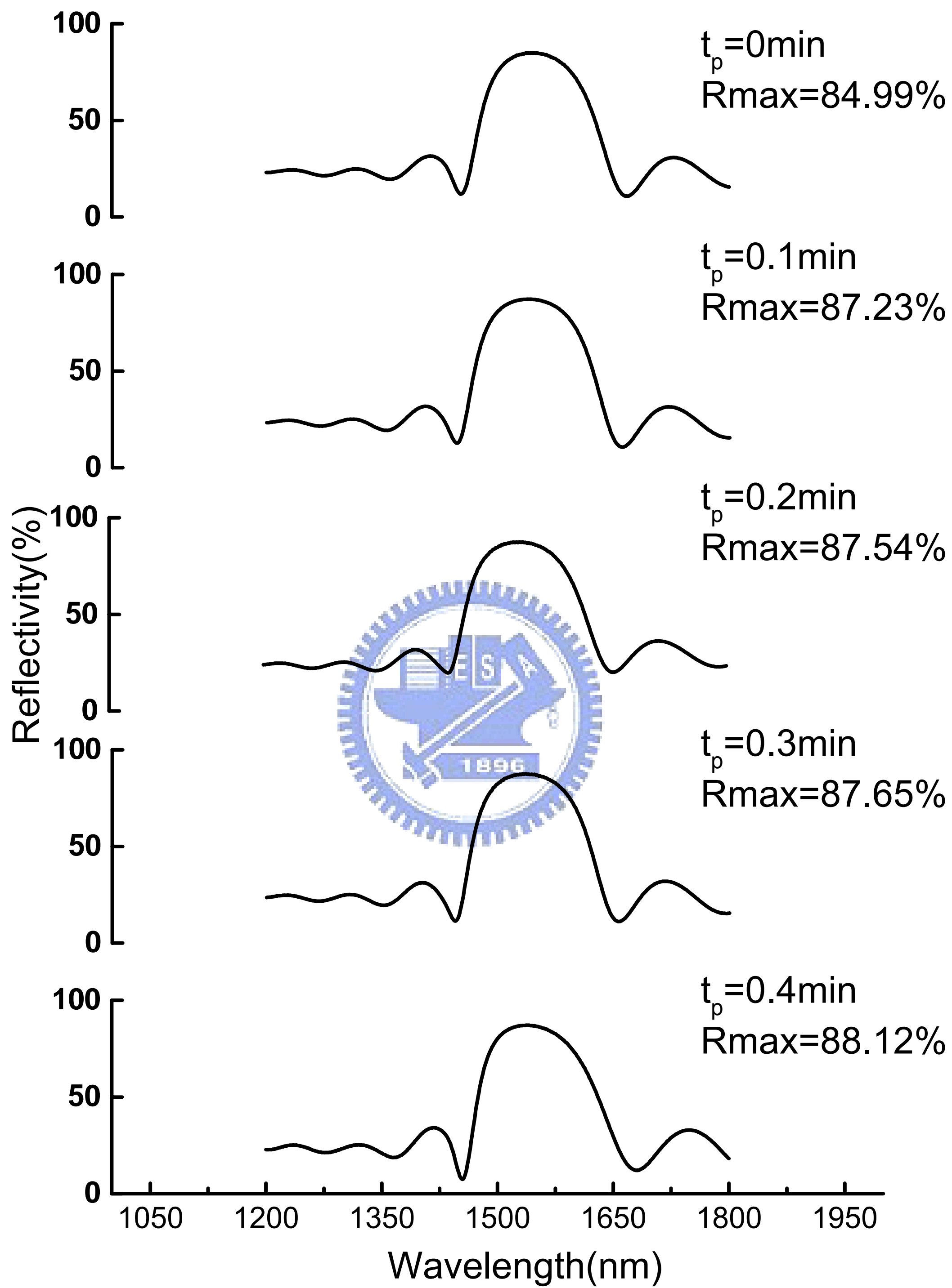

Figure 5-10 The reflectivity curves of 10 pairs InP/InGaAlAs DBRs grown with different interruption time t_p.

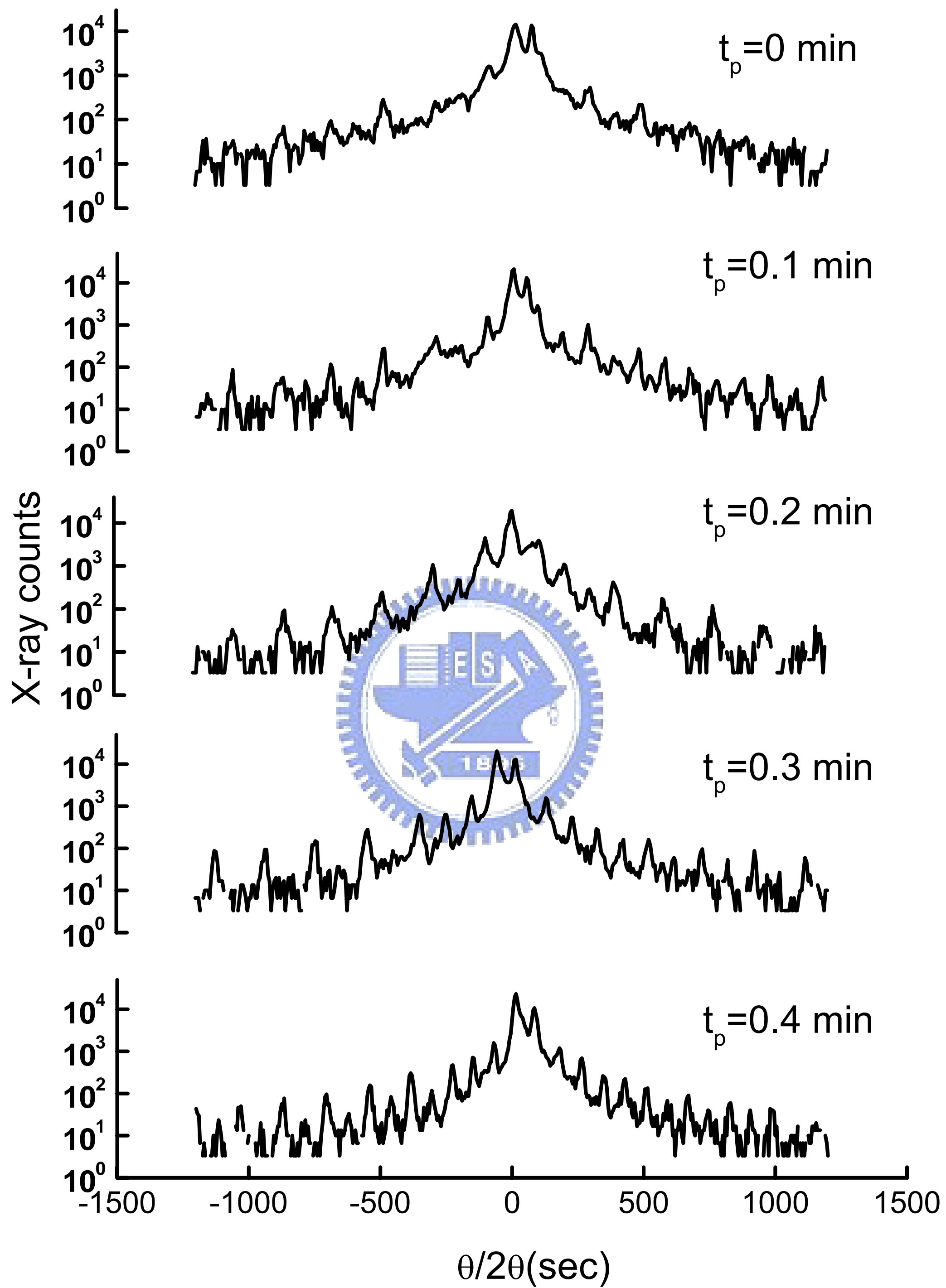

Figure 5-11 The X-ray diffraction patterns of 10 pairs InP/InGaAlAs DBRs grown with different interruption time t_p.

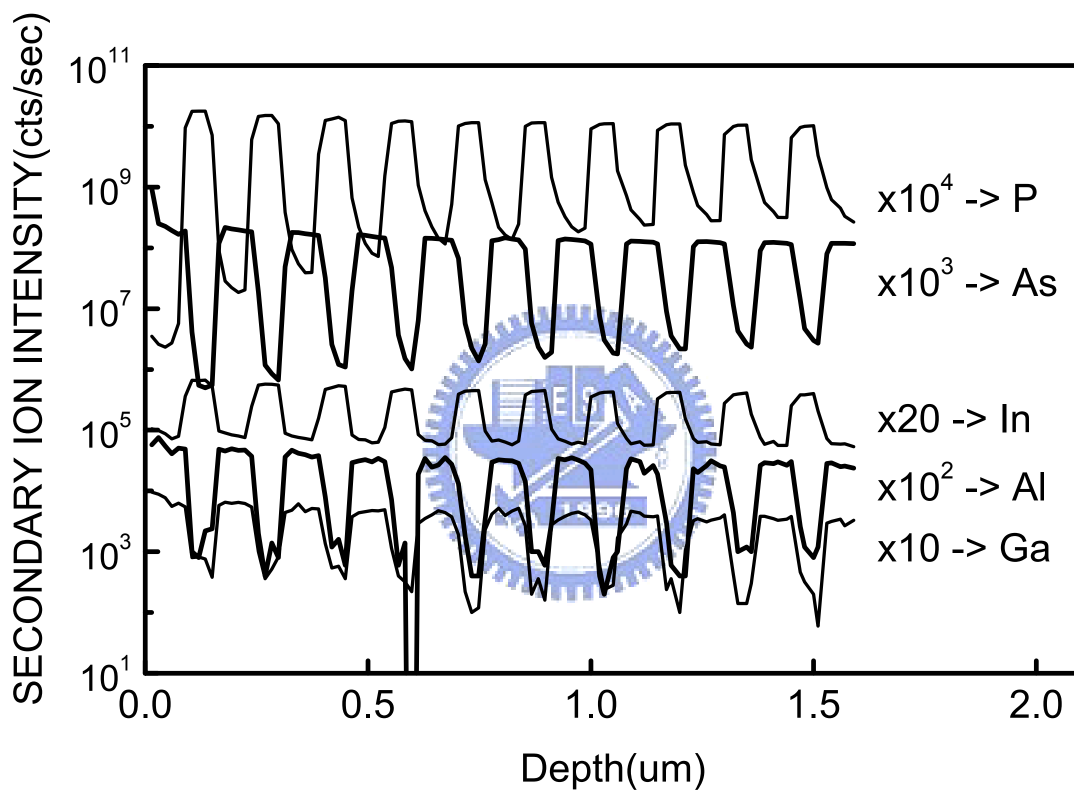

Figure 5-12 The SIMS results of InP/InGaAlAs DBRs grown with $t_p = 0.2$ minute.

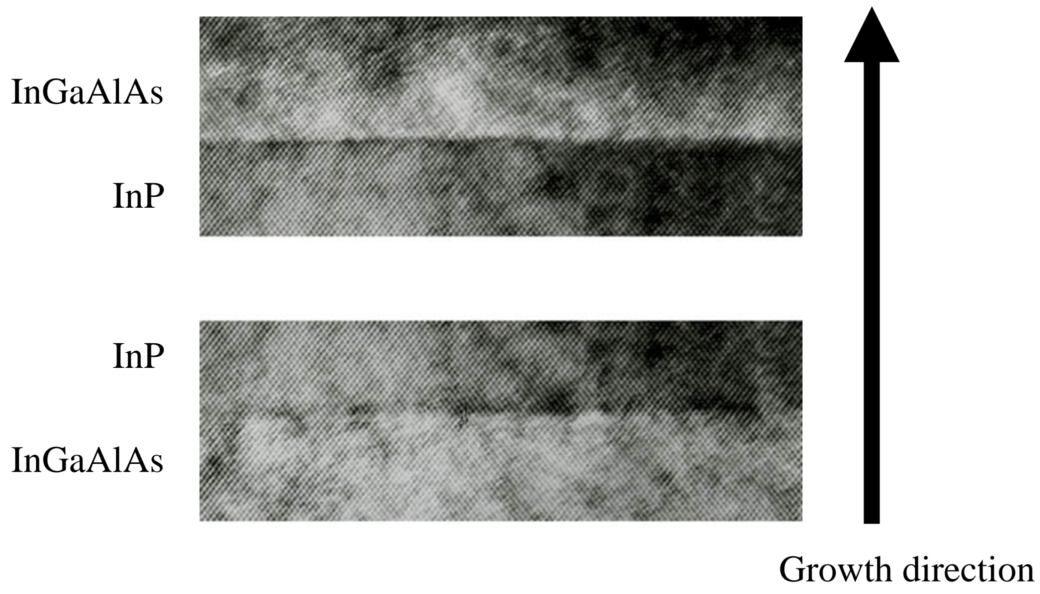

(a)

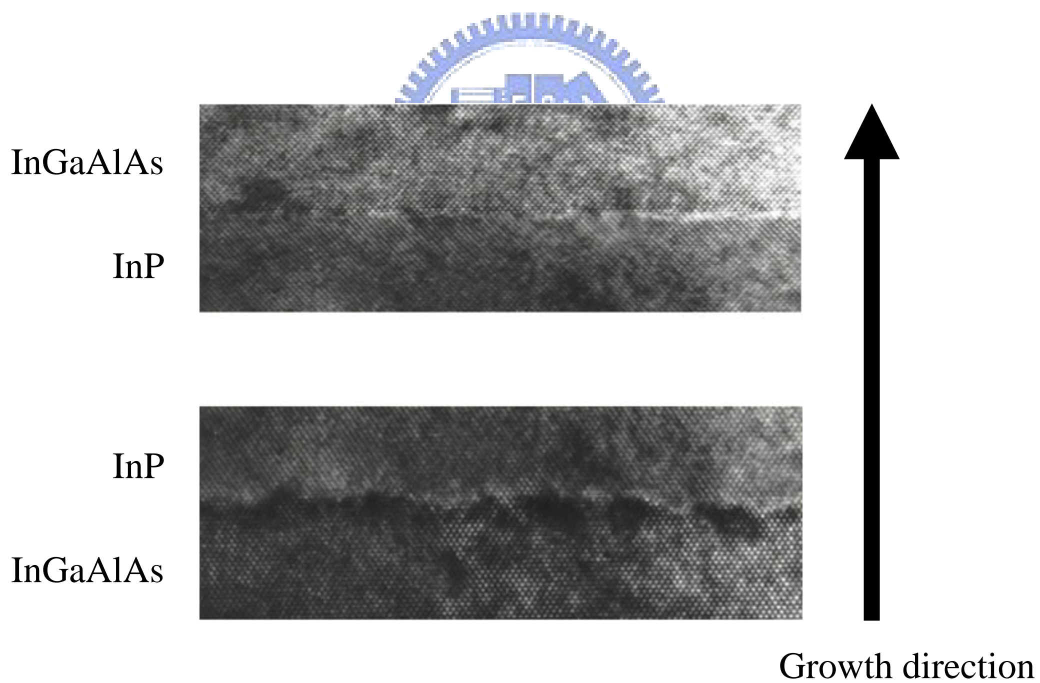

(b)

Figure 5-13 The interface conditions of InP/InGaAlAs DBRs examined by TEM with different growth interruption time; (a) interruption time t_p = 0.3 minute, (b) interruption time t_p = 0 minute.

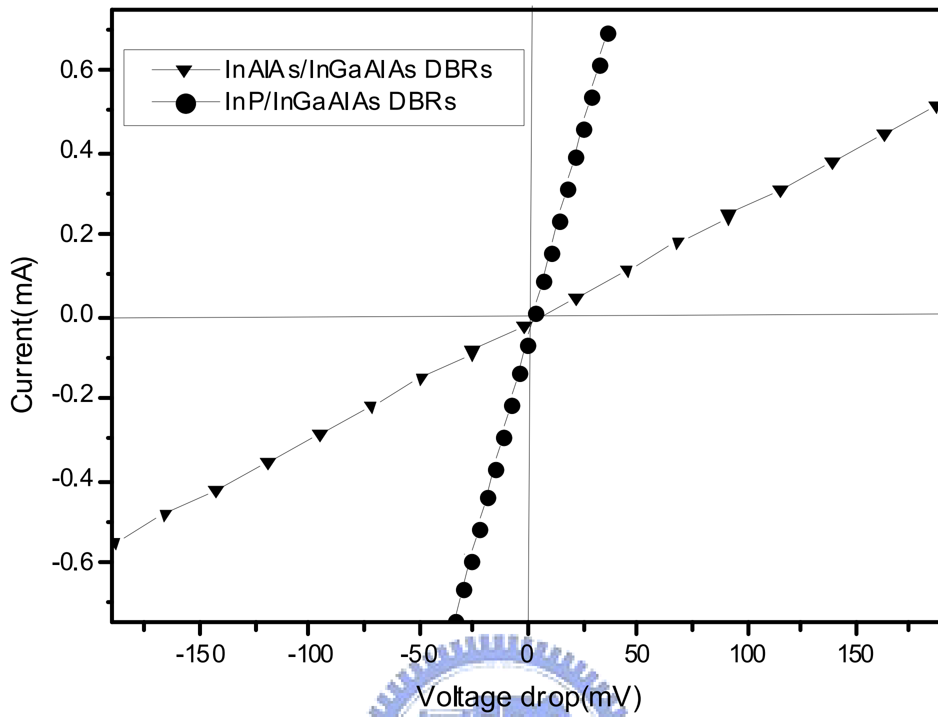

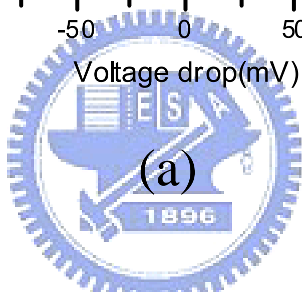

(a)

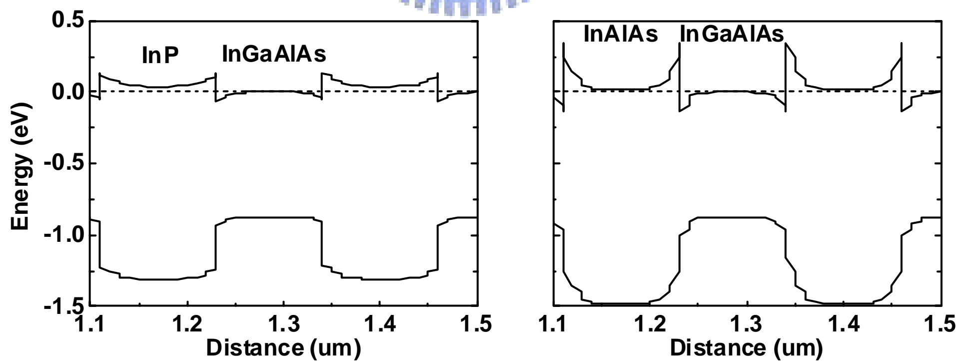

(b)

Figure 5-14 (a) The I-V curves of InP/InGaAlAs DBRs and InAlAs/InGaAlAs DBRs with round mesas of 50 μm in diameter. (b) simulation of the equilibrium band diagrams of the InP/InGaAlAs and InAlAs/InGaAlAs DBRs when the n-type concentration was chosen to be 1×10^{18} cm^{-3}. The dashed line is the Fermi level.

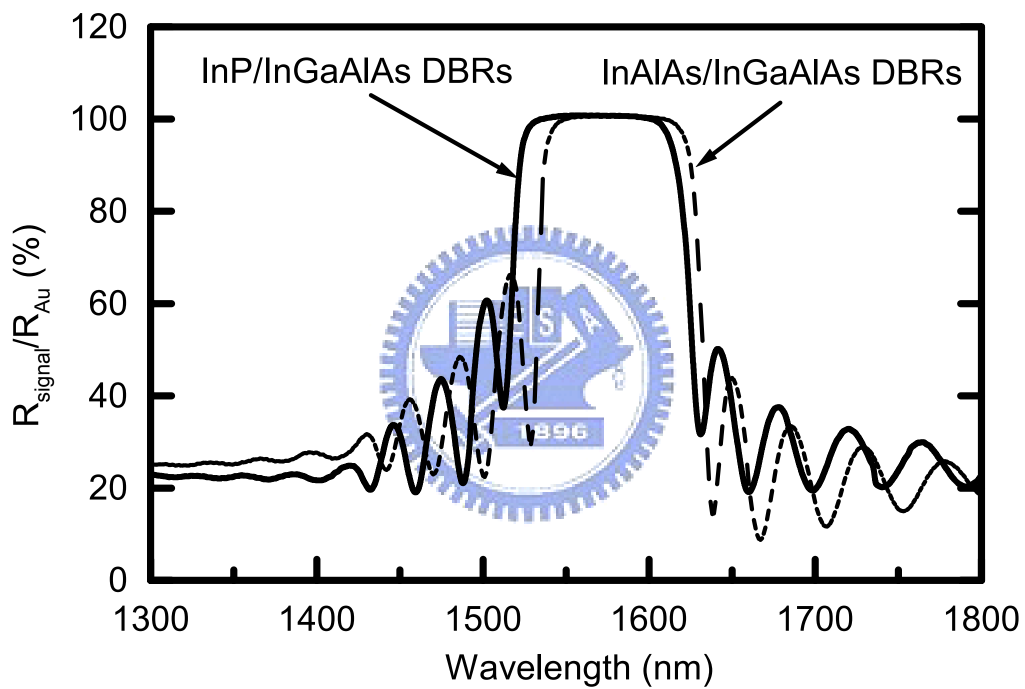

Figure 5-15 The reflectivity curves of 35 pairs InP/InGaAlAs and InAlAs/InGaAlAs DBRs measured by spectrometer.

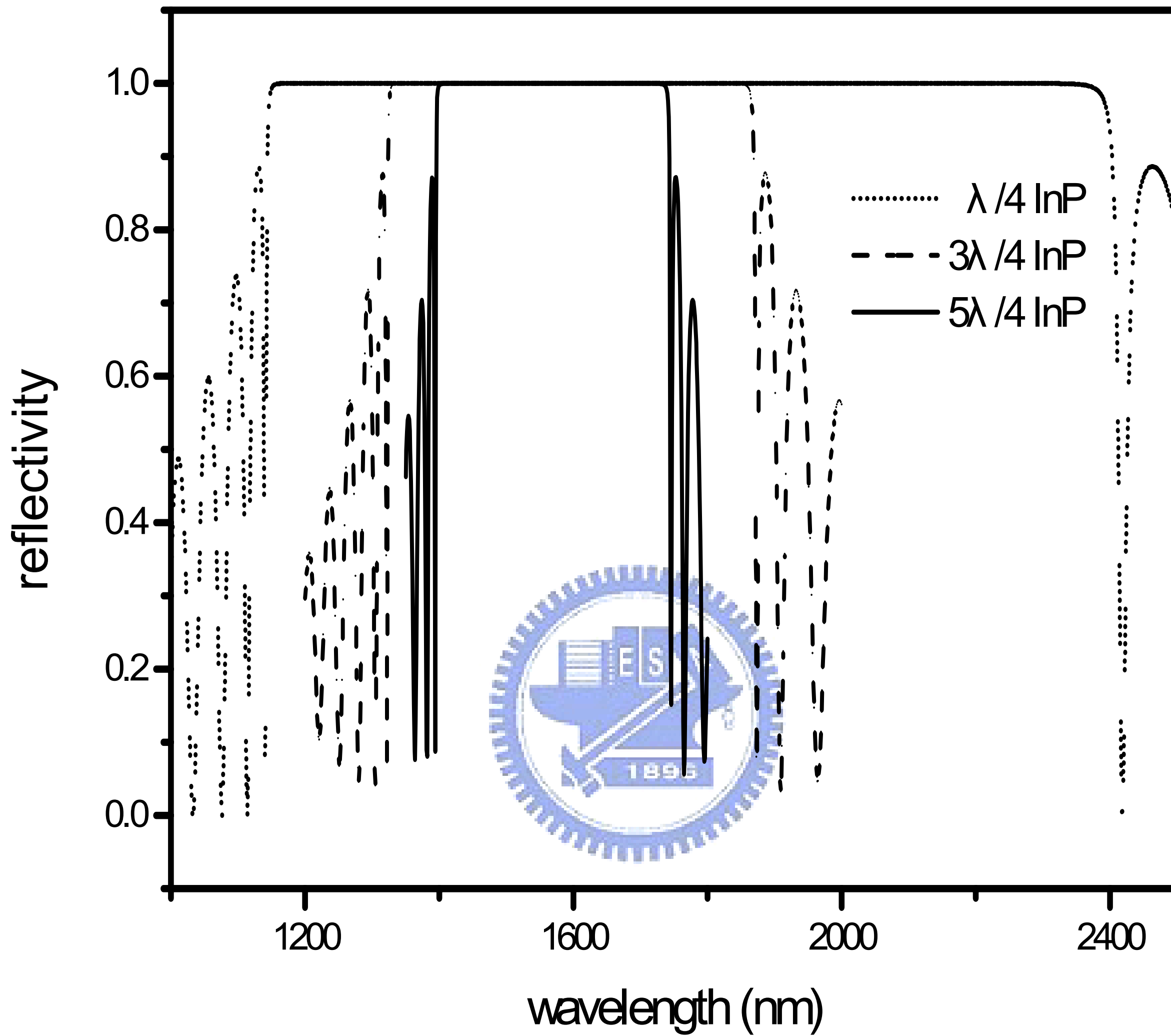

Figure 5-16 The reflectivity of three-pair of InP/airgap DBR structure with a fixed λ/4 InGaAs layer and different InP layer.

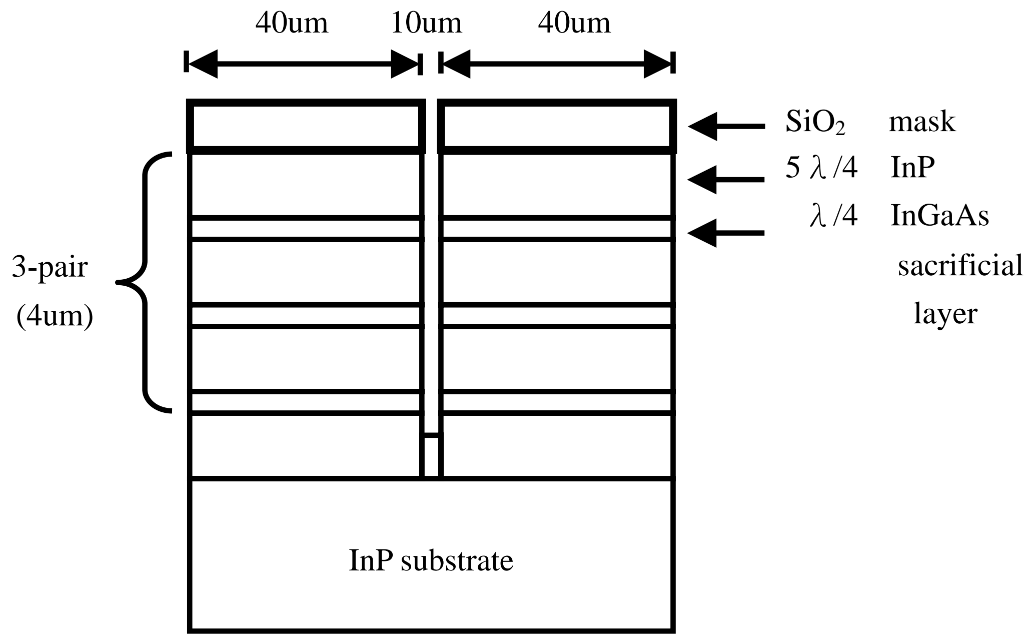

(a)

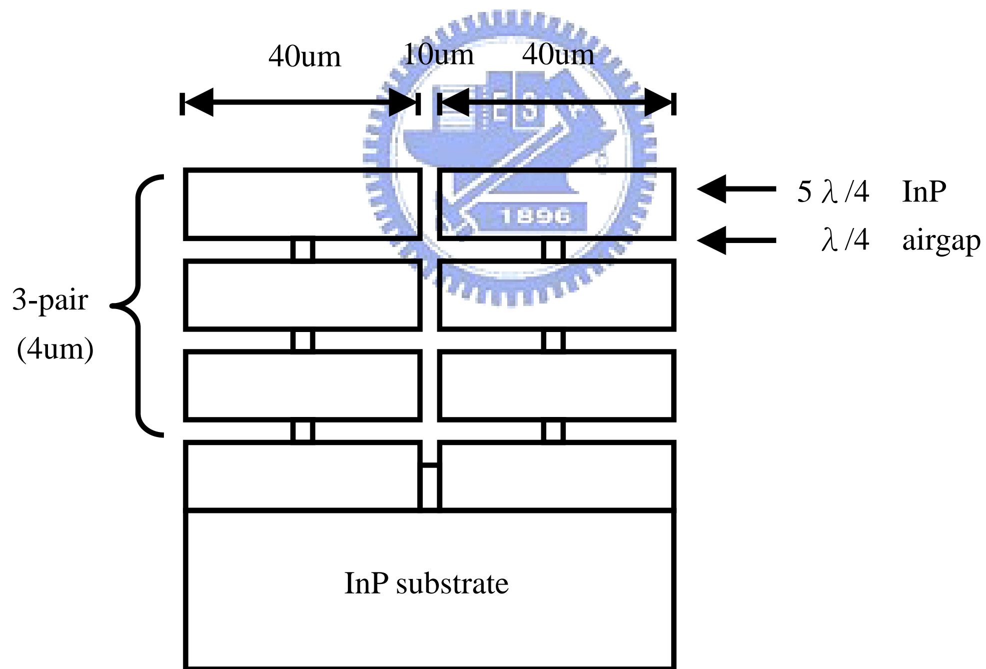

(b)

Figure 5-17 (a)Schematic diagram of the dry etched mesas. (b)Schematic cross section of the InP/airgap DBRs.

Figure 5-18 The cross section of the stable suspended InP/airgap DBRs captured by SEM.

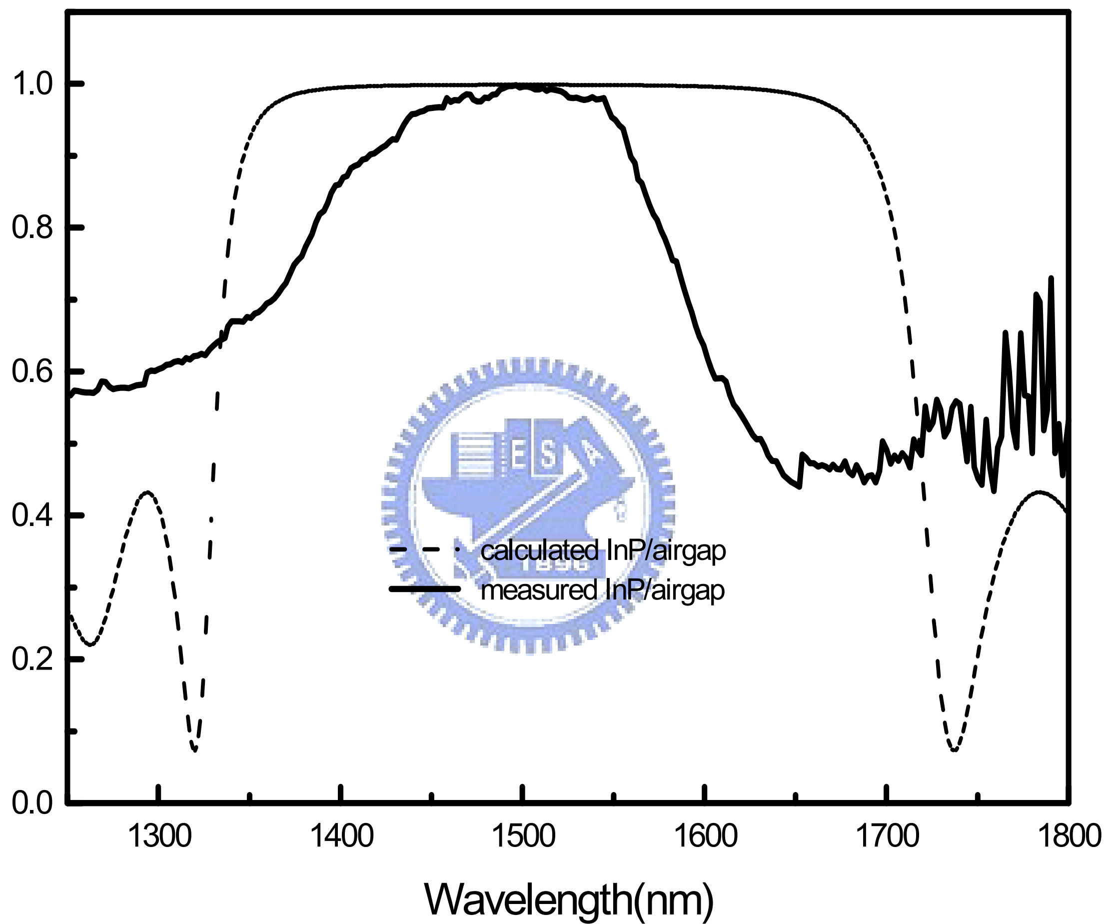

Figure 5-19 The calculated and measured reflectivity curves of the InP/airgap DBRs. Peak reflectivity is 99.9% at 1.54 μm.

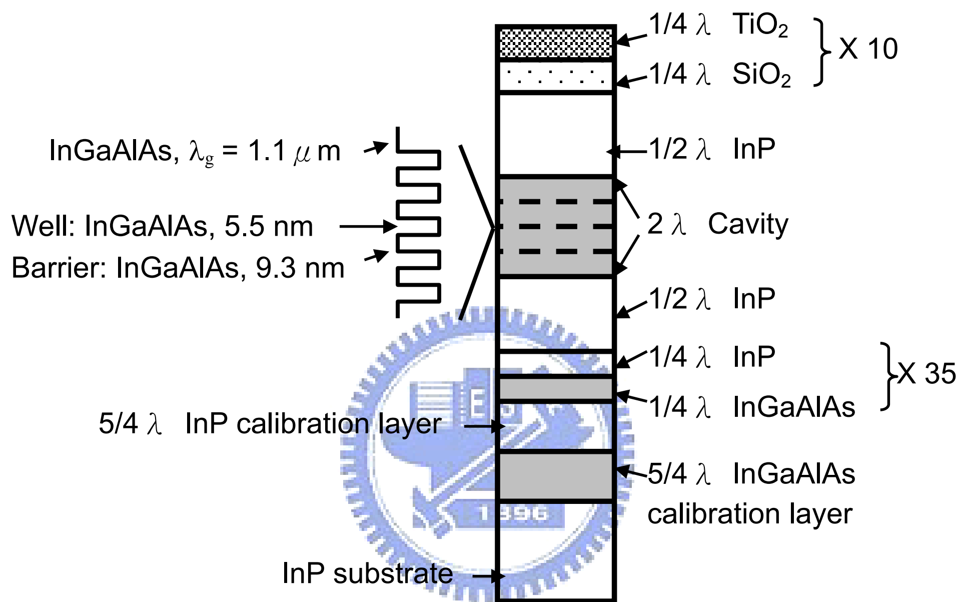

Figure 5-20 Schematic cross section of VCSELs.

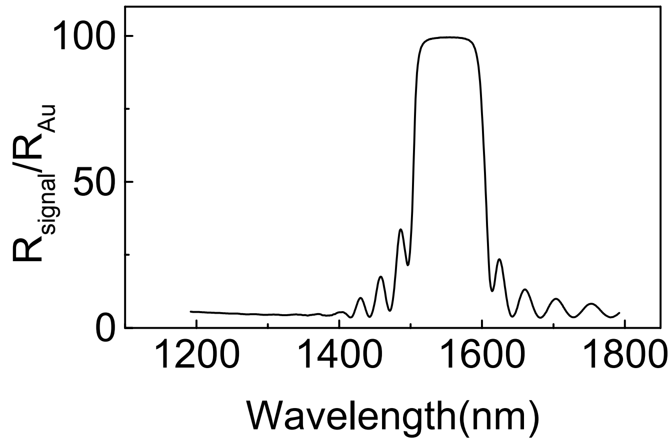

(a)

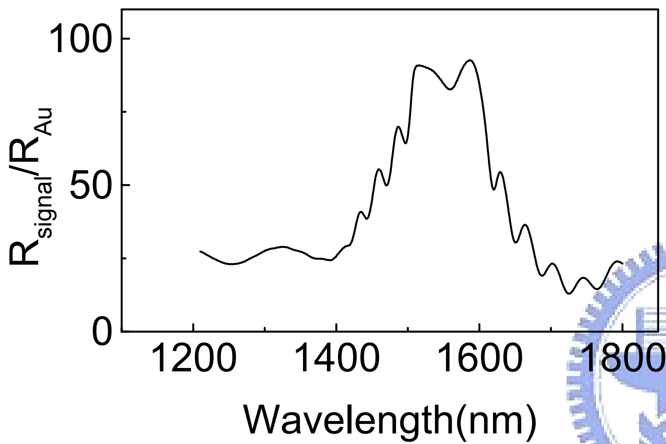

(b)

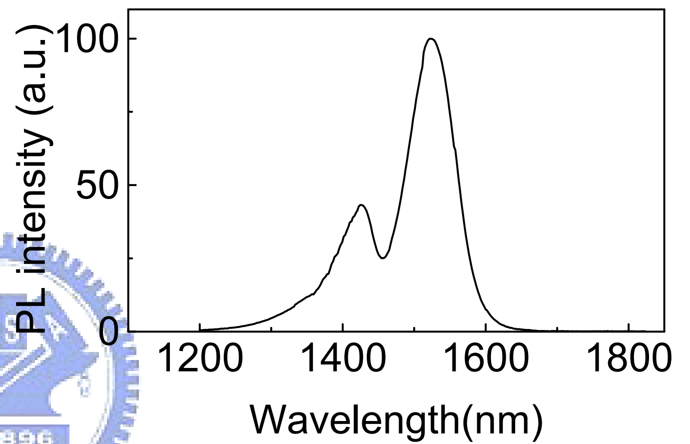

(c)

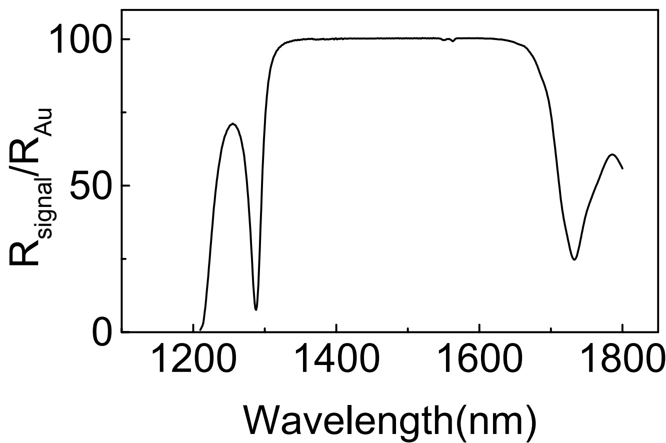

(d)

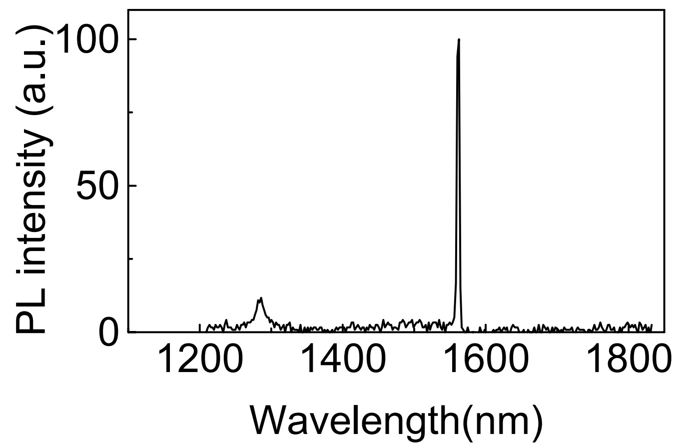

(e)

Figure 5-21 (a) Reflectance spectrum of 35 pairs InGaAlAs/InP DBRs. (b) Reflectance spectrum of a half VCSEL structure. (c) PL spectrum of SCMQWs. (d) Reflectance spectrum of a complete VCSEL structure. (e) PL spectrum of a complete VCSEL structure.

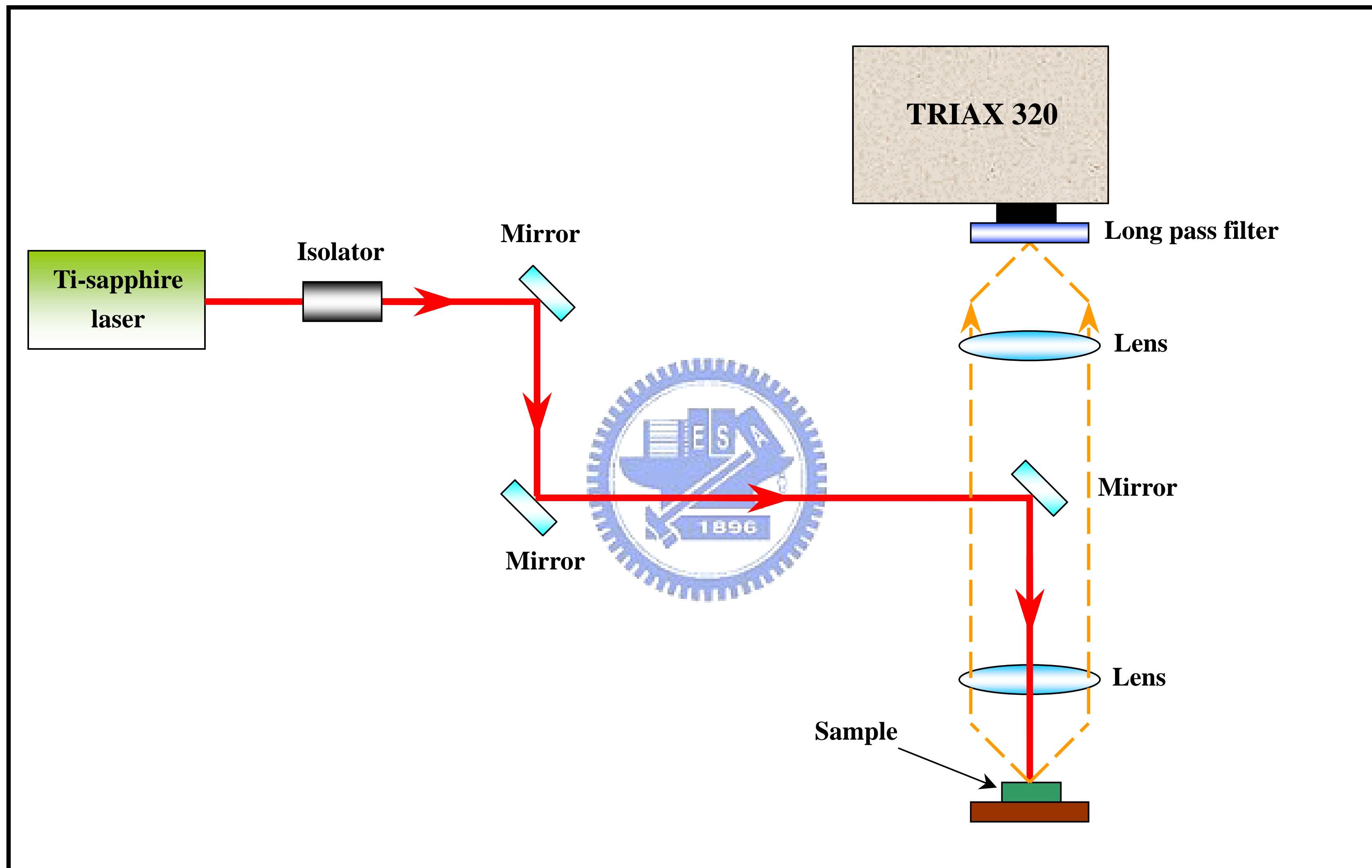

Figure 5-22 Schematic setup of optical pumping.

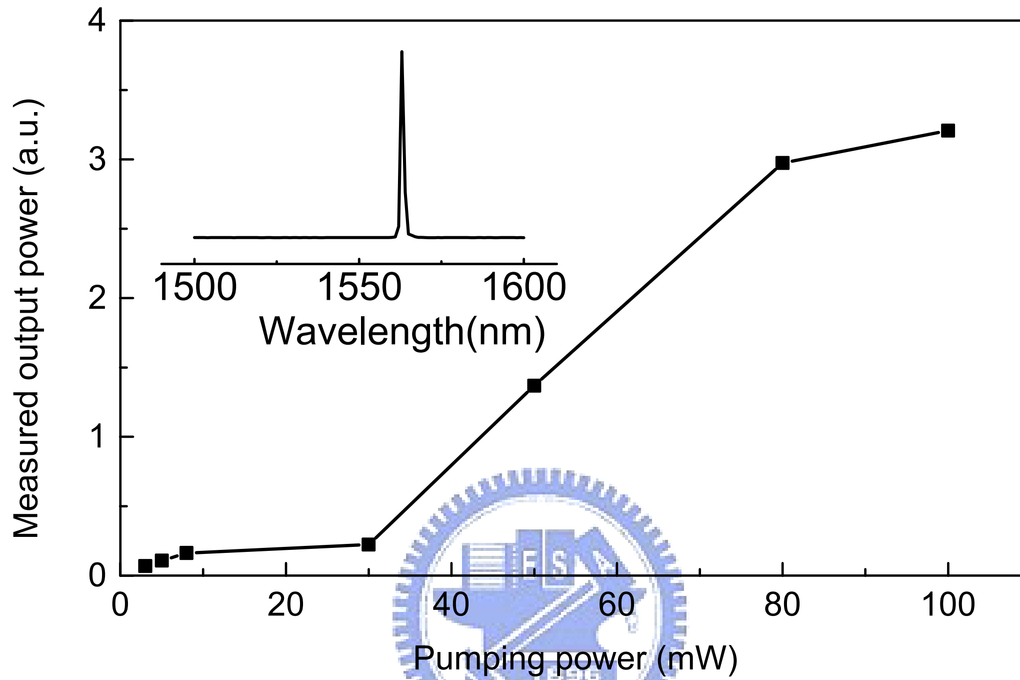

Figure 5-23 The VCSEL output power versus input laser pumping power characteristics at room temperature. The inset shows the VCSEL emission spectrum at the pumping power above the threshold. Peak emission wavelength is 1562 nm.

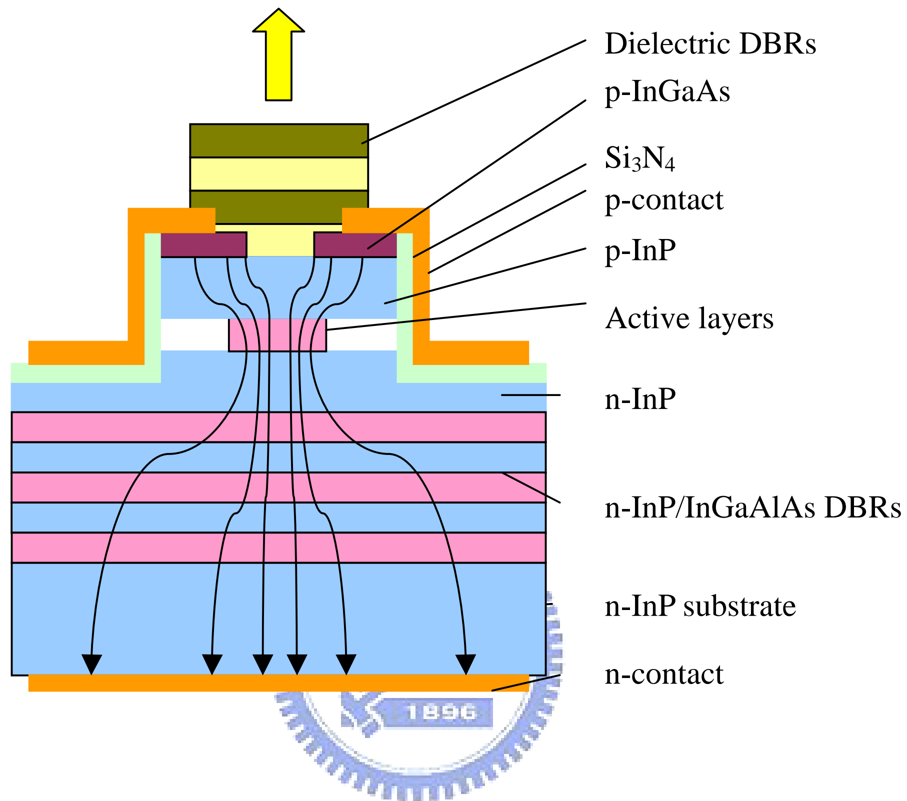

Fig. 5-24 Schematics of monolithically grown electrically pumped LW-VCSELs with Selectively etched undercut apertures.

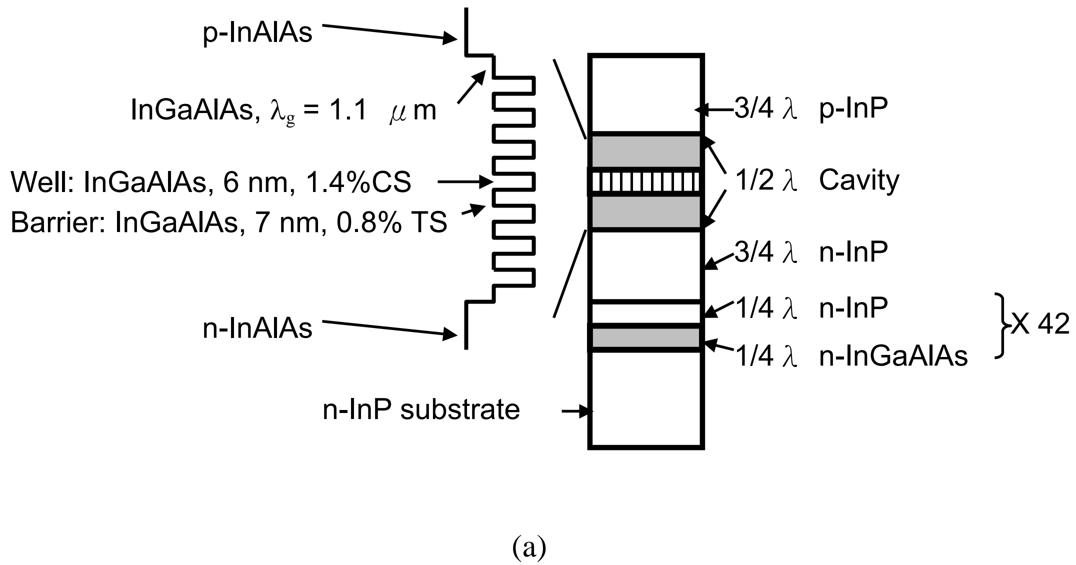

(a)

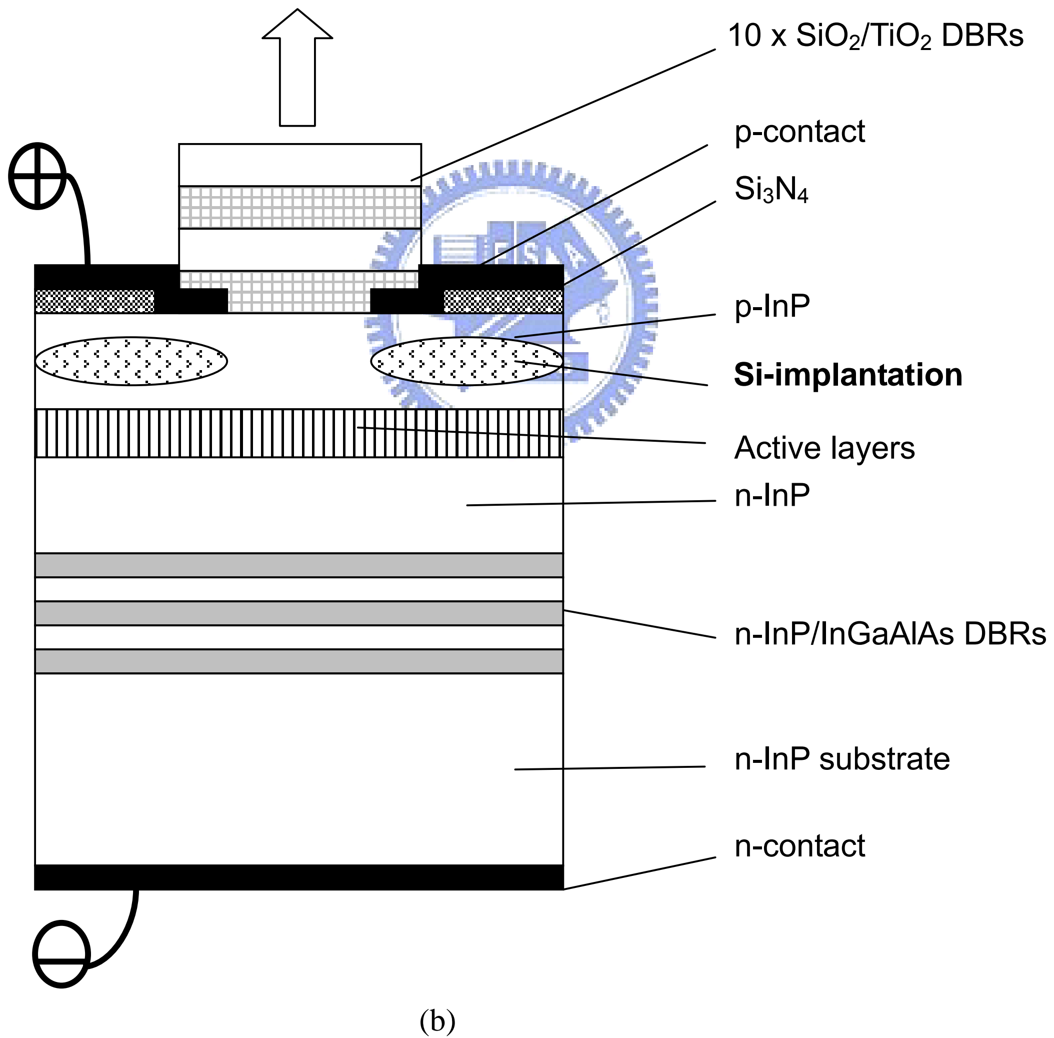

(b)

Figure 5-25 (a) Detailed descriptions of LW-VCSEL epitaxial structure preparing for ion-implantation. (b) Schematic of LW-VCSEL with Si-implanted current aperture.

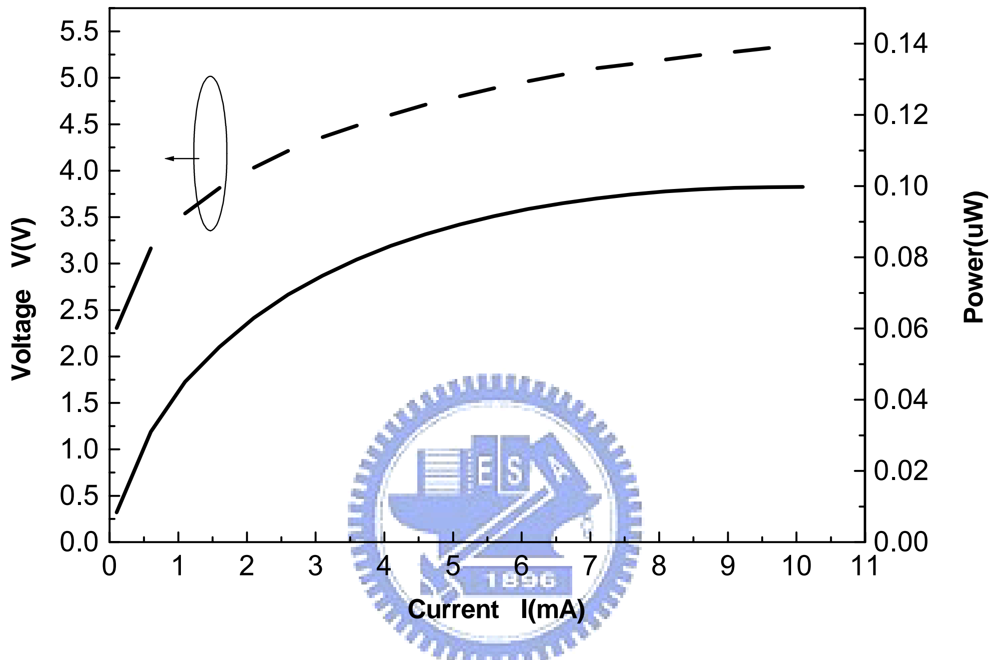

Figure 5-26 The voltage (dash line) and emission light output (solid line) versus driving current characteristics for InP-based LW-VCSELs with Si-implantation.

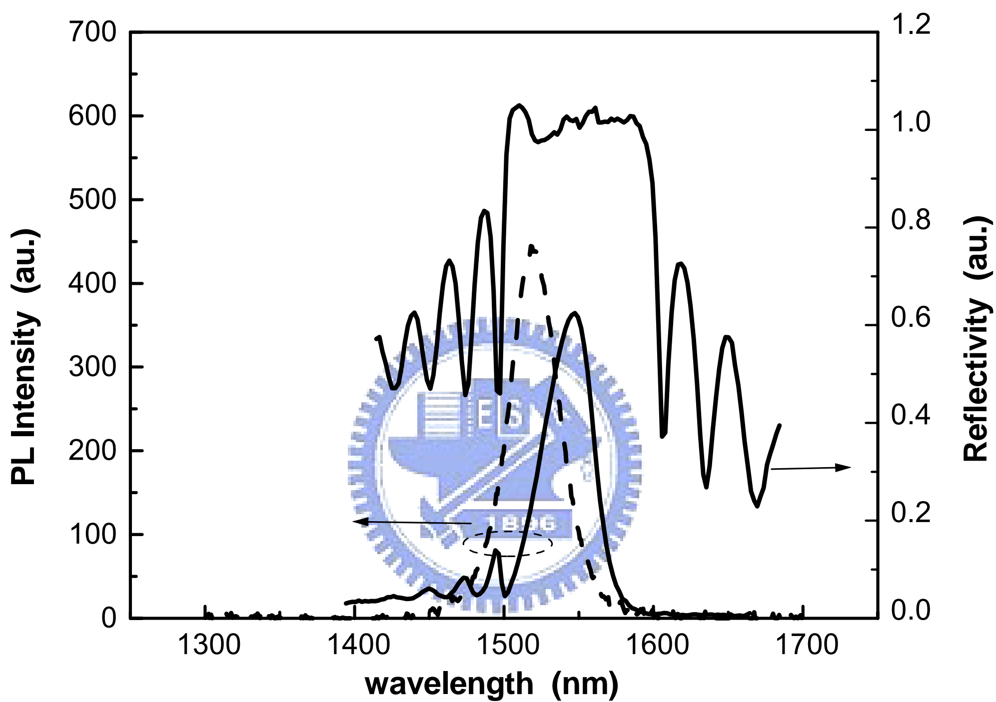

Figure 5-27 The reflectivity and PL curves (solid line) are measured with only the half-cavity. The PL peak is 1547.4 nm with FWHM of 38.6 nm in comparisons to 108.3 nm for PL curve of the original MQW. The dashed line is the EL spectrum for the full cavity structure of the LW-VCSEL with Si-implantation.

p-InAlAs

InGaAlAs, λ_g = 1.1 μm

Well: InGaAlAs, 6 nm, 1.4%CS

Barrier: InGaAlAs, 7 nm, 0.8% TS

n-InAlAs

n-InP

Tunnel junction

1/2 λ p-InP

1/2 λ Cavity

n-InP substrate

(a)

p^{++}-InGaAlAs, λ_g = 1.425 μm, 20 nm

p-InP

n^{++}-InP, 4nm

n-InP

n^{++}-InGaAs, 4 nm

(b)

p^{++}

n^{++}

-

+

(c)

Figure 5-28 (a) (b) Detailed descriptions of epitaxial structure for long wavelength LED with tunnel junction. (c) Schematic of operation principal in tunnel junction under the reverse bias.

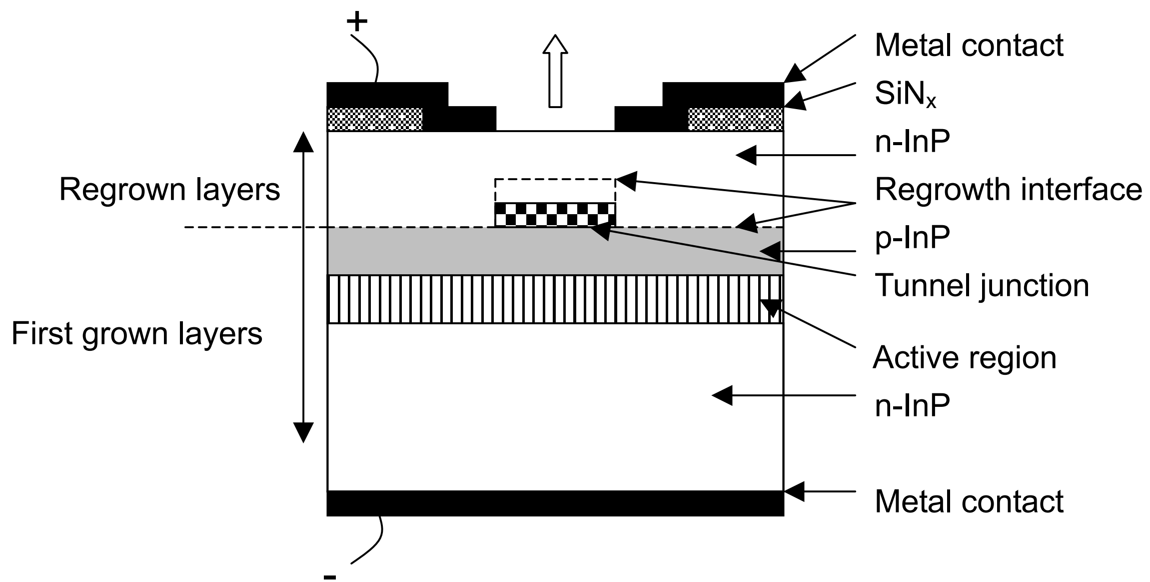

(a)

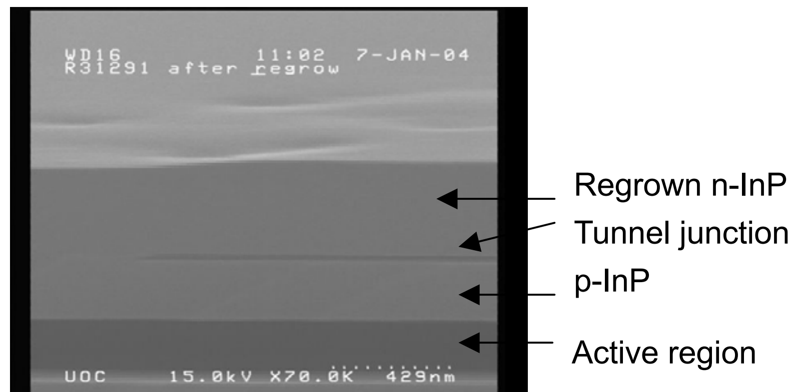

(b)

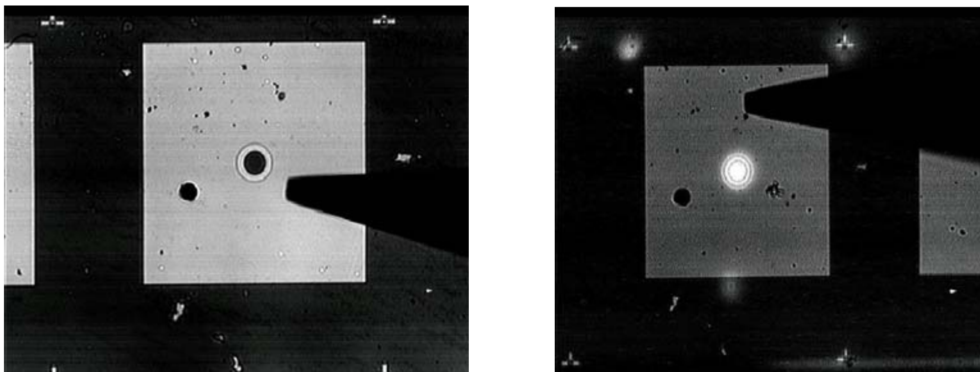

(c)

Figure 5-29 (a) Schematic of long wavelength LED structure with buried tunnel junction. (b) The cross-section SEM image of the buried tunnel junction after the regrowth process. (c) The top view of the long wavelength LED before and after electrical operations.

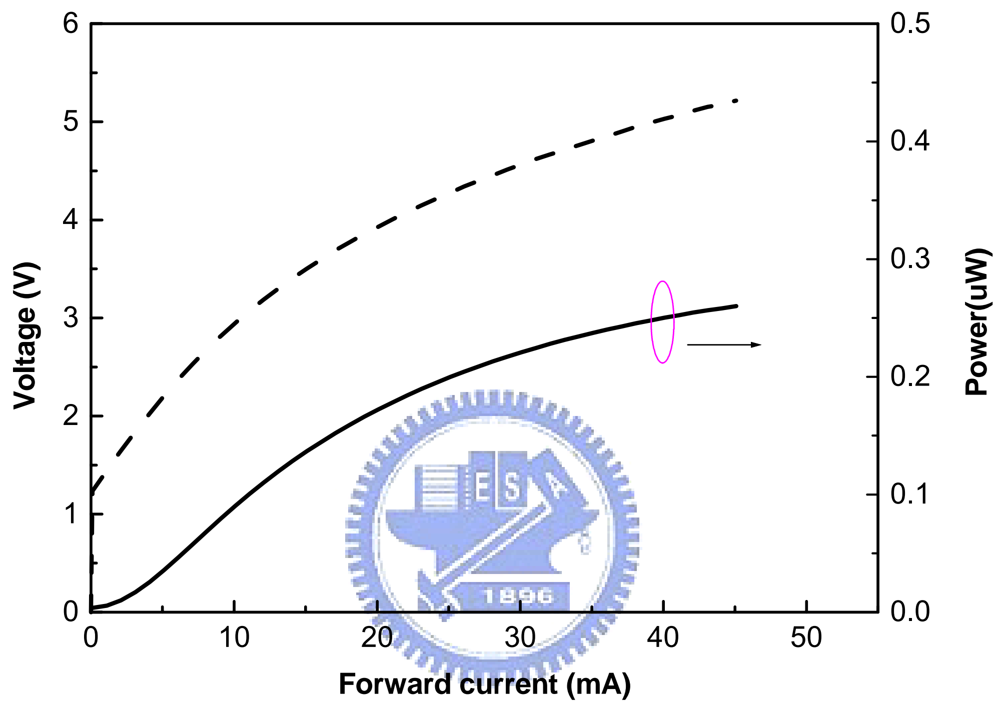

Figure 5-30 The voltage (dash line) and emission light output (solid line) versus driving current characteristics for the long wavelength LED with buried tunnel junction.

CHAPTER 6 Conclusions

6.1 Summary of short wavelength VCSELs

For InGaN/GaN-based VCSELs, we investigated low-In-content $In_xGa_{1-x}N$/GaN (x~0.18) QWs by MOCVD with various well thickness and number by means of photoluminescence (PL) and high-resolution x-ray diffraction (HRXRD) measurements. Finally, we also compared the different influences of these different growth conditions on the performance of IenGaN/GaN-based LEDs. It is shown clearly that the EL output power at 20 mA of low In-content (< 20 %) LED sample with six-wells and 3.2 nm-thick thickness is highest.

We have studied the effect of Si doping on the GaN barriers. As increasing Si doping in the barriers, the PL shows an increase of emission intensity and a blueshift of peak energy. With the same MQW emission peak at about 460 nm and driving current of 20 mA, it is found that the light output power of the LED with Si flow rate of ~ 0.19 sccm is ~20 % of magnitude higher than that of LED with Si flow rate of ~ 0.12 sccm. This result shows that PL intensity and LED output power of the MQW samples with Si-doped barrier layers are dramatically increased.

We designed and fabricated a GaN-based LED with an omnidirectional 1D PC. The omnidirectional 1D PC composed of alternately stacked TiO_2 and SiO_2 layers possesses a PBG within the blue regime of interest. With the same MQW emission peak at about 450 nm and driving current of 20 mA, it is found that the light output powers of the LED with and without 1D PC are about 11.7 mW and 6.5 mW, respectively. This result shows that the omnidirectional 1D PC has a higher reflectance and a wider reflection angle than the conventional DBR. Our finding has promising potential for the enhancement of output powers of commercial light

emitting devices.

We have demonstrated the optically pumped GaN-based VCSELs structure grown by MOCVD. The 25 pair AlN/GaN DBR structure and 3λ cavity layer were consisted in this VCSEL structure. The AlN/GaN mirror with 25 pairs of DBR can achieve the high reflectivity of 94 % and the wide FWHM of reflectance spectrum about 33 nm. The Ta_2O_5/SiO_2 mirror with 8 pairs of DBR can achieve the high reflectivity of 97.5 % and the wide FWHM of reflectance spectrum about 115nm. The stimulated emission of fabricated GaN-based VCSEL was achieved and observed by using the optical pumping system. The GaN VCSEL emits 448nm blue wavelength with a linewidth of 0.25 nm. It evidently expresses the behavior from spontaneous emission to stimulated emission.

6.2 Summary of long wavelength VCSELs

For InP-based VCSELs, we found out the optimized conditions of the active layers established by EEL. We have grown the InP/InGaAlAs and the InAlAs/InGaAlAs DBRs with excellent electrical and optical properties using MOCVD and the growth interruption technique. The DBRs show low resistance with an estimated resistance per DBR pair of 1.2×10^{-5} Ωcm^2 and 2.2×10^{-5} Ωcm^2 for InP/InGaAlAs and InAlAs/InGaAlAs DBRs, respectively. The maximum reflectivity of both DBRs exceeds 99% with a stopband width of 110 nm for InP/InGaAlAs DBR and 100 nm InAlAs/InGaAlAs DBR.

We have designed, fabricated, and demonstrated a rigid InP/airgap structure with high reflectivity at 1.54 μm using InGaAs as the sacrificial layer. The 3-pair InP/airgap DBR structure with 5 λ/4 thick InP layer was fabricated from the MOCVD

grown InP/InGaAs structure using H_2SO_4 solution as etching agent. The InP/airgap DBR has a peak reflectivity of 99.9 % at 1.54 μm with a stopband width of about 200 nm. The InP/airgap DBR structure was rigid and stable and should be applicable for 1.5 μm VCSELs.

We have successfully demonstrated the optically pumped InP-based VCSELs with the 35 pairs InP/InGaAlAs DBRs and 10 pairs SiO_2/TiO_2 top dielectric mirrors and a 2λ thick cavity composed periodic strain compensated MQWs to fully utilize the gain in every quantum well. The optically pumped VCSELs operated at room temperature with the threshold pumping power of 30 mW. The wavelength of the output beam is 1562 nm. The minimum linewidth above threshold is 1 nm limited by the resolution of the spectrometer. The equivalent threshold current density is calculated to be 2 kA/cm^2. We developed electrically driven continuous wave LW-VCSELs by using selectively etched undercut apertures technique, Si-implant technique, regrowth technique.

Paper list

(一) Journal paper:

1. C. F. Chu, Y. K. Wang, C. C. Yu, J. Y. Tsai, F. I. Lai, and S. C.Wang, "Low resistance ohmic contacts on p-type GaN using Ni/Pd/Au metallization," Applied Physics Letters, Vol. **77**, 3423, Nov.20, (2000).
2. C. F. Chu, C. K. Lee, C. C. Yu, Y. K. Wang, J. Y. Tsai, C. R. Yang, and S. C. Wang," High etching rate of GaN films by KrF excimer laser," Materials Science & Engineering B**82**, 42, (2001).
3. C. C. Yu, C. F. Chu, J. Y. Tsai, and S. C. Wang, "Investigation of beryllium implanted P-type GaN," Materials Science & Engineering B**82**, 82, (2001).
4. C. C. Yu, C. F. Chu, J. Y. Tsai, C. F. Lin, W. H. Lan, C. I. Chiang, and S. C. Wang, " Beryllium-implanted P-type GaN with high carrier concentration," Jpn. J. Appl. Phys.Vol. **40**, L417-L419, (2001).
5. C. C. Yu, C. F. Chu, J. Y. Tsai, S. C. Wang, "Electrical and optical properties of Be-implanted p-type GaN materials," J. Appl. Phys. Vol. **92**, No.4, 1881, (2002).
6. C. C. Yu, C. F. Chu, J. Y. Tsai, H. W. Huang, T. H. Hsueh, C. F. Lin, S. C. Wang, "Gallium Nitride nanorods fabrication by inductively coupled plasma reactive ion etching," Jpn. J. Appl. Phys. Vol. **41**, L910-L912, (2002).
7. Lu T.C., J. Y. Tsai, Chu J.T., Chang Y.S., Wang S.C., "InP/InGaAlAs distributed Bragg reflectors grown by low-pressure metal organic chemical vapor deposition", J CRYST GROWTH **250** (3-4): 305-312 (2003).
8. J. Y. Tsai, T. C. Lu and S. C. Wang, "High reflectivity distributed Bragg reflectors for 1.55 μm VCSELs using InP/airgap", Solid-State Electronics Vol **47**,10,1825-1828,

(2003).

9. T. C. Lu, J. Y. Tsai, H. C. Kuo, S. C. Wang, “Comparisons of InP/InGaAlAs and InAlAs/InGaAlAs distributed Bragg reflectors grown by metalorganic chemical vapor deposition”, Materials Science and Engineering B**107**, 66–69 (2004).
10. H. W. Huang, C. C. Kao, J. Y. Tsai, C. C. Yu, C. F. Chu, J. Y. Lee, S. Y. Kuo, C. F. Lin, H. C. Kuo and S. C. Wang, “Effect of rapid thermal annealing on beryllium implanted p-type GaN”, Material Sciences & Engineering B-Solid State Materials for Advanced Technology **107** (3): 237-240 (2004).
11. C. C. Kao, H. W. Huang, J. Y. Tsai, C. C. Lu, C. F. Lin, H. C. Kuo, and S. C. Wang, “Study of dry etching for GaN and InGaN-based laser structure using inductively coupled plasma reactive ion etching,” Materials Science and Engineering B**107**, p.283-288, (2004).
12. J. Y. Tsai, D. C. Wang, Y. H. Chang, T. H. Hseuh, M. Y. Tsai, H. C. Kuo and S. C. Wang, “Optical properties of ultra-high-density InGaN quantum dots grown by metalorganic chemical vapor deposition”, J. Appl. Phys. (submitted in Nov 2004)

(二) Conference paper:

1. Huimei Fang, Y. K. Wang, J. Y. Tsai, C. F. Chu, and S. C. Wang, "Atomic force microscope study of GaN films grown by hydride vapor phase epitaxy," SPIE Photonics Technology into the 21th Century: Semiconductors, Microstructures, and Nanostructures, Vol. 3899, paper , Nov. 1999
2. H. Fang, Y. K. Wang, J. Y. Tsai, C. F. Chu, and S. C. Wang, "Optical and structural properties of GaN films," Optics and Photonics Taiwan '99, paper FR-16-A-6, Dec. 1999
3. C. C. Yu, J. Y. Tsai, C. F. Chu, and S. C. Wang, "Study of Be-implanted P-type GaN,"

Optics and Photonics Taiwan '99, paper TH-12-A-8, Dec. 1999

4. C. F. Chu, Y. K. Wang, J. Y. Tsai, C. C. Yu, H. M. Fang, and S. C. Wang, "Investigation of KrF excimer laser etching of GaN films,"Optics and Photonics Taiwan '99, paper FR-16-A-7, Dec. 1999
5. C. F. Chu, C. K. Lee, C. C. Yu, J. Y. Tsai, S. C, Wang, and C. R. Yang," High etching rate of GaN films by KrF excimer laser," International Conference on Electronic Materials & European Materials Research Society Spring Meeting, paper C/P6, May, 2000
6. C. C. Yu, C. F. Chu, J. Y, Tsai, S. C. Wang, W. H. Lan, C. I. Ching, "Investigation of Beryllium implanted P-type GaN," International Conference on Electronic Materials & European Materials Research Society Spring Meeting, paperC/P7, May, 2000
7. C. F. Chu, C. K. Lee, C. C. Yu, Y. K. Wang, J. Y. Tsai, C. R. Yang, and S. C. Wang, "Laser etching GaN materials under various atmosphere conditions," International Workshop on Nitride Semiconductors (IWN2000), paper PME-33, Sept. 2000
8. C. C. Yu, J. Y. Tsai, C. F. Chu, and S. C. Wang, "Photoluminescence and electrical property of Beryllium implanted p-type GaN," International Workshop on Nitride Semiconductors (IWN2000), paper PTE-17, Sept. 2000
9. C. C. Yu, J. Y. Tsai, C. F. Chu, and S. C. Wang, “Beryllium implanted Mg-doped GaN with high hole concentration and low ohmic contact resistance,” International Photonics Conference, paper Th-S1-C001, Dec. 2000
10. S. C. Wang, C. F. Chu, C. C. Yu, Y. K. Wang, J. Y. Tsai, and F. I. Lai, “New metallization scheme for low resistance ohmic contacts to p-type GaN,” Proceedings of the International Symposia on III-Nitride Based Semiconductor Electronics and Optical Devices Vol. 2001-1, 139, April, 2001
11. S. C. Wang, C. F. Chu, C. C. Yu, and J. Y. Tsai, “Recent Advances in GaN light emitting devices,” 8th Micooptics Conference (MOC’01), invited paper M3, Oct. 2001
12. H. H. Huang, C. C. Yu, J. Y. Tsai, T. H. Hsueh, C. F. Chu, C. F. Lin, and S. C. Wang, “Dry

etching of GaN and InGaN laser structure using inductively coupled plasma," 2002 MRS Spring Meeting, paper K7.8, April 2002

13. C. C. Yu, C. F. Chu, J. Y. Tsai, H. W. Huang, T. H. Hsueh, C. f. Lin, and S. C. Wang, "Fabrication of controllable size and density GaN nanorods by inductively coupled plasma reactive ion etching," International Symposium on Compound Semiconductors (ISCS 2002), paper Tu-P-31, Oct. 2002
14. C. C. Yu, C. F. Chu, J. Y. Tsai, H. W. Huang, T. H. Hsieh, C. F. Lin, and S. C. Wang, "Fabrication of the GaN nanostructures by ICP," Optics and Photonics Taiwan '02, paper TB2-5, December 2002
15. J. Y. Tsai, T. C. Lu, and S. C. Wang, "MOCVD growth of InP/InGaAlAs distributed Bragg reflectors," 203rd The Electrochemical Society Meeting, paper J2-0785, May 2003
16. J. Y. Tsai, T. C. Lu, H. C. Kuo, and S. C. Wang, "MOCVD growth of high quality distributed Bragg reflectors for 1.55-μm VCSEL application," Optics and Photonics Taiwan '03, paper PA1-18, December 2003